UniMe
1548

University of Messina

Generalized continua. Foundations, material modeling, and uncertainty quantification.

Department of Engineering
PhD Program in Ingegneria e Chimica dei Materiali e delle Costruzioni (XXXVI Cycle, SSD ICAR/08)

PhD Candidate:
Gabriele La Valle

PhD Coordinator:
Prof. Edoardo Proverbio

PhD Supervisor:
Prof. Giovanni Falsone

Academic Year 2022/2023

Generalized continua. Foundations, material modeling, and uncertainty quantification.

Gabriele La Valle

This dissertation is submitted for the degree of
Doctor of Philosophy in Ingegneria e Chimica dei Materiali e delle Costruzioni

January 2024

I would like to dedicate this thesis to my loving parents. . .

Declaration

I hereby declare that except where specific reference is made to the work of others, the contents of this dissertation are original and have not been submitted in whole or in part for consideration for any other degree or qualification in this, or any other university. This dissertation is my own work and contains nothing which is the outcome of work done in collaboration with others, except as specified in the text and Acknowledgements.

Gabriele La Valle
January 2024

Acknowledgements

I thank my supervisor Professor Giovanni Falsone from University of Messina for the guidance and support. I thank Professor Francesco dell'Isola from University of L'Aquila who helps me in developing my skills both scientifically and personally. I would like to particularly thank Professor Christian Soize from Laboratoire Modélisation et Simulation Multi Echelle (MSME), Université Gustave Eiffel, for being an incredible mentor during my period of study and research in France.

I thank all the other colleagues, researchers, and professors who have worked with me in producing the results of this thesis: B.E. Abali, A. Ciallella, B. Desmorat, I. Giorgio, F. Hild, S. Massoumi, B. Smaniotto, M. Spagnuolo, E. Turco, A. Vintache.

Abstract

This dissertation is devoted to the modeling of architectured metamaterials and particle-based materials. Such materials generally necessitate the use of sophisticated continuum models to properly characterize their mechanical behavior and make accurate numerical predictions. To this purpose, generalized continua, which improve the classical (or Cauchy) continuum, have been a topic of interest in the last decade. This dissertation begins with a uniform presentation of four different generalized continua, namely the micropolar continuum, the micromorphic continuum, the second-gradient continuum, and the second-gradient-micropolar continuum. Special attention is paid to the Euler-Lagrange equations that are derived using the least action principle and the Levi-Civita tensor calculus. Then, the dissertation focuses on pantographic structures that represent a paradigmatic case of architectured metamaterials described by generalized continua. A novel torsional energy for pantographic sheets is proposed and experimentally validated. A novel second-gradient continuum model for pantographic blocks is proposed and experimentally validated through digital volume correlation techniques. The effect of pivots-related local defects on the mechanical response of pantographic sheets is investigated via a noninformative prior probabilistic model. Finally, random generalized continuum models for particle-based materials with uncertain constitutive parameters and fields are analyzed: response and numerical identification of random Timoshenko-Ehrenfest beams are carried out via a noninformative prior probabilistic model, and sensitivity analysis of a second-gradient continuum model for particle-based materials is performed via an informative prior probabilistic model based on the maximum entropy principle. To make the work self-consistent, in Appendix, an overview of Levi-Civita tensor algebra is given.

Table of contents

List of figures

List of tables

Chapter 1

General Introduction

1.1 Research positioning

The term *generalized continua* denotes the set of theories that refine and develop the *classical Cauchy continuum*. In the last decade, generalized continua have become an important ingredient for the mechanical modeling of materials for which the microstructure can be considered such as particle-based materials and *architectured metamaterials*. On the one hand, the term *metamaterials* is generally used to denote those materials that cannot be described by classical Cauchy continuum and that require generalized continua. On the other hand, the term *architectured metamaterial* is generally used to denote those materials that require generalized continua, while being formed by assembling components that can be described by classical Cauchy continuum. It should be noted that the term *granular materials* is improperly used in the literature to refer to particle-based materials.

This dissertation specifically focuses on the study of the most common generalized continua, on the construction, identification, and on simulations of deterministic and random models for particle-based materials and pantographic structures, the latter being a paradigmatic case of architectured metamaterials. Moreover, we present novel contributions to uncertainty quantification within the framework of generalized continua.

Among the most common generalized continua, one can list the *micropolar continuum*, the *micromorphic continuum*, the *second-gradient continuum*, and the *second-gradient-micropolar continuum*.

In micropolar continuum, each material particle is modeled as a rigid body with six degrees of freedom. The initial concepts regarding micropolar continuum were discussed already at the end of the 19th century by Kelvin, Helmholtz, Duhem, Voigt, and Cosserat brothers, and summarized in [27]. Later results can be found in Eremeyev et al. [41], Altenbach et al. [5, 4], Eremeyev and Pietraszkiewicz [42]. Interesting applications devoted

to particle-based materials can be found in [90, 96] and chiral mechanical metamaterials in [52, 58].

More generally, micromorphic continuum takes into account the micro deformation of each particle [43, 62, 53]. Particle-based material and chiral metamaterial applications were carried out by [95, 93, 28].

Finally, the deformation energy function combines the second-order derivatives of displacements in second-gradient continuum. Gabrio Piola was a pioneer of second-gradient continuum, whose contributions were summarized in [34, 30–32, 133]. It has become popular for describing particle-based materials [146] and metamaterials [142, 22, 24, 3, 33]

Regarding second-gradient-micropolar continuum, it appears there is no current literature. Yet, as will be demonstrated below, it lends to the physical significance of the double couples, which play a crucial role in the *modified couple stress theory* [145] that has widely been used in many research works [111, 87, 112].

The primary goals of this work are to provide a uniform presentation of the listed generalized continua via the *least action principle* (or, more generally, the *principle of virtual work*), to demonstrate the ability of second-gradient discrete and continuum models to describe pantographic structures, and to provide generalized models for particle-based materials taking into account uncertainties. In this dissertation, integral nonlocal theories [70, 45] will not be discussed (see Section 5.2 on future perspectives)

Pantographic structures are metamaterials consisting of a discrete grid of beams and *pivots* (also known as *hinges* in the literature) whose homogenization results in second-gradient mechanical models [3, 17, 11, 109]. Some of these homogenized models have been experimentally validated in [10, 12]. Numerous publications have contributed to the body of knowledge on this subject [22, 23, 38, 137]. In the present work, the torsional energy currently used for modeling pantographic sheets (2D) has been improved and experimentally validated, and a first second-gradient model for pantographic blocks (3D) has been proposed and experimentally validated.

Uncertainty quantification is essential for predictive engineering sciences. A review of stochastic methods for particle-based-effects uncertainties at the microscale on their response at the macroscale is provided in [100] using only first-gradient continuum models. Despite the inherent randomness of particle-based materials, uncertainties have not yet been accounted for in the second-gradient continuum theories; only a small number of works involving uncertain quantities have recently been proposed, not for particle-based materials but for fiber materials [16, 110]. In this work, the impact of uncertainty in material modeling is investigated for pantographic structures, micropolar beams, and particle-based second-gradient materials. In the first two cases, noninformative prior models of uncertainties have been used. In

the third case, an informative prior model has been developed using the *maximum entropy principle*. This work provides novel contributions to the analysis of pantographic sheets and particle-based second-gradient continua in accounting for uncertainties. Throughout the entire dissertation, it is emphasized how least action principle and maximum entropy principle can systematically be applied to derive fundamental equations in continuum mechanics and probabilistic models, respectively.

1.2 Organization of the dissertation

This dissertation is organized as follows. The Euler-Lagrange equations and the main theoretical concepts related to the most common generalized continua are presented in **Chapter 2**. **Chapter 3** concerns the modeling and experimental testing of pantographic structures. **Chapter 4** investigates micropolar beams and an existing particle-based second-gradient continuum. In **Chapter 3** and **4**, uncertainties related to the material parameters are considered. Below is a detailed explanation of these chapters.

- **Chapter 2** focuses on the derivation of Euler-Lagrange equations for the micropolar, the micromorphic, the second-gradient, and the second-gradient-micropolar continua. The equations are derived using the least action principle and the Levi-Civita tensor calculus, and they are valid for any deformation measure and external reference system. It cannot be claimed that the results and ideas presented in this chapter are completely novel, but to the author knowledge, there is no other presentation that provides such a uniform, comprehensive, and in-depth analysis of the role played by least action principle and tensor calculus on generalized continua.

- In **Chapter 3**, for modeling pantographic sheets (2D), a novel torsional energy is proposed and experimentally validated, which improves the one currently used in the literature. Despite being developed within the framework of discrete models, it is applicable within the framework of second-gradient continua. In addition, for modeling pantographic blocks (3D), a novel second-gradient continuum model is also proposed and experimentally validated. In the latter case, the experimental validation is conducted using digital volume correlation (DVC) techniques. Finally, using a noninformative prior probabilistic model, the effects of pivots-related local random uncertainties on pantographic sheets (2D) are studied.

- In **Chapter 4**, micropolar Timoshenko-Ehrenfest macro- and micro-beams with random material parameters are investigated using noninformative prior probabilistic models to account for uncertainties. Moreover, an informative prior probabilistic model for a

particle-based second-gradient continuum with uncertain parameters and uncertain constitutive fields is also proposed, which is based on the use of maximum entropy principle.

The notation is defined subsection by subsection.

1.3 Summary of the contributions

This dissertation deals with the foundation of generalized continua, modeling, and uncertain quantification of particle-based materials and pantographic structures, the letter being a paradigmatic case of architectured metamaterials. The main contributions of this work are summarized below.

- We unsuccessfully searched for a uniform presentation of generalized continua in the literature. Consequently, we provide a uniform presentation of generalized continua based on the least action principle and Levi-Civita tensor calculus. The micropolar continuum, the micromorphic continuum, the second-gradient continuum, and the second-gradient-micropolar continuum are studied, and the Euler-Lagrange equations are derived by considering a generic external reference system. It is proven that second-gradient-micropolar continuum implies the existence of double couples.

- We introduce and experimentally validate a novel deformation energy function for modeling the torsional behavior of pivots of pantographic sheets (2D) under bias extension tests.

- Similarly to the 2D case, we introduce and experimentally validate a novel second-gradient continuum model for modeling pantographic blocks (3D) under 3-point flexure tests. The experimental validation is based on digital volume correlation techniques.

- Within an application framework, we show that local pivot-related random defects do not significantly affect the mechanical response of pantographic sheets due to the redundant connections inside them.

- On one hand, we show that the analysis of macro-beams with random material parameters allows us to identify the Young modulus. On the other hand, we show that the analysis of micro-beams with random material parameters allows us to identify one 3D micropolar material parameter responsible for scale effects.

- After improving the analytical relationship between the deformation tensors of an existing second-gradient continuum model for particle-based materials, we formulate a

novel probabilistic model based on the maximum entropy principle for the particle-pair distance and the microscale stiffness parameters describing particle interactions. First, particle-pair distance and microscale stiffness parameters are assumed to be independent of spatial and orientation directions. Within an application framework, we prove that the randomness of the particle-pair distance between two consecutive particles has a major effect on the randomness of the mechanical response of a particle-based material. Second, particle-pair distance and microscale stiffness are modeled as random fields. Within an application framework, we prove that the coefficient of variation of the axial displacement is smaller than the coefficient of variations of the transversal one. Moreover, by increasing the number of particles with random positions, the particle-pair distance between two consecutive particles has a minor effect on the randomness of the mechanical response of a particle-based material.

Chapter 2

Uniform presentation of generalized continua

Following the ideas of Gabrio Piola, Joseph-Louis Lagrange, Raymond Mindlin, Richard Toupin, Leonid Ivanovich Sedov, Gerard Maugin, Paul Germain, and others, we have recognized the least action principle and, more generally, the principle of virtual work as the most effective tool for deriving the fundamental equations of a given theory of continuum mechanics. In addition, since the expression of the deformation energy density characterizes the type of admissible external loads for a considered continuum model, least action principle permits the determination of the external actions that the considered continuum model can sustain. This chapter provides an overview of the fundamental concepts about the micropolar, the micromorphic, the second-gradient, and the second-gradient-micropolar continua. Least action principle and Levi-Civita tensor calculus are systematically applied. Fundamental concepts of the Levi-Civita tensor algebra can be found in Appendix A.1. The methodology is borrowed from [53]. The Levi-Civita tensor calculus is an indispensable tool across various disciplines, including differential geometry, electromagnetism, the theory of relativity, and continuum mechanics. Its roots lie in the theory of matrices and determinants, with initial traces dating back to Leibniz, and its comprehensive development credited to Jacoby and Coyley. Voight was the first to recognize tensors as independent entities, while prominent figures like Grassmann, Hamilton, Gibbs, and Cristoffel also contributed to the contemplation of tensors. The modern version of tensor calculus can be traced back to the absolute tensor calculus of Ricci and Levi-Civita. To underscore the efficiency of the methods pioneered by Ricci and Levi-Civita, we echo Einstein words:

The gravitational equations represent a triumph of the tensor calculus originated by Ricci.

This work does not aim to address all the historical and technical aspects of tensor calculus. However, for further details, refer to [51, 97, 82]. In the following, tensors are referred to generic reference systems, necessitating metric tensors to define scalar products. This approach enables a clear distinction between covariant and contravariant components, crucial for preventing computational errors and easing the shift from a Lagrangian to an Eulerian description. Its practical implications span across significant domains such as astronomy, fluid dynamics, and aerospace engineering.

2.1 The micropolar continuum

Notation

Below A, B, i, and j are integers belonging to $\{1,2,3\}$.

$\mathcal{B}$: initial (Lagrangian) configuration.

$\partial\mathcal{B}$: boundary of $\mathcal{B}$.

Indices denoted by uppercase letters are chosen to indicate components of a tensor in the initial configuration and lowercase letters to indicate components of a tensor in the current configuration. Summation is intended over the repeated indices.

N_A: components of the outward-pointing normal N of $\partial\mathcal{B}$.

X^A: Lagrangian coordinates.

χ^i: component i of the configuration field χ.

v^i: component i of the translation velocity v.

G_{AB}: component (A,B) of the metric tensor G with respect to the initial configuration.

δ^A_B: component (A,B) of the second-order identity tensor I.

g_{ij}: component (i,j) of the metric tensor g in the current configuration.

Q^i_A: component (i,A) of the microrotation tensor Q.

ϑ_{BAj}: component (B,A,j) of the rotation velocity ϑ.

F^i_A: component (i,A) of the gradient of the configuration field F.

ρ: Lagrangian time-independent mass density.

J^{AB}: component (A,B) of the Lagrangian time-independent moment of inertia of material points J.

$\mathcal{A}_\pi$: action functional for the micropolar continuum.

$(\mathbb{P}_\pi)^i_A$: component (i,A) of the micropolar stress tensor $\mathbb{P}_\pi$.

$(\mathbb{M}_\pi)^i_A$: component (i,A) of the micropolar couple stress tensor $\mathbb{M}_\pi$.

$(\mathbb{V}_\pi)_j$: component j of the micropolar couple stress vector $\mathbb{V}_\pi$.

$(B_\pi)_j$: component j of the volumic forces B_π.

$(C_\pi)_j$: component j of the volumic couples C_π.

$(b_\pi)_j$: component j of the surface forces b_π.

$(c_\pi)_j$: component j of the surface couples c_π.

$[S]^T$, S: transpose of the second-order tensor S.

ϵ_{jAB}: permutation (or Levi-Civita) symbol.

$f_{,B}$: partial derivative of the function f with respect to X^B, *i.e*, $f_{,B} = \frac{\partial f}{\partial X^B}$.

dV and ds: volume and surface elements.

2.1.1 Kinematics of the micropolar continuum

The micropolar continuum consists of small, rigid particles, each of which is represented geometrically by a point X. Each particle is considered as a continuum itself at a lower scale, denoted by $S(X)$, whose center of mass is X. We refer to a material point of $S(X)$ by its spatial coordinate X'. With this assumption, one can write

$$(\chi')^i(X,X',t) = \chi^i(X,t) + Q^i_A(X,t)\left((X')^A - X^A\right), \tag{2.1}$$

where χ describes the configuration change of the center of mass X of each particle, the orthogonal microrotation tensor Q describes the rigid rotation of each particle, and χ' describes the configuration change of each material point X' within $S(X)$. These assumptions

allow describing the kinematical properties of each particle in a more refined way with respect to the classical continuum. Let $\mathcal{B}$ be the initial (or Lagrangian) configuration of the centers of mass X. From Eq. (2.1), we get

$$\frac{\partial \left(\chi'\right)^i (X,X',t)}{\partial t} = \frac{\partial \chi^i (X,t)}{\partial t} + \frac{\partial Q^i_A (X,t)}{\partial t} \left((X')^A - X^A \right) \tag{2.2}$$

and

$$\begin{aligned} &\int_{\mathcal{B}} \int_{S(X)} \left(\widehat{\varrho}\,(X,X')\, g_{ij}\, \frac{\partial \left(\chi'\right)^i (X,X',t)}{\partial t}\, \frac{\partial \left(\chi'\right)^j (X,X',t)}{\partial t} \right) dX dX' \\ &= \int_{\mathcal{B}} \left(\varrho\,(X)\, g_{ij} \frac{\partial \chi^i (X,t)}{\partial t}\, \frac{\partial \chi^j (X,t)}{\partial t} + J^{AB}(X)\, g_{ij}\, \frac{\partial Q^i_A (X,t)}{\partial t}\, \frac{\partial Q^j_B (X,t)}{\partial t} \right) dX \,, \end{aligned} \tag{2.3}$$

where

$$\varrho\,(X) = \int_{S(X)} \widehat{\varrho}\,(X,X')\, dX' \tag{2.4}$$

and

$$J^{AB}(X) = \int_{S(X)} \widehat{\varrho}\,(X,X') \left((X')^A - X^A \right) \left((X')^B - X^B \right) dX' \,. \tag{2.5}$$

The function $\varrho\,(X)$ refers to the Lagrangian time-independent mass density and the functions $J^{AB}(X)$ refers to the Lagrangian time-independent moment of inertia of each particle. Eq. (2.5) implies that $J^{AB} = J^{BA}$.

2.1.2 Deformation energy density and deformation measures

We refer to a function as *objective* if it satisfies the so-called principle of frame indifference that consists of three independent postulates: the principle of invariance under Euclidean transformations, the principle of invariance under superposed rigid-body motions, and the principle of frame-invariance of the constitutive equations under the change of observer [102]. In order for a function to be objective and, consequently, to represent an adequate deformation energy density, it must be invariant under a rigid motion in its current configuration. Let $\widetilde{W}^{\mathrm{def}}_{\pi}(\chi, Q, F, \nabla Q, X)$ be the specific deformation energy density. Since it must be objective, the equality

$$\widetilde{W}^{\mathrm{def}}_{\pi}(\chi, Q, F, \nabla Q, X) = \widetilde{W}^{\mathrm{def}}_{\pi}(O\chi + a, OQ, OF, O\nabla Q, X) \tag{2.6}$$

needs to be satisfied for any orthogonal transformation O and for any vector a. For any Q and for any χ, it is natural to choose $O = Q^T$ and $a = -Q^T\chi$. We get

$$\widetilde{W}^{\mathrm{def}}_{\pi}(\chi, Q, F, \nabla Q, X) = \widetilde{W}^{\mathrm{def}}_{\pi}(0, I, Q^T F, Q^T \nabla Q, X) \,. \tag{2.7}$$

Eq. (2.7) implies that if $\widetilde{W}_\pi^{\text{def}}$ is an objective function, then there exists a function W_π^{def} such that

$$\widetilde{W}_\pi^{\text{def}}(0, I, Q^T F, Q^T \nabla Q, X) = W_\pi^{\text{def}}(Q, F, \nabla Q, X) \ , \tag{2.8}$$

yielding

$$\widetilde{W}_\pi^{\text{def}}(\chi, Q, F, \nabla Q, X) = W_\pi^{\text{def}}(Q, F, \nabla Q, X) \ . \tag{2.9}$$

Eq. (2.7) also leads to the deformation measures E_π and Γ_π defined by

$$E_\pi = \frac{1}{2}\left(Q^T F - I\right) \quad , \quad \Gamma_\pi = Q^T \nabla Q \ , \tag{2.10}$$

which have the following component expressions:

$$(E_\pi)_{MN} = \frac{1}{2}\left(g_{ij}\, Q^j_M\, F^i_N - G_{MA}\, \delta^A_N\right) \quad , \quad (\Gamma_\pi)_{MNC} = G_{MA}\left(Q^T\right)^A_i\, Q^i_{N,C} \ . \tag{2.11}$$

It is natural to refer to the tensor E_π as the *micropolar stretch tensor* and to the tensor Γ_π as the *micropolar wryness tensor*. Since $Q^T F$ and $Q^T \nabla Q$ can be expressed as a function of E_π and Γ_π, it follows the existence of a function $\widehat{W}_\pi^{\text{def}}$ such that

$$W_\pi^{\text{def}}(Q, F, \nabla Q, X) = \widehat{W}_\pi^{\text{def}}(E_\pi, \Gamma_\pi, X) \ . \tag{2.12}$$

Micropolar stretch tensor and micropolar wryness tensor are only two of the possible deformation measures that can be introduced. Several alternatives have been proposed in the literature. Instead of Γ_π, some authors (see [102]) prefer to consider the tensor $\mathfrak{K}_\pi$ that, in components, is defined by

$$(\mathfrak{K}_\pi)_{MN} = \frac{1}{2}\, G_{BM}\, \epsilon^{BFC}\, G_{FA}\left(Q^T\right)^A_i\, Q^i_{C,N} \ , \tag{2.13}$$

where ϵ^{BFC} is equal to the permutation symbol ϵ_{BFC} for any B, F, and C. Moreover, Eq. (2.12) can be rewritten to underline the micro-macro relative rotation [76, 91, 71]. In the following, the Euler-Lagrange equations are derived by considering the deformation energy density as an objective function of Q, F, and ∇Q, $W_\pi^{\text{def}}(Q, F, \nabla Q, X)$. Thus, the derived equations are valid for any chosen combination of deformation measures.

2.1.3 Euler-Lagrange equations

Microrotation test function

The subsequent steps allow us to avoid using Euler angles, which would otherwise limit the generality of the dissertation. Let us consider the equality

$$\left(Q^T\right)_i^B Q_A^i = \delta_A^B \,. \tag{2.14}$$

If the variation of each member of Eq. (2.14) is evaluated, it is obtained

$$\left(\delta Q^T\right)_i^B Q_A^i = -\left(Q^T\right)_i^B \delta Q_A^i \,. \tag{2.15}$$

The transpose of Q and δQ implies

$$G^{AD}\,\delta Q_D^j\, g_{ji}\, Q_B^i + G^{AD}\, Q_D^j\, g_{ji}\,\delta Q_B^i = 0 \tag{2.16}$$

that, by multiplying each term for G_{FA}, yields

$$G_{FA}\, G^{AD} \delta Q_D^j\, g_{ji}\, Q_B^i + G_{FA}\, G^{AD}\, Q_D^j\, g_{ji}\,\delta Q_B^i = 0 \,. \tag{2.17}$$

Since $G_{FA}G^{AD} = \delta_F^D$, we have

$$\delta Q_F^j\, g_{ji}\, Q_B^i = -Q_F^i\, g_{ji}\,\delta Q_B^j \,. \tag{2.18}$$

It follows the existence of a vector function $\delta\omega$ such that

$$\delta Q_F^j\, g_{ji}\, Q_B^i = \epsilon_{kFB}\,\delta\omega^k \,. \tag{2.19}$$

It is natural to refer to $\delta\omega$ as the *microrotation test function*. It yields

$$\delta Q_F^j\, g_{ji}\, Q_B^i\, G^{BA} = \delta Q_F^j \left(Q^T\right)_j^A \,, \tag{2.20}$$

where the first term has been multiplied by G^{BA} and

$$\delta Q_F^j \left(Q^T\right)_j^A = G^{BA}\,\epsilon_{kFB}\,\delta\omega^k \,, \tag{2.21}$$

from which we get

$$\delta Q_F^j = G^{BM}\, Q_M^j\,\epsilon_{kFB}\,\delta\omega^k \,. \tag{2.22}$$

Eq. (2.22) is widely applied in the following and it allows us to couple the equilibrium equations without the introduction of the Euler angles for describing the rotation of each particle. The use of Euler angles would reduce the generality of the dissertation and would lead to numerical issues when large microrotations appear.

Action functional

Let us consider the action functional

$$\begin{aligned}\mathcal{A}_\pi = \int_{t_0}^{t_1} \int_{\mathcal{B}} \left(\frac{1}{2} \rho\, v^2 + \frac{1}{2} J\, \Theta^2 - W_\pi \left(\chi, Q, F, \nabla Q, X \right) \right) dV dt \\ + \int_{t_0}^{t_1} \int_{\partial \mathcal{B}} \left(-W_\pi^{\text{surf}} \left(\chi, Q, X \right) \right) ds\, dt \,,\end{aligned} \tag{2.23}$$

where

- the field χ denotes the configuration field;
- the fields ρ and J refer to the Lagrangian time-independent mass density and to the Lagrangian time-independent moment of inertia of material points;
- the fields $v = \frac{\partial \chi}{\partial t}$ and $\Theta = \frac{\partial Q}{\partial t}$ denote the Lagrangian-translation velocities and Lagrangian-rotation velocities;
- $\rho\, v^2 = g_{ab}\, v^a\, v^b$ and $J\, \Theta^2 = J^{BA}\, \Theta^i_{\ A}\, \Theta^k_{\ B}\, g_{ik}$;
- the potential $W_\pi \left(\chi, Q, F, \nabla Q, X \right)$ is related to the volume density of action;
- the potential $W_\pi^{\text{surf}} \left(\chi, Q, X \right)$ is related to the actions externally applied on the boundary $\partial \mathcal{B}$.

Potential W_π can be split into two addends: the objective deformation energy density W_π^{def} and the external conservative action of bulk loads U_π^{ext}, as follows

$$W_\pi \left(\chi, Q, F, \nabla Q, X \right) = W_\pi^{\text{def}} \left(Q, F, \nabla Q \right) + U_\pi^{\text{ext}} \left(\chi, Q, X \right) \,. \tag{2.24}$$

The first variation of the deformation energy-related portion of the action functional can be expressed as the sum of three terms,

$$\delta \mathcal{A}_\pi^{\text{def}} = \delta \mathcal{A}_{\pi F}^{\text{def}} + \delta \mathcal{A}_{\pi Q}^{\text{def}} + \delta \mathcal{A}_{\pi \nabla Q}^{\text{def}} \,, \tag{2.25}$$

where

$$\delta\mathcal{A}^{\text{def}}_{\pi F} = -\int_{t_0}^{t_1}\int_{\mathcal{B}} \frac{\partial W^{\text{def}}_{\pi}}{\partial F^i_A}\,\delta F^i_A\,dV\,dt\,, \tag{2.26}$$

$$\delta\mathcal{A}^{\text{def}}_{\pi Q} = -\int_{t_0}^{t_1}\int_{\mathcal{B}} \frac{\partial W^{\text{def}}_{\pi}}{\partial Q^j_F}\,\delta Q^j_F\,dV\,dt\,, \tag{2.27}$$

and

$$\delta\mathcal{A}^{\text{def}}_{\pi\nabla Q} = -\int_{t_0}^{t_1}\int_{\mathcal{B}} \frac{\partial W^{\text{def}}_{\pi}}{\partial Q^i_{M,B}}\,\delta Q^i_{M,B}\,dV\,dt\,. \tag{2.28}$$

Micropolar stress tensor

Let us compute the first variation $\delta\mathcal{A}^{\text{def}}_{\pi F}$. It yields

$$\delta\mathcal{A}^{\text{def}}_{\pi F} = -\int_{t_0}^{t_1}\int_{\partial\mathcal{B}} \frac{\partial W^{\text{def}}_{\pi}}{\partial F^i_A}\,N_A\,\delta\chi^i\,ds\,dt + \int_{t_0}^{t_1}\int_{\mathcal{B}} \frac{\partial}{\partial X^A}\left(\frac{\partial W^{\text{def}}_{\pi}}{\partial F^i_A}\right)\delta\chi^i\,dV\,dt\,. \tag{2.29}$$

Let $\mathbb{P}_\pi$ be the *micropolar stress tensor* defined by

$$(\mathbb{P}_\pi)^M_b = \frac{\partial W^{\text{def}}_{\pi}}{\partial F^b_M}. \tag{2.30}$$

Eq. (2.29) becomes

$$\delta\mathcal{A}^{\text{def}}_{\pi F} = -\int_{t_0}^{t_1}\int_{\partial\mathcal{B}} (\mathbb{P}_\pi)^M_b\,N_M\,\delta\chi^b\,ds\,dt + \int_{t_0}^{t_1}\int_{\mathcal{B}} \frac{\partial}{\partial X^M}\,(\mathbb{P}_\pi)^M_b\,\delta\chi^b\,dV\,dt\,. \tag{2.31}$$

First part of the micropolar stress vector

Let us consider the first variation $\delta\mathcal{A}^{\text{def}}_{\pi Q}$. It yields

$$\delta\mathcal{A}^{\text{def}}_{\pi Q} = -\int_{t_0}^{t_1}\int_{\mathcal{B}} \frac{\partial W^{\text{def}}_{\pi}}{\partial Q^i_F}\,\delta Q^j_F\,dV\,dt\,. \tag{2.32}$$

Eq. (2.14) leads to

$$\delta\mathcal{A}^{\text{def}}_{\pi Q} = -\int_{t_0}^{t_1}\int_{\mathcal{B}} \left(\mathbb{V}^{\text{I}}_\pi\right)_k\,\delta\omega^k\,dV\,dt\,, \tag{2.33}$$

where

$$\left(\mathbb{V}^{\text{I}}_\pi\right)_k = \frac{\partial W^{\text{def}}_{\pi}}{\partial Q^i_F}\,G^{BM}\,Q^i_M\,\epsilon_{kFB} \tag{2.34}$$

is named *first part of the micropolar stress vector*.

Micropolar couple stress tensor and micropolar stress vector

Let us consider the first variation $\delta\mathcal{A}^{\text{def}}_{\pi\nabla Q}$. It yields

$$\delta\mathcal{A}^{\text{def}}_{\pi\nabla Q} = -\int_{t_0}^{t_1}\int_{\mathcal{B}} \frac{\partial W^{\text{def}}_{\pi}}{\partial Q^i_{M,B}} \left(G^{NA}\, Q^i_{A,B}\, \epsilon_{jMN}\, \delta\omega^j + G^{NA}\, Q^i_{A}\, \epsilon_{jMN}\, \delta\omega^j_{,B} \right) dV\, dt \tag{2.35}$$

and

$$\begin{aligned} \delta\mathcal{A}^{\text{def}}_{\pi\nabla Q} = &-\int_{t_0}^{t_1}\int_{\mathcal{B}} \frac{\partial W^{\text{def}}_{\pi}}{\partial Q^i_{M,B}}\, G^{NA}\, Q^i_{A,B}\, \epsilon_{jMN}\, \delta\omega^j\, dV\, dt \\ &-\int_{t_0}^{t_1}\int_{\partial\mathcal{B}} \frac{\partial W^{\text{def}}_{\pi}}{\partial Q^i_{M,B}}\, G^{NA}\, Q^i_{A}\, \epsilon_{jMN}\, \delta\omega^j\, N_B\, ds\, dt \\ &+\int_{t_0}^{t_1}\int_{\mathcal{B}} \frac{\partial}{\partial X^B} \left(\frac{\partial W^{\text{def}}_{\pi}}{\partial Q^i_{M,B}}\, G^{NA}\, Q^i_{A}\, \epsilon_{jMN} \right) \delta\omega^j\, dV\, dt\ . \end{aligned} \tag{2.36}$$

Let $\mathbb{M}_\pi$ and $\mathbb{V}^{(\text{II})}_\pi$ be the tensors defined by

$$(\mathbb{M}_\pi)^B_j = \frac{\partial W^{\text{def}}_{\pi}}{\partial Q^i_{M,B}}\, G^{NA}\, Q^i_{A}\, \epsilon_{jMN} \quad , \quad \left(\mathbb{V}^{\text{II}}_\pi\right)_j = \frac{\partial W^{\text{def}}_{\pi}}{\partial Q^i_{M,B}}\, G^{NA}\, Q^i_{A,B}\, \epsilon_{jMN} \tag{2.37}$$

that are named *micropolar couple stress tensor* and *second part of the micropolar stress vector*, respectively. Eq. (2.36) becomes

$$\begin{aligned} \delta\mathcal{A}^{\text{def}}_{\pi\nabla Q} = &-\int_{t_0}^{t_1}\int_{\mathcal{B}} \left(\mathbb{V}^{\text{II}}_\pi\right)_j \delta\omega^j\, dV\, dt - \int_{t_0}^{t_1}\int_{\partial\mathcal{B}} (\mathbb{M}_\pi)^N_j\, N_N \delta\omega^j\, ds\, dt \\ &+\int_{t_0}^{t_1}\int_{\mathcal{B}} \frac{\partial}{\partial X^N} (\mathbb{M}_\pi)^N_j\, \delta\omega^j\, dV\, dt\ . \end{aligned} \tag{2.38}$$

External actions

Let us consider the first variation $\delta\mathcal{A}^{\text{ext}}_\pi$. It yields

$$\delta\mathcal{A}^{\text{ext}}_\pi = \int_{t_0}^{t_1}\int_{\mathcal{B}} (B_\pi)_b\, \delta\chi^b\, dV dt + \int_{t_0}^{t_1}\int_{\mathcal{B}} (C_\pi)_j\, \delta\omega^j\, dV dt\ , \tag{2.39}$$

where

$$(B_\pi)_b = -\frac{\partial U^{\text{ext}}_\pi}{\partial \chi^b} \quad , \quad (C_\pi)_j = -\frac{\partial U^{\text{ext}}_\pi}{\partial Q^k_F} G^{BM} Q^k_M \epsilon_{jFB}\ . \tag{2.40}$$

Let us consider the first variation $\delta\mathcal{A}_\pi^{\text{surf}}$. It yields

$$\delta\mathcal{A}_\pi^{\text{surf}} = \int_{t_0}^{t_1}\int_{\partial\mathcal{B}} (b_\pi)_b\,\delta\chi^b\,ds\,dt + \int_{t_0}^{t_1}\int_{\partial\mathcal{B}} (c_\pi)_j\,\delta\omega^j\,ds\,dt\,, \tag{2.41}$$

where

$$(b_\pi)_b = -\frac{\partial W_\pi^{\text{surf}}}{\partial\chi^b} \quad , \quad (c_\pi)_j = -\frac{\partial W_\pi^{\text{surf}}}{\partial Q_F^k}\,G^{BM}\,Q_M^k\,\epsilon_{jFB}\,. \tag{2.42}$$

kinetic contributions

Let us consider the first variation $\delta\mathcal{A}_\pi^{\text{kin}}$. It yields

$$\delta\mathcal{A}_\pi^{\text{kin}} = \int_{t_0}^{t_1}\int_{\mathcal{B}} \left(\rho\,g_{ab}\,v^a\,\delta v^b + J^{BA}\,\delta\Theta_A^i\,\Theta_B^k\,g_{ik}\right) dV dt\,. \tag{2.43}$$

Let us define

$$\begin{aligned}\delta\mathcal{A}_{\pi\Theta}^{\text{kin}} &= \int_{t_0}^{t_1}\int_{\mathcal{B}} J^{BA}\,\delta\Theta_A^i\,\Theta_B^k\,g_{ik}\,dV dt \\ &= \int_{t_0}^{t_1}\int_{\mathcal{B}} J^{BA}\,g_{ik}\Theta_B^k\,\frac{\partial\delta Q_A^i}{\partial t}\,dV dt\,.\end{aligned} \tag{2.44}$$

By replacing Eq. (2.14) into (2.44), we arrive to

$$\delta\mathcal{A}_{\pi\Theta}^{\text{kin}} = \int_{t_0}^{t_1}\int_{\mathcal{B}} J^{BA}\,g_{ik}\Theta_B^k\left(G^{NM}\,\Theta_M^i\,\epsilon_{jAN}\,\delta\omega^j + G^{NM}\,Q_M^i\,\epsilon_{jAN}\,\frac{\partial\delta\omega^j}{\partial t}\right) dV dt\,. \tag{2.45}$$

For fixed value of j and N, and without summation over A that is fixed too, the following equality holds

$$\begin{aligned}&J^{BA}\,g_{ik}\,\Theta_B^k\,G^{NM}\,\Theta_M^i\,\epsilon_{jAN} + J^{BN}\,g_{ik}\,\Theta_B^k\,G^{AM}\,\Theta_M^i\,\epsilon_{jNA} \\ &= J^{BA}\,g_{ik}\,\Theta_B^k\,G^{NM}\,\Theta_M^i\,\epsilon_{jAN} - J^{BA}\,g_{ik}\,\Theta_B^k\,G^{AM}\,\Theta_M^i\,\epsilon_{jAN} = 0\end{aligned} \tag{2.46}$$

Thus, for any j, it yields

$$J^{BA}\,g_{ik}\Theta_B^k G^{NM}\Theta_M^i\epsilon_{jAN} = 0 \tag{2.47}$$

and

$$\delta\mathcal{A}_{\pi\Theta}^{\text{kin}} = \int_{t_0}^{t_1}\int_{\mathcal{B}} J^{BA}\,\vartheta_{BAj}\,\frac{\partial\delta\omega^j}{\partial t}\,dV dt\,, \tag{2.48}$$

where

$$\vartheta_{BAj} = g_{ik}\,\Theta_B^k\,G^{NM}\,Q_M^i\,\epsilon_{jAN}\,. \tag{2.49}$$

Equilibrium equations

The equilibrium equations, in Lagrangian description, are listed below:

- on the volume $\mathcal{B}$,

$$-\frac{\partial(\rho v_b)}{\partial t}+\frac{\partial}{\partial X^M}\left(\mathbb{P}_\pi\right)_b^M+\left(B_\pi\right)_b=0\,, \tag{2.50}$$

$$-\frac{\partial(J^{AB}\vartheta_{BAj})}{\partial t}+\frac{\partial}{\partial X^N}\left(\mathbb{M}_\pi\right)_j^N-\left(\mathbb{V}_\pi\right)_j+\left(C_\pi\right)_j=0\,, \tag{2.51}$$

where $\mathbb{V}=\mathbb{V}^{(\mathrm{I})}+\mathbb{V}^{(\mathrm{II})}$ could be referred to as *micropolar stress vector*;

- on the boundary $\partial\mathcal{L}$

$$-\left(\mathbb{P}_\pi\right)_b^M N_M+\left(b_\pi\right)_b=0\,, \tag{2.52}$$

$$-\left(\mathbb{M}_\pi\right)_j^N N_N+\left(c_\pi\right)_j=0\,. \tag{2.53}$$

All the derived expressions are functions of the microrotation tensor Q. On one hand, Eqs. (2.52) and (2.53) imply that the subdomains of the micropolar continuum exchange with each other forces per unit area, $\mathbb{P}_\pi$, and couples per unit area, $\mathbb{M}_\pi$. On the other hand, Eq. (2.51) implies that a couple of forces per unit area, $\mathbb{V}_\pi$, acts on each subdomain of the micropolar continuum.

2.2 The micromorphic continuum

Notation

Below A, B, i, and j are integers belonging to $\{1,2,3\}$. Summation is intended over repeated indices.

$\mathcal{B}$: initial (Lagrangian) configuration.

$\partial\mathcal{B}$: boundary of $\mathcal{B}$.

Indices denoted by uppercase letters are chosen to indicate components of a tensor in the initial configuration and lowercase letters to indicate components of a tensor in the current configuration. Summation is intended over the repeated indices.

N_A: components of the outward-pointing normal N of $\partial\mathcal{B}$.

X^A: Lagrangian coordinates.

χ^i: component i of the configuration field χ.

$(\chi')^i$: component i of the micromorphic configuration field χ.

v^i: component i of the translation velocity v.

G_{AB}: component (A,B) of the metric tensor G with respect to the reference system in the initial configuration.

g_{ij}: component (i,j) of the metric tensor g with respect to the reference system in the current configuration.

δ^A_B: component (A,B) of the second-order identity tensor I.

ϵ_{jAB}: component (j,A,B) of the permutation (or Levi-Civita) tensor ϵ.

$P^i_{\ A}$: component (i,A) of the micromorphic second-order configuration tensor P.

φ_{Bi}: component (B,i) of the microvelocity φ.

F^i_A: component (i,A) of the gradient of the configuration field F, $F^i_A = \frac{\partial \chi^i}{\partial X^A}$.

ρ: Lagrangian time-independent mass density.

J^{AB}: component (A,B) of the Lagrangian time-independent moment of inertia of material points J.

$\mathcal{A}_\mu$: action functional for the micropolar continuum.

$\left(\mathbb{P}_\mu\right)^i_{\ A}$: component (i,A) of the micropolar stress tensor $\mathbb{P}_\mu$.

$\left(\mathbb{S}_\mu\right)^i_{\ A}$: component (i,A) of the microstress tensor $\mathbb{S}_\mu$.

$\left(\mathbb{H}_\mu\right)^{AB}_i$: component (A,B,i) of the hyper microstress tensor $\mathbb{H}_\mu$.

$\left(B_\mu\right)_j$: component j of the volumic forces B_μ.

$\left(\mathfrak{B}_\mu\right)_j$: component j of the volumic doubleforces $\mathfrak{B}_\mu$.

$\left(b_\mu\right)_j$: component j of the surface forces b_μ.

$\left(\mathfrak{b}_\mu\right)_j$: component j of the surface doubleforces $\mathfrak{b}_\mu$.

$[S]^T$, S: transpose of the second-order tensor S.

ϵ_{jAB}: permutation (or Levi-Civita) symbol.

$f_{,B}$: partial derivative of the function f with respect to X^B, *i.e*, $f_{,B} = \frac{\partial f}{\partial X^B}$.

dV and ds: volume and surface elements.

2.2.1 Kinematic of the micromorphic continuum

Placement functions

The micropolar continuum consists of small, deformable particles, each of which is represented geometrically by a point X. Each particle is considered as a continuum itself, denoted by $S(X)$, whose center of mass is X. We refer to a material point of $S(X)$ by its spatial coordinate X'. With this assumption, one can write

$$(\chi')^i(X,X',t) = \chi^i(X,t) + P^i_{\ A}(X,t)\left((X')^A - X^A\right), \tag{2.54}$$

where χ describes the configuration change of the center of mass X of each particle, P describes the deformation of each particle, and χ' describes the configuration change of each material point X' within $S(X)$. These assumptions allow describing the kinematical properties of each particle in a more refined way with respect to the classical continuum. Let $\mathcal{B}$ be the initial (or Lagrangian) configuration of the centers of mass X. From Eq. (2.54), we get

$$\frac{\partial (\chi')^i(X,X',t)}{\partial t} = \frac{\partial \chi^i(X,t)}{\partial t} + \frac{\partial P^i_{\ A}(X,t)}{\partial t}\left((X')^A - X^A\right) \tag{2.55}$$

and

$$\begin{aligned} &\int_{\mathcal{B}}\int_{S(X)} \widehat{\varrho}(X,X')\, g_{ij}\, \frac{\partial (\chi')^i(X,X',t)}{\partial t}\, \frac{\partial (\chi')^j(X,X',t)}{\partial t}\, dX dX' \\ &= \int_{\mathcal{B}} \left(\varrho(X)\, g_{ij}\, \frac{\partial \chi^i(X,t)}{\partial t}\, \frac{\partial \chi^j(X,t)}{\partial t} + J^{AB}(X)\, g_{ij}\, \frac{\partial P^i_{\ A}(X,t)}{\partial t}\, \frac{\partial P^j_{\ B}(X,t)}{\partial t} \right) dX\,, \end{aligned} \tag{2.56}$$

where $\varrho(X)$ and $J^{AB}(X)$ are defined by Eq. (2.5) that implies $J^{AB} = J^{BA}$.

2.2.2 Deformation energy density and deformation measures

Let $\widetilde{W}^{\text{def}}_{\mu}(\chi, P, F, \nabla P, X)$ be the specific deformation energy density. Since it must be objective, the equality

$$\widetilde{W}^{\text{def}}_{\mu}(\chi, P, F, \nabla P, X) = \widetilde{W}^{\text{def}}_{\mu}(O\chi + a, OP, OF, O\nabla P, X) \tag{2.57}$$

needs to be satisfied for any orthogonal transformation O and for any vector a. Let us consider the polar decomposition of P, $P = R_\mu V_\mu$, where $V_\mu = \left(P^T P\right)^{1/2}$. It yields

$$R_\mu = P\left(P^T P\right)^{-1/2} \quad , \quad R_\mu^T = \left[\left(P^T P\right)^{-1/2}\right]^T P^T \, . \tag{2.58}$$

For any P and for any χ, it is natural to choose $O = P^T$ and $a = -P^T\chi$. We get

$$\begin{aligned}&\widetilde{W}_\mu(\chi, P, F, \nabla P, X)\\ &\quad = \widetilde{W}_\mu\left(0, \left[\left(P^T P\right)^{-1/2}\right]^T P^T P, \left[\left(P^T P\right)^{-1/2}\right]^T P^T F, \left[\left(P^T P\right)^{-1/2}\right]^T P^T \nabla P, X\right).\end{aligned} \tag{2.59}$$

Eq. (2.59) implies that if $\tilde{W}_\mu^{\text{def}}$ is an objective function, then there exists a function W_μ^{def} such that

$$\begin{aligned}&\widetilde{W}_\mu\left(0, \left[\left(P^T P\right)^{-1/2}\right]^T P^T P, \left[\left(P^T P\right)^{-1/2}\right]^T P^T F, \left[\left(P^T P\right)^{-1/2}\right]^T P^T \nabla P, X\right)\\ &\qquad\qquad = W_\mu^{\text{def}}(P, F, \nabla P, X)\end{aligned} \tag{2.60}$$

and

$$\widetilde{W}_\mu^{\text{def}}(\chi, P, F, \nabla P, X) = W_\mu^{\text{def}}(P, F, \nabla P, X) \, . \tag{2.61}$$

Eq. (2.59) leads also to the deformation measures E_μ, G_μ and Γ_μ defined by

$$E_\mu = \frac{1}{2}\left(P^T F - I\right) \quad , \quad G_\mu = \frac{1}{2}\left(P^T P - I\right) \quad , \quad \Gamma_\mu = P^T \nabla P \, , \tag{2.62}$$

which have the following component expressions:

$$\left(E_\mu\right)_{MN} = \frac{1}{2}\left(g_{ij} P_M^j F_N^i - G_{MA}\,\delta_N^A\right) \quad , \quad \left(G_\mu\right)_{MN} = \frac{1}{2}\left(g_{ij} P_M^j P_N^i - G_{MA}\,\delta_N^A\right) , \tag{2.63}$$

$$\left(\Gamma_\mu\right)_{MNC} = G_{MA}\left(P^T\right)_i^A P_{N,C}^i \, . \tag{2.64}$$

It is natural to refer to the tensor E_μ as the *micromorphic stretch tensor*, to the tensor G_μ as the *micromorphic Green-Saint-Venant tensor*, and to the tensor Γ_μ as the *micromorphic wryness tensor*. Since $P^T F$, $P^T P$, and $P^T \nabla P$ can be expressed as a function of E_μ, G_μ, and Γ_μ, it follows the existence of a function $\widehat{W}_\mu^{\text{def}}$ such that

$$W_\mu^{\text{def}}(P, F, \nabla P, X) = \widehat{W}_\mu^{\text{def}}\left(E_\mu, G_\mu, \Gamma_\mu, X\right) \, . \tag{2.65}$$

Micromorphic stretch tensor, micromorphic Green-Saint-Venant tensor, and micromorphic wryness tensor are only three of the possible deformation measures that can be introduced. Several alternatives have been proposed in the literature. In the following, the Euler-Lagrange equations are derived by representing deformation energy density as an objective function of P, F, and ∇P, $W_\mu^{\text{def}}(P, F, \nabla P, X)$. Thus, the derived equations are valid for any chosen combination of deformation measures.

2.2.3 Euler-Lagrange equations

Action functional

Let us consider the action functional

$$\begin{aligned}\mathcal{A}_\mu = \int_{t_0}^{t_1} \int_{\mathcal{B}} \left(\frac{1}{2}\rho\, v^2 + \frac{1}{2} J\, \Phi^2 - W_\mu\left(\chi, F, P, \nabla P, X\right) \right) dV dt \\ + \int_{t_0}^{t_1} \int_{\partial\mathcal{B}} \left(-W_\mu^{surf}\left(\chi, P, X\right) \right) ds\, dt\,,\end{aligned} \tag{2.66}$$

where

- the field χ denotes the configuration field;
- the fields ρ and I refer to the Lagrangian time-independent mass density and to the Lagrangian time-independent moment of inertia of material points;
- the fields $v = \frac{\partial \chi}{\partial t}$ and $\Phi = \frac{\partial P}{\partial t}$ denote the Lagrangian-translation velocities and Lagrangian-translation microvelocities;
- $\rho v^2 = g_{ab}\, v^a\, v^b$ and $J\,\Phi^2 = J^{BA}\, \Phi^i_{\ A}\, \Phi^k_{\ B}\, g_{ik}$;
- the potential $W_\mu\left(\chi, F, P, \nabla P, X\right)$ is related to the volume density of action;
- the potential $W_\mu^{\text{surf}}\left(\chi, P, X\right)$ is related to the actions externally applied on the boundary $\partial\mathcal{B}$.

Potential W_μ can be split into two addends: the objective specific deformation energy density W^{def} and the external conservative action of bulk loads U_μ^{ext}, as follows

$$W_\mu\left(\chi, F, P, \nabla P, X\right) = W_\mu^{\text{def}}\left(F, P, \nabla P\right) + U_\mu^{\text{ext}}\left(\chi, P, X\right)\,. \tag{2.67}$$

The first variation of the deformation energy-related portion of the action functional can be expressed as the sum of three terms,

$$\delta\mathcal{A}^{\mathrm{def}}_{\mu} = \delta\mathcal{A}^{\mathrm{def}}_{\mu F} + \delta\mathcal{A}^{\mathrm{def}}_{\mu P} + \delta\mathcal{A}^{\mathrm{def}}_{\mu \nabla P} \,, \tag{2.68}$$

where

$$\delta\mathcal{A}^{\mathrm{def}}_{\mu F} = -\int_{t_0}^{t_1}\int_{\mathcal{B}} \frac{\partial W^{\mathrm{def}}_{\mu}}{\partial F^i_A}\,\delta F^i_A \, dV dt \,, \tag{2.69}$$

$$\delta\mathcal{A}^{\mathrm{def}}_{\mu P} = -\int_{t_0}^{t_1}\int_{\mathcal{B}} \frac{\partial W^{\mathrm{def}}_{\mu}}{\partial P^j_F}\,\delta P^j_F \, dV dt \,, \tag{2.70}$$

and

$$\delta\mathcal{A}^{\mathrm{def}}_{\mu \nabla P} = -\int_{t_0}^{t_1}\int_{\mathcal{B}} \frac{\partial W^{\mathrm{def}}_{\mu}}{\partial P^i_{M,B}}\,\delta P^i_{M,B} \, dV dt \,. \tag{2.71}$$

Micromorphic stress tensor

Let us compute the first variation $\delta\mathcal{A}^{\mathrm{def}}_{\mu F}$. It yields

$$\delta\mathcal{A}^{\mathrm{def}}_{\mu F} = -\int_{t_0}^{t_1}\int_{\partial\mathcal{B}} \frac{\partial W^{\mathrm{def}}_{\mu}}{\partial F^i_A} N_A\,\delta\chi^i \, ds\, dt + \int_{t_0}^{t_1}\int_{\mathcal{B}} \frac{\partial}{\partial X^A}\left(\frac{\partial W^{\mathrm{def}}_{\mu}}{\partial F^i_A}\right)\delta\chi^i \, dV\, dt \,. \tag{2.72}$$

Let $\mathbb{P}$ be the *micromorphic stress tensor* defined by

$$\left(\mathbb{P}_{\mu}\right)^A_i = \frac{\partial W^{\mathrm{def}}_{\mu}}{\partial F^i_A} \,. \tag{2.73}$$

Eq. (2.72) becomes

$$\delta\mathcal{A}^{\mathrm{def}}_{\mu F} = -\int_{t_0}^{t_1}\int_{\partial\mathcal{B}} \left(\mathbb{P}_{\mu}\right)^A_i N_A\,\delta\chi^i \, ds\, dt + \int_{t_0}^{t_1}\int_{\mathcal{B}} \frac{\partial}{\partial X^A}\left(\mathbb{P}_{\mu}\right)^A_i \delta\chi^i \, dV\, dt \,. \tag{2.74}$$

Microstress tensor

Let us consider the first variation $\delta\mathcal{A}^{\mathrm{def}}_{\mu P}$. It yields

$$\delta\mathcal{A}^{\mathrm{def}}_{\mu P} = -\int_{t_0}^{t_1}\int_{\mathcal{B}} \frac{\partial W^{\mathrm{def}}_{\mu}}{\partial P^j_F}\,\delta P^j_F \, dV dt \,. \tag{2.75}$$

Let $\mathbb{S}$ be the *microstress tensor* defined by

$$\left(\mathbb{S}_\mu\right)_i^A = \frac{\partial W_\mu^{\text{def}}}{\partial P^i_A} \ . \tag{2.76}$$

Eq. (2.75) becomes

$$\delta\mathcal{A}^{\text{def}}_{\mu P} = -\int_{t_0}^{t_1}\int_{\mathcal{B}} \left(\mathbb{S}_\mu\right)_j^F \delta P^j_F \, dV dt \ . \tag{2.77}$$

Hyper microstress tensor

Let us consider the first variation $\delta\mathcal{A}^{\text{def}}_{\mu\nabla P}$. It yields

$$\delta\mathcal{A}^{\text{def}}_{\mu\nabla P} = \int_{t_0}^{t_1}\int_{\partial\mathcal{B}} -\frac{\partial W_\mu^{\text{def}}}{\partial P^i_{A,B}} \delta P^i_A \, N_B \, ds \, dt + \int_{t_0}^{t_1}\int_{\mathcal{B}} \frac{\partial}{\partial X^B}\left(\frac{\partial W_\mu^{\text{def}}}{\partial P^i_{A,B}}\right) \delta P^i_A \, dV \, dt \ . \tag{2.78}$$

Let us introduce the tensor $\mathbb{H}_\mu$ defined by

$$\left(\mathbb{H}_\mu\right)_i^{AB} = \frac{\partial W_\mu^{\text{def}}}{\partial P^i_{A,B}} \ , \tag{2.79}$$

which could be named *hyper microstress tensor*. Eq. (2.78) becomes

$$\delta\mathcal{A}^{\text{def}}_{\mu\nabla P} = \int_{t_0}^{t_1}\int_{\partial\mathcal{B}} -\left(\mathbb{H}_\mu\right)_i^{AB} \delta P^i_A N_B \, ds \, dt + \int_{t_0}^{t_1}\int_{\mathcal{B}} \frac{\partial}{\partial X^B}\left(\mathbb{H}_\mu\right)_i^{AB} \delta P^i_A \, dV \, dt \ . \tag{2.80}$$

External actions

Let us consider the first variation $\delta\mathcal{A}^{\text{ext}}_\mu$. It yields

$$\delta\mathcal{A}^{\text{ext}}_\mu = \int_{t_0}^{t_1}\int_{\mathcal{B}} \left(B_\mu\right)_b \delta\chi^b \, dV dt + \int_{t_0}^{t_1}\int_{\mathcal{B}} \left(\mathfrak{B}_\mu\right)_i^A \delta P^i_A \, dV dt \ , \tag{2.81}$$

where

$$\left(B_\mu\right)_b = -\frac{\partial \mathcal{U}^{\text{ext}}}{\partial \chi^b} \quad , \quad \left(\mathfrak{B}_\mu\right)_i^A = -\frac{\partial \mathcal{U}^{\text{ext}}}{\partial P^i_A} \ . \tag{2.82}$$

Let us consider the first variation $\delta\mathcal{A}^{\text{surf}}_\mu$. It yields

$$\delta\mathcal{A}^{\text{surf}}_\mu = \int_{t_0}^{t_1}\int_{\partial\mathcal{B}} \left(b_\mu\right)_b \delta\chi^b \, ds \, dt + \int_{t_0}^{t_1}\int_{\partial\mathcal{B}} \left(\mathfrak{b}_\mu\right)_i^A \delta P^i_A \, ds \, dt \ , \tag{2.83}$$

where

$$\left(b_\mu\right)_b = -\frac{\partial W_\mu^{\text{surf}}}{\partial \chi^b} \quad , \quad \left(\mathfrak{b}_\mu\right)_i^A = -\frac{\partial W_\mu^{\text{surf}}}{\partial P_A^i} \, . \tag{2.84}$$

kinetic contributions

Let us consider the first variation $\delta \mathcal{A}_\mu^{\text{kin}}$. It yields

$$\delta \mathcal{A}_\mu^{\text{kin}} = \int_{t_0}^{t_1} \int_{\mathcal{B}} \left(\rho \, g_{ab} \, v^a \, \delta v^b + J^{BA} \, \delta \Phi_A^i \, \Phi_B^k \, g_{ik} \right) dV dt \, . \tag{2.85}$$

Let us define

$$\begin{aligned} \delta \mathcal{A}_{\mu\Phi}^{\text{kin}} &= \int_{t_0}^{t_1} \int_{\mathcal{B}} J^{BA} \, \delta \Phi_A^i \, \Phi_B^k \, g_{ik} \, dV dt \\ &= \int_{t_0}^{t_1} \int_{\mathcal{B}} J^{BA} \, g_{ik} \Phi_B^k \, \frac{\partial \delta P_A^i}{\partial t} \, dV dt \, . \end{aligned} \tag{2.86}$$

It yields

$$\delta \mathcal{A}_{\mu\Phi}^{\text{kin}} = \int_{t_0}^{t_1} \int_{\mathcal{B}} J^{BA} \varphi_{Bi} \frac{\partial \delta P_A^i}{\partial t} \, dV dt \, , \tag{2.87}$$

where

$$\varphi_{Bi} = g_{ik} \Phi_B^k \, . \tag{2.88}$$

Equilibrium equations

The equilibrium equations, in the Lagrangian description, are listed below:

- on the volume $\mathcal{B}$:

$$-\frac{\partial (\rho v_b)}{\partial t} + \frac{\partial}{\partial X^M} \left(\mathbb{P}_\mu\right)_b^M + \left(B_\mu\right)_b = 0 \, , \tag{2.89}$$

$$-\frac{\partial (J^{AB} \varphi_{Bi})}{\partial t} + \frac{\partial}{\partial X^B} \left(\mathbb{H}_\mu\right)_i^{AB} + \left(\mathfrak{B}_\mu\right)_i^A = 0 \, ; \tag{2.90}$$

- on the boundary $\partial \mathcal{B}$:

$$-\left(\mathbb{P}_\mu\right)_b^M N_M + \left(b_\mu\right)_b = 0 \, , \tag{2.91}$$

$$-\left(\mathbb{H}_\mu\right)_i^{AB} N_B + \left(\mathfrak{b}_\mu\right)_i^A = 0 \, . \tag{2.92}$$

Eqs. (2.91) and (2.92) imply that the subdomains of the micromorphic continuum exchange with each other forces per unit area, $\mathbb{P}_\mu$, and double forces per unit area, $\mathbb{H}_\mu$.

2.3 Second-gradient classic continuum

Notation

Below A, B, D, i, and j are integers belonging to $\{1,2,3\}$. Summation is intended over repeated indices.

$\mathcal{B}$: initial (Lagrangian) configuration.

$\partial\mathcal{B}$: boundary of $\mathcal{B}$.

$\partial\partial\mathcal{B}$: edges of $\mathcal{B}$.

Indices denoted by uppercase letters are chosen to indicate components of a tensor in the initial configuration and lowercase letters to indicate components of a tensor in the current configuration. Summation is intended over the repeated indices.

N_A: components of the outward-pointing normal N of $\partial\mathcal{B}$.

ν_A: components of the outward-pointing normal ν of $\partial\partial\mathcal{B}$.

X^A: Lagrangian coordinates.

χ^i: component i of the configuration field χ.

v^i: component i of the translation velocity v.

G_{AB}: component (A,B) of the metric tensor G in the initial configuration.

δ^A_B: component (A,B) of the second-order identity tensor I.

g_{ij}: component (i,j) of the metric tensor g in the current configuration.

ϵ_{jAB}: component (j,A,B) of the permutation (or Levi-Civita) tensor ϵ.

$m_{\perp}{}^D_A$: component (D,A) of the operator of orthogonal projection $m_\perp$.

$m_{\parallel}{}^D_A$: component (D,A) of the operator of parallel projection $m_\parallel$.

F^i_A: component (i,A) of the gradient of the configuration field F.

ρ: Lagrangian time-independent mass density.

$\mathcal{A}_\sigma$: action functional for the micropolar continuum.

$(\mathbb{P}_\sigma)^i_A$: component (i,A) of the Piola stress tensor $\mathbb{P}_\sigma$.

$(\mathbb{H}_\sigma)^{AB}_i$: component (A,B,i) of the hyper stress tensor $\mathbb{H}_\sigma$.

$(B_\sigma)_j$: component j of the volume forces B_σ.

$(\mathbb{B}_\sigma)_j$: component j of the volumic doubleforces $\mathbb{B}_\sigma$.

$(b_\sigma)_j$: component j of the surface forces b_σ.

$(\beta_\sigma)_j$: component j of the length forces β_σ.

$[S]^T$, S: transpose of the second-order tensor S.

ϵ_{jAB}: permutation (or Levi-Civita) symbol.

$f_{,B}$: partial derivative of the function f with respect to X^B, *i.e*, $f_{,B} = \frac{\partial f}{\partial X^B}$.

dV, ds, and $d\ell$: volume, surface, and length elements.

2.3.1 Deformation measures

Let $\widetilde{W}^{\text{def}}_\sigma(\chi, F, \nabla F, X)$ be the specific deformation energy density. Since it must be objective, the equality

$$\tilde{W}^{\text{def}}_\sigma(\chi, F, \nabla F, X) = \tilde{W}^{\text{def}}_\sigma(O\chi + a, OF, O\nabla F, X) \tag{2.93}$$

needs to be satisfied for any orthogonal transformation O and for any vector a. Let us consider the polar decomposition of F, $F = R_\sigma V_\sigma$, where $V_\sigma = \left(F^T F\right)^{1/2}$. It yields

$$R_\sigma = F\left(F^T F\right)^{-1/2} \quad , \quad R^T_\sigma = \left[\left(F^T F\right)^{-1/2}\right]^T F^T \, . \tag{2.94}$$

For any F and for any χ, it is natural to choose $O = R^T_\sigma$ and $a = -R^T_\sigma \chi$. We get

$$\widetilde{W}_\sigma(\chi, F, \nabla F, X) = \widetilde{W}_\sigma\left(0, \left[\left(F^T F\right)^{-1/2}\right]^T F^T F, \left[\left(F^T F\right)^{-1/2}\right]^T F^T \nabla F, X\right) . \tag{2.95}$$

Eq. (2.95) implies that if $\tilde{W}^{\text{def}}_\sigma$ is an objective function of χ, F, and ∇F, then there exists a function W^{def}_σ such that

$$\widetilde{W}_\sigma\left(0,\left[\left(F^TF\right)^{-1/2}\right]^T F^TF,\left[\left(F^TF\right)^{-1/2}\right]^T F^T\nabla F,X\right)=W_\sigma^{\text{def}}\left(F,\nabla F,X\right) \tag{2.96}$$

and

$$\widetilde{W}_\sigma^{\text{def}}\left(\chi,F,\nabla F,X\right)=W_\sigma^{\text{def}}\left(F,\nabla F,X\right)\ . \tag{2.97}$$

Eq. (2.95) leads also to the deformation measures G_σ and Γ_σ defined by

$$G_\sigma=\frac{1}{2}\left(F^TF-I\right)\quad,\quad \Gamma_\sigma=F^T\nabla F\ . \tag{2.98}$$

which have the following component expressions:

$$(G_\sigma)_{MN}=\frac{1}{2}\left(g_{ij}\,F^j_M\,F^i_N-G_{MA}\,\delta^A_N\right)\quad,\quad (\Gamma_\sigma)_{MNC}=G_{MA}\left(F^T\right)^A_i F^i_{N,C}\ . \tag{2.99}$$

It is natural to refer to the tensor G_σ as the *Green-Saint-Venant stretch tensor* and to the tensor Γ_σ as the *second-gradient wryness tensor*. The Green-Saint-Venant stretch tensor gives the change in length of an *infinitesimal material segment* (also named *fiber* or *material line element*). From a historical standpoint, its use emerges in [19, 86, 114, 81, 25]. Since F^TF and $F^T\nabla F$ can be expressed as a function of G_σ and Γ_σ, it follows the existence of a function $\widehat{W}_\sigma^{\text{def}}$ such that

$$W_\sigma^{\text{def}}\left(F,\nabla F,X\right)=\widehat{W}_\sigma^{\text{def}}\left(G_\sigma,\Gamma_\sigma,X\right)\ . \tag{2.100}$$

Green-Saint-Venant stretch tensor and second-gradient wryness tensor are just two of the possible deformation measures that can be introduced. Many alternatives have been proposed in the literature. In the following, the Euler-Lagrange equations are derived by assuming deformation energy density as an objective function of F, and ∇F, $W_\sigma^{\text{def}}\left(F,\nabla F,X\right)$. Consequently, the derived equations hold for any chosen combination of deformation measures.

2.3.2 Euler-Lagrange equations

Action functional

Let us consider the action functional

$$\begin{aligned}\mathcal{A}_\sigma = \int_{t_0}^{t_1} \int_{\mathcal{B}} \left(\frac{1}{2} \rho\, v^2 - W_\sigma \left(\chi, F, \nabla F, X \right) \right) dV dt \\ + \int_{t_0}^{t_1} \int_{\partial\mathcal{B}} \left(-W_\sigma^{\text{surf}} \left(\chi, \frac{\partial \chi}{\partial N}, X \right) \right) ds\, dt + \int_{t_0}^{t_1} \int_{\partial\partial\mathcal{B}} \left(-W_\sigma^{\text{lgth}} \left(\chi, X \right) \right) d\ell\, dt \,,\end{aligned} \tag{2.101}$$

where

- the field χ denotes the configuration field;
- the field $v = \frac{\partial \chi}{\partial t}$ denotes the velocity field;
- the field ρ denote the Lagrangian time independent mass density;
- $\rho\, v^2 = g_{ab}\, v^a\, v^b$;
- the potential $W_\sigma(\chi, F, \nabla F, X)$ is the volumic density of action;
- the potential $W_\sigma^{\text{surf}}(\chi, \frac{\partial \chi}{\partial N}, X)$ is related to the actions externally applied on the boundary $\partial\mathcal{B}$;
- the potential $W_\sigma^{\text{lgth}}(\chi, X)$ is related to the actions externally applied on the edges $\partial\partial\mathcal{B}$.

Potential W_σ can be split into two addends, the objective specific deformation energy W_σ^{def} and the external conservative actions of bulk loads U_σ^{ext}, as follows

$$W_\sigma \left(\chi, F, \nabla F, X \right) = W_\sigma^{\text{def}} \left(F, \nabla F, X \right) + U_\sigma^{\text{ext}} \left(\chi, X \right) \,. \tag{2.102}$$

The first variation of the deformation energy-related portion of the action functional can be expressed as the sum of three terms,

$$\delta \mathcal{A}_\sigma^{\text{def}} = \delta \mathcal{A}_{\sigma F}^{\text{def}} + \delta \mathcal{A}_{\sigma \nabla F}^{\text{def}} \,, \tag{2.103}$$

where

$$\delta \mathcal{A}_{\sigma F}^{\text{def}} = \int_{t_0}^{t_1} \int_{\mathcal{B}} \left(-\frac{\partial W_\sigma^{\text{def}}}{\partial F_A^i} \left(F, \nabla F, X \right) \right) \delta F_A^i \, dV dt \tag{2.104}$$

and

$$\delta \mathcal{A}_{\sigma \nabla F}^{\text{def}} = \int_{t_0}^{t_1} \int_{\mathcal{B}} \left(-\frac{\partial W_\sigma^{\text{def}}}{\partial F_{A,B}^i} \left(F, \nabla F, X \right) \right) \delta F_{A,B}^i \, dV dt \,. \tag{2.105}$$

First stress tensor

Let us consider the first variation $\delta\mathcal{A}^{\text{def}}_{\sigma F}$. We get

$$\delta\mathcal{A}^{\text{def}}_{\sigma F} = -\int_{t_0}^{t_1}\int_{\partial\mathcal{B}} \frac{\partial W^{\text{def}}_{\sigma}}{\partial F^i_A} N_A\,\delta\chi^i\,ds\,dt + \int_{t_0}^{t_1}\int_{\mathcal{B}} \frac{\partial}{\partial X^A}\left(\frac{\partial W^{\text{def}}_{\sigma}}{\partial F^i_A}\right)\delta\chi^i\,dV\,dt\,. \tag{2.106}$$

Let $\mathbb{P}$ be the *first stress tensor* defined by

$$(\mathbb{P}_\sigma)^A_i = \frac{\partial W^{\text{def}}_{\sigma}}{\partial F^i_A}\,. \tag{2.107}$$

We get

$$\delta\mathcal{A}^{\text{def}}_{\sigma F} = -\int_{t_0}^{t_1}\int_{\partial\mathcal{B}} (\mathbb{P}_\sigma)^A_i\, N_A\,\delta\chi^i\,ds\,dt + \int_{t_0}^{t_1}\int_{\mathcal{B}} \frac{\partial}{\partial X^A}\,(\mathbb{P}_\sigma)^A_i\,\delta\chi^i\,dV\,dt\,. \tag{2.108}$$

Hyper and effective stress tensors

Let us consider the first variation $\delta\mathcal{A}^{\text{def}}_{\sigma\nabla F}$. It yields

$$\delta\mathcal{A}^{\text{def}}_{\sigma\nabla F} = -\int_{t_0}^{t_1}\int_{\partial\mathcal{B}} \frac{\partial W^{\text{def}}_{\sigma}}{\partial F^i_{A,B}}\,\delta F^i_A\,N_B\,ds\,dt + \int_{t_0}^{t_1}\int_{\mathcal{B}} \frac{\partial}{\partial X^B}\left(\frac{\partial W^{\text{def}}_{\sigma}}{\partial F^i_{A,B}}\right)\delta F^i_A\,dV\,dt\,. \tag{2.109}$$

The second integral of Eq. (2.109) is equal to

$$\begin{aligned}\int_{t_0}^{t_1}\int_{\mathcal{B}} \frac{\partial}{\partial X^B}\left(\frac{\partial W^{\text{def}}_{\sigma}}{\partial F^i_{A,B}}\right)\delta F^i_A\,dV\,dt &= \int_{t_0}^{t_1}\int_{\partial\mathcal{B}} \frac{\partial}{\partial X^B}\left(\frac{\partial W^{\text{def}}_{\sigma}}{\partial F^i_{A,B}}\right)N_A\delta\chi^i\,ds\,dt\\ &\quad -\int_{t_0}^{t_1}\int_{\mathcal{B}} \frac{\partial^2}{\partial X^A\partial X^B}\left(\frac{\partial W^{\text{def}}_{\sigma}}{\partial F^i_{A,B}}\right)\delta\chi^i\,dV\,dt\,.\end{aligned} \tag{2.110}$$

Let us introduce the tensor $\mathbb{H}_\sigma$ defined by

$$(\mathbb{H}_\sigma)^{AB}_i = \frac{\partial W^{\text{def}}_{\sigma}}{\partial F^i_{A,B}}\,, \tag{2.111}$$

which could be named *hyper stress tensor*, and let us introduce the tensor $\bar{\mathbb{P}}_\sigma$ defined by

$$\left(\bar{\mathbb{P}}_\sigma\right)^A_i = (\mathbb{P}_\sigma)^A_i + \frac{\partial\,(\mathbb{H}_\sigma)^{AB}_i}{\partial X^B}\,, \tag{2.112}$$

which could be named *effective stress tensor*. Tensor $\bar{\mathbb{P}}_\sigma$ plays a crucial role in the translation equilibrium of the continuum.

Double and edge contact forces

The first integral of the second term of Eq. (2.110) gives

$$\begin{aligned} -\int_{t_0}^{t_1}\int_{\partial\mathcal{B}} \frac{\partial W_\sigma^{\text{def}}}{\partial F^i_{A,B}}\delta F^i_A N_B\, ds\, dt &= -\int_{t_0}^{t_1}\int_{\partial\mathcal{B}} \left(\frac{\partial W_\sigma^{\text{def}}}{\partial F^i_{A,B}} N_B\right)\delta\chi^i_{,A}\, ds\, dt \\ &= -\int_{t_0}^{t_1}\int_{\partial\mathcal{B}} \left(\frac{\partial W_\sigma^{\text{def}}}{\partial F^i_{A,B}} N_B\right)\delta\chi^i_{,C}\delta^C_A\, ds\, dt\ . \end{aligned} \tag{2.113}$$

From Eq. (2.113), we get

$$\begin{aligned} -\int_{t_0}^{t_1}\int_{\partial\mathcal{B}} \left(\frac{\partial W_\sigma^{\text{def}}}{\partial F^i_{A,B}} N_B\right)\delta\chi^i_{,C}\,\delta^C_A\, ds\, dt &= -\int_{t_0}^{t_1}\int_{\partial\mathcal{B}} \left(\frac{\partial W_\sigma^{\text{def}}}{\partial F^i_{A,B}} N_B\right)\delta\chi^i_{,C}\left(m_{\perp A}{}^C + m_{\parallel A}{}^C\right) ds\, dt \\ &= -\int_{t_0}^{t_1}\int_{\partial\mathcal{B}} \left(\frac{\partial W_\sigma^{\text{def}}}{\partial F^i_{A,B}} N_B\right)\delta\chi^i_{,C}\left(m_{\perp D}{}^C\, m_{\perp A}{}^D + m_{\parallel D}{}^C\, m_{\parallel A}{}^D\right) ds\, dt\ . \end{aligned} \tag{2.114}$$

On one hand, the first integral of the second term of Eq. (2.114) is equal to

$$-\int_{t_0}^{t_1}\int_{\partial\mathcal{B}} \left(\frac{\partial W_\sigma^{\text{def}}}{\partial F^i_{A,B}} N_B\right) N^C N_A \delta\chi^i_{,C}\, ds\, dt = -\int_{t_0}^{t_1}\int_{\partial\mathcal{B}} \left(\frac{\partial W_\sigma^{\text{def}}}{\partial F^i_{A,B}} N_B N_A\right)\frac{\partial\delta\chi^i}{\partial N}\, ds\, dt \tag{2.115}$$

and we name *double contact forces* the quantities

$$\frac{\partial W_\sigma^{\text{def}}}{\partial F^i_{A,B}} N_B N_A\ . \tag{2.116}$$

On the other hand, the second integral of Eq. (2.114) is equal to

$$\begin{aligned} &-\int_{t_0}^{t_1}\int_{\partial\mathcal{B}} \left(\frac{\partial W_\sigma^{\text{def}}}{\partial F^i_{A,B}} N_B\right)\delta\chi^i_{,C}\left(m_{\parallel D}{}^C\, m_{\parallel A}{}^D\right) ds\, dt \\ &= \int_{t_0}^{t_1}\int_{\partial\mathcal{B}} \frac{\partial}{\partial X^C}\left(\frac{\partial W_\sigma^{\text{def}}}{\partial F^i_{A,B}} N_B\, m_{\parallel A}{}^D\right) m_{\parallel D}{}^C\,\delta\chi^i\, ds\, dt \\ &-\int_{t_0}^{t_1}\int_{\partial\mathcal{B}} \frac{\partial}{\partial X^C}\left(\frac{\partial W_\sigma^{\text{def}}}{\partial F^i_{A,B}} N_B\, m_{\parallel A}{}^D\,\delta\chi^i\right) m_{\parallel D}{}^C\, ds\, dt \end{aligned} \tag{2.117}$$

and the Gauss Theorem for embedded manifolds leads to

$$-\int_{t_0}^{t_1}\int_{\partial\mathcal{B}}\frac{\partial}{\partial X^C}\left(\frac{\partial W_\sigma^{\rm def}}{\partial F^i_{A,B}}N_B\, m_{\|A}^{\ D}\,\delta\chi^i\right)m_{\|D}^{\ C}\,ds\,dt=-\int_{t_0}^{t_1}\int_{\partial\partial\mathcal{B}}\left(\frac{\partial W_\sigma^{\rm def}}{\partial F^i_{A,B}}N_B\,\nu_A\right)\delta\chi^i\,d\ell\,dt\ . \tag{2.118}$$

We name *edge contact forces* the quantities

$$\frac{\partial W_\sigma^{\rm def}}{\partial F^i_{A,B}}N_B\nu_A\ . \tag{2.119}$$

External actions

Let us consider the first variation $\delta\mathcal{A}^{\rm ext}$. It yields

$$\delta\mathcal{A}_\sigma^{\rm ext}=\int_{t_0}^{t_1}\int_{\mathcal{B}}(B_\sigma)_b\,\delta\chi^b\,dV\,dt\ , \tag{2.120}$$

where

$$(B_\sigma)_b=-\frac{\partial U_\sigma^{\rm ext}}{\partial\chi^b}\ . \tag{2.121}$$

Let us consider the first variation $\delta\mathcal{A}_\sigma^{\rm surf}$. It yields

$$\delta\mathcal{A}_\sigma^{\rm surf}=\int_{t_0}^{t_1}\int_{\partial\mathcal{B}}(b_\sigma)_b\,\delta\chi^b\,ds\,dt+\int_{t_0}^{t_1}\int_{\partial\mathcal{B}}(\mathbb{B}_\sigma)_b\,\frac{\partial\delta\chi^b}{\partial N}\,ds\,dt \tag{2.122}$$

where

$$(b_\sigma)_b=-\frac{\partial W_\sigma^{\rm surf}}{\partial\chi^b}\quad,\quad(\mathbb{B}_\sigma)_b=-\frac{\partial W_\sigma^{\rm surf}}{\frac{\partial\chi^b}{\partial N}}\ . \tag{2.123}$$

Let us consider the first variation $\delta\mathcal{A}_\sigma^{\rm lgth}$. It yields

$$\delta\mathcal{A}_\sigma^{\rm lgth}=\int_{t_0}^{t_1}\int_{\partial\partial\mathcal{B}}(\beta_\sigma)_b\,\delta\chi^b\,d\ell dt\ , \tag{2.124}$$

where

$$(\beta_\sigma)_b=-\frac{\partial W_\sigma^{\rm lgth}}{\partial\chi^b}\ . \tag{2.125}$$

Equilibrium equations

The equilibrium equations, in the Lagrangian description, are listed below:

- on the volume $\mathcal{B}$,

$$-\frac{\partial(\rho v_b)}{\partial t}+\frac{\partial}{\partial X^M}\left(\bar{\mathbb{P}}_\sigma\right)_b^M+(B_\sigma)_b=0\,; \tag{2.126}$$

- on the boundary $\partial\mathcal{B}$,

$$\left(-\bar{\mathbb{P}}_\sigma\right)_b^M N_M+\frac{\partial}{\partial X^C}\left(\frac{\partial W_\sigma^{\mathrm{def}}}{\partial F_{A,B}^b}N_B\,m_{\|A}^{\ D}\right)m_{\|D}^{\ C}+(b)_b=0\,, \tag{2.127}$$

$$-\frac{\partial W_\sigma^{\mathrm{def}}}{\partial F_{A,B}^b}N_B\,N_A+(\mathbb{B}_\sigma)_b=0\,; \tag{2.128}$$

- on the edges $\partial\partial\mathcal{B}$,

$$-\frac{\partial W_\sigma^{\mathrm{def}}}{\partial F_{A,B}^b}N_B\,\nu_A+(\beta_\sigma)_b=0\,. \tag{2.129}$$

On one hand, Eqs. (2.127) and (2.128) imply that the subdomains of the second-gradient continuum exchange with each other forces per unit area, forces per unit area depending on the curvature of the *Cauchy cut*, and double forces. On the other hand, Eq. (2.129) implies that the subdomains of the second-gradient continuum exchange with each other also forces per unit length.

2.4 Second-gradient-micropolar continuum

Notation

Below A, B, D, i, and j are integers belonging to $\{1,2,3\}$. Summation is intended over repeated indices.

$\mathcal{B}$: initial (Lagrangian) configuration.

$\partial\mathcal{B}$: boundary of $\mathcal{B}$.

$\partial\partial\mathcal{B}$: edges of $\mathcal{B}$.

Indices denoted by uppercase letters are chosen to indicate components of a tensor in the initial configuration and lowercase letters to indicate components of a tensor in the current configuration. Summation is intended over the repeated indices.

N_A: components of the outward-pointing normal N of $\partial\mathcal{B}$.

ν_A: components of the outward-pointing normal ν of $\partial\partial\mathcal{B}$.

X^A: Lagrangian coordinates.

χ^i: component i of the configuration field χ.

v^i: component i of the translation velocity v.

G_{AB}: component (A, B) of the metric tensor G in the initial configuration.

g_{ij}: component (i, j) of the metric tensor g in the current configuration.

δ^A_B: component (A, B) of the second-order identity tensor I.

$m_\perp{}^D_A$: component (D, A) of the operator of orthogonal projection $m_\perp$.

$m_\parallel{}^D_A$: component (D, A) of the operator of parallel projection $m_\parallel$.

Q^i_A: component (i, A) of the microrotation tensor Q.

ϑ_{BAj}: component (B, A, j) of the rotation velocity ϑ.

F^i_A: component (i, A) of the gradient of the configuration field F.

ρ: Lagrangian time-independent mass density.

J^{AB}: component (A, B) of the Lagrangian time-independent moment of inertia of each particle J.

$\mathcal{A}_{\sigma\pi}$: action functional for the micropolar continuum.

$\left(\bar{\mathbb{P}}_{\sigma\pi}\right)^i_A$: component (i, A) of the effective second-gradient-micropolar stress tensor $\bar{\mathbb{P}}$.

$\left(\bar{\mathbb{M}}_{\sigma\pi}\right)^i_A$: component (i, A) of the effective second-gradient-micropolar couple-stress tensor $\bar{\mathbb{M}}$.

$\left(\mathbb{V}_{\sigma\pi}\right)_j$: component j of the second-gradient-micropolar couple-stress vector $\mathbb{V}_{\sigma\pi}$.

$\left(B_{\sigma\pi}\right)_j$: component j of the volumic forces $B_{\sigma\pi}$.

$\left(C_{\sigma\pi}\right)_j$: component j of the volumic couples $C_{\sigma\pi}$.

$\left(b_{\sigma\pi}\right)_j$: component j of the surface forces $b_{\sigma\pi}$.

$\left(c_{\sigma\pi}\right)_j$: component j of the surface couples $c_{\sigma\pi}$.

$\left(\mathbb{B}_{\sigma\pi}\right)_j$: component j of the surface doubleforces $\mathbb{B}_{\sigma\pi}$.

$(\mathbb{C}_{\sigma\pi})_j$: component j of the surface doublecouples $\mathbb{C}_{\sigma\pi}$.

$(\beta_{\sigma\pi})_j$: component j of the edge forces $\beta_{\sigma\pi}$.

$(\mathfrak{c}_{\sigma\pi})_j$: component j of the edge forces $\mathfrak{c}_{\sigma\pi}$.

$[S]^T$, S: transpose of the second-order tensor S.

ϵ_{jAB}: permutation (or Levi-Civita) symbol.

$f_{,B}$: partial derivative of the function f with respect to X^B, *i.e*, $f_{,B} = \frac{\partial f}{\partial X^B}$.

dV, ds, and $d\ell$: volume, surface, and length elements.

2.4.1 Deformation energy density and deformation measures

Let $\widetilde{W}^{\text{def}}_{\sigma\pi}(\chi, Q, F, \nabla Q, \nabla F, \nabla\nabla Q, X)$ be the specific deformation energy density. Since it must be objective, the equality

$$\widetilde{W}^{\text{def}}_{\sigma\pi}(\chi, Q, F, \nabla Q, \nabla F, \nabla\nabla Q, X) = \widetilde{W}^{\text{def}}_{\sigma\pi}(O\chi + a, OQ, OF, O\nabla Q, O\nabla F, O\nabla\nabla Q, X) \tag{2.130}$$

needs to be satisfied for any orthogonal transformation O and for any vector a. For any Q and for any χ, it is natural to choose $O = Q^T$ and $a = -Q^T\chi$. We get

$$\widetilde{W}_{\sigma\pi}(\chi, Q, F, \nabla Q, \nabla F, \nabla\nabla Q, X) = \widetilde{W}^{\text{def}}_{\sigma\pi}\left(0, I, Q^T F, Q^T\nabla Q, Q^T\nabla F, Q^T\nabla\nabla Q, X\right) . \tag{2.131}$$

Eq. (2.131) implies that if $\tilde{W}^{\text{def}}_{\sigma\mu}$ is an objective function, then there exists a function $W^{\text{def}}_{\sigma\pi}$ such that

$$\widetilde{W}^{\text{def}}_{\sigma\pi}\left(0, I, Q^T F, Q^T\nabla Q, Q^T\nabla F, Q^T\nabla\nabla Q, X\right) = W^{\text{def}}_{\sigma\pi}(Q, F, \nabla Q, \nabla F, \nabla\nabla Q, X) \tag{2.132}$$

and

$$\widetilde{W}_{\sigma\pi}(\chi, Q, F, \nabla Q, \nabla F, \nabla\nabla Q, X) = W^{\text{def}}_{\sigma\pi}(Q, F, \nabla Q, \nabla F, \nabla\nabla Q, X) . \tag{2.133}$$

Eq. (2.131) leads also to the deformation measures E_π, Γ_π, $\Gamma_{\sigma\pi}$, and $K_{\sigma\pi}$ defined by

$$E_\pi = \frac{1}{2}\left(Q^T F - I\right) \quad , \quad \Gamma_\pi = Q^T\nabla Q \quad , \quad \Gamma_{\sigma\pi} = Q^T\nabla F \quad , \quad K_{\sigma\pi} = Q^T\nabla\nabla Q , \tag{2.134}$$

which have the following component expressions:

$$\begin{aligned}(E_\pi)_{MN} &= \frac{1}{2}\left(g_{ij}\,Q^j_M\,F^i_N - G_{MA}\,\delta^A_N\right) \quad , \quad (\Gamma_\pi)_{MNC} = G_{MA}\left(Q^T\right)^A_i Q^i_{N,C}\,, \\ (\Gamma_{\sigma\pi})_{MNC} &= G_{MA}\left(Q^T\right)^A_i F^i_{N,C} \quad , \quad (K_{\sigma\pi})_{MNCD} = G_{MA}\left(Q^T\right)^A_i Q^i_{N,CD}\,.\end{aligned} \tag{2.135}$$

It is natural to refer to the tensor $\Gamma_{\sigma\pi}$ as the *second-gradient-micropolar wryness tensor* and to the tensor $K_{\sigma\pi}$ as the *second second-gradient-micropolar wryness tensor*. Since Q^TF, $Q^T\nabla Q$, $Q^T\nabla F$, and $Q^T\nabla\nabla Q$ can be expressed as a function of E_π, Γ_π, $\Gamma_{\sigma\pi}$, and $K_{\sigma\pi}$, it follows the existence of a function $\widehat{W}^{\text{def}}_{\sigma\pi}$ such that

$$W^{\text{def}}_{\sigma\pi}\left(Q,F,\nabla Q,\nabla F,\nabla\nabla Q,X\right) = \widehat{W}^{\text{def}}_{\sigma\pi}\left(E_\pi,\Gamma_\pi,\Gamma_{\sigma\pi},K_{\sigma\pi},X\right). \tag{2.136}$$

In the following, the Euler-Lagrange equations are derived by considering deformation energy density as an objective function of Q,F, ∇Q, ∇F, and $\nabla\nabla Q$, $\widehat{W}^{\text{def}}_{\sigma\pi}\left(E_\pi,\Gamma_\pi,\Gamma_{\sigma\pi},K_{\sigma\pi},X\right)$. Thus, the derived equations are valid for any chosen combination of deformation measures.

2.4.2 Euler-Lagrange equations

Let us consider the action functional

$$\begin{aligned}\mathcal{A} = \int_{t_0}^{t_1}\int_{\mathcal{B}}\left(\frac{1}{2}\rho\,v^2 + \frac{1}{2}J\,\Theta^2 - W_{\sigma\pi}\left(\chi,Q,F,\nabla Q,\nabla F,\nabla\nabla Q,X\right)\right)dV\,dt \\ + \int_{t_0}^{t_1}\int_{\partial\mathcal{B}}\left(-W^{\text{surf}}_{\sigma\pi}\left(\chi,\frac{\partial\chi}{\partial N},Q,\frac{\partial Q}{\partial N},X\right)\right)ds\,dt + \int_{t_0}^{t_1}\int_{\partial\partial\mathcal{B}}\left(-W^{\text{lgth}}_{\sigma\pi}\left(\chi,Q,X\right)\right)d\ell\,dt\,,\end{aligned} \tag{2.137}$$

where

- the field χ denotes the configuration field;
- the fields ρ and I refer to the Lagrangian time-independent mass density and to the Lagrangian time-independent moment of inertia of material points;
- the fields $v = \frac{\partial\chi}{\partial t}$ and $\Theta = \frac{\partial Q}{\partial t}$ denote the Lagrangian-translation velocities and Lagrangian-rotation velocities;
- $\rho\,v^2 = g_{ab}v^a v^b$ and $J\,\Theta^2 = J^{BA}\,\Theta^i_A\,\Theta^k_B\,g_{ik}$;
- the potential $W_{\sigma\pi}\left(\chi,Q,F,\nabla F,\nabla Q,\nabla\nabla Q,X\right)$ is related to the volume density of action;

- the potential $W^{\text{surf}}_{\sigma\pi}(\chi, Q, X)$ is related to the actions externally applied on the boundary $\partial\mathcal{B}$;
- the potential $W^{\text{lgth}}_{\sigma\pi}(\chi, Q, X)$ is related to the actions externally applied on the edges $\partial\partial\mathcal{B}$.

Potential $W_{\sigma\pi}$ can be split into two addends: the objective specific deformation energy density $W^{\text{def}}_{\sigma\pi}$ and the external conservative action of bulk loads $U^{\text{ext}}_{\sigma\pi}$, as follows

$$W_{\sigma\pi}(\chi, Q, F, \nabla F, \nabla Q, \nabla\nabla Q, X) = W^{\text{def}}_{\sigma\pi}(Q, F, \nabla F, \nabla Q, \nabla\nabla Q) + U^{\text{ext}}_{\sigma\pi}(\chi, Q, X) \ . \quad (2.138)$$

The first variation of the deformation energy-related portion of the action functional can be expressed as the sum of three terms,

$$\delta\mathcal{A}^{\text{def}}_{\sigma\pi} = \delta\mathcal{A}^{\text{def}}_{\sigma\pi F} + \delta\mathcal{A}^{\text{def}}_{\sigma\pi Q} + \delta\mathcal{A}^{\text{def}}_{\sigma\pi\nabla F} + \delta\mathcal{A}^{\text{def}}_{\sigma\pi\nabla Q} + \delta\mathcal{A}^{\text{def}}_{\sigma\pi\nabla\nabla Q} \ , \quad (2.139)$$

where

$$\delta\mathcal{A}^{\text{def}}_{\sigma\pi F} = -\int_{t_0}^{t_1}\int_{\mathcal{B}} \frac{\partial W^{\text{def}}_{\sigma\pi}}{\partial F^i_A}\,\delta F^i_A\, dV dt \ , \quad (2.140)$$

$$\delta\mathcal{A}^{\text{def}}_{\sigma\pi Q} = -\int_{t_0}^{t_1}\int_{\mathcal{B}} \frac{\partial W^{\text{def}}_{\sigma\pi}}{\partial Q^j_F}\,\delta Q^j_F\, dV dt \ , \quad (2.141)$$

$$\delta\mathcal{A}^{\text{def}}_{\sigma\pi\nabla F} = -\int_{t_0}^{t_1}\int_{\mathcal{B}} \frac{\partial W^{\text{def}}_{\sigma\pi}}{\partial F^i_{M,B}}\,\delta F^i_{M,B}\, dV dt \ , \quad (2.142)$$

$$\delta\mathcal{A}^{\text{def}}_{\sigma\pi\nabla Q} = -\int_{t_0}^{t_1}\int_{\mathcal{B}} \frac{\partial W^{\text{def}}_{\sigma\pi}}{\partial Q^i_{M,B}}\,\delta Q^i_{M,B}\, dV dt \ , \quad (2.143)$$

and

$$\delta\mathcal{A}^{\text{def}}_{\sigma\pi\nabla\nabla Q} = -\int_{t_0}^{t_1}\int_{\mathcal{B}} \frac{\partial W^{\text{def}}_{\sigma\pi}}{\partial Q^i_{M,BC}}\,\delta Q^i_{M,BC}\, dV dt \ . \quad (2.144)$$

First second-gradient-micropolar stress tensor

Let us consider the first variation $\delta\mathcal{A}^{\text{def}}_{\sigma\pi F}$. We get

$$\delta\mathcal{A}^{\text{def}}_{\sigma\pi F} = -\int_{t_0}^{t_1}\int_{\partial\mathcal{B}} \frac{\partial W^{\text{def}}_{\sigma\pi}}{\partial F^i_A} N_A \delta\chi^i\, ds\, dt + \int_{t_0}^{t_1}\int_{\mathcal{B}} \frac{\partial}{\partial X^A}\left(\frac{\partial W^{\text{def}}_{\sigma\pi}}{\partial F^i_A}\right)\delta\chi^i\, dV dt \ . \quad (2.145)$$

Let $\mathbb{P}$ be the *second-gradient-micropolar stress tensor* defined by

$$(\mathbb{P}_{\sigma\pi})_i^A = \frac{\partial W^{\text{def}}_{\sigma\pi}}{\partial F^i_A} \,, \tag{2.146}$$

which leads to

$$\delta\mathcal{A}^{\text{def}}_{\sigma\pi F} = -\int_{t_0}^{t_1}\int_{\partial\mathcal{B}} (\mathbb{P}_{\sigma\pi})_i^A \, N_A \, \delta\chi^i \, ds \, dt + \int_{t_0}^{t_1}\int_{\mathcal{B}} \frac{\partial}{\partial X^A} (\mathbb{P}_{\sigma\pi})_i^A \, \delta\chi^i \, dV \, dt \,. \tag{2.147}$$

First part of the second-gradient-micropolar stress vector

Let us consider the first variation $\delta\mathcal{A}^{\text{def}}_{\sigma\pi Q}$. It yields

$$\delta\mathcal{A}^{\text{def}}_{\sigma\pi Q} = -\int_{t_0}^{t_1}\int_{\mathcal{B}} \frac{\partial W^{\text{def}}_{\sigma\pi}}{\partial Q^i_F} \, \delta Q^j_F \, dV \, dt \,. \tag{2.148}$$

If Eq. (2.14) is taken into account, we get

$$\delta\mathcal{A}^{\text{def}}_{\sigma\pi Q} = -\int_{t_0}^{t_1}\int_{\mathcal{B}} \left(\mathbb{V}^{\text{I}}_{\sigma\pi}\right)_k \delta\omega^k \, dV dt \,, \tag{2.149}$$

where

$$\left(\mathbb{V}^{\text{I}}_{\sigma\pi}\right)_k = \frac{\partial W^{\text{def}}_{\sigma\pi}}{\partial Q^i_F} \, G^{BM} \, Q^i_M \, \epsilon_{kFB} \tag{2.150}$$

is the *first part of the second-gradient-micropolar stress vector*.

Hyper and effective second-gradient-micropolar stress tensors

Let us consider the first variation $\delta\mathcal{A}^{\text{def}}_{\sigma\pi\nabla F}$. We get

$$\delta\mathcal{A}^{\text{def}}_{\sigma\pi\nabla F} = -\int_{t_0}^{t_1}\int_{\partial\mathcal{B}} \frac{\partial W^{\text{def}}_{\sigma\pi}}{\partial F^i_{A,B}} \, \delta F^i_A \, N_B \, ds \, dt + \int_{t_0}^{t_1}\int_{\mathcal{B}} \frac{\partial}{\partial X^B}\left(\frac{\partial W^{\text{def}}_{\sigma\pi}}{\partial F^i_{A,B}}\right) \delta F^i_A \, dV dt \,. \tag{2.151}$$

The second integral of the second term gives:

$$\begin{aligned}\int_{t_0}^{t_1}\int_{\mathcal{B}} \frac{\partial}{\partial X^B}\left(\frac{\partial W^{\text{def}}_{\sigma\pi}}{\partial F^i_{A,B}}\right) \delta F^i_A \, dV dt = &\int_{t_0}^{t_1}\int_{\partial\mathcal{B}} \frac{\partial}{\partial X^B}\left(\frac{\partial W^{\text{def}}_{\sigma\pi}}{\partial F^i_{A,B}}\right) N_A \, \delta\chi^i \, ds \, dt \\ &- \int_{t_0}^{t_1}\int_{\mathcal{B}} \frac{\partial^2}{\partial X^A \partial X^B}\left(\frac{\partial W^{\text{def}}_{\sigma\pi}}{\partial F^i_{A,B}}\right) \delta\chi^i \, dV dt \,.\end{aligned} \tag{2.152}$$

Let us define the *hyper second-gradient-micropolar stress tensor* $\mathbb{H}_{\sigma\pi}$

$$(\mathbb{H}_{\sigma\pi})_i^{AB} = \frac{\partial W_{\sigma\pi}^{\text{def}}}{\partial F^i_{A,B}} \tag{2.153}$$

and the *effective second-gradient-micropolar stress tensor* $\bar{\mathbb{P}}_{\sigma\pi}$ equal to

$$\left(\bar{\mathbb{P}}_{\sigma\pi}\right)_i^A = (\mathbb{P}_{\sigma\pi})_i^A + \frac{\partial\,(\mathbb{H}_{\sigma\pi})_i^{AB}}{\partial X^B}\ . \tag{2.154}$$

First part of the second-gradient-micropolar couple stress tensor and second part of the second-gradient-micropolar stress vector

Let us compute the first variation $\delta\mathcal{A}^{\text{def}}_{\sigma\pi\nabla Q}$. It yields

$$\delta\mathcal{A}^{\text{def}}_{\sigma\pi\nabla Q} = -\int_{t_0}^{t_1}\int_{\mathcal{B}} \frac{\partial W_{\sigma\pi}^{\text{def}}}{\partial Q^i_{M,B}}\left(G^{NA}\,Q^i_{A,B}\,\epsilon_{jMN}\,\delta\omega^j + G^{NA}\,Q^i_A\,\epsilon_{jMN}\,\delta\omega^j_{,B}\right) dV dt \tag{2.155}$$

and

$$\begin{aligned}\delta\mathcal{A}^{\text{def}}_{\sigma\pi\nabla Q} = &-\int_{t_0}^{t_1}\int_{\mathcal{B}} \frac{\partial W_{\sigma\pi}^{\text{def}}}{\partial Q^i_{M,B}}\,G^{NA}\,Q^i_{A,B}\,\epsilon_{jMN}\,\delta\omega^j\,dV dt\\ &-\int_{t_0}^{t_1}\int_{\partial\mathcal{B}} \frac{\partial W_{\sigma\mu}^{\text{def}}}{\partial Q^i_{M,B}}\,G^{NA}\,Q^i_A\,\epsilon_{jMN}\,\delta\omega^j\,N_B\,ds\,dt\\ &+\int_{t_0}^{t_1}\int_{\mathcal{B}} \frac{\partial}{\partial X^B}\left(\frac{\partial W_{\sigma\pi}^{\text{def}}}{\partial Q^i_{M,B}}\,G^{NA}\,Q^i_A\,\epsilon_{jMN}\right)\delta\omega^j\,dV dt\ .\end{aligned} \tag{2.156}$$

We refer to the tensor $\mathbb{M}_{\sigma\pi}$ as the *Piola-type couple stress tensor* and to the vector $\mathbb{V}^{(\text{II})}_{\sigma\pi}$ as the *second Lagrangian stress vector*. They are defined by

$$\left(\mathbb{M}^{\text{I}}_{\sigma\pi}\right)_j^B = \frac{\partial W_{\sigma\pi}^{\text{def}}}{\partial Q^i_{M,B}}\,G^{NA}\,Q^i_A\,\epsilon_{jMN} \quad , \quad \left(\mathbb{V}^{\text{II}}_{\sigma\pi}\right)_j = \frac{\partial W_{\sigma\pi}^{\text{def}}}{\partial Q^i_{M,B}}\,G^{NA}\,Q^i_{A,B}\,\epsilon_{jMN}\ . \tag{2.157}$$

Positions (2.157) and one integration by parts lead to

$$\begin{aligned}\delta\mathcal{A}^{\text{def}}_{\sigma\pi\nabla Q} = &-\int_{t_0}^{t_1}\int_{\mathcal{B}}\left(\mathbb{V}^{\text{II}}_{\sigma\pi}\right)_j\delta\omega^j\,dV dt\\ -\int_{t_0}^{t_1}\int_{\partial\mathcal{B}}\left(\mathbb{M}^{\text{I}}{}_{\sigma\pi}\right)_j^N N_N\,\delta\omega^j\,ds\,dt &+\int_{t_0}^{t_1}\int_{\mathcal{B}}\frac{\partial}{\partial X^N}\left(\mathbb{M}^{\text{I}}{}_{\sigma\pi}\right)_j^N\delta\omega^j\,dV dt\ .\end{aligned} \tag{2.158}$$

Hyper and effective second-gradient-micropolar couple stress tensors

Let us consider the first variation $\delta\mathcal{A}^{\text{def}}_{\sigma\pi\nabla\nabla Q}$. We get

$$\delta\mathcal{A}^{\text{def}}_{\sigma\pi\nabla\nabla Q} = -\int_{t_0}^{t_1}\int_{\mathcal{B}} \frac{\partial W^{\text{def}}_{\sigma\pi}}{\partial Q^i_{M,BC}} \Big(G^{NA}\, Q^i_{A,BC}\, \epsilon_{jMN}\, \delta\omega^j + G^{NA}\, Q^i_{A,B}\, \epsilon_{jMN}\, \delta\omega^j_{,C} + G^{NA}\, Q^i_{A,C}\, \epsilon_{jMN}\, \delta\omega^j_{,B} + G^{NA}\, Q^i_{A}\, \epsilon_{jMN}\, \delta\omega^j_{,BC} \Big)\, dV dt \tag{2.159}$$

that is equal to

$$\delta\mathcal{A}^{\text{def}}_{\sigma\pi\nabla\nabla Q} = -\int_{t_0}^{t_1}\int_{\mathcal{B}} \frac{\partial W^{\text{def}}_{\sigma\pi}}{\partial Q^i_{M,BC}} \Big(G^{NA}\, Q^i_{A,BC}\, \epsilon_{jMN}\, \delta\omega^j + 2\, G^{NA}\, Q^i_{A,B}\, \epsilon_{jMN}\, \delta\omega^j_{,C} + G^{NA}\, Q^i_{A}\, \epsilon_{jMN}\, \delta\omega^j_{,BC} \Big)\, dV dt \tag{2.160}$$

Let us define the *third part of the second-gradient-micropolar stress vector*

$$\left(\mathbb{V}^{\text{III}}_{\sigma\pi}\right)_k = \frac{\partial W^{\text{def}}_{\sigma\pi}}{\partial Q^i_{M,BC}} \left(G^{NA}\, Q^i_{A,BC}\, \epsilon_{kMN} \right) . \tag{2.161}$$

From the second integral of Eq. (2.160), we have

$$\begin{aligned} &-\int_{t_0}^{t_1}\int_{\mathcal{B}} \frac{\partial W^{\text{def}}_{\sigma\pi}}{\partial Q^i_{M,BC}} \left(2\, G^{NA}\, Q^i_{A,B}\, \epsilon_{jMN}\, \delta\omega^j_{,C} \right) dV dt \\ &= -\int_{t_0}^{t_1}\int_{\partial\mathcal{B}} \frac{\partial W^{\text{def}}_{\sigma\pi}}{\partial Q^i_{M,BC}} \left(2\, G^{NA}\, Q^i_{A,B}\, \epsilon_{jMN} \right) N_C\, \delta\omega^j\, ds\, dt \\ &+\int_{t_0}^{t_1}\int_{\mathcal{B}} \frac{\partial}{\partial X^C} \frac{\partial W^{\text{def}}_{\sigma\pi}}{\partial Q^i_{M,BC}} \left(2\, G^{NA}\, Q^i_{A,B}\, \epsilon_{jMN} \right) \delta\omega^j\, dV dt \end{aligned} \tag{2.162}$$

that leads to the definition of the second part of the Piola-type couple stress tensor

$$\left(\mathbb{M}^{\text{II}}_{\sigma\pi}\right)^C_k = \frac{\partial W^{\text{def}}_{\sigma\pi}}{\partial Q^i_{M,BC}} \left(2\, G^{NA}\, Q^i_{A,B}\, \epsilon_{kMN} \right) . \tag{2.163}$$

The third integral of the second term of Eq. (2.160) can be manipulated. We arrive to

$$\begin{aligned}
&-\int_{t_0}^{t_1}\int_{\mathcal{B}} \frac{\partial W^{\mathrm{def}}_{\sigma\pi}}{\partial Q^i_{M,BC}}\, G^{NA}\, Q^i_A\, \epsilon_{jMN}\, \delta\omega^j_{,BC}\, dV dt \\
&= -\int_{t_0}^{t_1}\int_{\partial\mathcal{B}} \left(\frac{\partial W^{\mathrm{def}}_{\sigma\pi}}{\partial Q^i_{M,BC}}\, G^{NA}\, Q^i_A\, \epsilon_{jMN}\right) N_C\, \delta\omega^j_{,B}\, ds\, dt \\
&+\int_{t_0}^{t_1}\int_{\mathcal{B}} \frac{\partial}{\partial X^C}\left(\frac{\partial W^{\mathrm{def}}_{\sigma\mu}}{\partial Q^i_{M,BC}}\, G^{NA}\, Q^i_A\, \epsilon_{jMN}\right) \delta\omega^j_{,B}\, dV dt\ .
\end{aligned} \tag{2.164}$$

The second term of Eq. (2.164) is equal to

$$\begin{aligned}
&\int_{t_0}^{t_1}\int_{\mathcal{B}} \frac{\partial}{\partial X^C}\left(\frac{\partial W^{\mathrm{def}}_{\sigma\pi}}{\partial Q^i_{M,BC}}\, G^{NA}\, Q^i_A\, \epsilon_{jMN}\right) \delta\omega^j_{,B}\, dV dt \\
&= \int_{t_0}^{t_1}\int_{\partial\mathcal{B}} \frac{\partial}{\partial X^C}\left(\frac{\partial W^{\mathrm{def}}_{\sigma\pi}}{\partial Q^i_{M,BC}}\, G^{NA}\, Q^i_A\, \epsilon_{jMN}\right) N_B\, \delta\omega^j\, ds\, dt \\
&-\int_{t_0}^{t_1}\int_{\mathcal{B}} \frac{\partial^2}{\partial X^B \partial X^C}\left(\frac{\partial W^{\mathrm{def}}_{\sigma\pi}}{\partial Q^i_{M,BC}}\, G^{NA}\, Q^i_A\, \epsilon_{jMN}\right) \delta\omega^j\, dV dt\ .
\end{aligned} \tag{2.165}$$

Let us define the *Hyper second-gradient-micropolar couple stress tensor* $\tilde{\mathbb{H}}_{\sigma\pi}$,

$$\left(\tilde{\mathbb{H}}_{\sigma\pi}\right)^{BC}_{j} = \frac{\partial W^{\mathrm{def}}_{\sigma\pi}}{\partial Q^i_{M,BC}}\, G^{NA}\, Q^i_A \epsilon_{jMN} \tag{2.166}$$

and the *effective second-gradient-micropolar couple stress tensor* $\bar{\mathbb{M}}_{\sigma\mu}$,

$$\left(\bar{\mathbb{M}}_{\sigma\pi}\right)^{B}_{k} = \left(\mathbb{M}^{\mathrm{I}}_{\sigma\pi}\right)^{B}_{k} + \left(\mathbb{M}^{\mathrm{II}}_{\sigma\pi}\right)^{B}_{k} + \frac{\partial}{\partial X^C}\left(\mathbb{H}_{\sigma\pi}\right)^{BC}_{k}\ . \tag{2.167}$$

Double and edge second-gradient-micropolar contact couples

The first term of Eq. (2.164) gives

$$\begin{aligned}
&-\int_{t_0}^{t_1}\int_{\partial\mathcal{B}} \left(\frac{\partial W^{\mathrm{def}}_{\sigma\pi}}{\partial Q^i_{M,BC}}\, G^{NA}\, Q^i_A\, \epsilon_{jMN}\right) N_C\, \delta\omega^j_{,B}\, ds\, dt \\
&= -\int_{t_0}^{t_1}\int_{\partial\mathcal{B}} \left(\frac{\partial W^{\mathrm{def}}_{\sigma\pi}}{\partial Q^i_{M,BC}}\, G^{NA}\, Q^i_A\, \epsilon_{jMN}\right) N_C\, \delta\omega^j_{,D}\, \delta^D_B\, ds\, dt \\
&= -\int_{t_0}^{t_1}\int_{\partial\mathcal{B}} \left(\frac{\partial W^{\mathrm{def}}_{\sigma\pi}}{\partial Q^i_{M,BC}}\, G^{NA}\, Q^i_A\, \epsilon_{jMN}\right) N_C \left(m_{\perp}{}^D_B + m_{\parallel}{}^D_B\right) \delta\omega^j_{,D}\, ds\, dt\ .
\end{aligned} \tag{2.168}$$

Moreover, it holds

$$\begin{aligned} &-\int_{t_0}^{t_1}\int_{\partial\mathcal{B}}\left(\frac{\partial W^{\mathrm{def}}_{\sigma\pi}}{\partial Q^i_{M,BC}}\,G^{NA}\,Q^i_A\,\epsilon_{jMN}\right)N_C\left(m_{\perp}{}^D_B+m_{\parallel}{}^D_B\right)\delta\omega^j_{,D}\,ds\,dt \\ =&-\int_{t_0}^{t_1}\int_{\partial\mathcal{B}}\left(\frac{\partial W^{\mathrm{def}}_{\sigma\pi}}{\partial Q^i_{M,BC}}\,G^{NA}\,Q^i_A\,\epsilon_{jMN}\right)N_C\left(m_{\perp}{}^D_F\,m_{\perp}{}^F_B+m_{\parallel}{}^D_F\,m_{\parallel}{}^F_B\right)\delta\omega^j_{,D}\,ds\,dt\ . \end{aligned} \tag{2.169}$$

Eq. (2.169) can be split into two integral. The first one implies

$$\begin{aligned} &-\int_{t_0}^{t_1}\int_{\partial\mathcal{B}}\left(\frac{\partial W^{\mathrm{def}}_{\sigma\pi}}{\partial Q^i_{M,BC}}\,G^{NA}\,Q^i_A\,\epsilon_{jMN}\right)N_C\,N^D\,N_B\,\delta\omega^j_{,D}\,ds\,dt \\ &=-\int_{t_0}^{t_1}\int_{\partial\mathcal{B}}\left(\frac{\partial W^{\mathrm{def}}_{\sigma\pi}}{\partial Q^i_{M,BC}}\,G^{NA}\,Q^i_A\,\epsilon_{jMN}\right)N_C\,N_B\,\frac{\partial\delta\omega^j}{\partial N}\,ds\,dt \end{aligned} \tag{2.170}$$

and leads to the *double second-gradient-micropolar contact couples* defined by

$$\left(\frac{\partial W^{\mathrm{def}}_{\sigma\pi}}{\partial Q^i_{M,BC}}\,G^{NA}\,Q^i_A\,\epsilon_{jMN}\right)N_C\,N_B\ . \tag{2.171}$$

The second one implies

$$\begin{aligned} &-\int_{t_0}^{t_1}\int_{\partial\mathcal{B}}\left(\frac{\partial W^{\mathrm{def}}_{\sigma\pi}}{\partial Q^i_{M,BC}}\,G^{NA}\,Q^i_A\,\epsilon_{jMN}\right)N_C\left(m_{\parallel}{}^D_F\,m_{\parallel}{}^F_B\right)\delta\omega^j_{,D}\,ds\,dt \\ =&-\int_{t_0}^{t_1}\int_{\partial\mathcal{B}}\frac{\partial}{\partial X^D}\left(\frac{\partial W^{\mathrm{def}}_{\sigma\pi}}{\partial Q^i_{M,BC}}\,G^{NA}\,Q^i_A\,\epsilon_{jMN}\,m_{\parallel}{}^F_B\,N_C\,\delta\omega^j\right)m_{\parallel}{}^D_F\,ds\,dt \\ &+\int_{t_0}^{t_1}\int_{\partial\mathcal{B}}\frac{\partial}{\partial X^D}\left(\frac{\partial W^{\mathrm{def}}_{\sigma\pi}}{\partial Q^i_{M,BC}}\,G^{NA}\,Q^i_A\,\epsilon_{jMN}\,m_{\parallel}{}^F_B N_C\right)m_{\parallel}{}^D_F\delta\omega^j\,ds\,dt \end{aligned} \tag{2.172}$$

and its second term gives

$$\begin{aligned} &-\int_{t_0}^{t_1}\int_{\partial\partial\mathcal{B}}\left(\frac{\partial W^{\mathrm{def}}_{\sigma\pi}}{\partial Q^i_{M,BC}}\,G^{NA}\,Q^i_A\,\epsilon_{jMN}N_C\right)m_{\parallel}{}^F_B\,m_{\parallel}{}^D_F\,\nu_D\,\delta\omega^j\,d\ell dt = \\ &\qquad-\int_{t_0}^{t_1}\int_{\partial\partial\mathcal{B}}\left(\frac{\partial W^{\mathrm{def}}_{\sigma\pi}}{\partial Q^i_{M,BC}}\,G^{NA}\,Q^i_A\,\epsilon_{jMN}N_C\right)\nu_B\,\delta\omega^j\,d\ell dt\,. \end{aligned} \tag{2.173}$$

The quantity

$$\left(\frac{\partial W^{\mathrm{def}}_{\sigma\pi}}{\partial Q^i_{M,BC}}\,G^{NA}\,Q^i_A\,\epsilon_{jMN}\,N_C\right)\nu_B \tag{2.174}$$

is naturally named *edge second-gradient-micropolar contact couples*.

External actions

Let us consider the first variation $\delta\mathcal{A}^{\text{ext}}_{\sigma\pi}$. It yields

$$\delta\mathcal{A}^{\text{ext}}_{\sigma\pi} = \int_{t_0}^{t_1}\int_{\mathcal{B}} (B_{\sigma\pi})_b\,\delta\chi^b\,dV\,dt + \int_{t_0}^{t_1}\int_{\mathcal{B}} (C_{\sigma\pi})_j\,\delta\omega^j\,dV\,dt\,, \tag{2.175}$$

where

$$(B_{\sigma\pi})_b = -\frac{\partial U^{\text{ext}}_{\sigma\pi}}{\partial\chi^b} \quad , \quad (C_{\sigma\pi})_j = -\frac{\partial U^{\text{ext}}_{\sigma\pi}}{\partial Q^k_F}\,G^{BM}\,Q^k_M\,\epsilon_{jFB}\,. \tag{2.176}$$

Let us consider the first variation $\delta\mathcal{A}^{\text{surf}}_{\sigma\pi}$. It yields

$$\begin{aligned}\delta\mathcal{A}^{\text{surf}}_{\sigma\pi} = &\int_{t_0}^{t_1}\int_{\partial\mathcal{B}} (b_{\sigma\pi})_b\,\delta\chi^b\,ds\,dt + \int_{t_0}^{t_1}\int_{\partial\mathcal{B}} (\mathbb{B}_{\sigma\pi})_b\,\frac{\partial\,(\delta\chi)^b}{\partial N}\,ds\,dt\\ &+\int_{t_0}^{t_1}\int_{\partial\mathcal{B}} (c_{\sigma\pi})_j\,\delta\omega^j\,ds\,dt + \int_{t_0}^{t_1}\int_{\partial\mathcal{B}} (\mathbb{C}_{\sigma\pi})_j\,\frac{\partial\,(\delta\omega)^j}{\partial N}\,ds\,dt\,,\end{aligned} \tag{2.177}$$

where

$$(b_{\sigma\pi})_b = -\frac{\partial W^{\text{surf}}_{\sigma\pi}}{\partial\chi^b} \quad , \quad (\mathbb{B}_{\sigma\pi})_b = -\frac{\partial W^{\text{surf}}_{\sigma\pi}}{\frac{\partial\chi^b}{\partial N}} \tag{2.178}$$

and

$$(c_{\sigma\pi})_j = -\frac{\partial W^{\text{surf}}_{\sigma\pi}}{\partial Q^k_F}\,G^{BM}\,Q^k_M\,\epsilon_{jFB} \quad , \quad (\mathbb{C}_{\sigma\pi})_j = -\frac{\partial W^{\text{surf}}_{\sigma\pi}}{\frac{\partial Q^k_F}{\partial N}}\,G^{BM}\,Q^k_M\,\epsilon_{jFB}\,. \tag{2.179}$$

Let us consider the first variation $\delta\mathcal{A}^{\text{lgth}}_{\sigma\pi}$. It yields

$$\delta\mathcal{A}^{\text{lgth}}_{\sigma\pi} = \int_{t_0}^{t_1}\int_{\partial\partial\mathcal{B}} (\beta_{\sigma\pi})_b\,\delta\chi^b\,d\ell\,dt + \int_{t_0}^{t_1}\int_{\partial\partial\mathcal{B}} (\mathfrak{c}_{\sigma\pi})_j\,\delta\omega^j\,d\ell\,dt\,, \tag{2.180}$$

where

$$(\beta_{\sigma\pi})_b = -\frac{\partial W^{\text{lgth}}_{\sigma\pi}}{\partial\chi^b}\,, \tag{2.181}$$

$$(\mathfrak{c}_{\sigma\pi})_j = -\frac{\partial W^{\text{lgth}}_{\sigma\pi}}{\partial Q^k_F}\,G^{BM}\,Q^k_M\,\epsilon_{jFB}\,. \tag{2.182}$$

2.4.3 Equilibrium equations

The equilibrium equations, in the Lagrangian description, are listed below:

- on the volume $\mathcal{B}$,

$$-\frac{\partial(\rho v_b)}{\partial t}+\frac{\partial}{\partial X^M}\left(\bar{\mathbb{P}}_{\sigma\pi}\right)_b^M+(B_{\sigma\pi})_b=0\,, \tag{2.183}$$

$$\frac{\partial(J^{AB}\vartheta_{BAj})}{\partial t}+\frac{\partial}{\partial X^N}\left(\bar{\mathbb{M}}_{\sigma\pi}\right)_j^N-(\mathbb{V}_{\sigma\pi})_j+(C_{\sigma\pi})_j=0\,; \tag{2.184}$$

- on the boundary $\partial\mathcal{B}$,

$$\left(-\bar{\mathbb{P}}_{\sigma\pi}\right)_b^M N_M+\frac{\partial}{\partial X^C}\left(\frac{\partial W^{\mathrm{def}}_{\sigma\pi}}{\partial F^b_{A,B}}N_B\,m_{\|A}^{\ D}\right)m_{\|D}^{\ C}+(b_{\sigma\pi})_b=0\,, \tag{2.185}$$

$$\left(-\bar{\mathbb{M}}_{\sigma\pi}\right)_j^M N_M+\frac{\partial}{\partial X^D}\left(\frac{\partial W^{\mathrm{def}}_{\sigma\pi}}{\partial Q^i_{M,BC}}G^{NA}\,Q^i_{\ A}\,\epsilon_{jMN}\,m_{\|B}^{\ F}\,N_C\right)m_{\|F}^{\ D}+(c_{\sigma\pi})_j=0\,, \tag{2.186}$$

$$-\left(\frac{\partial W^{\mathrm{def}}_{\sigma\pi}}{\partial F^b_{A,B}}\right)N_B\,N_A+(\mathbb{B}_{\sigma\pi})_b=0\,, \tag{2.187}$$

$$-\left(\frac{\partial W^{\mathrm{def}}_{\sigma\pi}}{\partial Q^i_{M,BC}}G^{NA}\,Q^i_{\ A}\,\epsilon_{jMN}\right)N_C\,N_B+(\mathbb{C}_{\sigma\pi})_j=0\,; \tag{2.188}$$

- on the edges $\partial\partial\mathcal{B}$,

$$-\frac{\partial W^{\mathrm{def}}_{\sigma\pi}}{\partial F^b_{A,B}}N_B\,\nu_A+(\beta_{\sigma\pi})_b=0\,, \tag{2.189}$$

$$-\left(\frac{\partial W^{\mathrm{def}}_{\sigma\pi}}{\partial Q^i_{M,BC}}G^{NA}\,Q^i_{\ A}\,\epsilon_{jMN}\,N_C\right)\nu_B+(\mathfrak{c}_{\sigma\pi})_j=0\,. \tag{2.190}$$

On the one hand, Eqs. (2.185) and (2.186) imply that the subdomains of the second-gradient-micropolar continuum exchange with each other forces per unit area, forces per unit area depending on the curvature of the *Cauchy cut*, couples per unit area, and couples per unit area depending on the curvature of the *Cauchy cut*. On the other hand, Eqs. (2.187) and (2.188) imply that the subdomains of the second-gradient-micropolar continuum exchange with each other also double forces and double couples. Finally, Eqs. (2.189) and (2.190) imply that forces and couples per unit length are also shared.

2.5 Summarizing the main results

- The micropolar continuum is an assembly of small rigid particles that can translate and rotate. By means of the least action principle, it has been proven (see Eqs. (2.50)

to (2.53)) that the subdomains of micropolar continuum interact with each other via forces per unit area and moments per unit area.

- The micromorphic continuum is an assembly of small particles that can translate and deform. By means of least action principle, it has been proven (see Eqs. (2.89) to (2.92)) that the subdomains of micromorphic continuum interact with each other via forces per unit area and double forces per unit area.

- The second-gradient continuum is an assembly of small particles that can just translate. By means of least action principle, it has been proven (see Eqs. (2.126) to (2.129)) that the subdomains of second-gradient continuum interact with each other via forces per unit area, forces per unit area depending on the curvature of the Cauchy cut, and forces per unit length.

- The second-gradient-micropolar continuum is an assembly of small particles that can translate and rotate. By means of least action principle, it has been proven (see Eqs. (2.183) to (2.190)) that the subdomains of second-gradient-micropolar continuum interact with each other via forces and couples per unit area, forces and couples per unit area depending on the curvature of the Cauchy cut, forces and couples per unit length.

- Recent applications of the listed generalized continua concern particle-based and composite materials and metamaterials. Applications in the framework of biological and biomedical fields are in progress.

Chapter 3

Pantographic structures

This chapter is divided into three sections. Section 3.1 is derived from the paper [79]. Recent findings regarding pantographic sheets (2D) are presented. Section 3.2 is derived from the paper [21] in which new results concerning pantographic blocks (3D) are presented. Section 3.3 is derived from the paper [73] in which the effects of pivot-related defects on the mechanical response of pantographic sheets are analyzed. For pantographic sheets, we use both a discrete Hencky-type model and a continuous model. However, for pantographic blocks, only a continuous approach is used. This decision arises from the greater degrees of freedom of pantographic blocks, for which continuous models offer computational advantages.

3.1 Novel torsional energy for pantographic sheets

The pantographic sheet consists of a discrete grid of beams and pivots (hinges). We categorize three distinct scales, namely the macroscopic, mesoscopic, and microscopic scales. On the macroscale, the pantographic sheet is represented as a second-gradient continuum. Transitioning to the mesoscale, it is conceptualized as an assembly of extensional springs linked by rotational springs to account for bending and shear effects. On the microscale, it is an assembly of beams and pivots. This section introduces a novel torsional energy for simulating the torsion of pivots via mesoscale modeling. This energy improves the one proposed in [33].

The section is organized as follows. In Subsection 3.1.1, we summarize the experimental setup used to test metallic (ME) pantographic sheets, as well as the obtained results. For the analysis of pantographic sheets, the discrete model currently used in the literature is summarized in Subsection 3.1.2. Subsection 3.1.3 introduces novel torsional energy and its properties. In Subsection 3.1.4, a numerical identification in accordance with the experimental data is performed, and the theoretical force-elongation curves obtained are compared to the

experimental ones. Both ME and polyamide (PA) pantographic sheets display a high level of matching. Regarding the experimental results for the PA samples, we refer to paper [33].

Notation

w_a: local axial strain energy.

w_b: local bending strain energy.

w_s: local torsional (or shear) strain energy given in [33].

W_s: novel torsional (or shear) strain energy proposed.

ψ_1, ψ_2: angles used for describing the deformation of polyamide (PA) pantographic structures.

d_1, d_2: Euclidean distances used for describing the deformation of metallic (ME) pantographic structures.

R_x: axial reaction force.

λ: rate of the displacement with respect to the maximal displacement before the first pivot collapse.

3.1.1 Experimental motivations

The development of additive manufacturing and 3D printing enabled the creation of objects with an extremely fine microstructure that was virtually impossible a decade ago. Among these, pantographic sheets can be printed, which consist of a planar grid obtained by superimposing two families of beams (fibers) that are connected by small cylinders usually referred to as pivots (hinges). To accurately describe their mechanical behavior, at least three terms in the strain energy must be considered: beam elongation, beam bending, and pivot torsion.

Below, we report the experimental force-elongation curves of pantographic sheets subjected to bias-extension tests. Bias-extension tests permit the simultaneous analyses of extensional, shear, and bending mechanical effects. The deformation shape of a sample subjected to a bias test can be separated into three regions (see Fig. 3.1):

- the clamped ends (A) in which extensional deformations dominate;
- the central zone (S) in which shear effects are primarily present;

- the region (B) in which bending deformations are predominant.

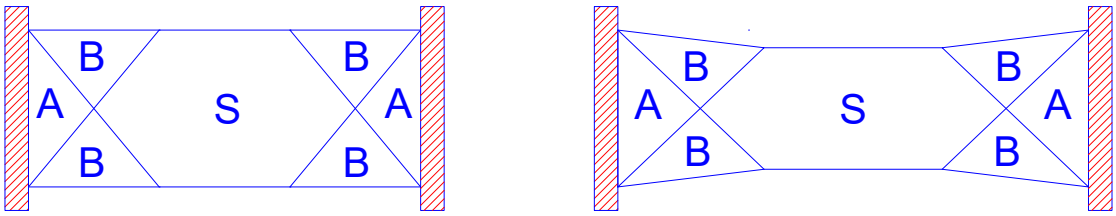

Fig. 3.1 Bias extension test: areas characterized by different predominant energies.

Bias extensional tests have been performed on three metallic pantographic sheets[1]. The tested samples have been clamped at both ends, with one end remaining fixed and the other being longitudinally displaced at a rate of 50 μm/s. The experiments have been carried out in LMPS-Laboratoire de Mécanique de Paris-Saclay. In Fig. 3.2, four load steps are displayed for the bias test performed on one of the three ME samples. The quantity $\widehat{u}_x = 25\,\text{mm}$ denotes the longitudinal displacement following which the first collapse of a pivot occurred. The

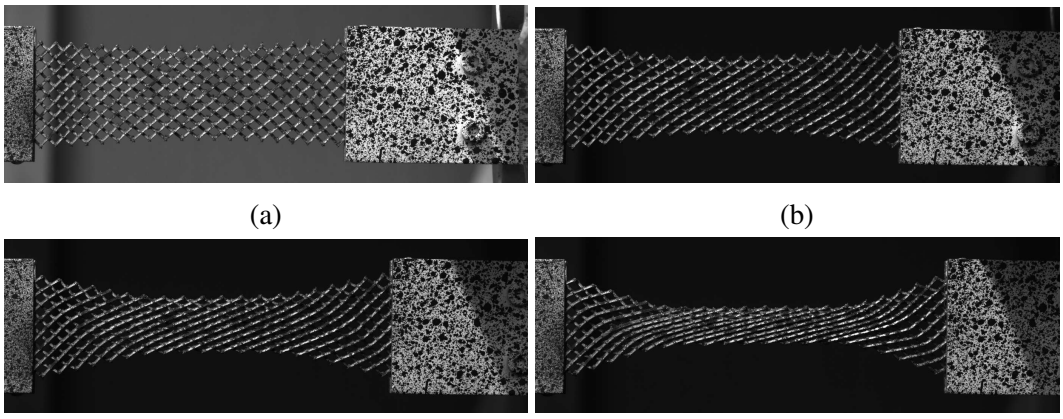

Fig. 3.2 Bias test of a ME pantographic sheet sample: (a) $0.25\,\widehat{u}_x$, (b) $0.5\,\widehat{u}_x$, (c) $0.75\,\widehat{u}_x$ and (d) $\widehat{u}_x$.

force-elongation curve of a ME sample until total collapse is depicted in Fig. 3.3, which is illustrative of a larger set of experiments and has been used as an example for the identification. In this instance, the bias test has been conducted by using two loading paths:

- the samples have been loaded and unloaded after reaching 9.26 mm, (see the red portion of the curve in Fig. 3.3);

[1]The samples, in 316L stainless steel, were fabricated at Laboratoire PIMM of École Nationale Supérieure des Arts et Métiers in France by using the SLM125HL setup from SLM solutions.

- then, the samples have been loaded up to the limit of total collapse (see the blue portion of the curve in Fig. 3.3).

Before the collapse of the first pivot, the force-elongation curve undergoes a change in concavity (Fig. 3.3). In light of this, we intend to introduce a model capable of capturing

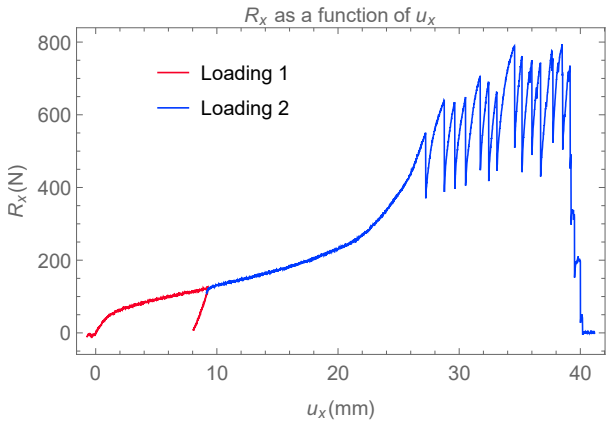

Fig. 3.3 $u_x \mapsto R_x$ experimental curve of a ME pantographic sample in bias elongation test.

the mechanical response of both metallic and polyamide specimens with the fewest possible parameters. Regarding the experimental results pertaining to polyamide samples, we refer the reader to [33]

3.1.2 Discrete mechanical model

Various types of pantographic sheet models have been proposed in the literature:

- meso-models that consist of an assembly of Euler-Bernoulli beams with axial, bending, and torsional stiffnesses [6, 40];
- Hencky-type models in which the microstructure is modeled by means of extensional springs interconnected by two families of rotational springs to account for bending and torsional (or shear) effects [138, 137, 139, 141].

Once homogenized, both models result in second-gradient continua. In this section, the Hencky-type model is used (see Fig. 3.4). The strain energy is assumed to be the sum of three uncoupled contributions related to stretching, bending, and torsion [138]. Stretching, bending, and torsional energies are denoted by w_a, w_b and w_s and are defined as follows [38]:

$$w_a(\ell) = \frac{1}{2} k_a (\ell - \ell_0)^2 \ , \tag{3.1}$$

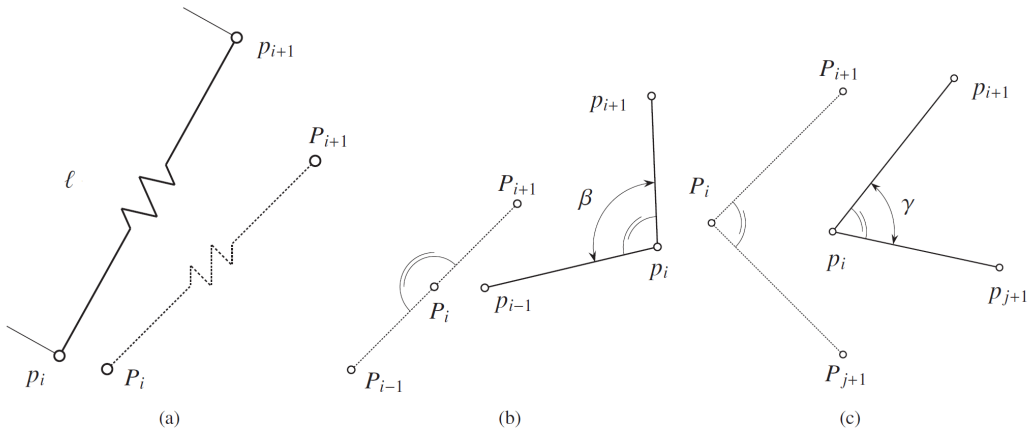

Fig. 3.4 Hencky-type model with (a) axial extensional springs, (b) bending rotational springs, and (c) torsional rotational springs.

$$w_b(\beta) = k_b\,(cos\beta + 1)\ , \tag{3.2}$$

$$w_s(\gamma) = \frac{1}{2}\widetilde{k}_s\left(\gamma - \frac{\pi}{2}\right)^{\widetilde{a}}\ , \tag{3.3}$$

where k_a, k_b and $\widetilde{k}_s$ represent the axial, bending and shear stiffnesses, respectively. The symbols $\ell_0 = \left\|\overrightarrow{P_iP_{i+1}}\right\|$, $\ell = \left\|\overrightarrow{p_ip_{i+1}}\right\|$ denote, respectively, the initial and the actual lengths of the beams. The operator $\|\cdot\|$ represents the Euclidean norm. The quantities β and γ in Eq. (3.2) can be calculated in terms of the pivot displacements using the Carnot theorem. In Fig. 3.4(c), the geometric significance of the angle γ is highlighted. This type of shear energy is unsuitable for describing the force-elongation curve of metallic pantographic sheets depicted in Fig. 3.3, which is characterized by a significant change in concavity. In addition, the second derivative of the specific energy function $w_s(\cdot)$, defined in Eq.(3.3), tends to infinity if $\widetilde{a} < 2$ and γ tends to $\pi/2$. This feature may result in numerical problems. Simple numerical simulations reveal that modifying the functions describing the axial and bending energies, $w_a(\cdot)$ and $w_b(\cdot)$, has no appreciable effect on the matching between the identified theoretical and experimental force-elongation curves. In this regard, the function $w_s(\cdot)$ is essential, and a novel specific shear energy that improves the one in Eq. (3.3) is introduced below. In addition to discrete models, the proposed energy can be used in the continuum models that result from a homogenization procedure.

3.1.3 Novel shear nonlinearity model

Our purpose is to find the torsion energy function $w_s(\cdot)$ for matching the force-elongation curves for both metallic and polyamide pantographic sheets. The local axial and bending

energy functions, $w_a(\cdot)$ and $w_b(\cdot)$, given by Eqs. (3.1)-(3.2) are not changed since, as mentioned, they play no significant role in the concavity change of the force-displacement curve.

Proposed is a phenomenological two-parameter shear energy that can model the high changes in the concavity of the force-elongation curve, with one parameter responsible for the change in concavity. In this regard, a novel local shear energy, $W_s(\cdot)$, is introduced by considering a constitutive law relating the torsional moment M to the shear angle γ via an arctangent $(\cdot)$ function

$$M(\gamma) = k_s \arctan\left[a\left(\gamma - \frac{\pi}{2}\right)\right], \tag{3.4}$$

where k_s and α are the two parameters of constitutive law (3.4). Observe that samples undergo permanent deformations after unloading (see the red part of Fig. 3.3) indicating that pivots are affected by plastic deformations. In future works, plastic deformations or damage in pivots will be discussed further. Some results are already available in the literature [132, 134]. In plasticity, the $\exp(\cdot)$, $\log(\cdot)$, $\tan(\cdot)$ or $\arctan(\cdot)$ functions are typically used in the modeling of hardening. As a result, it is reasonable to consider the $\arctan(\cdot)$ function for modeling torsional moments, and this choice should not be considered as *data-driven* but as *theory-driven*. Eq. (3.4) yields the specific torsional energy, W_s. Since,

$$\frac{\partial W_s(\gamma)}{\partial \gamma} = M(\gamma), \tag{3.5}$$

then, the specific shear energy can be obtained by integrating Eq. (3.4) with the condition $W_s(\pi/2) = 0$,

$$W_s(\gamma) = k_s\left(\left(\gamma - \frac{\pi}{2}\right)\arctan\left(a\left(\gamma - \frac{\pi}{2}\right)\right) - \frac{\log\left(a^2\left(\gamma - \frac{\pi}{2}\right)^2 + 1\right)}{2a}\right). \tag{3.6}$$

The first derivative and the second derivative of W_s with respect to γ are bounded in the interval $[0, \pi]$ and for any positive number α. Fig. 3.5 shows the influence of the material parameter a on the shear energy, $W_s(\cdot)$, the first derivative, $\frac{\partial W_s}{\partial \gamma}(\cdot)$, and the second derivative, $\frac{\partial^2 W_s}{\partial \gamma^2}(\cdot)$. The curves of Fig. 3.5 correspond to $k_s = 1/\arctan(\frac{a\pi}{2})$ such that $M_s = 1$ when $\gamma = \pi$. As expected, due to the boundness, there are no infinite values obtained in any of the three cases. Accordingly, the proposed energy is appropriate for numerical simulations.

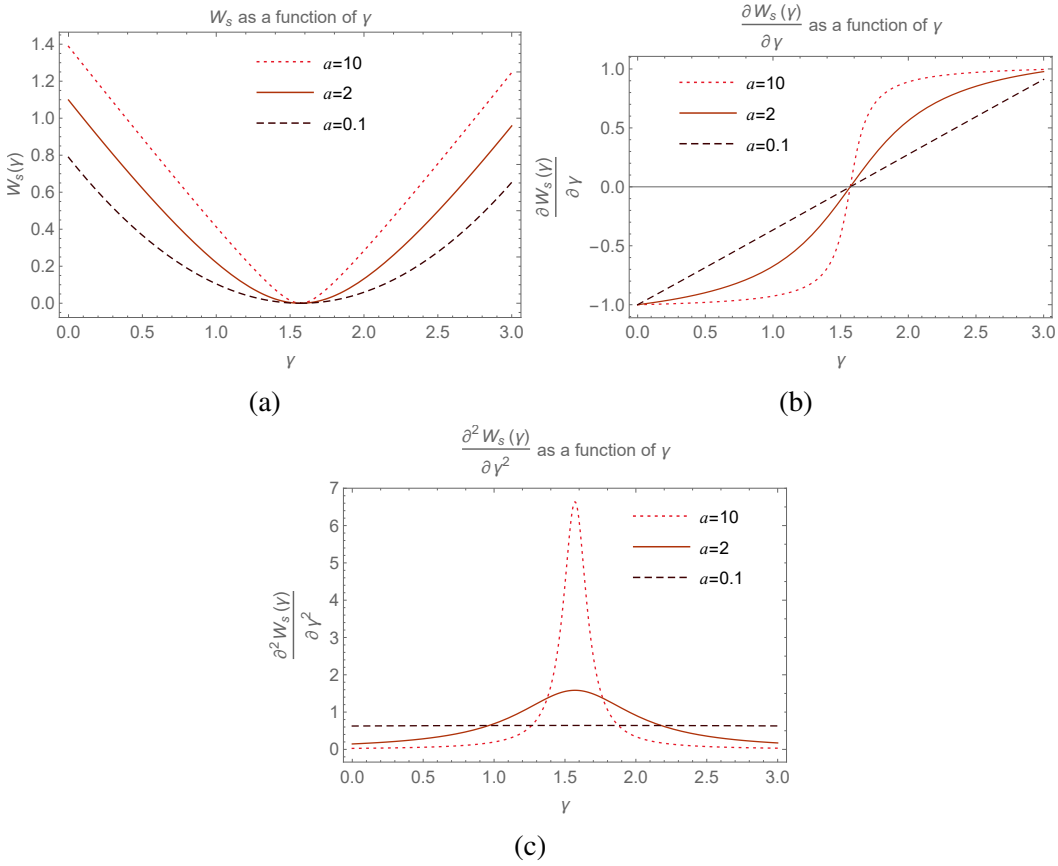

Fig. 3.5 Parametric study of energy density: (a) W_s, (b) $\frac{\partial W_s}{\partial \gamma}$ and (c) $\frac{\partial^2 W_s}{\partial \gamma^2}$.

3.1.4 Numerical identification procedure

The characterization of a polyamide sample presented in [33] is based on the use of the two angles ψ_1 and ψ_2, which are physical quantities representative of the deformation process. The angle ψ_1 allows us to describe the shear deformation in the shear-dominated region of the specimen, whereas the angle ψ_2 allows us to describe the bending deformation in the bending-dominated region of the specimen.

Two Euclidean distances d_1 and d_2 are preferred here to describe the metallic samples, whose geometrical definition is shown in Fig. 3.6. The distances d_1 and d_2 are mean quantities associated with shear- and bending-dominated behavior, whereas the angles ψ_1 and ψ_2 are local descriptors. The numerical procedure for the identification consists of the minimization

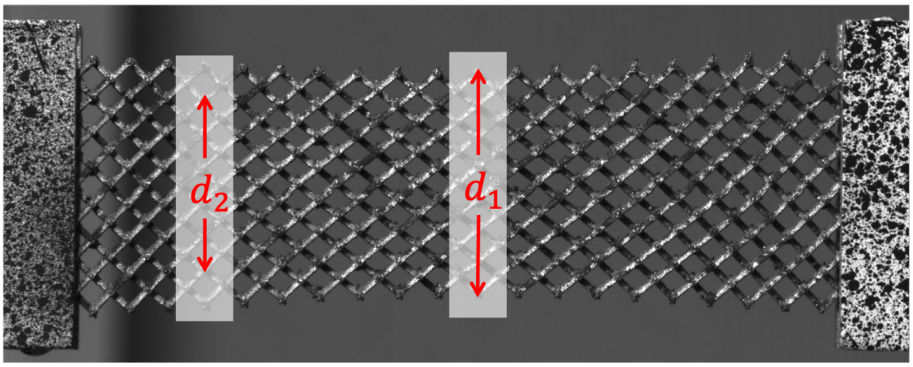

Fig. 3.6 Geometrical definition of d_1 and d_2 in the configuration $0.25\,\widehat{u}_x$.

of a function $f(a, k_a, k_b, k_s)$,

$$f(\alpha, k_a, k_b, k_s) = \sum_{i=1}^{N} \left(R_i - R_i^*\right)^2 + \sum_{i=1}^{N} \left(p_i^{(1)} - p_i^{(1)*}\right)^2 + \sum_{i=1}^{N} \left(p_i^{(2)} - p_i^{(2)*}\right)^2 , \tag{3.7}$$

where $(p^{(1)}, p^{(2)})$ stands for (ψ_1, ψ_2) or (d_1, d_2), the superscript $*$ denotes the experimental values of the considered descriptor, and N is the total number of the experimental points.

In Eq.(3.7), the various contributions can be summarized as

- the reaction force R considered as function of the displacement;
- the distance d_1 (or angle ψ_1) in the shear-dominated region of the specimen considered as a function of the displacement;
- the distance d_2 (or angle ψ_2) in the bending-dominated region of the specimen considered as a function of the displacement.

The identification process is been performed in terms of displacements but in terms of a dimensionless parameter $\lambda \in [0,1]$ defined by the ratio between the prescribed displacement and a maximal prescribed displacement before the first hinge collapse: $\lambda = u_x/\widehat{u}_x$, where u_x is the current axial displacement.[2]

3.1.5 Identification example

By comparing experimental findings and theoretical numerical simulations for polyamide and metallic pantographic sheets, the effectiveness of the proposed expression of shear energy is proven in the following.

Polyamide pantographic sample

The numerical identification procedure is performed with four experimental values corresponding to $\lambda \in \left\{\frac{1}{4}, \frac{1}{2}, \frac{3}{4}, 1\right\}$ for each of the three curves relative to (λ, R_x), (λ, ψ_1), and (λ, ψ_2). For the proposed energy expression, the parameters (a, k_a, k_b, k_s) that best fit the experimental data have been identified.

In Figs. 3.7-3.8-3.9, we reproduce the experimental results [33] for polyamide specimens. In these figures, the graphs $\lambda \mapsto R_x$, $\lambda \mapsto \psi_1$, and $\lambda \mapsto \psi_2$ are shown. The parameter α is mainly responsible for the change in the concavity of the force-elongation curve.

Metallic pantographic samples

The numerical identification procedure is performed with only three experimental values corresponding to $\lambda \in \left\{\frac{1}{4}, \frac{1}{2}, \frac{3}{4}\right\}$ for each of the three curves relative to R_x, $d_1^{(0)} - d_1$ and $d_2^{(0)} - d_2$. For the proposed energy expression, the parameters (a, k_a, k_b, k_s) that best fit the experimental data are identified.

Let $d_1^{(0)}$ and $d_2^{(0)}$ be the values of d_1 and d_2 in the initial configuration. The graphs $\lambda \mapsto R_x$, $\lambda \mapsto d_1^{(0)} - d_1$ and $\lambda \mapsto d_2^{(0)} - d_2$ are shown in Fig. 3.9, 3.10, and 3.10. It should be noted that the high chance in the concavity is accurately modeled with the proposed shear energy (3.6).

The experimental values for $\lambda = 1$ are not used in the identification procedure because the numerical simulation cannot capture the high increase at the end of the loading. The mechanism underlying this significant increase is still under investigation, but it may be related to self-contact between beams in the bending-dominated behavior region (B) (see Figs. 3.2(d)).

[2]The minimization procedure is performed by means of the *fmincon* function in the MATLAB® environment

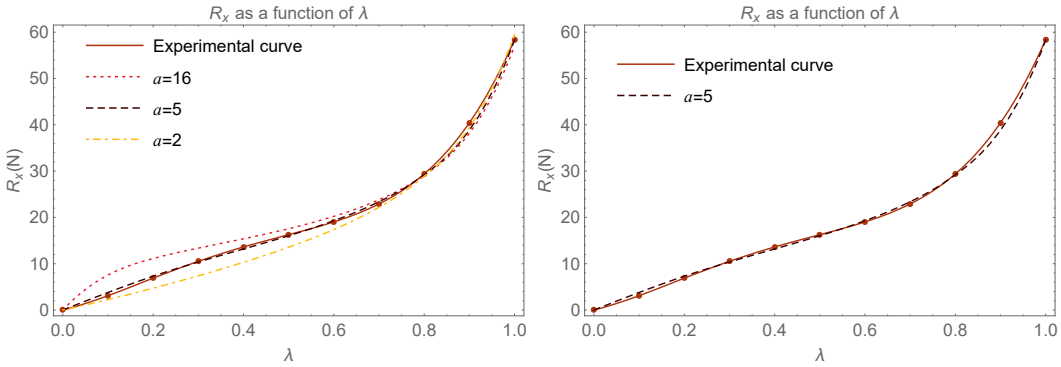

(a) (b)

Fig. 3.7 $\lambda \mapsto R_x$ curves (a) for different values of a and (b) for the identified value $a = 5$.

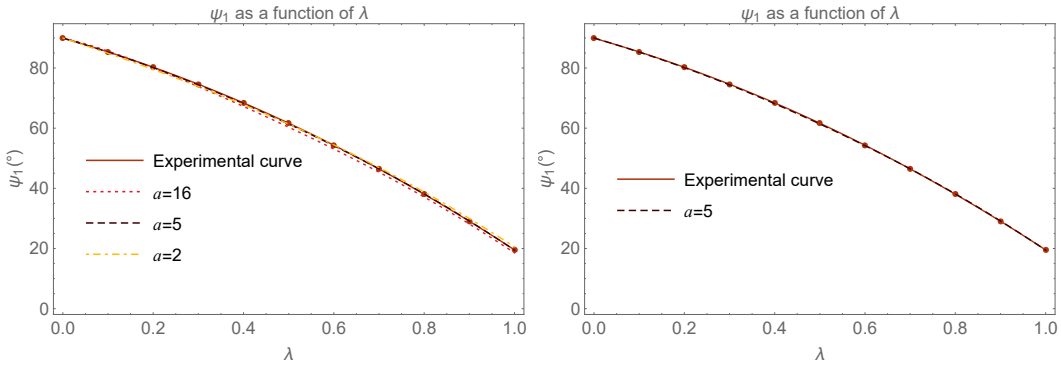

(a) (b)

Fig. 3.8 $\lambda \mapsto \psi_1$ curves (a) for different values of a and (b) for the identified value $a = 5$.

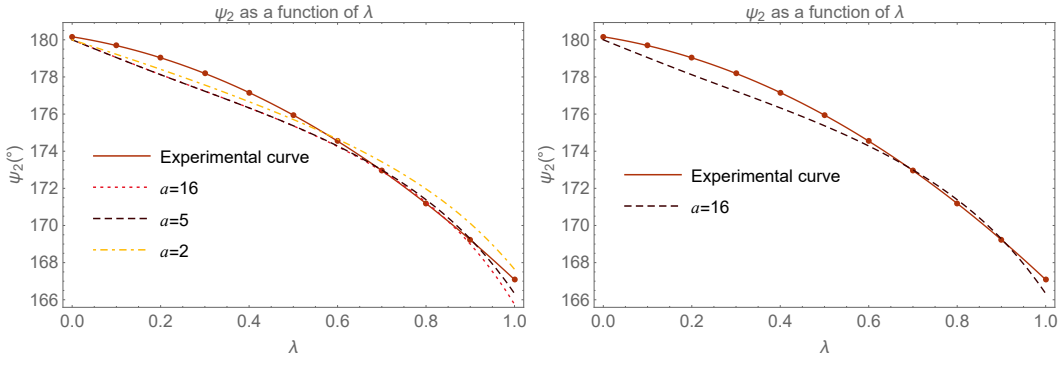

(a) (b)

Fig. 3.9 $\lambda \mapsto \psi_2$ curves (a) for different values of a and (b) for the identified value $a = 5$.

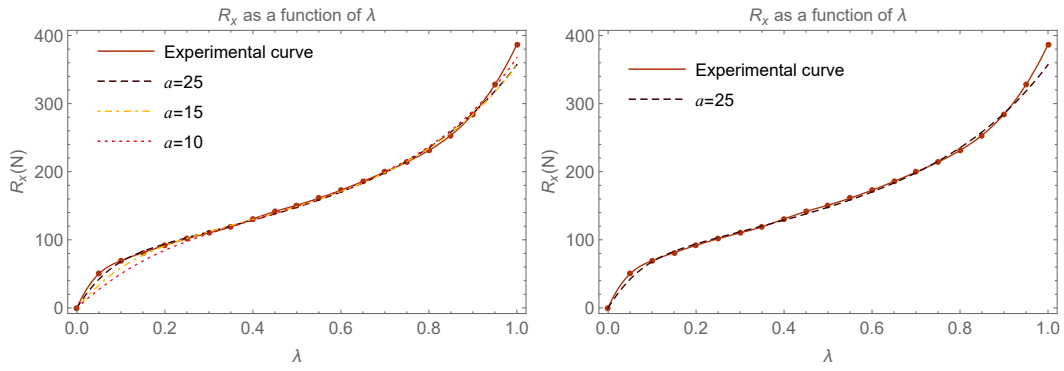

(a) (b)

Fig. 3.10 $\lambda \mapsto R_x$ curves (a) for different values of a and (b) for the identified value $a = 25$.

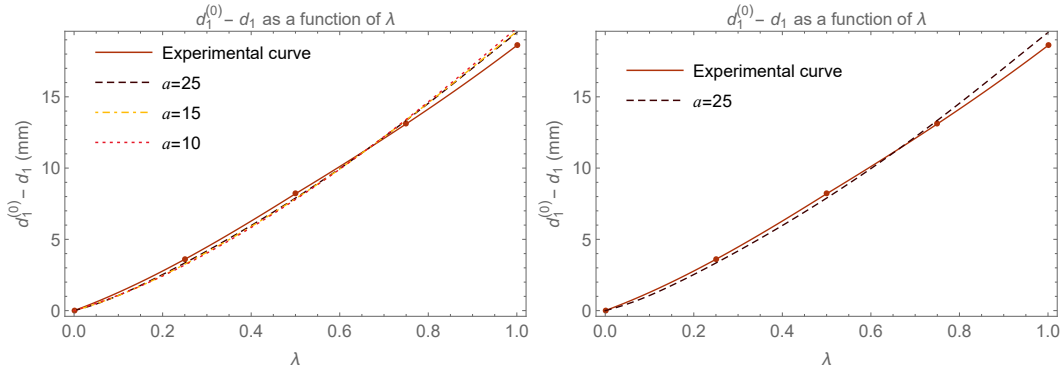

(a) (b)

Fig. 3.11 $\lambda \mapsto d_1^{(0)} - d_1$ curve (a) for different values of a (b) for the identified value $a = 25$.

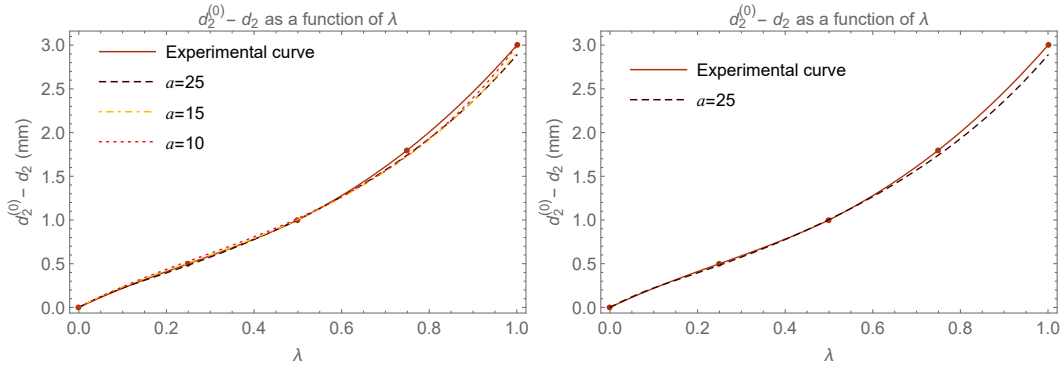

(a) (b)

Fig. 3.12 $\lambda \mapsto d_2^{(0)} - d_2$ curve (a) for different values of a (b) for the identified value $a = 25$.

3.2 Deformation mode in 3-point flexure on pantographic block

Pantographic blocks (3D) are made by assembling pantographic sheets (2D). A first attempt to investigate such a 3D metamaterial can be found in [46, 147]. This section introduces a novel second-gradient continuum model for simulating their mechanical behavior. The mathematical model is experimentally validated by means of Digital Volume Correlation (DVC) techniques [50, 142].

The section is organized as follows. Subsection 3.2.1 introduces a novel second-gradient model for the pantographic block and discusses the experimental setup. Experiments are conducted using a prescribed load parallel to the pantographic sheets that constitute the pantographic block being tested. For the initial and final deformation configurations, the DVC results are discussed in Subsection 3.2.2. First, the displacement fields are analyzed. The motions of the pivots are then reported to identify the mode of deformation of the pantographic block. In Subsection 3.2.3, numerical simulations are performed in which the prescribed load is orthogonal (and not parallel) to the pantographic sheets. In order to validate the numerical results for this case, additional experimental campaigns are required and are in progress at the University of L'Aquila in collaboration with the International Research Centre on Mathematics and Mechanics of Complex Systems (M&MoCS).

Notation

$\boldsymbol{L}$, $\boldsymbol{M}$: directions of the beams (fibers) in the initial configuration.

$\boldsymbol{N}$: direction of the pivots (hinges) in the initial configuration.

$\boldsymbol{F}$: gradient of the configuration field $\boldsymbol{\chi}$, $\boldsymbol{F} = \nabla\boldsymbol{\chi}$.

$\boldsymbol{\ell}$, $\boldsymbol{m}$: directions of the beams (fibers) in the actual configuration.

$\boldsymbol{n}$: direction of the pivots (hinges) in the actual configuration.

$\lambda - 1$, $\mu - 1$: axial deformation measures of the beams.

$\eta - 1$: axial deformation measure of the pivots.

γ: shear deformation measure.

κ_{tL}, κ_{tM}: twist deformation measures of the beams.

κ_{nL}, κ_{nM}: flexure deformation measures of the beams normal to the plane of the beams.

κ_{gL}, κ_{gM}: geodesic flexure deformation measures of the beams.

ρ: grey level residual.

Φ_c: sum of squares of grey level residuals in the representative volume of interest (ROI).

Φ_m: penalty term considered in the Hencky-elasticity regularization.

$\times$: cross product of two vectors.

$\cdot$: scalar product of two vectors.

3.2.1 Model-initialized DVC of in-situ flexure

Strain energy of pantographic blocks

The internal architecture of the pantographic block (Fig. 3.13) is organized along three distinct orthogonal directions. Two of them define the pantographic plane of the scissor mechanism, and the directions of the so-called beams (fibers) are given by the unit vectors **L** and **M** in the reference configuration. The third direction, defined by the vector **N**, represents the axis of the pivots (hinges). The images of these three vectors in the current (or deformed) configuration are given by

$$\lambda \boldsymbol{\ell} = \boldsymbol{F}\mathbf{L} \quad , \quad \mu \boldsymbol{m} = \boldsymbol{F}\mathbf{M} \quad , \quad \eta \boldsymbol{n} = \boldsymbol{F}\mathbf{N} \tag{3.8}$$

where $\boldsymbol{F}$ is the gradient of the configuration field $\boldsymbol{\chi}$, $\boldsymbol{\ell}$, $\boldsymbol{m}$, and $\boldsymbol{n}$ are the unit vectors in the current configuration under the transformation $\boldsymbol{F}$. It is assumed that the behavior of the pantographic block is the same for all parallel planes to the plane π defined by the vectors **L** and **M**. Let us introduce the strain energy [60, 140, 57]

$$\begin{aligned} w_\pi = \frac{1}{2}\Big[&\mathrm{K}_e((\lambda-1)^2+(\mu-1)^2)+\mathrm{K}_s\gamma^2+ \\ &\mathrm{K}_t\ (\kappa_{tL}^2+\kappa_{tM}^2)+\mathrm{K}_n\ (\kappa_{nL}^2+\kappa_{nM}^2)+\mathrm{K}_g\ (\kappa_{gL}^2+\kappa_{gM}^2)\Big] \end{aligned} \tag{3.9}$$

that has two main contributions: i) the first-gradient part based on the deformation measures $(\lambda-1)$, $(\mu-1)$, and γ, which represent the change of length in directions of vectors **L** and **M** as well as the change of angle between these two directions in the deformation process from the reference to the current configuration as defined by Equation (3.10); ii) the second-gradient

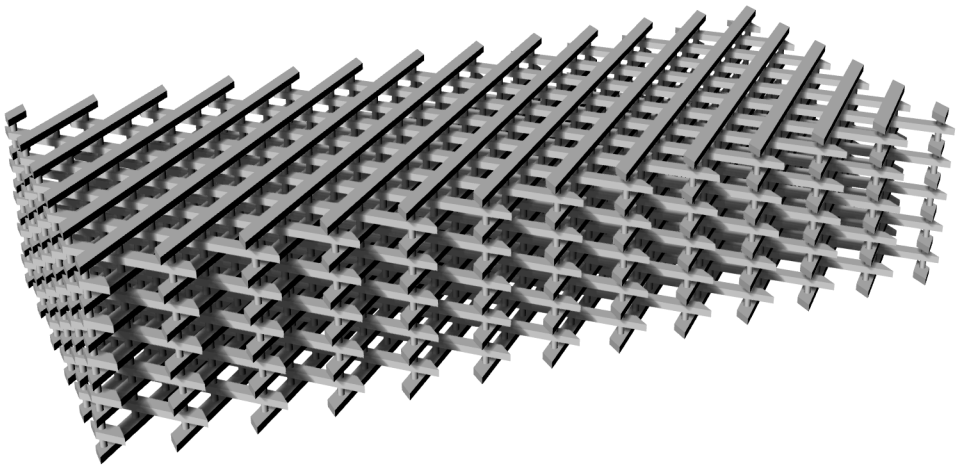

Fig. 3.13 Nominal geometry of a pantographic block.

part based on the deformation measures representing twist and curvature in directions of vectors **L** and **M**, respectively. The distortion angle between **L** and **M** is given by,

$$\sin\gamma = \boldsymbol{\ell}\cdot\boldsymbol{m}\ , \tag{3.10}$$

while the measures of twist deformation, flexure normal to the plane π, and geodesic flexure read

$$\kappa_{tL} = (\boldsymbol{n}\times\boldsymbol{\ell})\cdot\frac{\mathrm{d}\boldsymbol{n}}{\mathrm{d}S_L} \quad , \quad \kappa_{nL} = \boldsymbol{n}\cdot\frac{\mathrm{d}\boldsymbol{\ell}}{\mathrm{d}S_L} \quad , \quad \kappa_{gL} = -(\boldsymbol{n}\times\boldsymbol{\ell})\cdot\frac{\mathrm{d}\boldsymbol{\ell}}{\mathrm{d}S_L} \tag{3.11}$$

and

$$\kappa_{tM} = (\boldsymbol{n}\times\boldsymbol{m})\cdot\frac{\mathrm{d}\boldsymbol{n}}{\mathrm{d}S_M} \quad , \quad \kappa_{nM} = \boldsymbol{n}\cdot\frac{\mathrm{d}\boldsymbol{m}}{\mathrm{d}S_M} \quad , \quad \kappa_{gM} = -(\boldsymbol{n}\times\boldsymbol{m})\cdot\frac{\mathrm{d}\boldsymbol{m}}{\mathrm{d}S_M} \tag{3.12}$$

for the beams along the directions **L** and **M**, respectively. In Equations (3.11) and (3.12), S_L and S_M are the abscissae along the two fiber directions. The energy density (3.9) is based on a Kirchhoff beam model [56, 63].

The behavior in the direction **N** was assumed to be only characterized by first-gradient terms

$$w_N = \frac{1}{2}\left\{\mathrm{K}_{eN}(\eta-1)^2 + \mathrm{K}_{sN}(\gamma_{LN}^2+\gamma_{MN}^2) + 2\,\mathrm{K}_c\left[(\lambda-1)(\eta-1)+(\mu-1)(\eta-1)\right]\right\}\ , \tag{3.13}$$

where the first contribution represents a storage of elastic energy due to a change of length in the direction **N**; the second term is related to the shear in the plane defined by **L** and **N** as well as in the plane defined by **M** and **N**; the last term represents an exchange of energy

between stretching modes in the pantographic plane π and the orthogonal direction **N**. The shear strains are defined as

$$\sin\gamma_{LN} = \boldsymbol{\ell}\cdot\boldsymbol{n}\,, \quad \sin\gamma_{MN} = \boldsymbol{m}\cdot\boldsymbol{n}\,, \tag{3.14}$$

where K_e, K_s, K_t, K_n, K_g, K_{eN}, K_{sN}, and K_c are material parameters. It is then assumed that the strain energy density w of the pantographic block is the sum of the two contributions given by Equations (3.9) and (3.13), $w = w_\pi + w_N$.

Experimental setup

A 3-point flexural test is performed on a pantographic block that has been produced at the Warsaw University of Technology by selective laser sintering (SLS) using PA2200 polyamide powder, beginning with the nominal geometry shown in Fig. 3.13. The dimensions of the pantographic block under test are 121.8 mm, 56.8 mm, and 26 mm. These directions are referred to as longitudinal, vertical, and transverse corresponding to the $\{x\}$, $\{z\}$, and $\{y\}$ axes, respectively. An in situ 3-point flexural test is performed by prescribing a displacement in the pantographic plane, parallel to the side of length 56.8 mm. The pantographic block under test is obtained by assembling 11 layers of beams, with each pair of successive layers connected by 138 pivots (13 vertical rows of 6 pivots alternating with 12 rows of 5 pivots), for a total of 1 380 pivots. The cross-section of the beams has dimensions 2×1 mm^2, and the connecting cylinders have diameter and length equal to 0.90 mm and 1.5 mm, respectively. The 3-point flexural test is conducted by prescribing a displacement in the pantographic plane, parallel to the vertical z axis. The test is monitored via micro-computed x-ray tomography [89] to acquire 3D scans of the reference and deformed configurations [18]. The three ABS supports used in the 3-point flexural test have been 3D-printed using Fused Deposition Modeling (FDM). Two supports are attached to the bottom plate on the testing machine at a distance of 8.2 mm, and the third is attached to the top plate, in correspondence to the middle horizontal position of the others. The test is conducted up to the testing stroke limit of the machine, controlling the lower motion of the supports. Between the specimen and the supports, corrugated cardboard (undulated polypropylene sheets) are added to prevent the beam ends from locking with respect to the supports.

Six tomographic scans are acquired during the experiment. Two of these six scans correspond to the unloaded configuration: the first is used as the reference scan, while the second is used to evaluate measurement uncertainties and the baseline level for the correlation residuals. By increasing the stroke, four scans are acquired in the deformed configurations. After the acquisition of the undeformed scans, a 10-mm spacer is installed to permit larger

displacements at the testing stroke limit of the machine. After an additional 14 mm stroke, the first scan is acquired. The next three scans are acquired every 5 mm. Hence, scans from 1 to 4 are acquired for a total prescribed displacement of 24, 29, 34, and 39 mm, respectively. The reaction force and stroke are continuously recorded during the test (Fig. 3.15). The hardware parameters of the experiment are reported in Table B.1.

In Fig. 3.14 a section of three of the reconstructed volumes is shown (reference configuration and scans corresponding to 24 and 39 mm prescribed displacements). For the sake of conciseness, the majority of the results will focus on scans 1 and 4. The acquired section is initially parallel to the pantographic plane allowing a fiber layer to be clearly visible in the unloaded configuration (Fig. 3.14(a)). In Fig. 3.14(b,c), due to out-of-plane motions, the acquired sections are no longer parallel to the fiber layer. In the cited figures, the pivots connecting the layers are visible as small white dots. Fig. 3.14(c) shows that the beams deform significantly, especially at the final deformation level. The magnitude of the vertical displacements is equal to hundreds of voxels, making DVC analyses extremely challenging. In Fig. 3.15, the reaction force-stroke recorded data are shown. At zero displacement of the actuator, a large vertical black bar is obtained, which shows the fluctuation of the reaction forces during the acquisition of the scans in the unloaded configuration, as well as during the installation of the spacers. From 0 to 10 mm, there are no available data. The reaction force measured during the loading steps is illustrated in light gray. The four consecutive black vertical bars represent force acquisitions during tomographic scans. A linear response is shown by the plot. Nevertheless, a small hardening effect appears in the final portion of the loading history, which is related to the triggering of beam flexure for large displacements, and associated with the activation of second-gradient contributions of the placement field. In the first part of the loading history, the beams actually tend not to deform because it is less costly in terms of energy to concentrate the deformation in the connecting pivots. It is worth noting the beams remain almost unbent until the first deformation step (Fig. 3.14(b)), while the subsequent loading steps cause the beam to bend increasingly (Fig. 3.14(c)). To describe this bending, higher-order derivatives of the displacements are required that are not involved in the classical (or Cauchy) continuum. Thus, it is crucial to understand second-gradient continuum models to fully characterize this type of metamaterials [64]. In the present experiment, the energy contribution associated with the elongation of the beams is negligible as expected [131]. No significant nonlinear deformation mechanisms (plasticity and/or damage) appear during the tests as evidenced by the essentially linear response.

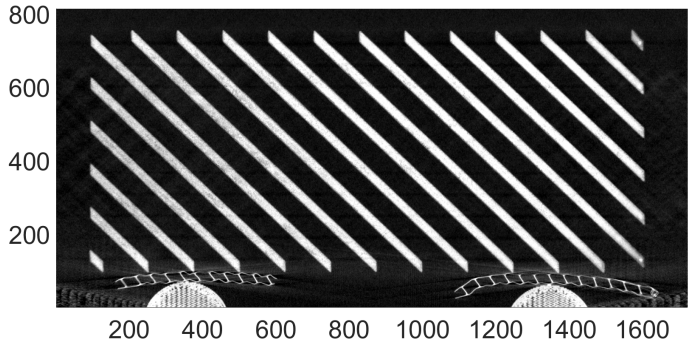

(a)

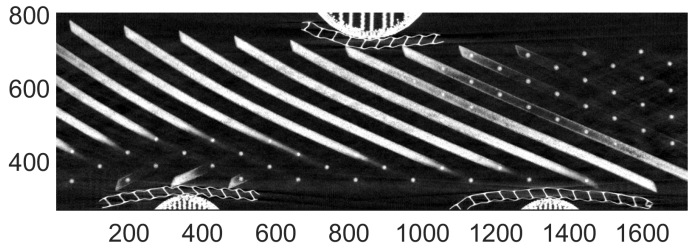

(b)

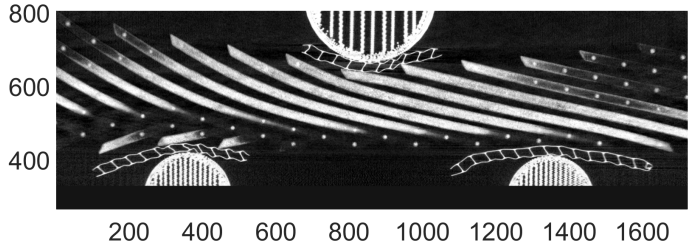

(c)

Fig. 3.14 Sections in the pantographic plane $\{x, z\}$ for the different scanned configurations: (a) reference (unloaded) configuration; (b) 24 mm and (c) 39 mm prescribed displacements. Axis labels are expressed in voxels.

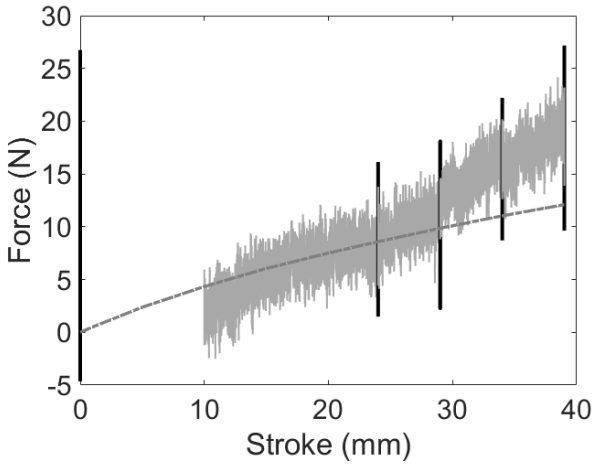

Fig. 3.15 Comparison between measured force vs. prescribed displacement of the specimen during scan acquisition (vertical black bars) as well as loading steps (light gray), and predicted response via FE simulations (dash-dotted dark gray line).

Parameter calibration

DVC analysis is initialized by considering the deformation shape predicted by the second-gradient model exposed in Section 3.1.2, whose parameters are calibrated to fit the force-stroke response (see Fig. 3.15) up to the first loading step (24 mm deflection). The calibrated parameters are reported in Table 3.1.

Table 3.1 Calibrated model parameters.

K_e	1.4×10^5 N/m
K_s	13 N/m
K_g	9.5×10^{-2} Nm
K_n	1.2×10^{-2} Nm
K_t	10^{-2} Nm
K_{eN}	6.5 MN/m^2
K_{sN}	35 MN/m^2
K_c	2.6 MN/m^2

Mesh in the reference configuration

For analyzing the previous test, FE-based DVC [116, 68] is performed. The sought displacement field $\mathbf{u}$ is expressed as

$$\mathbf{u}(\mathbf{x},\{\boldsymbol{\nu}\}) = \sum_i \upsilon_i \mathbf{N_i}(\mathbf{x}) \,, \tag{3.15}$$

where $\mathbf{N_i}(\mathbf{x})$ are the vectorial shape functions associated with the nodal displacements υ_i, gathered in the column vector $\{\boldsymbol{\upsilon}\}$, which are the unknowns to be measured. To determine them, we consider the gray level residual ρ computed for each voxel belonging to the region of interest (ROI),

$$\rho(\mathbf{x}, \{\boldsymbol{\upsilon}\}) = I_0(\mathbf{x}) - I_t(\mathbf{x} + \mathbf{u}(\mathbf{x}, \{\boldsymbol{\upsilon}\})) \,, \tag{3.16}$$

where I_0 and I_t are the gray levels for every voxel in the reference and deformed scans. Thus, the measured nodal displacements read

$$\{\boldsymbol{\upsilon}\}_{meas} = \arg\min_{\{\boldsymbol{\upsilon}\}} \Phi_c^2(\{\boldsymbol{\upsilon}\}) \tag{3.17}$$

with

$$\Phi_c^2(\{\boldsymbol{\upsilon}\}) = \sum_{\mathbf{x} \in ROI} \rho^2(\mathbf{x}, \{\boldsymbol{\upsilon}\}) \,. \tag{3.18}$$

A penalty term is considered to perform so-called Hencky-elasticity regularization [35]

$$\Phi_m^2(\{\boldsymbol{\upsilon}\}) = \{\boldsymbol{\upsilon}\}^\top [\mathbf{K}]^\top [\mathbf{K}] \{\boldsymbol{\upsilon}\} \,, \tag{3.19}$$

so that, to determine the nodal displacements via regularized DVC, the weighted sum is minimized

$$\{\boldsymbol{\upsilon}\}_{\text{meas}} = \arg\min_{\{\boldsymbol{\upsilon}\}} \left(\Phi_c^2(\{\boldsymbol{\upsilon}\}) + w_m \Phi_m^2(\{\partial\boldsymbol{\upsilon}\}) \right) \,, \tag{3.20}$$

where $\{\partial\boldsymbol{\upsilon}\}$ denotes the column vector of incremental displacements from one analysis to the next, and $[\mathbf{K}]$ the rectangular stiffness matrix associated with bulk and free surface nodes. In Hencky-elasticity regularization, the regularization weight w_m is proportional to a length, referred to as regularization length ℓ_m, raised to the power 4 [135]. Section 3.2.1 will discuss the choice of the regularization length.

An FE mesh of the specimen is needed for performing the DVC analysis. In our study, the starting point is the STL model of the to-be-printed pantographic structure. Fig. 3.16 shows the mesh in the nominal configuration generated with Gmsh [54]. Modeling the beams and pivots necessitates the use of different mesh elements due to their significantly different dimensions. In this type of application, due to small printing errors, incorrect sample placement, and the possible application of preload, the reference (experimental) configuration typically does not precisely match the printing geometry. For this reason, a backtracking procedure [8] is required to fit the mesh constructed from the nominal printing geometry to the reference scan of the unloaded configuration. The backtracked mesh needs to be cropped by removing the last two vertical rows of pivots on both sides of the specimen, which, in the maximum deformed configuration, would end up outside the monitored volume (Fig. 3.14).

The considered mesh consists of 37 759 nodes and 141 882 T4 elements with a mean size of 6 vx (calculated as the cube root of the average elementary volume).

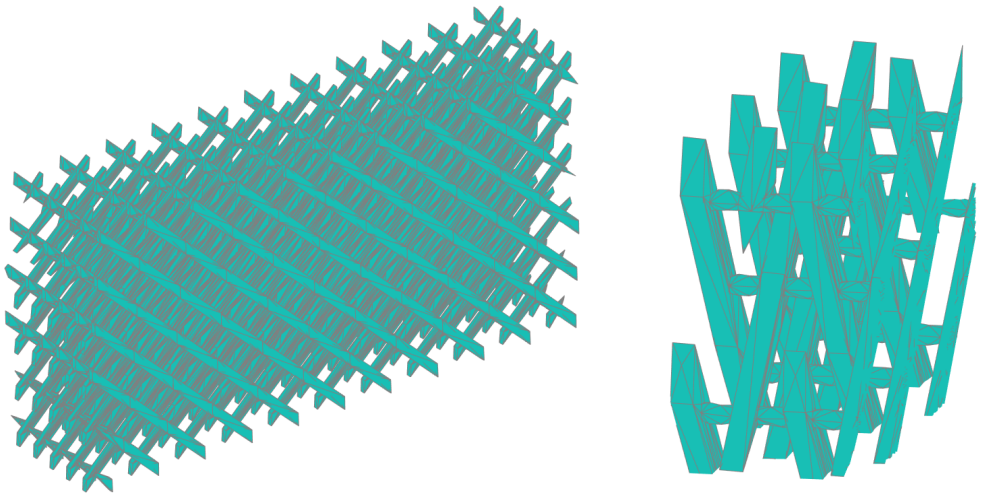

(a) (b)

Fig. 3.16 FE mesh in the nominal configuration. Overall (a) and detail of the hinge meshing (b).

The reconstructed volumes are registered using the Correli 3.0 framework [83] in which Hencky's regularization is implemented (Table B.2). The measured displacement field **u** are parameterized using the nodal displacements associated with the finite element discretization based on 4-noded (T4) tetrahedra [68].

DVC initialization

Large displacements between successive acquisitions of the deformed configuration (Fig. 3.14), which are also attributable to the peculiar structure of the studied block, made DVC analyses challenging. The prescribed displacements relative to the reference configuration are 24, 29, 34, and 39 mm for the four deformed configurations. Expressed in voxels, they correspond to 290, 350, 410, and 470 vx, respectively. Therefore, these amplitudes are quite large in comparison to the height of the specimen (56.8 mm or 684 vx). Particularly challenging is measuring the first deformed configuration (Fig. 3.14(b)). Suitable initialization of DVC analyses is required to enable convergence.

To this reason, DVC is *model-initialized*, *i.e*, finite element (FE) simulations are performed with the commercial code *COMSOL Multiphysics*® using the model introduced and calibrated in Subsection 3.2.1. A rectangular parallelepiped of equal size to the sample size tested is

numerically analyzed. The positions of the pivot numerically predicted are used to initialize the pivot motions.

Due to buckling in the transverse direction caused by imperfections that are not accounted for in the second-gradient model exposed in Subsection 3.2.1, an additional correction consisting of a rigid translation in the transverse direction is required to improve the deformation predicted by the model. This phenomenon is not negligible due to the small dimensions of the specimens (26 mm in width), which makes a displacement of the order of 5 mm (or 60 vx) comparable to the size of a mesostructure unitary cell. Fig. 3.17 shows the positions of the pivots predicted by the numerical simulation for a 24 mm prescribed displacement drawn in one section of the first deformed volume.

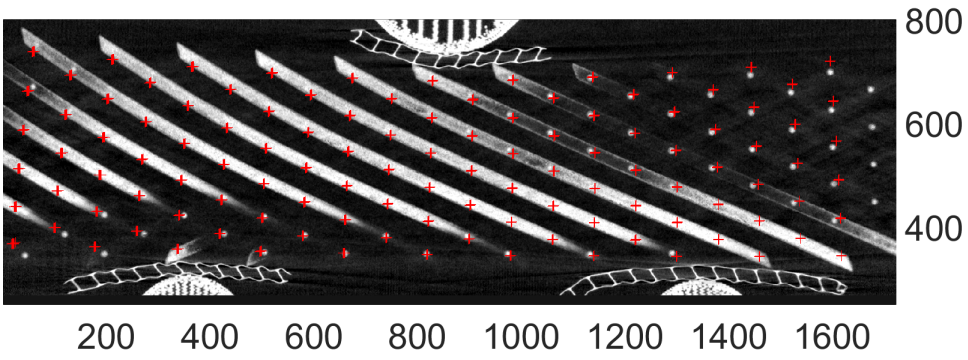

Fig. 3.17 Numerically predicted positions of the pivots (red + symbols) drawn on a section of scan 1 (prescribed displacement 24 mm). Actual positions of the pivots are visible as small white dots. Axis labels are expressed in voxels.

Direct DVC calculations

Due to the previous initialization, We run DVC analyses on the 4 deformed scans (always using as reference the undeformed scan). The DVC calculations are stopped when the L^2-norm of displacement corrections are less than 10^{-1} vx. This level corresponds to the standard displacement uncertainty obtained by performing DVC analysis on the repeat scans acquired before the sample deformation. The regularization length is selected as explained below.

Fig. 3.18(a) shows the root mean square (RMS) gray level residual Φ_c versus the equilibrium gap Φ_m for different regularization lengths. The five data for each regularization length correspond, with increasing gray level residual, to scan 0 (second scan in the unloaded configuration), and scans 1 to 4 of the deformed configurations. The analysis of scan 0 provides information on the stopping criterion for the L^2-norm of displacements. Scans 1

to 3 have comparable residuals, indicating that the analysis is successful. Extremely high deformations result in increased gray-level residuals for the fourth scan. The equilibrium gap Φ_m decreases as the regularization length increases.

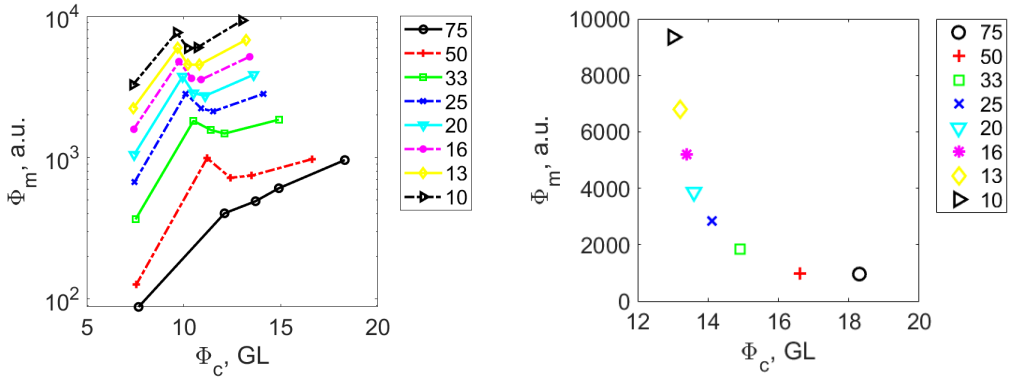

(a) (b)

Fig. 3.18 (a) Equilibrium gap Φ_m vs. gray level residual Φ_c for the five analyzed scans and for different regularization lengths (expressed in voxels). (b) Corresponding plot in arithmetic scale for scan 4.

The criterion used to select the optimal regularization weight is to look for the maximum curvature (L-curve criterion [67]) in the graph above for the maximum prescribed displacement, in arithmetic scale (Fig. 3.18(b)). The regularization length $\ell_m = 25$ vx (Table B.2) is selected that, according to this criterion, provides the best trade-off between Φ_c and Φ_m. For this regularization length, the gray level residuals are shown in Appendix B.2.

3.2.2 DVC results

The DVC results for the initial and final deformed configurations are discussed below. The displacement fields are first analyzed. Then, the motions of the pivots are reported to assess the mode of block deformation.

Displacement fields

The measured displacement fields in the three directions are displayed in Figs. 3.19 and 3.20. As expected, the displacement amplitudes are very large compared to the overall dimensions of the specimen and, consequently, compared to the dimensions of the elementary pantographic cell. The flexural displacement is prescribed in the vertical direction, and the primary effect is that the entire specimen is shortened considerably in that direction, almost uniformly. The bottom of the specimen remains essentially flat, with almost no noticeable curvature. The

curvature under the top support is very slight compared to the right side of the specimen and became more pronounced on the left side of the specimen (Fig. 3.20(a), see also Fig. 3.14). This phenomenon is caused by the design of the specimen that is characterized by an odd number of pantographic sheets.

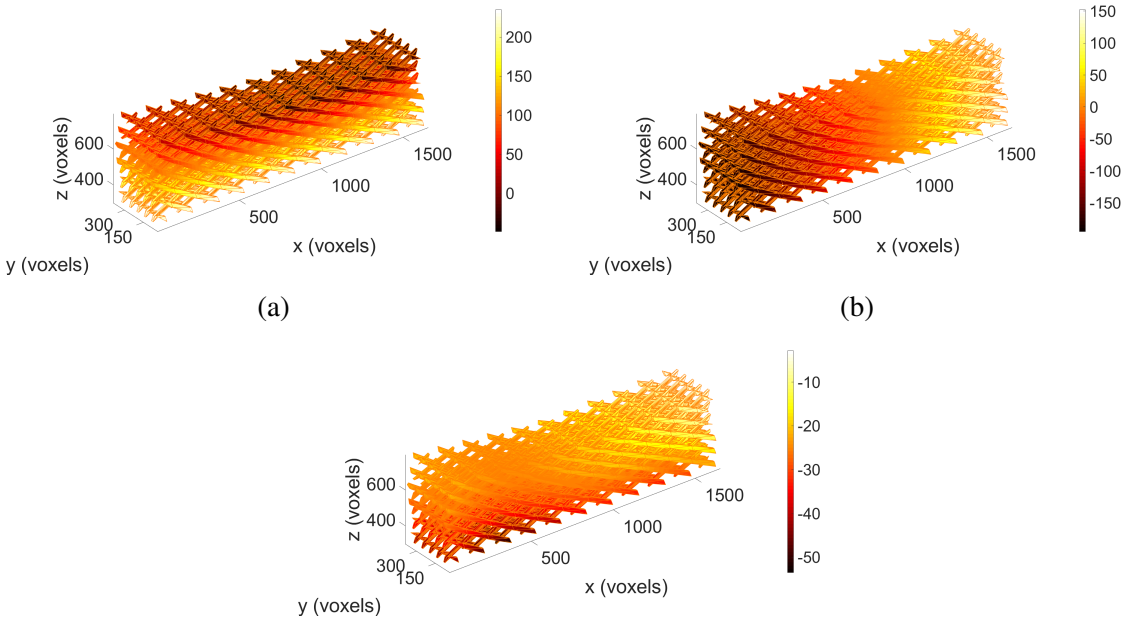

Fig. 3.19 DVC measured vertical (a), longitudinal (b) and transverse (c) displacement fields for the first loading step (24 mm). Labels are expressed in voxels. The displacements are shown on the mesh in its deformed configuration.

The range of vertical displacement levels found for both scans is consistent with the prescribed stroke (see a dynamic range of color bars in Figs. 3.19 and 3.20). Specifically, the prescribed displacements of 24 and 39 mm correspond to 290 and 470 vx, respectively. It is worth noting that the minimum displacements are not equal to zero. This is due to the fact that when cropping the volumes after reconstruction, the deformed sample is centered and thus the top support has apparent translations (Fig. 3.14).

As a result of the mesostructure behavior, given the prescribed flexural displacement, the specimen significantly elongates in the longitudinal direction. The deformation is concentrated initially in the pivots, where shear deformation occurs [22], while the beams deform considerably less and the pantographic structure converts the vertical compression into longitudinal elongation. The quantification of this effect is shown in Figs. 3.19(b) and 3.20(b), where longitudinal displacement measurements are shown on the deformed configurations of

the specimen. The range of measured displacements is 344 vx (about 28.5 mm) for the first scan and 445 vx (about 36.9 mm) for the last one.

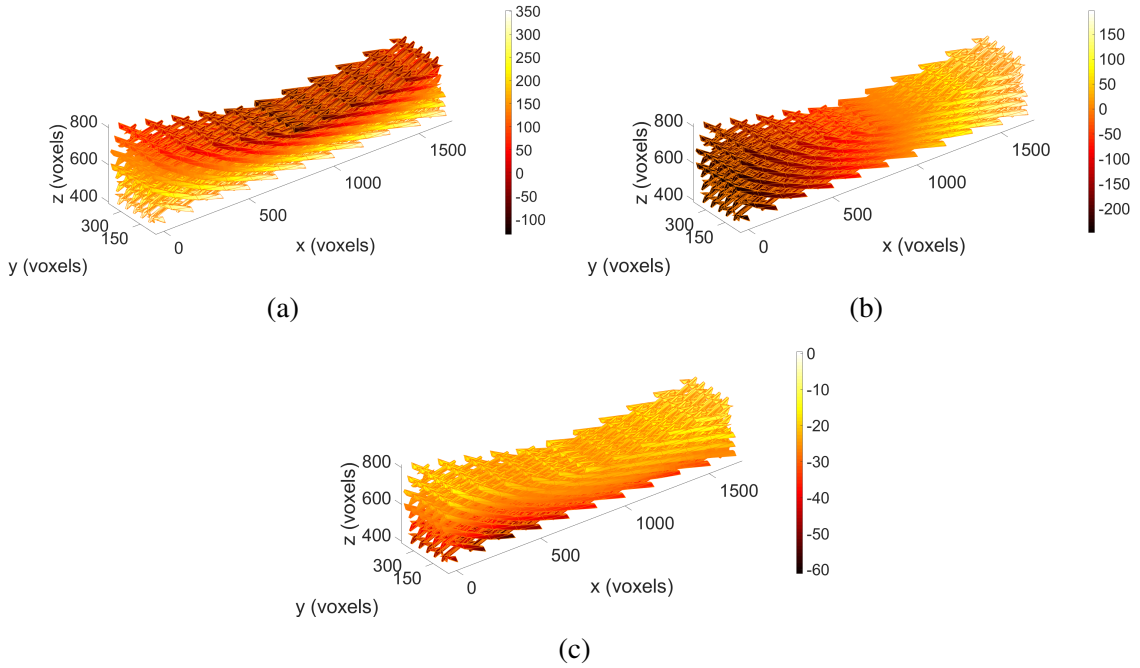

Fig. 3.20 DVC measured vertical (a), longitudinal (b) and transverse (c) displacement fields for the last loading step (39 mm). Labels are expressed in voxels. The displacements are shown on the mesh in its deformed configuration.

Lastly, significant displacements are measured in the transverse direction relative to the size of the elementary cell of the microstructure. In Figs. 3.19(c) and 3.20(c), the measured transverse displacements are displayed on the meshes in deformed configurations. It is interesting to note that the displacements are not significantly changing for the reported scans. The measured range varies from 52 vx for scan 1 to 60 vx for the last one (from 4.3 mm to 5 mm, respectively). This level is of the same order of magnitude as the elementary cell size in the periodic design, which is exactly 5 mm.

Hinge kinematics

It is of interest to extract some information about the pivots from these experimental data, as the continuous model described in Subsection 3.2.1 has been developed to predict the geometric center positions of the interconnecting pivots. Piola-identification conjecture underlies the use of the continuous model for similar mesostructured media where the geometric centers of the pivots are chosen as control points [37, 33]. As said before, the numerical prediction of the position of the pivots in the deformed configurations is the basis

of the initialization of the applied DVC procedure (Fig. 3.17). Let us now address some considerations based on the analysis of the hinge motions.

Having successfully carried out FE-based DVC analyses, the behavior of various constituents of the tested metamaterial could be studied for different deformed configurations. We decide to focus on the mesh elements that in the nominal geometry are related to the pivots. Fig. 3.21 shows the configuration of the pivots in their reference state and in the deformed configuration with maximum deflection. Details of Fig. 3.21 are shown in Fig. 3.22

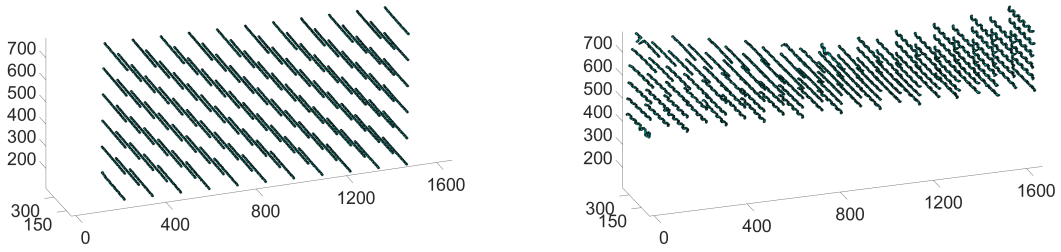

Fig. 3.21 Configuration of pivots in the (a) reference (unloaded) and (b) last deformed (39 mm deflection) configurations. Labels are expressed in voxels.

where a set of pivots in the $\{y, z\}$ plane (orthogonal to the pantographic plane) is plotted in the configurations corresponding to scan 1 and 4. The cross-sections of the pantographic block remain nearly planar and rectangular. While the vertical length of the sections (parallel to the prescribed displacement) decreases, the transverse sides (orthogonal to the flexural displacement) remain almost unchanged.

Deformation mode

We analyze the deformation mode by focusing on the deformed shape of the top surface. The top surface is approximated by means of a surface built by interpolating the positions of the center of mass of four consecutive central top horizontal rows of pivots as highlighted on one $\{x, z\}$ section in Fig. 3.23(a). These rows are chosen to locally study the surface of the pantographic block affected by the highest longitudinal curvature, avoiding the top pivots where artifacts could occur due to direct support contact.

The interpolation is carried out by searching for the six coefficients of a complete second-order polynomial interpolation $z = \mathcal{P}_2(x, y)$ that provides the best fit of the pivot positions based on the least-squares method. The paraboloid obtained by interpolation is studied to evaluate the principal curvatures. Fig. 3.23(b) shows both the interpolating paraboloid and

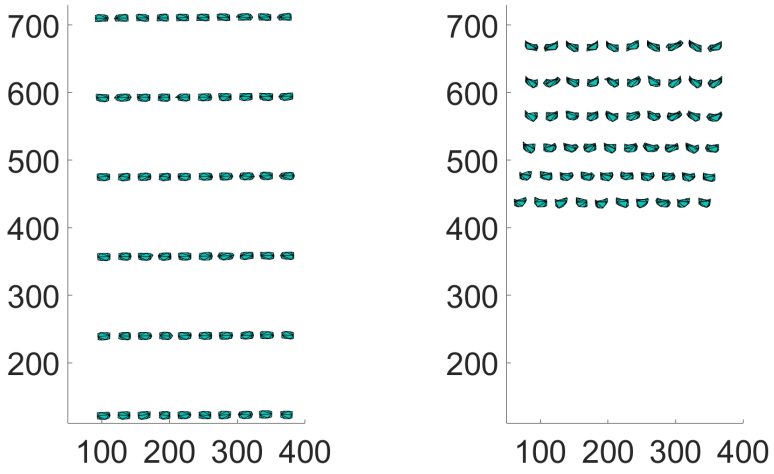

(a) (b)

Fig. 3.22 Detail of Fig. 3.21. Comparison of the same cross-section in the {y,z} plan for (a) the reference (unloaded) and (b) last deformed (39 mm deflection) configurations. Labels are expressed in voxels.

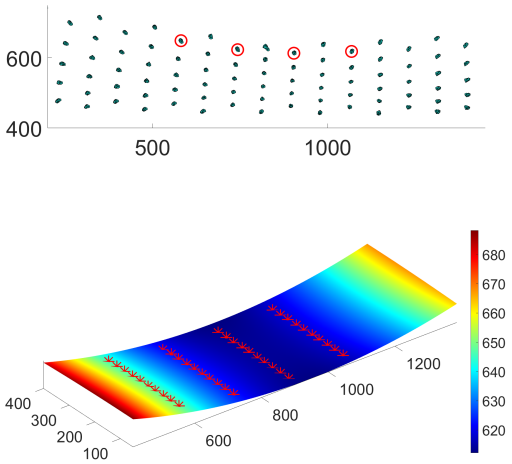

Fig. 3.23 (a) Selected pivots for building the interpolating top surface on one {x,z} section. (b) Paraboloid interpolating the vertical positions of the center of mass of the selected pivots, and actual positions of the centers of mass of the pivots measured via DVC for 39 mm deflection (red markers). Labels are expressed in voxels.

the actual positions of the centers of mass of the pivots measured by DVC for the maximum deflection.

The curvatures of the paraboloid are investigated to distinguish the kind of deformation mode, namely, anticlastic (saddle shape), synclastic (eggshell shape), or monoclastic (cylindrical shape). At the critical point, denoted here by X_C, local evaluations of the Gaussian curvature and the two principal curvatures are performed. Let $K(X_C) = \kappa_1(X_c)\kappa_2(X_C)$ be the Gaussian curvature, where κ_1 and κ_2 are the principal curvatures [108]. The deformation mode corresponds to $K > 0$ for synclastic surfaces, $K < 0$ for anticlastic surfaces, and $K = 0$ with κ_1 and κ_2 that do not vanish for monoclastic surfaces. Due to the already-discussed asymmetry of the deformed shape of the specimen, the critical point is not exactly centered in the middle of the specimen but slightly shifted toward the right end.

In this case, small negative Gaussian curvatures K are found (Table 3.2). The principal directions associated with the principal curvatures are parallel to the longitudinal and transverse directions of the sample. Both principal curvatures are quite small, with the transverse curvature being roughly 20% of the longitudinal one, but with opposite sign, indicating a weak anticlastic mode. Nevertheless, since the transverse radius of curvature is significantly larger than the specimen side dimensions and the Gaussian curvature is small, the deformation mode is predominantly monoclastic (*i.e*, the deformed surface is well approximated by a monoclastic mode).

Table 3.2 Curvatures assessed from experimental measurements and numerical simulations.

Surface	Longitudinal curvature	Transverse curvature	Gaussian curvature K
Fig. 3.23(b)	6.5×10^{-3} mm^{-1}	-1.3×10^{-3} mm^{-1}	-8.45×10^{-6} mm^{-2}
Fig. 3.26	3.8×10^{-3} mm^{-1}	-8.1×10^{-5} mm^{-1}	-3.08×10^{-7} mm^{-2}
Fig. 3.28(a)	12.7×10^{-3} mm^{-1}	-4.6×10^{-3} mm^{-1}	-5.84×10^{-5} mm^{-2}
Fig. 3.28(b)	9.9×10^{-3} mm^{-1}	-4.9×10^{-3} mm^{-1}	-4.81×10^{-5} mm^{-2}

3.2.3 Numerical simulations

This section deals with the numerical simulations that mimic the 3-point flexural test. It is shown the comparison between the predicted deformation mode and the one experimentally observed. Finally, results are presented considering another flexural configuration to induce an anticlastic deformation.

Predicted deformation mode

The continuum macro-model postulated in Section 3.2.1 was further investigated to predict the deformed shapes of the pantographic block in a 3-point flexural test. It is noteworthy that the DVC analyses have required the prediction of second-gradient model for the initialization step, but the final results are independent of the theoretical model. In Figs. 3.24 and 3.25, the displacement fields are reported along the three directions for prescribed deflections of 24 and 39 mm, corresponding to the first and final scans of the test (Section 3.2.1). Similar conclusions are drawn from intermediate steps, which are omitted for brevity. Correspondence with the reported experimental results is very good (Figs. 3.19 and 3.20). The proposed model is incapable of predicting transverse displacements in the actual test (likely caused by sliding). Transverse displacements are negligible in the numerical simulations, and buckling effects are not considered. Note that in all plots, the lines on the model are material lines, allowing for an easier comparison of numerical results with the experimental one. In contrast, as also

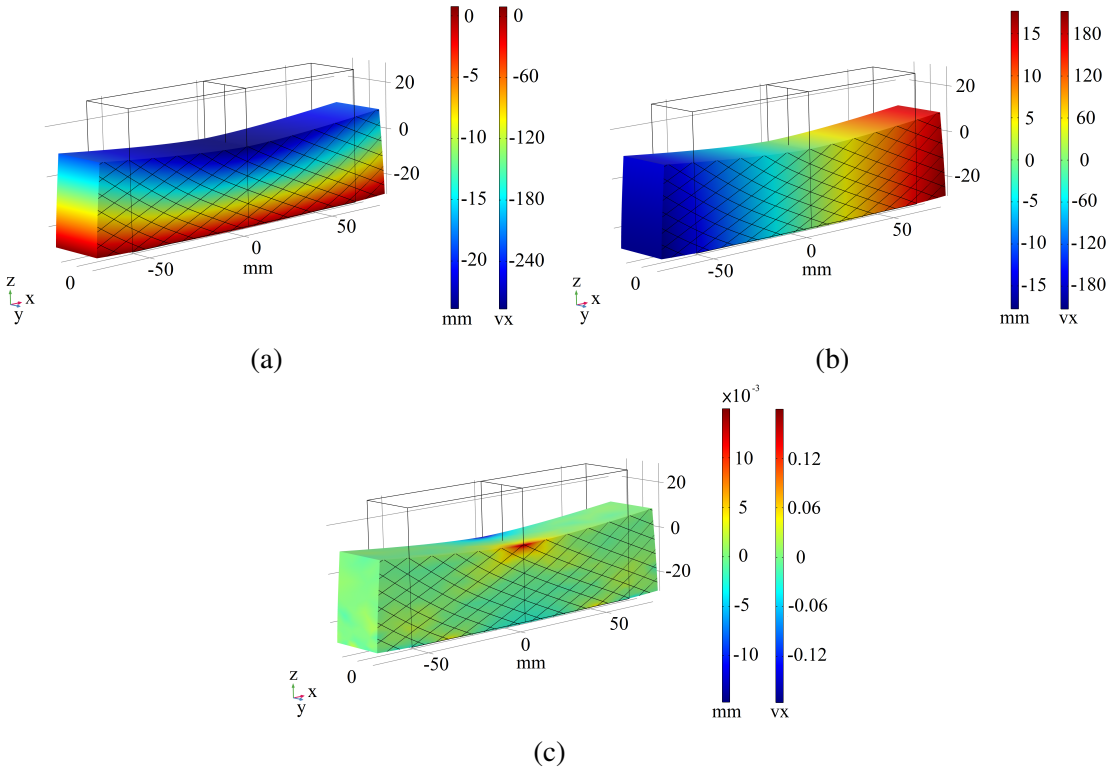

Fig. 3.24 FE results for a prescribed deflection of 24 mm in the vertical direction. (a) Vertical, (b) longitudinal, and (c) transverse displacement fields.

shown in Fig. 3.17, the correspondence between the theoretical and experimental vertical displacements is quite good. Lastly, the theoretical model cannot predict any asymmetry

in terms of vertical displacements. To compare the deformation mode of the numerically

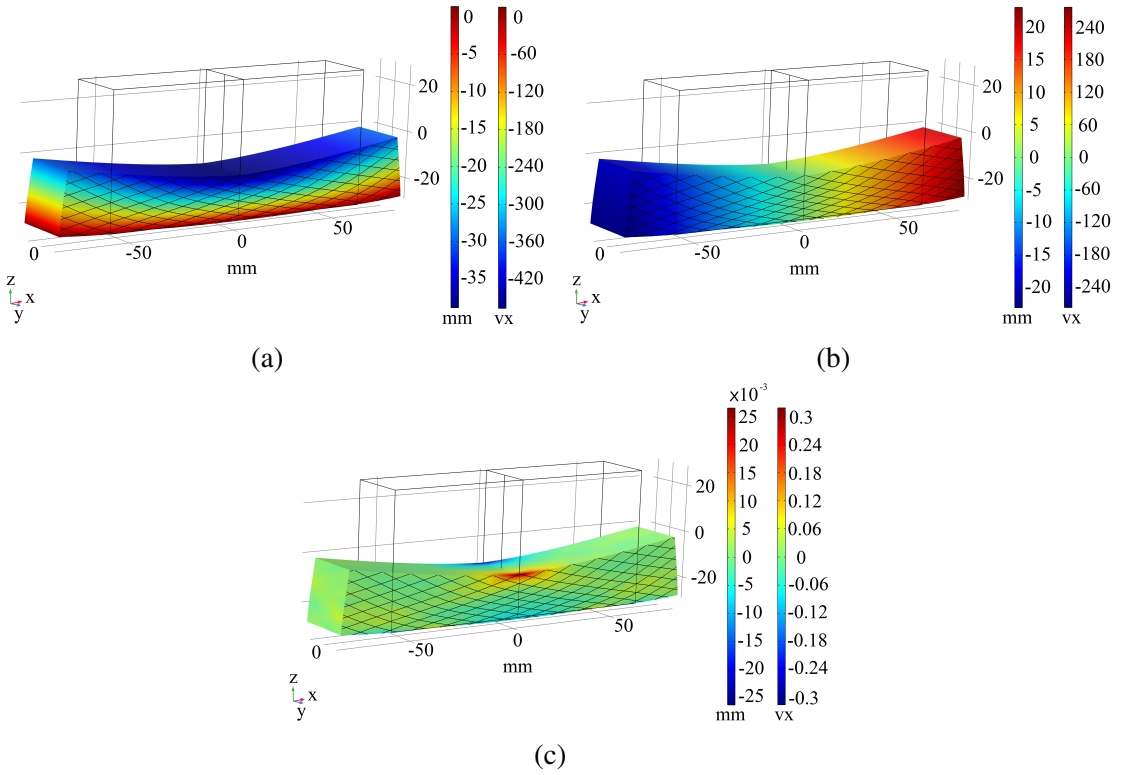

Fig. 3.25 FE simulation results for a prescribed displacement of 39 mm in the vertical direction. (a) Vertical, (b) longitudinal, and (c) transverse displacement fields.

obtained top surface with the one experimentally measured, the first is studied in the same way as the second. By interpolating the positions of the points corresponding to the real pivots chosen for the experimental case, a paraboiloid with six coefficients is built a shown in Fig. 3.26. Consistent with the experiment, the Gaussian curvature K is negligible at the critical point, and the deformation mode is monoclastic.

3.2.4 Anticlastic deformation mode

Numerical simulations are finally performed for a second case in which the prescribed load is orthogonal to the pantographic plane. Due to the anisotropy of the model and material, it is of interest to study the behavior of this metamaterial under different loading directions. The parameters used in this novel simulation are the same as those gathered in Table 3.1. The same boundary conditions are implemented as in the previous simulations. In Fig. 3.27, the three displacement field components obtained via FE analysis are displayed on the deformed configuration for a 10 mm applied deflection. The bottom side of the specimen no longer

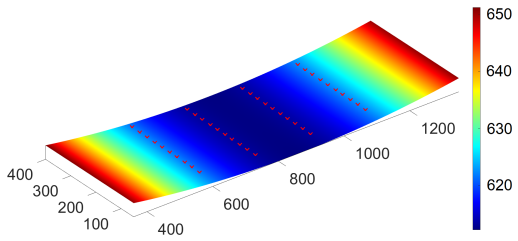

Fig. 3.26 Paraboloid interpolating the vertical positions of the center of mass of the selected pivots, and positions of the centers of mass of the pivots predicted by numerical simulations (red markers).

remains flat. It lowers in the middle and raises at the ends by rotating the cross-sections. Further, the displacements in the transverse direction, $\{z\}$-axis direction in Fig. 3.27, are no longer negligible. The elongation and flexure of the pantographic planes are clearly visible. An anticlastic deformation mode appears in this case, namely, the curvatures in the longitudinal and transverse directions are nonzero and of opposite sign. The top and bottom pantographic surfaces are studied by constructing the interpolating paraboloids similarly to what has been done in the previous cases. The top and bottom surfaces are reported in Fig. 3.28. The Gaussian curvature evaluated at the critical point of the surface is negative. The two principal directions associated with the principal curvatures are again the longitudinal and transverse directions. Regarding the principal curvatures, the transverse one is very close for both top and bottom surfaces, while the longitudinal one increases by nearly 30% from the bottom to the top surface (Table 3.2).

3.3 The effect of pivots-related random defects on the response of pantographic sheets

Pantographic structures attracted the attention of many scientists because of their nonclassical mechanical behaviors. Despite several studies conducted in this field, the role played by uncertainties has not been investigated in the literature yet. In the present section, we provide a contribution to this topic. A simplified probabilistic analysis is applied to investigate the effects of local axial, bending, and torsional defects on their mechanical responses. The suggested approach involves a generalization of an existing theoretical result and the use of Monte Carlo simulations to derive probability density functions, mean values, standard deviations, and coefficients of variation of the random kinematic unknowns. As demonstrated by the results, pantographic structures are not particularly affected by random local defects due

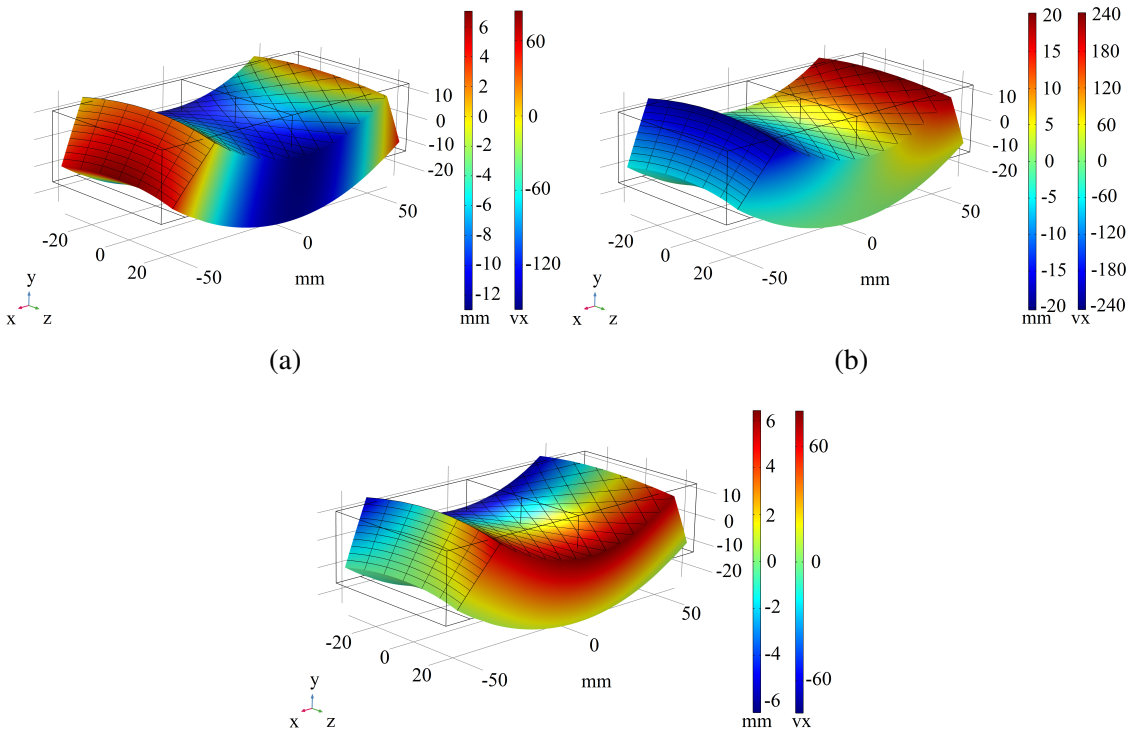

Fig. 3.27 FE simulation results for a prescribed displacement of 10 mm in the vertical direction. (a) Vertical, (b) longitudinal, and (c) transverse displacement fields.

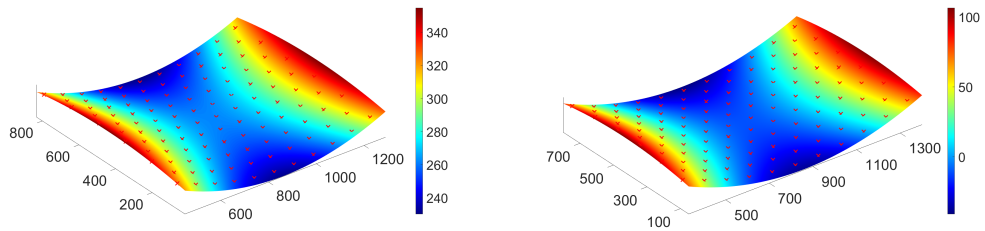

Fig. 3.28 Paraboloid interpolating the vertical positions of the center of mass of the pivots in the top (a) and bottom (b) planes, and positions of the centers of mass of these pivots predicted by numerical simulations (red markers).

to their redundant connections. In addition, the interdependencies between their substructures, beams, and pivots make it difficult to find the locations where the placement of defects reduces or maximizes the randomness of the mechanical responses. Work is currently being conducted on the subject.

This section is organized as follows. In Section 3.3.1, the second-gradient continuum model for pantographic sheets is presented. In Section 3.3.2, a result already published in the literature [48] is used for a theory-driven construction of analytical relationships that connect material uncertainties-related random variables to displacements. Finally, in Section 3.3.3, the built analytical relationships are used for the analysis of uncertainty propagation and the derivation of probability density functions, mean values, and standard deviations of random horizontal displacements.

Notation

Below M, N, F, i, and j are integers belonging to $\{1,2,3\}$.

A lowercase letter such as x, η, u is a real deterministic variable except when used as an integer index as i, j, etc. Greek letters α, β, η and τ are neither deterministic variables or integers as subscripts.

A boldface lower case letter such as $\boldsymbol{x}$, $\boldsymbol{\eta}$, $\boldsymbol{u}$ is a real deterministic vector.

An upper case letter such as X, H, U is a real random variable except when used as an integer index as A, B, etc.

A boldface upper case letter such as $\boldsymbol{X}$, $\boldsymbol{H}$, $\boldsymbol{U}$ is a vector random variable.

A lower case letter between brackets such as $[\boldsymbol{x}]$, $[\boldsymbol{\eta}]$, $[\boldsymbol{u}]$ is a real deterministic matrix.

$\mathcal{H}$: Heaviside function.

$[\delta]_{ij}$: Kronecker delta.

q^M: Lagrangian coordinates. In this section, stochastic considerations are introduced, wherein the symbol $\boldsymbol{q}$ is preferred for denoting the Lagrangian coordinates, as the symbol X is reserved for the random quantities.

χ^i: component i of the configuration field χ.

d_1^N, d_2^F: the directions of the beams (fibers) of pantographic sheets.

ψ: deformation energy functional.

X_p^i: random variable associated with the i-th pivots-related imperfection.

U_j^1: random variable associated to the horizontal displacement in j with $j = A, B, C, D, E$.

$\rho\left(q_i^1, q_i^2\right)$: area affected by pivot-related random defects in the neighborhood of $\boldsymbol{q} = (q_i^1, q_i^2)$ with $i = 1, 2, 3$. Three local pivot-related random defects are considered.

3.3.1 Defining the second-gradient continuum model for pantographic sheets

Let us consider the work by dell'Isola et al. [33], where a micro-macro identification procedure *à* la Piola allows to derive the deformation energy of a pantographic sheet (2D) under the hypotheses of large deformations and in-plane loads. The deformation energy denoted by $\psi(\boldsymbol{\chi})$ is expressed as the sum of stretching, bending, and torsional contributions denoted by $\psi_{\mathrm{a}}(\boldsymbol{\chi})$, $\psi_{\mathrm{b}}(\boldsymbol{\chi})$, and $\psi_{\mathrm{p}}(\boldsymbol{\chi})$, respectively:

$$\psi(\boldsymbol{\chi}) = \psi_{\mathrm{a}}(\boldsymbol{\chi}) + \psi_{\mathrm{b}}(\boldsymbol{\chi}) + \psi_{\mathrm{p}}(\boldsymbol{\chi}) \ , \tag{3.21}$$

where $\chi : \mathcal{B} \to \mathcal{E}$ is the configuration field defined from the initial (or Lagrangian) configuration $\mathcal{B}$ to the actual (or Eulerian) one $\mathcal{E}$. If ℓ_1 and ℓ_2 are the dimensions of the rectangular pantographic sheet, it is $\mathcal{B} = [0, \ell_1] \times [0, \ell_2]$. The functional $\psi_{\mathrm{a}}(\boldsymbol{\chi})$, $\psi_{\mathrm{b}}(\boldsymbol{\chi})$, and $\psi_{\mathrm{p}}(\boldsymbol{\chi})$ are defined by

$$\psi_{\mathrm{a}}(\boldsymbol{\chi}) = \sum_{\alpha=1}^{2} \int_{\mathcal{B}} \frac{k_{\mathrm{a}}}{2} \left(\| [\boldsymbol{f}(\boldsymbol{\chi})](\boldsymbol{q})\, \boldsymbol{d}_\alpha \| - 1 \right)^2 d\boldsymbol{q} \ , \tag{3.22}$$

$$\begin{aligned} \psi_{\mathrm{b}}(\boldsymbol{\chi}) = & \sum_{\alpha=1}^{2} \int_{\mathcal{B}} \frac{k_{\mathrm{b}}}{2} \left(\left(\frac{\nabla [\boldsymbol{f}(\boldsymbol{\chi})](\boldsymbol{q}) \mid \boldsymbol{d}_\alpha \otimes \boldsymbol{d}_\alpha \cdot \nabla [\boldsymbol{f}(\boldsymbol{\chi})](\boldsymbol{q}) \mid \boldsymbol{d}_\alpha \otimes \boldsymbol{d}_\alpha}{\| [\boldsymbol{f}(\boldsymbol{\chi})](\boldsymbol{q})\, \boldsymbol{d}_\alpha \|^2} \right) \right) d\boldsymbol{q} \\ & - \sum_{\alpha=1}^{2} \int_{\mathcal{B}} \frac{k_{\mathrm{b}}}{2} \left(\left(\frac{[\boldsymbol{f}(\boldsymbol{\chi})](\boldsymbol{q})\, \boldsymbol{d}_\alpha}{\| [\boldsymbol{f}(\boldsymbol{\chi})](\boldsymbol{q})\, \boldsymbol{d}_\alpha \|} \cdot \frac{\nabla [\boldsymbol{f}(\boldsymbol{\chi})](\boldsymbol{q}) \mid \boldsymbol{d}_\alpha \otimes \boldsymbol{d}_\alpha}{\| [\boldsymbol{f}(\boldsymbol{\chi})](\boldsymbol{q})\, \boldsymbol{d}_\alpha \|} \right)^2 \right) d\boldsymbol{q} \ , \end{aligned} \tag{3.23}$$

$$\psi_{\mathrm{p}}(\boldsymbol{\chi}) = \int_{\mathcal{B}} \frac{k_{\mathrm{p}}}{2} \left| \arccos \left(\frac{[\boldsymbol{f}(\boldsymbol{\chi})](\boldsymbol{q})\, \boldsymbol{d}_1}{\| [\boldsymbol{f}(\boldsymbol{\chi})](\boldsymbol{q})\, \boldsymbol{d}_1 \|} \cdot \frac{[\boldsymbol{f}(\boldsymbol{\chi})](\boldsymbol{q})\, \boldsymbol{d}_2}{\| [\boldsymbol{f}(\boldsymbol{\chi})](\boldsymbol{q})\, \boldsymbol{d}_2 \|} \right) - \frac{\pi}{2} \right|^{\gamma} d\boldsymbol{q} \ , \tag{3.24}$$

in which $\boldsymbol{d}_1$ and $\boldsymbol{d}_2$ define the unit vectors parallel to the two orders of beams, $[\boldsymbol{f}(\boldsymbol{\chi})](\boldsymbol{q}) = \nabla \boldsymbol{\chi}(\boldsymbol{q})$ is the gradient of the configuration field. The generic component β of the vector

$\nabla[\boldsymbol{f}(\boldsymbol{\chi})] \mid \boldsymbol{d}_\alpha \otimes \boldsymbol{d}_\alpha$, which is denoted by $(\nabla[\boldsymbol{f}(\boldsymbol{\chi})] \mid \boldsymbol{d}_\alpha \otimes \boldsymbol{d}_\alpha)^\beta$, is equal to the second directional derivative of χ^β , $(\nabla[\boldsymbol{f}(\boldsymbol{\chi})] \mid \boldsymbol{d}_\alpha \otimes \boldsymbol{d}_\alpha)^\beta = \partial\left(\partial\chi^\beta/\partial\boldsymbol{d}^\alpha\right)/\partial\boldsymbol{d}^\alpha$. The symbol "$\cdot$" is the standard Euclidean scalar product and the symbol $\|\cdot\|$ denotes the associated norm. Eqs. (3.22), (3.23), and (3.24) are rewritten in the Levi-Civita notation, where the directions of the beams are assumed to be constant in $\mathcal{B}$:

$$\psi_{\mathrm{a}}(\boldsymbol{\chi}) = \sum_{\alpha=1}^{2} \int_{\mathcal{B}} \frac{k_{\mathrm{a}}}{2} \left(\left([\delta]_{ij} \frac{\partial \chi^i(\boldsymbol{q})}{\partial q^A} \frac{\partial \chi^j(\boldsymbol{q})}{\partial q^B} d_\alpha^A d_\alpha^B \right)^{\frac{1}{2}} - 1 \right)^2 d\boldsymbol{q} \,, \tag{3.25}$$

$$\begin{aligned} \psi_{\mathrm{b}}(\boldsymbol{\chi}) = & \sum_{\alpha=1}^{2} \int_{\mathcal{B}} \frac{k_{\mathrm{b}}}{2} \left(\left(\frac{[\delta]_{ij} \frac{\partial \chi^i(\boldsymbol{q})}{\partial q^A \partial q^B} \frac{\partial \chi^j(\boldsymbol{q})}{\partial q^C \partial q^D} d_\alpha^A d_\alpha^B d_\alpha^C d_\alpha^D}{[\delta]_{km} \frac{\partial \chi^k(\boldsymbol{q})}{\partial q^E} \frac{\partial \chi^m(\boldsymbol{q})}{\partial q^F} d_\alpha^E d_\alpha^F} \right) \right) d\boldsymbol{q} \\ & - \sum_{\alpha=1}^{2} \int_{\mathcal{B}} \frac{k_{\mathrm{b}}}{2} \left(\left(\frac{[\delta]_{ij} \frac{\partial \chi^i(\boldsymbol{q})}{\partial q^C} \frac{\partial \chi^j(\boldsymbol{q})}{\partial q^A \partial q^B} d_\alpha^C d_\alpha^A d_\alpha^B}{[\delta]_{km} \frac{\partial \chi^k(\boldsymbol{q})}{\partial q^E} \frac{\partial \chi^m(\boldsymbol{q})}{\partial q^F} d_\alpha^E d_\alpha^F} \right)^2 \right) d\boldsymbol{q} \,, \end{aligned} \tag{3.26}$$

$$\psi_{\mathrm{p}}(\boldsymbol{\chi}) = \int_{\mathcal{B}} \frac{k_{\mathrm{p}}}{2} \left| \arccos\left(\frac{[\delta]_{ij} \frac{\partial \chi^i(\boldsymbol{q})}{\partial q^A} \frac{\partial \chi^j(\boldsymbol{q})}{\partial q^B} d_1^A d_2^B}{\left([\delta]_{km} \frac{\partial \chi^k(\boldsymbol{q})}{\partial q^C} \frac{\partial \chi^m(\boldsymbol{q})}{\partial q^D} d_1^C d_1^D \right)^{\frac{1}{2}} \left([\delta]_{n\ell} \frac{\partial \chi^n(\boldsymbol{q})}{\partial q^E} \frac{\partial \chi^\ell(\boldsymbol{q})}{\partial q^F} d_2^E d_2^F \right)^{\frac{1}{2}}} \right) - \frac{\pi}{2} \right|^\gamma d\boldsymbol{q} \,, \tag{3.27}$$

where summation is intended over repeated indices. The constants k_{a}, k_{b}, k_{p}, and γ are the material parameters. Since 3D printing can cause defects in each subcomponent of the pantographic sheets, uncertainties have to be taken into account and then each material parameter is modeled by a random variable. In the following, the effect of local pivots-related random defects on the mechanical response of pantographic sheets is investigated.

3.3.2 Deterministic theory-driven analytical relationship between defects-related random variables and displacements

The main goal of the present section is to find a theory-driven analytical relationship to describe the transformation between the input random variables associated with local defects and the output random displacements of pantographic sheets. For this purpose, we use the statistical analysis proposed in [48], which is devoted to uncertain computational models generated by the finite element discretization of static linear elastic structures with uncertain parameters.

Implementation of the probabilistic model of uncertainties in the computational model

By using finite element discretization, it is known that the solution of a linear mechanical system can be reduced to the solution of a linear system of equations. Typically, this linear system of equations is written as $[\boldsymbol{k}]\boldsymbol{u} = \boldsymbol{g}$, where $[\boldsymbol{k}]$ is the positive-definite stiffness matrix, $\boldsymbol{u}$ is the vector of the nodal kinematic unknowns, and $\boldsymbol{g}$ is related to the external applied loads.

On the one hand, let us assume that the mechanical system is affected by a single source of material parameters-related uncertainty, and let us refer to the random variable associated with this uncertainty as X. In addition, let us suppose that matrix $[\boldsymbol{k}]$ is a linear function of random variable X, $[\boldsymbol{k}(X)] = [\boldsymbol{k}_0] + X\,[\boldsymbol{k}_1]$ in which $[\boldsymbol{k}_0]$ is a positive-definite matrix and where $[\boldsymbol{k}_1]$ is symmetric. It is assumed the probability distribution of X is such that the random matrix $[\boldsymbol{k}(X)]$ is invertible almost surely and that the second-order moment of the Frobenius norm of $[\boldsymbol{k}(X)]^{-1}$ is finite. Since X is a random variable, then $\boldsymbol{u}(X)$ is a random vector. These hypotheses imply that $\boldsymbol{u}(X)$ is a second-order random variable. The vector $\boldsymbol{u}(X)$ can be written as the sum of a deterministic quantity $\boldsymbol{u}_0 = \boldsymbol{u}(0)$, and a random addend $\boldsymbol{u}_1(X)$: $\boldsymbol{u}(X)=\boldsymbol{u}_0+\boldsymbol{u}_1(X)$. Let $[\boldsymbol{\phi}]$ and $[\boldsymbol{\lambda}]$ be the matrices of the eigenvectors and the eigenvalues of the generalized eigenvalue problem that is defined by

$$[\boldsymbol{k}_1][\boldsymbol{\phi}] = [\boldsymbol{k}_0][\boldsymbol{\phi}][\boldsymbol{\lambda}]\ . \tag{3.28}$$

Since $[\boldsymbol{k}_0]$ is positive definite and $[\boldsymbol{k}_1]$ is symmetric, the eigenvalues are real and $[\boldsymbol{\phi}]$ is such that $[\boldsymbol{\phi}]^T[\boldsymbol{k}_0][\boldsymbol{\phi}] = [I]$ and $[\boldsymbol{\phi}]^T[\boldsymbol{k}_1][\boldsymbol{\phi}] = [\boldsymbol{\lambda}]$. Let $\boldsymbol{y}_0$ and $\boldsymbol{y}_1$ be the solutions of the linear matrix equations,

$$[\boldsymbol{\phi}]\,\boldsymbol{y}_0 = \boldsymbol{u}_0 \quad , \quad [\boldsymbol{\phi}]\,\boldsymbol{y}_1(X) = \boldsymbol{u}_1(X)\ . \tag{3.29}$$

Consequently, component $u^\ell(X)$ of $\boldsymbol{u}(X)$ can be written (see [48]) as

$$u^\ell(X) = -\sum_{m=1}^{p} X\,[\phi]^\ell_m \frac{1}{1+X\,[\lambda]^m_m}[\lambda]^m_m\,(y_0)^m + (u_0)^\ell \tag{3.30}$$

in which p is the number of nonzero eigenvalues.

We now consider a system that depends on n random variables $X^1, X^2, \ldots, X^n$ such that

$$\left([\boldsymbol{k}_0] + \sum_{i=1}^{n} X^i[\boldsymbol{k}_i]\right)\boldsymbol{u}(\boldsymbol{X}) = \boldsymbol{g}\ . \tag{3.31}$$

As for the case of single random variable X, it assumed that the random Eq. 3.33 admits a unique second-order solution. Let $[\boldsymbol{\phi}_i]$ and $[\boldsymbol{\lambda}_i]$ be the matrices of the eigenvectors and the

eigenvalues of the generalized eigenvalue problem that is defined by

$$[\boldsymbol{k}_i][\boldsymbol{\phi}] = [\boldsymbol{k}_0][\boldsymbol{\phi}_i][\boldsymbol{\lambda}_i] \ . \tag{3.32}$$

As previously, since $[\boldsymbol{k}_0]$ is positive definite and $[\boldsymbol{k}_i]$ is symmetric, the eigenvalues are real and $[\boldsymbol{\phi}_i]$ is such that $[\boldsymbol{\phi}_i]^T[\boldsymbol{k}_0][\boldsymbol{\phi}_i] = [I]$ and $[\boldsymbol{\phi}_i]^T[\boldsymbol{k}_i][\boldsymbol{\phi}_i] = [\boldsymbol{\lambda}_i]$. Consequently, component $u^\ell(\boldsymbol{X})$ of $\boldsymbol{u}(X)$ can be written (see [48]) as

$$u^\ell\left(X^1, X^2, \ldots, X^n\right) \approx -\sum_{i=1}^{n}\sum_{m_i=1}^{p_i} X^i\,[\phi_i]^\ell_{m_i}\,\frac{1}{1+X^i\,[\lambda_i]^{m_i}_{m_i}}[\lambda_{\mathrm{i}}]^{m_i}_{m_i}\,(y_{0i})^{m_i} + (u_0)^\ell \ , \tag{3.33}$$

where p_i is the number of nonzero eigenvalues of the matrices $[\boldsymbol{\lambda}_i]$, and $\boldsymbol{y}_{0i}$ is the solutions of the linear matrix equations,

$$[\boldsymbol{\phi}_i]\,\boldsymbol{y}_{0i} = \boldsymbol{u}_0 \ . \tag{3.34}$$

The next Subsubsection discusses the range of applicability of Eq. (3.33) and, consequently, the limitation and validity of the performed approximation.

Revisiting the hypotheses to obtain a second-order random solution using perturbation analysis

The hypotheses made before imply that material parameters-related uncertainties are small enough. Let us suppose that $\boldsymbol{X} = \varepsilon\,\widehat{\boldsymbol{X}}$ with $\varepsilon \ll 1$ and let us consider the Taylor expansion of $\boldsymbol{u}\,(\boldsymbol{X})$ truncated at the second order, yields

$$\boldsymbol{u}\left(\varepsilon\,\widehat{\boldsymbol{X}}\right) = \boldsymbol{u}_0 + \varepsilon\,\boldsymbol{u}_1^{(1)}\left(\widehat{\boldsymbol{X}}\right) + \varepsilon^2\,\boldsymbol{u}_1^{(2)}\left(\widehat{\boldsymbol{X}}\right) + o\left(\varepsilon^3\right) \ . \tag{3.35}$$

Eq. (3.31) writes

$$\left([\boldsymbol{k}_0] + \sum_{i=1}^{n}\varepsilon\,\widehat{X}^i[\boldsymbol{k}_i]\right)\left(\boldsymbol{u}_0 + \varepsilon\,\boldsymbol{u}_1^{(1)}\left(\widehat{\boldsymbol{X}}\right) + \varepsilon^2\,\boldsymbol{u}_1^{(2)}\left(\widehat{\boldsymbol{X}}\right) + o\left(\varepsilon^3\right)\right) = \boldsymbol{g} \ . \tag{3.36}$$

Since $[\boldsymbol{k}_0]\,\boldsymbol{u}_0 = \boldsymbol{g}$, algebraic calculations and polynomial equality leads to

$$\boldsymbol{u}_1^{(1)}\left(\widehat{X}^1, \widehat{X}^2, \ldots, \widehat{X}^n\right) = -\sum_{i=1}^{n}\widehat{X}^i\,[\boldsymbol{k}_i]\,\boldsymbol{u}_0 \tag{3.37}$$

and

$$\begin{aligned}\boldsymbol{u}_1^{(2)}\left(\widehat{X}^1,\widehat{X}^2,\ldots,\widehat{X}^n\right) &= -\sum_{j=1}^{n}\widehat{X}^j\,[\boldsymbol{k}_j]\boldsymbol{u}_1^{(1)}\left(\widehat{X}^1,\widehat{X}^2,\ldots,\widehat{X}^n\right)\\ &= \sum_{i=1}^{n}\sum_{j=1}^{n}\widehat{X}^i\,\widehat{X}^j\,[\boldsymbol{k}_i]\,[\boldsymbol{k}_j]\,\boldsymbol{u}_0\,.\end{aligned} \tag{3.38}$$

By replacing Eqs. (3.37) and (3.38) into Eq. (3.35), we get

$$\boldsymbol{u}\left(\varepsilon\,\widehat{X}^1,\varepsilon\,\widehat{X}^2,\ldots,\varepsilon\,\widehat{X}^n\right)=\boldsymbol{u}_0-\varepsilon\sum_{i=1}^{n}\widehat{X}^i\,[\boldsymbol{k}_i]\,\boldsymbol{u}_0+\varepsilon^2\sum_{i=1}^{n}\sum_{j=1}^{n}\widehat{X}^i\,\widehat{X}^j\,[\boldsymbol{k}_i][\boldsymbol{k}_j]\,\boldsymbol{u}_0+o\left(\varepsilon^3\right)\,. \tag{3.39}$$

Now, let us define $\boldsymbol{u}_{1i}^{(1)}(X^i)$ as the first-order single response resulting from each random variable $X^i=\varepsilon\,\widehat{X}^i$ acting independently, $\boldsymbol{u}_{1i}^{(1)}(X^i)=-X^i\,[\boldsymbol{k}_i]\,\boldsymbol{u}_0$. It yields

$$\boldsymbol{u}\left(X^1,X^2,\ldots,X^n\right)=\boldsymbol{u}_0+\sum_{i=1}^{n}\boldsymbol{u}_{1i}^{(1)}\left(X^i\right)+\sum_{i=1}^{n}\sum_{j=1}^{n}X^i\,X^j\,[\boldsymbol{k}_i]\,[\boldsymbol{k}_j]\,\boldsymbol{u}_0+o\left(\varepsilon^3\right)\,. \tag{3.40}$$

If Eq. (3.39) is considered and if the Taylor expansion of $\boldsymbol{u}_1(\boldsymbol{X})$ is truncated at the first order, we get

$$\boldsymbol{u}\left(X^1,X^2,\ldots,X^n\right)=\boldsymbol{u}_0+\sum_{i=1}^{n}\boldsymbol{u}_{1i}^{(1)}\left(X^i\right)+o\left(\varepsilon^2\right)\approx\boldsymbol{u}_0+\sum_{i=1}^{n}\boldsymbol{u}_{1i}^{(1)}\left(X^i\right)\,. \tag{3.41}$$

Eq. (3.41) proves that if ε (*i.e*, the randomness of the system) is small enough to approximate $\boldsymbol{u}(\boldsymbol{X})$ by means of a first-order polynomial, then Eq. (3.33) is valid and rational functions describe the relationship between material parameters-related random variables $\boldsymbol{X}$ and random nodal displacements of a structure analyzed by means of FE methods $u^l(\boldsymbol{X})$.

In contrast to the paper proposed in [48], Eq. (3.33) will not be used here for numerically calculating the random response of the system, but this algebraic representation using rational functions will be used instead of a polynomial representation.

3.3.3 Sentivity of pantographic sheets with respect to local random pivots-related defects

To fabricate specimens of pantographic sheets, the limitations of 3D printing technology and the inherent inhomogeneities of the material itself cause random variability in the mechanical properties. In addition, this type of metamaterial is strongly affected by defects associated with

pivots. For this reason, let us consider the energy functional (3.21) where the deterministic parameter k_{p} is replaced with the random field $\theta \mapsto \{(\boldsymbol{X}_p(\theta), \boldsymbol{q}) \mapsto \kappa_{\mathrm{p}}(\boldsymbol{X}_p(\theta), \boldsymbol{q})\}$, which is defined as a piecewise random field in the initial configuration $\mathcal{B}$. The random variable $\boldsymbol{X}_{\mathrm{p}} = (X^1_{\mathrm{p}}, X^2_{\mathrm{p}}, X^3_{\mathrm{p}})$ model local pivots-related defects.

Geometry, load, deterministic and random mechanical properties

A pantographic sheet is considered whose dimensions are $\ell_1 = 6.8 \times 10^{-2}\,\mathrm{m}$ and $\ell_2 = 2.04 \times 10^{-1}\,\mathrm{m}$. Three local defects are introduced that are supposed concentrated in the bidimensional subdomains $\rho\left(q^1_i, q^2_i\right)$ of $\mathcal{B}$ defined by

$$\rho\left(q^1_i, q^2_i\right) = \left\{\left(q^1, q^2\right) \in \mathcal{B} \,:\, \left|q^1 - q^1_i\right| < \frac{1}{200}\ell_2 \,,\, \left|q^2 - q^2_i\right| < \frac{1}{200}\ell_2\right\}, \tag{3.42}$$

with $i = 1, 2, 3$ (see Fig. 3.29) and where the couples (q^1_i, q^2_i) are defined by

$$\left(q^1_1, q^2_1\right) = \left(\frac{\ell_2}{2} - \frac{s}{2}, \frac{\ell_1}{2} + \frac{s}{2}\right) \quad , \quad \left(q^1_2, q^2_2\right) = \left(\frac{\ell_2}{3} - \frac{s}{2}, \frac{\ell_1}{3} - \frac{s}{2}\right) , \tag{3.43}$$

$$\left(q^1_3, q^2_3\right) = \left(\frac{\ell_2}{3} + \frac{s}{2}, \frac{\ell_1}{3} + \frac{s}{2}\right) , \tag{3.44}$$

in which s is equal to $\ell_2/200$. About the boundary conditions, we assume

$$u^1\left(0, q^2\right) = 0\,\mathrm{m} \quad , \quad u^1\left(\ell_2, q^2\right) = 5.63 \times 10^{-2}\,\mathrm{m}\,. \tag{3.45}$$

Assume the axial and bending stiffnesses as well as the mean value of the torsional stiffness field to be

$$k_{\mathrm{a}} = 1.34 \times 10^5\,\mathrm{N/m} \quad , \quad k_{\mathrm{b}} = 1.92 \times 10^{-2}\,\mathrm{Nm} \quad , \quad \bar{k}_{\mathrm{p}} = 1.59 \times 10^2\,\mathrm{N/m}\,, \tag{3.46}$$

which are the values typically selected for polyamide pantographic sheets [33].

Noninformative prior probabilistic model for local random material-related defects

Let $\boldsymbol{q} \mapsto r_1(\boldsymbol{q})$ and $\boldsymbol{q} \mapsto r_2(\boldsymbol{q})$ two rectangular functions defined by

$$r_1\left(\frac{q^1 - q^1_i}{2s}\right) = \mathcal{H}\left(q^1 - \left(q^1_1 - s\right)\right) - \mathcal{H}\left(q^1 - \left(q^1_1 + s\right)\right) , \tag{3.47}$$

$$r_2\left(\frac{q^2-q_i^2}{2s}\right)=\mathcal{H}\left(q^2-\left(q_1^2-s\right)\right)-\mathcal{H}\left(q^2-\left(q_1^2+s\right)\right)\,, \tag{3.48}$$

where s is equal to $\ell_2/200$ and $\mathcal{H}$ is the Heaviside function. Rectangular functions (3.47) and (3.48) allow us to model the random stiffness field κ_{p} as

$$\kappa_{\mathrm{p}}\left(\boldsymbol{X}_{\mathrm{p}},\boldsymbol{q}\right)=\bar{k}_{\mathrm{p}}\left(1+\sum_{i=1}^{3}X_{\mathrm{p}}^{i}\,r_1\left(\frac{q^1-q_i^1}{2s}\right)r_2\left(\frac{q^2-q_i^2}{2s}\right)\right)\,, \tag{3.49}$$

where $\boldsymbol{X}_{\mathrm{p}}=(X_{\mathrm{p}}^1,X_{\mathrm{p}}^2,X_{\mathrm{p}}^3)$, $\boldsymbol{q}=(q^1,q^2)$, $\bar{k}_{\mathrm{p}}$ is the mean values of the torsional random stiffness field. The symbol X_{p}^i denotes uniformly distributed random variables on the interval $[-1,1]$ that are associated with the torsional random defects located in the region $\rho(q_i^1,q_i^2)$.

Deterministic relationship between defected-related random variables and displacements

We build functional relationships between the local horizontal displacements in some points of the sample and the random variables associated with the torsional random defects located in the regions $\rho(q_i^1,q_i^2)$ with $i=1,2,3$ (see Eqs. (3.43)-(3.44)). We choose five points q_j with j=A,B,C,D, and E (see Fig. 3.33 (a)) whose coordinates are

$$\left(q_{\mathrm{A}}^1,q_{\mathrm{A}}^2\right)=\left(4.284\times10^{-2}\,\mathrm{m},6.610\times10^{-3}\,\mathrm{m}\right)\,, \tag{3.50}$$

$$\left(q_{\mathrm{B}}^1,q_{\mathrm{B}}^2\right)=\left(7.337\times10^{-2}\,\mathrm{m},4.173\times10^{-2}\,\mathrm{m}\right)\,, \tag{3.51}$$

$$\left(q_{\mathrm{C}}^1,q_{\mathrm{C}}^2\right)=\left(9.792\times10^{-2}\,\mathrm{m},1.981\times10^{-2}\,\mathrm{m}\right)\,, \tag{3.52}$$

$$\left(q_{\mathrm{D}}^1,q_{\mathrm{D}}^2\right)=\left(1.122\times10^{-1}\,\mathrm{m},6.470\times10^{-2}\,\mathrm{m}\right)\,, \tag{3.53}$$

and

$$\left(q_{\mathrm{E}}^1,q_{\mathrm{E}}^2\right)=\left(1.448\times10^{-1}\,\mathrm{m},4.819\times10^{-2}\,\mathrm{m}\right)\,. \tag{3.54}$$

Let us consider each random variable X_{p}^i acting independently. The functional relationships $X_{\mathrm{p}}^i\mapsto u_{ji}^1(X_{\mathrm{p}}^i)$ are built by solving eleven deterministic finite element models for eleven different values of X_{p}^i and then interpolating using rational functions. The use of rational functions is led by Eq. (3.33). The deterministic numerical analyses are based on standard energy minimization techniques through the application of the standard FEM packages in COMSOL Multiphysics®. Regarding accuracy, a free tetrahedral mesh with 8 470 domain elements, 268 boundary elements, 78 394 degrees of freedom, and discretization by means of Argyris polynomials are chosen (see Fig. 3.30). In Fig. 3.31, the logarithm of the specific

deformation energy obtained for $X_{\mathrm{p}}^{i}=0$ is shown. In Fig. 3.32, the difference between the horizontal displacements obtained with $X_{\mathrm{p}}^{i}=0$ and the one obtained with only X_{p}^{1} different from zero, $X_{\mathrm{p}}^{1}=0.8$, is shown. It is deduced that one portion of the sample stretches while another portion contracts. Finally, the relationship $(X_{\mathrm{p}}^{1},X_{\mathrm{p}}^{2},X_{\mathrm{p}}^{3})\mapsto u_{j123}^{1}(X_{\mathrm{p}}^{1},X_{\mathrm{p}^{2}},X_{\mathrm{p}}^{3})$ with

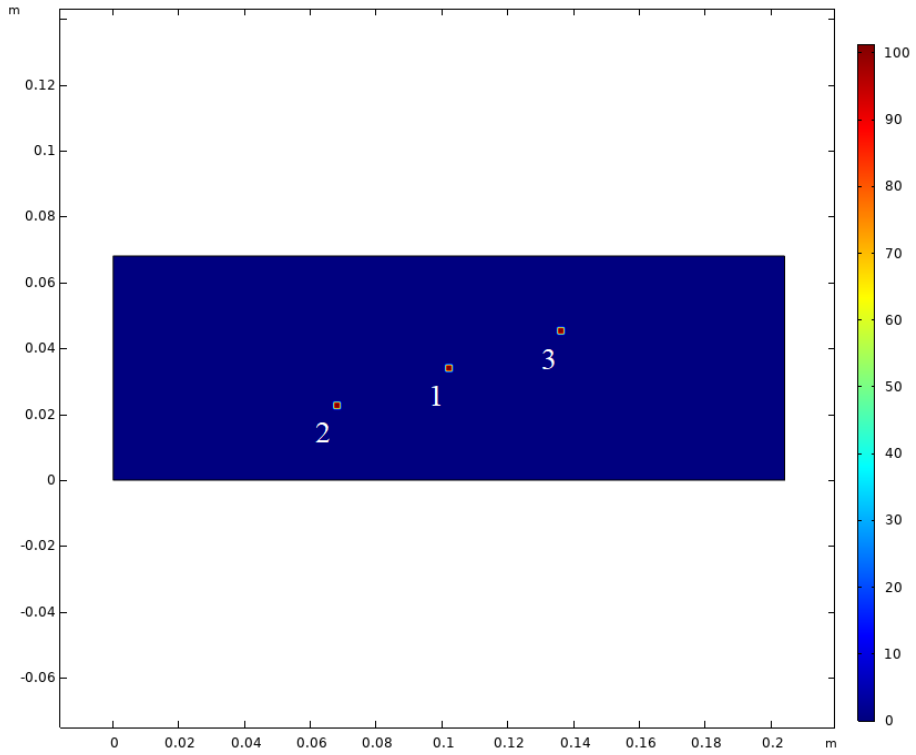

Fig. 3.29 Position of defects.

j=A,B,C,D, and E is approximated as

$$u_{j123}^{1}\left(X_{\mathrm{p}}^{1},X_{\mathrm{p}}^{2},X_{\mathrm{p}}^{3}\right)\approx -2u_{j0}^{1}+\sum_{i=1}^{3}u_{ji}^{1}\left(X_{\mathrm{p}}^{i}\right)\ . \tag{3.55}$$

where u_{j0}^{1} is equal to $u_{j1}^{1}(0)$, which, in turn, is equal to $u_{j2}^{1}(0)$ and $u_{j3}^{1}(0)$. Eq. (3.55) and Monte Carlo numerical simulation allow us to approximately estimate the stochastic response of the system. We call U_{j}^{1} the random variable defined by $U_{j}^{1}=u_{j123}^{1}(X_{\mathrm{p}}^{1},X_{\mathrm{p}}^{2},X_{\mathrm{p}}^{3})$.

Monte Carlo numerical simulation as a stochastic solver

The construction of the probability density functions, mean values, and standard deviations of the random horizontal displacements affected by local random torsional defects is based

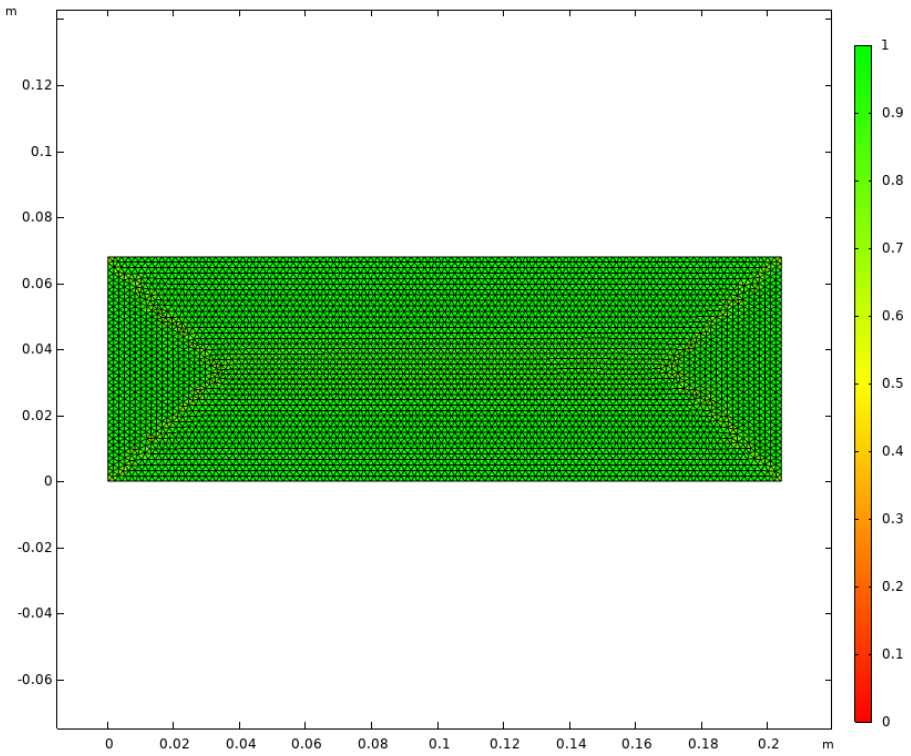

Fig. 3.30 Chosen mesh.

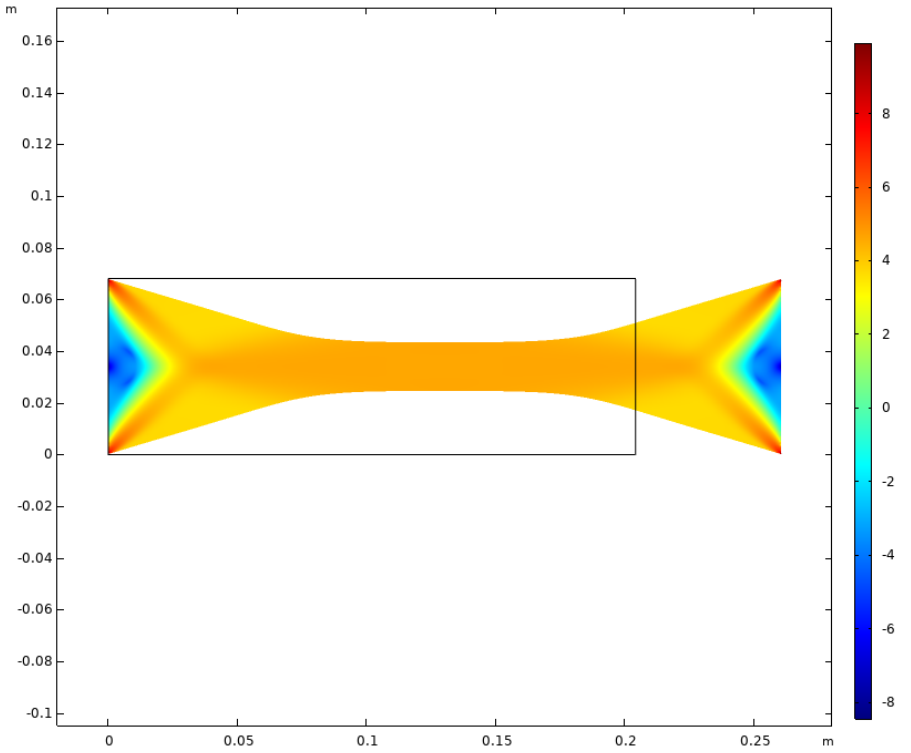

Fig. 3.31 Logarithm of the deformation energy without defect.

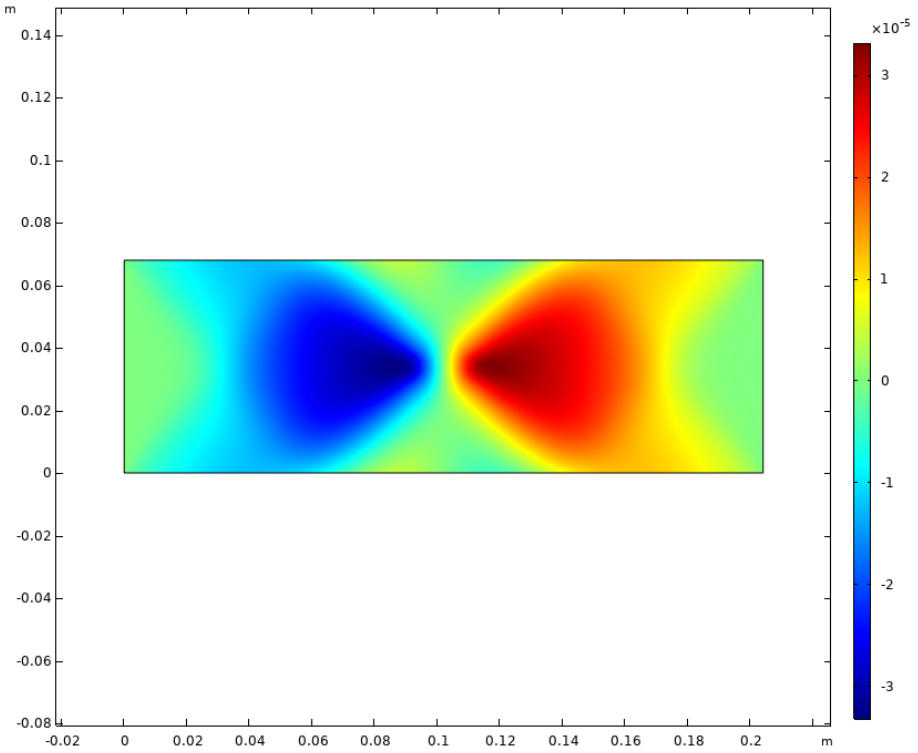

Fig. 3.32 Difference between the horizontal displacements obtained without defects and $X_{\mathrm{p}}^{1} = 0.8$.

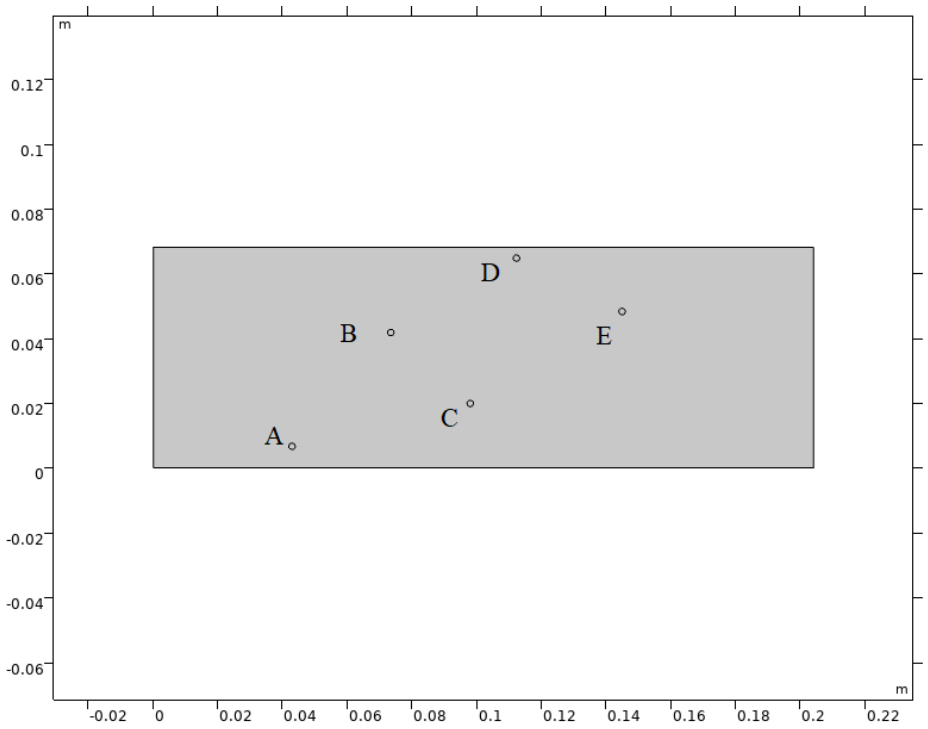

Fig. 3.33 Position of the points A, B, C, D, and E.

on the use of the MC numerical simulation of Eq. (3.55). The steps of the stochastic solver are as follows.

1. Generation of n independent realizations of the uniformly distributed random variables $X_{\mathrm{p}}^{i}(\theta_1)$, $X_{\mathrm{p}}^{i}(\theta_2)$, ..., $X_{\mathrm{p}}^{i}(\theta_n)$ with $i = 1, 2, 3$.
2. Computation of n independent realizations $U_j^1(\theta_1), U_j^1(\theta_2), \ldots, U_j^1(\theta_n)$ using Eq. (3.55).
3. Computation of the numerical probability density functions $p_{U_j^1}(u_j^1)$, the mean values $\mu_{U_j^1}$, the standard deviations $\sigma_{U_j^1}$, and the coefficients of variation $\mathrm{Cv}_{U_j^1}$ of the random variables U_j^1 with j=A,B,C,D, and E.

Quantification of uncertainty propagation

In Table 3.3, mean values, coefficients of variation, and standard deviations of the random variables U_j^1 are presented. Then, since we are facing a strongly nonlinear mechanical problem, the numerical probability density functions $u_j^1 \mapsto p_{U_j^1}(u_j^1)$ of the random variables U_j^1 are built and shown in Fig. 3.34. It is shown that local random torsional defects have very little impact on the horizontal displacements, although the defect-related random variables X_{p}^{i} vary within a significant range $[-1, 1]$. This is due to the redundant connections inside pantographic sheets, which results in standard deviations of approximately -7. For the same reason, local standard deviations are not strictly influenced by the distance from the location of the defects. Counter-intuitively, the standard deviation of the horizontal displacement U_E^1, denoted by $\sigma_{U_E^1}$, is bigger when the defect is placed in q_1 rather than in q_3. A significant difference between the standard deviations of U_C^1 and U_D^1, denoted by $\sigma_{U_C^1}$ and $\sigma_{U_D^1}$, exists when the defect is located in q_2, although C and D are almost equally distant from the point q_2 itself. The global behavior makes it difficult to predict the region most affected by torsional defects and to hypothesize the localizations of imperfections for maximizing or minimizing local standard deviations. A study on this problem will be considered in the future.

Exploring Alternatives in Modeling Random Defects

In this section, random defects have been modeled as uniformly distributed random variables to maximize the randomness of the system. However, this model can be improved by incorporating several constraints.

Under the hypothesis of k_a, k_b, and k_s modeled as random variables K_a, K_b, and K_s, we assume that K_a, K_b, and K_s are defined in $\mathbb{R}^+$, their mean values $\mathbb{E}\{K_a\}$, $\mathbb{E}\{K_b\}$, and $\mathbb{E}\{K_s\}$ are finite, and $\log(K_a K_b K_s)$ is finite for physical consistency. Following the same steps as in Section 4.2.2, it can be easily proven that K_a, K_b, and K_s result in statistically independent

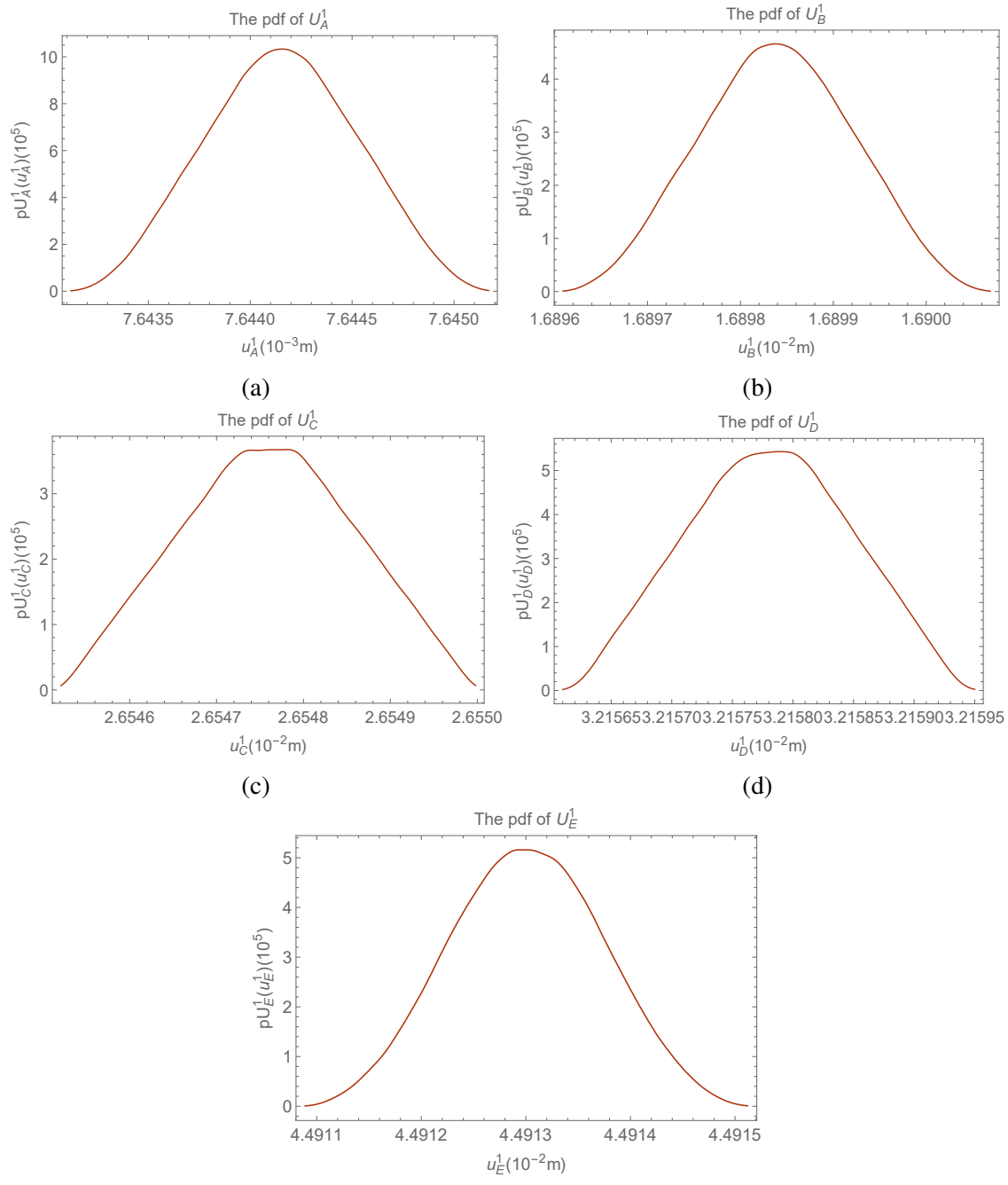

Fig. 3.34 (a) Graph $u_A^1 \mapsto p_{U_A^1}(u_A^1)$ of the pdf of U_A^1, (b) graph $u_B^1 \mapsto p_{U_B^1}(u_B^1)$ of the pdf of U_B^1, (c) graph $u_C^1 \mapsto p_{U_C^1}(u_C^1)$ of the pdf of U_C^1, (d) graph $u_D^1 \mapsto p_{U_D^1}(u_D^1)$ of the pdf of U_D^1, and (e) Graph $u_E^1 \mapsto p_{U_E^1}(u_E^1)$. The pdfs have been built by means of MC numerical simulations with 5×10^5 samples and the kernel density estimation (KDE) method.

Table 3.3 Mean values $\mu_{U_j^1}$, standard deviations $\sigma_{U_j^1}$, and coefficients of variation $\mathrm{Cv}_{U_j^1}$ of the random variables U_j^1 with j=A,B,C,D, and E.

$\mu_{U_A^1}$	$\mu_{U_B^1}$	$\mu_{U_C^1}$	$\mu_{U_D^1}$	$\mu_{U_E^1}$
7.64×10^{-3} m	1.69×10^{-2} m	2.65×10^{-2} m	3.21×10^{-2} m	4.49×10^{-3} m
$\sigma_{U_A^1}$	$\sigma_{U_B^1}$	$\sigma_{U_C^1}$	$\sigma_{U_D^1}$	$\sigma_{U_E^1}$
3.65×10^{-7} m	8.08×10^{-7} m	9.85×10^{-7} m	6.64×10^{-7} m	7.21×10^{-7} m
$\mathrm{Cv}_{U_A^1}$	$\mathrm{Cv}_{U_B^1}$	$\mathrm{Cv}_{U_C^1}$	$\mathrm{Cv}_{U_D^1}$	$\mathrm{Cv}_{U_E^1}$
4.78×10^{-3} ‰	4.78×10^{-3} ‰	3.71×10^{-3} ‰	2.07×10^{-3} ‰	1.60×10^{-3} ‰

Gamma-distributed random variables, whose statistical fluctuations are described by a single parameter.

If k_a, k_b, and k_s are modeled as random fields $\{\boldsymbol{q} \mapsto K_a(\boldsymbol{q})\}$, $\{\boldsymbol{q} \mapsto K_b(\boldsymbol{q})\}$, and $\{\boldsymbol{q} \mapsto K_s(\boldsymbol{q})\}$, preserving at $\boldsymbol{q}$ the same hypotheses as before, these random fields can be constructed using the same technique as presented in Section 4.3.2, which requires the construction of a homogeneous, second-order, non-Gaussian random fields.

Numerous probabilistic models could be proposed for k_a, k_b, and k_s. Here, we have discussed some of the many possible ones.

3.4 Summarizing the main results

- In Section 3.1, the two-parameter shear energy given in [33] has been improved to precisely represent experimental bias tests on PA and ME pantographic sheets. The proposed shear energy (see Eq. (3.6)) captures the high changes in concavity in the force-elongation curve experimentally observed.

- Overcoming some issues related to the model proposed in [33] for pantographic sheets, the torsional energy introduced in Section 3.1 does not have the numerical disadvantage of an infinite value for the second derivative of the shear energy with respect to the initial equilibrium configuration.

- Although the torsional energy proposed in Section 3.1 has been developed to characterize the mechanical response of pantographic sheets for monotonic loadings in bias-extension tests, it is also applicable to model their mechanical behavior under combinations of shear and axial loadings for which experimental campaigns are currently underway.

- For isotropic and linear elastic materials subjected to 3-point flexure, the coupling between local transverse elongation and flexure induces anticlastic curvatures. The latter

is described by the Saint-Venant solution [98, 80, 120]. Conversely, second-gradient materials are governed by strain energies that are more general. In Section 3.2, DVC analyses have proven that a pantographic block, when subjected to 3-point flexure with prescribed displacements parallel to the pantographic plane, experiences deformations are well approximated by a monoclastic mode for the top surface, while the bottom surface remains essentially flat.

- The second-order continuum model introduced and described in Section 3.2 for the pantographic block exhibits a rather satisfactory agreement with the experimental data, especially in predicting the displacements and the monoclastic deformation mode. The model parameters have been globally calibrated using the force vs. stroke curve. Further kinematic data should be used in the future to calibrate the parameters. A generalization is expected of the results already described in [49, 55, 103, 59].

- In Section 3.2, after investigating the flexural response of a pantographic block with prescribed displacements in the pantographic plane, it has been natural to explore its deformation mode with displacements applied in the direction orthogonal to the pantographic plane. An anticlastic mode has been predicted. This difference is not unexpected given that the pantographic block is modeled here by second-order derivatives of displacements along the pantographic planes and first-order derivatives along its thickness. Further tests are required to confirm these theoretical results. Additional experimental efforts will examine the dynamic behavior of such metamaterials (see also [20, 47]).

- Large displacements and periodicity of pantographic structures have caused difficulties in performing DVC analysis. The model-driven initialization of the DVC analyses has proven to be highly successful in overcoming these problems. The model-driven initialization of the DVC analysis may also be used when initialization is complicated by other factors, such as the onset of damage or fracture, by employing more precise models [148, 105].

- Finally, in Section 3.3, the effect of local uncertainties on pantographic sheets has been investigated. It is shown that a small number of pivot-related imperfections have negligible influence on the mechanical response of the system. This influence should increase when the number of defects is increasing.

Chapter 4

Particle-based materials

In Chapter 2, we have dealt with the foundations of generalized continua. Among these, the micropolar continuum, the micromorphic continuum, the second-gradient continuum, and the second-gradient-micropolar continuum have been uniformly presented. In Chapter 3, we have experimentally validated the capability of second-gradient models to predict the mechanical behavior of pantographic sheets and pantographic blocks, and we have investigated the effects of pivots-related random defects on the mechanical response of pantographic sheets. This chapter is composed of sections 4.1, 4.2, and 4.3. Two models for particle-based materials are presented. The first section is derived from the papers [75, 74], the second from the paper [72], and the third from a collaboration with Professor Christian. Soize.

4.1 Response and identification of random micropolar Timoshenko-Ehrenfest beams

In this section, the derivation of the Timoshenko-Ehrenfest beam equations is introduced within the framework of linear elasticity, starting from the 3D micropolar continuum model presented in Section 2.1. Two novel closed-form solutions of these equations are proposed that are useful for a preliminary study on uncertainty propagation. In [99, 117], more complex deterministic micropolar beam models for lattice beams have been developed. Despite the advancements in complex 3D numerical calculations, the study of beam theory (1D) remains highly relevant. Beam theory simplifies structural analysis, offering foundational insights, efficient computations for limited resources, and fundamental concepts essential for various practical scenarios. It remains valid in cases where one dimension significantly dominates, providing accurate results without the need for 3D models. While 3D models are indispensable for complexity, beam theory continues to serve as a practical and crucial

tool in understanding basic principles and streamlining analyses for specific engineering applications.

This section is organized as follows. In Subsection 4.1.1, the Timoshenko-Ehrenfest beam equations are derived for the micropolar continuum within the framework of linear elasticity. Under the assumption of continuously varying material properties along the axis, we propose three approximated closed-form solutions. Typically, with such material properties, beams are referred to as *axially functionally graded beams* [69, 119]. Subsection 4.1.2 deals with these mechanical properties that are modeled by random fields and constitute a preliminary study for the uncertainty propagation using a noninformative prior probability model. The proposed results also find application in the analysis of step beams [88, 39].

Notation

Below i is an integer belonging to $\{1,2,3\}$ and j is an integer belonging to $\mathbb{R}$.

A lowercase letter such as x, η, u is a real deterministic variable except when used as an integer as i, j, etc.

An upper case letter such us X, H, U is a real random variable except when used as an integer index as A, B, etc.

$\mathbb{1}_B$: indicator function of a set B.

$\mathrm{Tr}\,(A)$: trace of a matrix A.

$\|A\|$: Frobenius norm of a matrix A.

$\mathcal{H}$: Heaviside function.

$f^{(k)}$: function whose k-th derivative is function f.

x, y, z: Lagrangian coordinates.

v_i: component i of the local displacement field v.

ϕ_i: component i of the local microrotation field ϕ.

Q: microrotation tensor.

u: beam transversal displacement field.

w: beam horizontal displacement field.

φ: beam rotation field.

f: externally applied axial load.

q: externally applied transversal load.

ε: linearized strain tensor.

Ω: linearized macrorotation tensor.

$\mathfrak{K}$: linearized wryness tensor.

ι: deterministic moment of beams inertia.

σ: deterministic area of the beams cross-section.

4.1.1 Micropolar Timoshenko-Ehrenfest beam equations

Deformation energy for the linear micropolar continuum

Within the framework of the linear micropolar continuum, under the hypothesis of isotropy with respect to the stretch and wryness tensors, the deformation energy density is written as

$$\begin{aligned} W^{\text{def}}(\varepsilon, \mathfrak{k}) &= \frac{\lambda_E}{2}(\operatorname{Tr}(\varepsilon))^2 + \mu_E \|_S\varepsilon\|^2 + \xi_{\mathcal{R}} \|_A\varepsilon\|^2 \\ &+ \frac{\lambda_\Gamma}{2}(\operatorname{Tr}(\mathfrak{k}))^2 + \left(\frac{\mu_\Gamma + \xi_\Gamma}{2}\right) \|_S\mathfrak{k}\|^2 + \left(\frac{\mu_\Gamma - \xi_\Gamma}{2}\right) \|_A\mathfrak{k}\|^2 \end{aligned} \tag{4.1}$$

where ε is the linearized form of the micropolar stretch tensor defined in Eq. (2.11), and $\mathfrak{k}$ is the linearized form of the micropolar wryness tensor defined in Eq. (2.13). The stiffness fields $z \mapsto \lambda_E(z)$ and $z \mapsto \mu_E(z)$ defines the Lamé parameters. The stiffness field $z \mapsto \xi_{\mathcal{R}}(z)$ stands for the material parameter related to the micro-macro relative rotation, and the stiffness fields $z \mapsto \lambda_\Gamma(z)$ and $z \mapsto \mu_\Gamma(z)$ define the material parameters related to wryness tensor. The pre-subscripts S and A distinguish the symmetric and skewsymmetric parts of ε and $\mathfrak{k}$. On the one hand, micropolar stretch tensor ε depends on the local displacement v and on the microrotation tensor Q. On the other hand, wryness tensor $\mathfrak{k}$ depends on the gradient of microrotation field Q. We denote by $\phi(x, y, z)$ the axial vector associated with the skewsymmetric part ${}_AQ(x, y, z)$ of $Q(x, y, z)$, $\phi(x, y, z) = \operatorname{axl}({}_AQ(x, y, z))$. We refer to ϕ as the *local microrotation field*.

Defining the deterministic micropolar beam model

Within the framework of the micropolar continuum and Timoshenko-Ehrenfest beam, it is natural to approximate the local displacement field components $v_i(x,y,z)$ and the local microrotation field components $\phi_i(x,y,z)$ as below,

$$v_1(x,y,z)=0 \quad , \quad v_2(x,y,z)=u(z) \quad , \quad v_3(x,y,z)=w(z)+y\,\varphi(z)\,, \tag{4.2}$$

$$\phi_1(x,y,z)=\varphi(z) \quad , \quad \phi_2(x,y,z)=0 \quad , \quad \phi_3(x,y,z)=0\,, \tag{4.3}$$

where $z\mapsto w(z)$ and $z\mapsto u(z)$ are the beam axial and transversal displacement fields, $z\mapsto\varphi(z)$ denotes the beam microrotation field. By replacing Eqs. (4.2) and (4.3) into Eq. (4.1), and by evaluating the first variation, yield the equilibrium equations of the micropolar Timoshenko-Ehrenfest beams in the area of linear elasticity. We get

$$\frac{d}{dz}\left(\bar{e}(z)\,\sigma\frac{dw(z)}{dz}\right)+f(z)=0\,, \tag{4.4}$$

$$\frac{d}{dz}\left[\bar{g}(z)\,\sigma\left(\frac{du(z)}{dz}+\varphi(z)\right)\right]+q(z)=0\,, \tag{4.5}$$

$$\frac{d}{dz}\left[\left(c(z)\,\sigma+\bar{e}(z)\,\iota\right)\frac{d\varphi(z)}{dz}\right]-\bar{g}(z)\,\sigma\left(\frac{du(z)}{dz}+\varphi(z)\right)=0\,, \tag{4.6}$$

with the boundary conditions

$$\left[\bar{e}(z)\,\sigma\frac{dw(z)}{dz}\delta w(z)\right]_0^{\ell}=0 \quad , \quad \left[\bar{g}(z)\,\sigma\left(\frac{du(z)}{dz}+\varphi(z)\right)\delta u(z)\right]_0^{\ell}=0\,, \tag{4.7}$$

$$\left[\left(c(z)\,\sigma+\bar{e}(z)\,\iota\right)\frac{d\varphi(z)}{dz}\delta\varphi(z)\right]_0^{\ell}=0\,, \tag{4.8}$$

where $z\mapsto f(z)$ and $z\mapsto q(z)$ are the axial and transversal external loads, σ is the beam area, ι is the beam moment of inertia, and ℓ the beam length. The stiffness fields $z\mapsto\bar{e}(z)$ and $z\mapsto\bar{g}(z)$ are defined by

$$\bar{e}(z)=e(z)\,\eta(z) \quad , \quad \bar{g}(z)=g(z)+\xi_{\mathcal{R}}(z) \quad , \quad c(z)=\mu_{\Gamma}(z)/2\,, \tag{4.9}$$

where $e(z)$ is the Young modulus and $g(z)$ is the shear deformation modulus at z. It is natural to refer to $\bar{e}(z)$ as the *generalized Young modulus* at z, to $\bar{g}(z)$ as the *generalized shear deformation modulus* at z, and to $c(z)$ as the *generalized micropolar modulus* at z.

Since $\lambda_E(z)$ and $\mu_E(z)$ are the classical Lamé parameters at z, we have

$$\mu_E(z) = g(z) \quad , \quad \lambda_E(z) = \frac{\nu(z)\, e(z)}{(1+\nu(z))(1-2\nu(z))} , \tag{4.10}$$

where $\nu(z)$ is the Poisson coefficient at z. The field $z \mapsto \eta(z)$ is defined by

$$\eta(z) = \frac{1-\nu(z)}{(1+\nu(z))(1-2\nu(z))} . \tag{4.11}$$

The shear stiffness at z, $\bar{g}(z)\sigma$, can be divided by a parameter $\chi(z)$, known as the *shear correction factor*, although this is not a direct result of the monodimensional approximation of Eq. (4.1). More generally, one can introduce an axial stiffness field $z \mapsto a(z)$, a bending stiffness field $z \mapsto b(z)$, and a shear stiffness field $z \mapsto t(z)$. The micropolar Timoshenko-Ehrenfest beam equations are then rewritten as

$$\frac{d}{dz}\left(a(z)\frac{dw(z)}{dz}\right) + f(z) = 0 , \tag{4.12}$$

$$\frac{d}{dz}\left[t(z)\left(\frac{du(z)}{dz} + \varphi(z)\right)\right] + q(z) = 0 , \tag{4.13}$$

$$\frac{d}{dz}\left[b(z)\frac{d\varphi(z)}{dz}\right] - t(z)\left(\frac{du(z)}{dz} + \varphi(z)\right) = 0 , \tag{4.14}$$

with the boundary conditions

$$\left[a(z)\frac{dw(z)}{dz}\delta w(z)\right]_0^\ell = 0 \quad , \quad \left[t(z)\left(\frac{du(z)}{dz} + \varphi(z)\right)\delta u(z)\right]_0^\ell = 0 , \tag{4.15}$$

$$\left[b(z)\frac{d\varphi(z)}{dz}\delta\varphi(z)\right]_0^\ell = 0 , \tag{4.16}$$

where

$$a(z) = \bar{e}(z)\sigma \quad , \quad b(z) = c(z)\sigma + \bar{e}(z)\iota \quad , \quad t(z) = \frac{\bar{g}(z)\sigma}{\chi(z)} . \tag{4.17}$$

On the one hand, if $\bar{e}(z)$ and $c(z)$ have the same order of magnitude, for microbeams, the magnitude of the moment of inertia ι is negligible in comparison to that of area σ. We have

$$b(z) = c(z)\sigma + \bar{e}(z)\iota \approx c(z)\sigma . \tag{4.18}$$

On the other hand, for macrobeams, we get

$$b(z) = c(z)\,\sigma + \bar{e}(z)\,\iota \approx \bar{e}(z)\,\iota\ . \tag{4.19}$$

These remarks imply that the introduced model, despite its simplicity, can capture scale effects. It predicts an increasing bending stiffness by decreasing the dimensions of the cross-section with respect to the classical models.

Approximated closed-form solutions

Following are closed-form relationships between displacements $w(z)$ and $u(z)$, and axial, bending, and shear stiffness $a(z)$, $b(z)$, and $t(z)$. These relationships can be considered as an approximation of the solution of the system of equations (4.12), (4.13), and (4.14) with the boundary conditions (4.15) and (4.16). The stiffness fields are stepwise defined by means of the Heaviside function $\mathcal{H}$ as follows,

$$a(z) \approx \widehat{a}_1 + \sum_{i=2}^{n} (\widehat{a}_i - \widehat{a}_{i-1})\,\mathcal{H}(z - z_i)\ , \tag{4.20}$$

$$b(z) \approx \widehat{b}_1 + \sum_{i=2}^{n} \left(\widehat{b}_i - \widehat{b}_{i-1}\right)\mathcal{H}(z - z_i)\ , \tag{4.21}$$

$$t(z) \approx \widehat{t}_1 + \sum_{i=2}^{n} \left(\widehat{t}_i - \widehat{t}_{i-1}\right)\mathcal{H}(z - z_i)\ , \tag{4.22}$$

where n is the number of intervals and $z_i = z_{i-1} + \ell/n$ with $z_1 = 0$. In the following, given a generic function $f : z \mapsto f(z)$, the symbol $f^{(i)}$ represents a function whose i-th derivative is f.

Simply supported micropolar beams

The integration of Eq. (4.13) with respect to z yields

$$t(z)\left(\frac{du(z)}{dz} + \varphi(z)\right) = -q^{(1)}(z) + k_1\ . \tag{4.23}$$

By adding Eq. (4.23) to Eq. (4.14), we obtain

$$\frac{d}{dz}\left[b(z)\,\frac{d\varphi(z)}{dz}\right] = -q^{(1)}(z) + k_1\ . \tag{4.24}$$

Eq. (4.24) can be integrated to obtain

$$\frac{d\varphi(z)}{dz} = \frac{-q^{(2)}(z) + k_1 z + k_2}{b(z)} \,. \tag{4.25}$$

Replacing Eq. (4.21) into Eq. (4.25), it can be written as

$$\frac{d\varphi(z)}{dz} \approx \frac{-q^{(2)}(z_1) + k_1 z_1 + k_2}{\widehat{b}_1} + \sum_{i=2}^{n} \left(\frac{-q^{(2)}(z_i) + k_1 z_i + k_2}{\widehat{b}_i} - \frac{-q^{(2)}(z_{i-1}) + k_1 z_{i-1} + k_2}{\widehat{b}_{i-1}} \right) \mathcal{H}(z - z_i) \,. \tag{4.26}$$

Since for a simply supported beam, two of the four boundary conditions are

$$\left.\frac{d\varphi(z)}{dz}\right|_{z=0} = 0 \quad , \quad \left.\frac{d\varphi(z)}{dz}\right|_{z=\ell} = 0 \,, \tag{4.27}$$

we get also

$$k_1 = \frac{q^{(2)}(\ell)}{\ell} \quad , \quad k_2 = 0 \,. \tag{4.28}$$

To shorten the equations writing, it is useful to introduce the function

$$\widehat{q}^{(2)}(z) = -q^{(2)}(z) + \frac{q^{(2)}(\ell)}{\ell} z \,. \tag{4.29}$$

Eqs. (4.26), (4.28), and (4.29) lead to

$$\frac{d\varphi(z)}{dz} \approx \frac{\widehat{q}^{(2)}(z_1)}{\widehat{b}_1} + \sum_{i=2}^{n} \left(\frac{\widehat{q}^{(2)}(z_i)}{\widehat{b}_i} - \frac{\widehat{q}^{(2)}(z_{i-1})}{\widehat{b}_{i-1}} \right) \mathcal{H}(z - z_i) \tag{4.30}$$

that can be integrated to give:

$$\varphi(z) \approx k_3 + \frac{\widehat{q}^{(2)}(z_1)}{\widehat{b}_1} z + \sum_{i=2}^{n} \left(\frac{\widehat{q}^{(2)}(z_i)}{\widehat{b}_i} - \frac{\widehat{q}^{(2)}(z_{i-1})}{\widehat{b}_{i-1}} \right) \mathcal{R}(z - z_i) \,, \tag{4.31}$$

where $\mathcal{R}(z)$ is the generalized 1-th order Ramp function, which is defined as follows:

$$\mathcal{R}(z - z_i) = \begin{cases} 0 \quad , \quad z \le z_i \,, \\ z - z_i \quad , \quad z > z_i \,, \end{cases} \tag{4.32}$$

Replacing Eq. (4.31) into Eq. (4.23) yields

$$\begin{aligned}\frac{du(z)}{dz} \approx -k_3 + \frac{\widehat{q}^{(1)}(z_1)}{\widehat{t}_1} + \sum_{i=2}^{n}\left(\frac{\widehat{q}^{(1)}(z_i)}{\widehat{t}_i} - \frac{\widehat{q}^{(1)}(z_{i-1})}{\widehat{t}_{i-1}}\right)\mathcal{H}(z-z_i) \\ -\frac{\widehat{q}^{(2)}(z_1)}{\widehat{b}_1}z - \sum_{i=2}^{n}\left(\frac{\widehat{q}^{(2)}(z_i)}{\widehat{b}_i} - \frac{\widehat{q}^{(2)}(z_{i-1})}{\widehat{b}_{i-1}}\right)\mathcal{R}(z-z_i)\,.\end{aligned} \tag{4.33}$$

Eq. (4.33) can be integrated and an explicit expression of the transversal displacement is achieved,

$$\begin{aligned}u(z) \approx -k_3 z + k_4 + \frac{\widehat{q}^{(1)}(z_1)}{\widehat{t}_1}z + \sum_{i=2}^{n}\left(\frac{\widehat{q}^{(1)}(z_i)}{\widehat{t}_i} - \frac{\widehat{q}^{(1)}(z_{i-1})}{\widehat{t}_{i-1}}\right)\mathcal{R}(z-z_i) \\ -\frac{\widehat{q}^{(2)}(z_1)}{\widehat{b}_1}\frac{z^2}{2} - \sum_{i=2}^{n}\left(\frac{\widehat{q}^{(2)}(z_i)}{\widehat{b}_i} - \frac{\widehat{q}^{(2)}(z_{i-1})}{\widehat{b}_{i-1}}\right)\mathcal{Q}(z-z_i)\ ,\end{aligned} \tag{4.34}$$

where $\mathcal{Q}$ denotes the 2-th order ramp function defined by

$$\mathcal{Q}(z-z_i) = \begin{cases} 0 & , \quad z \le z_i\,, \\ \frac{(z-z_i)^2}{2} & , \quad z > z_i\,. \end{cases} \tag{4.35}$$

Since we are dealing with a simply supported beam, we have

$$u(z) = 0 \quad , \quad u(\ell) = 0\,, \tag{4.36}$$

and the integration constant k_3 is given by

$$\begin{aligned}k_3 = \frac{1}{\ell}\left[\frac{\widehat{q}^{(1)}(z_1)}{\widehat{t}_1}\ell + \sum_{i=2}^{n}\left(\frac{\widehat{q}^{(1)}(z_i)}{\widehat{t}_i} - \frac{\widehat{q}^{(1)}(z_{i-1})}{\widehat{t}_{i-1}}\right)\mathcal{R}(\ell-z_i)\right] \\ +\frac{1}{\ell}\left[-\frac{\widehat{q}^{(2)}(z_1)}{\widehat{b}_1}\frac{\ell^2}{2} - \sum_{i=2}^{n}\left(\frac{\widehat{q}^{(2)}(z_i)}{\widehat{b}_i} - \frac{\widehat{q}^{(2)}(z_{i-1})}{\widehat{b}_{i-1}}\right)\mathcal{Q}(\ell-z_i)\right]\,,\end{aligned} \tag{4.37}$$

while the integration constant k_4 is equal to zero. In the same way, it is possible to solve the differential equation governing the axial behavior. By integrating twice Eq. (4.12) with respect to z, we get

$$w(z) \approx -k_1 z + k_2 - \frac{f^{(1)}(z_1)}{\widehat{a}_1}z - \sum_{i=2}^{n}\left(\frac{f^{(1)}(z_i)}{\widehat{a}_i} - \frac{f^{(1)}(z_{i-1})}{\widehat{a}_{i-1}}\right)\mathcal{R}(z-z_i)\,. \tag{4.38}$$

The constants k_1 and k_2 are calculated by using the boundary conditions,

$$w(0) = 0 \quad , \quad w(\ell) = 0 \, . \tag{4.39}$$

We obtain

$$k_2 = 0 \quad , \quad k_1 = \frac{1}{\ell}\left[-\frac{f^{(1)}(z_1)}{\widehat{a}_1}\ell - \sum_{i=2}^{n}\left(\frac{f^{(1)}(z_i)}{\widehat{a}_i} - \frac{f^{(1)}(z_{i-1})}{\widehat{a}_{i-1}} \right) \mathcal{R}(\ell - z_i) \right] . \tag{4.40}$$

Cantilever micropolar beams

The boundary conditions for a cantilever beam are written as

$$u(0) = 0 \quad , \quad \varphi(0) = 0 \quad , \quad \left. \frac{d\varphi(z)}{dz} \right|_{z=\ell} = 0 \quad , \quad \left. \frac{du(z)}{dz} + \varphi(z) \right|_{z=\ell} = 0 \, . \tag{4.41}$$

The procedures outlined in Subsection 4.1.1 is repeated. The the transversal displacement is given by

$$\begin{aligned} u(z) \approx & \frac{\widehat{q}^{(1)}(z_1)}{\widehat{t}_1} z + \sum_{i=2}^{n}\left(\frac{\widehat{q}^{(1)}(z_i)}{\widehat{t}_i} - \frac{\widehat{q}^{(1)}(z_{i-1})}{\widehat{t}_{i-1}} \right) \mathcal{R}(z - z_i) \\ & - \frac{\widehat{q}^{(2)}(z_1)}{\widehat{b}_1}\frac{z^2}{2} - \sum_{i=2}^{n}\left(\frac{\widehat{q}^{(2)}(z_i)}{\widehat{b}_i} - \frac{\widehat{q}^{(2)}(z_{i-1})}{\widehat{b}_{i-1}} \right) \mathcal{Q}(z - z_i) \, , \end{aligned} \tag{4.42}$$

where, in this case, $\widehat{q}^{(2)}(z)$ is defined by

$$\widehat{q}^{(2)}(z) = -q^{(2)}(z) + q^{(1)}(\ell)\, z + q^{(2)}(\ell) - q^{(1)}(\ell)\, \ell \, . \tag{4.43}$$

Similar relationships to those presented in Eqs. (4.34) and (4.42) can be also derived under different constraint conditions.

4.1.2 Random solution of micropolar Timoshenko-Ehrenfest beam model with material uncertainties in the application framework

In this section, the random fields are defined on a probability space $(\Theta, \mathcal{T}, \mathcal{P})$, and any element of Θ is denoted by θ. The deterministic fields $\bar{e} : z \mapsto \bar{e}(z)$, $\bar{g} : z \mapsto \bar{g}(z)$, and $c : z \mapsto c(z)$ are modeled by the random fields $\bar{E} : \theta \mapsto \left\{ z \mapsto \bar{E}(z, \theta) \right\}$, $\bar{G} : \theta \mapsto \{ z \mapsto \bar{G}(z, \theta) \}$, and $C : \theta \mapsto \{ z \mapsto C(z, \theta) \}$. Hence, the axial stiffness $a : z \mapsto a(z)$, the bending stiffness $b : z \mapsto b(z)$, and the shear stiffness $t : z \mapsto t(z)$ are modeled by the random fields $A : \theta \mapsto \{ z \mapsto A(z, \theta) \}$,

$B : \theta \mapsto \{z \mapsto B(z,\theta)\}$, and $T : \theta \mapsto \{z \mapsto T(z,\theta)\}$. We assume that these fields are stepwise random functions defined into five intervals whose steps are identified by the coordinates $\widehat{z}_2 = \ell/5$, $\widehat{z}_3 = \widehat{z}_2 + \ell/5$, $\widehat{z}_4 = \widehat{z}_3 + \ell/5$, and $\widehat{z}_5 = \widehat{z}_4 + \ell/5$,

$$\bar{E}(z) = \bar{E}_1 + \sum_{i=2}^{5} \left(\bar{E}_i - \bar{E}_{i-1}\right) \mathcal{H}(z - \widehat{z}_i) \ , \tag{4.44}$$

$$\bar{G}(z) = \bar{G}_1 + \sum_{i=2}^{5} \left(\bar{G}_i - \bar{G}_{i-1}\right) \mathcal{H}(z - \widehat{z}_i) \ , \tag{4.45}$$

$$C(z) = C_1 + \sum_{i=2}^{5} (C_i - C_{i-1}) \mathcal{H}(z - \widehat{z}_i) \ . \tag{4.46}$$

We define $\bar{B}_i = \bar{E}_i \iota + C_i \sigma$ and $\bar{T}_i = \bar{G}_i \sigma/\chi$ with $i = 1, 2, \ldots, 5$, and consequently,

$$\begin{aligned} B(z) &= B_1 + \sum_{i=2}^{5} (B_i - B_{i-1}) \mathcal{H}(z - \widehat{z}_i) \\ &= \widehat{B}_1 + \sum_{i=2}^{n} \left(\widehat{B}_i - \widehat{B}_{i-1}\right) \mathcal{H}(z - z_i) \ , \end{aligned} \tag{4.47}$$

$$\begin{aligned} T(z) &= T_1 + \sum_{i=2}^{5} (T_i - T_{i-1}) \mathcal{H}(z - \widehat{z}_i) \\ &= \widehat{T}_1 + \sum_{i=2}^{n} \left(\widehat{T}_i - \widehat{T}_{i-1}\right) \mathcal{H}(z - z_i) \ , \end{aligned} \tag{4.48}$$

where $n = 100$. The displacement fields $w : z \mapsto w(z)$ and $u : z \mapsto u(z)$ are replaced with the random displacement fields $W : \theta \mapsto \{z \mapsto W(z,\theta)\}$ and $U : \theta \mapsto \{z \mapsto U(z,\theta)\}$. Our problem consists in estimating the probability density functions (pdfs) of the random variables $W(z)$ and $U(z)$ given the prior pdfs of $\bar{E}_i$, $\bar{G}_i$ and C_i, and viceversa.

Noninformative prior probabilistic model for random material parameters

We suppose that $\bar{E}_1, \bar{E}_2, \ldots, \bar{E}_5$ are independent positive-valued random variables whose prior probability density functions defined by

$$p_{\bar{E}_i}(\bar{e}_i) = \frac{\mathbb{1}_{\mathbb{R}^+}(\bar{e}_i) \frac{1}{\sqrt{2\pi}\sigma_{\bar{E}_i}} \exp\left\{-\frac{1}{2\sigma^2_{\bar{E}_i}} \left(\bar{e}_i - m_{\bar{E}_i}\right)^2\right\}}{\int_0^{+\infty} \frac{1}{\sqrt{2\pi}\sigma_{\bar{E}_i}} \exp\left\{-\frac{1}{2\sigma^2_{\bar{E}_i}} \left(\bar{e}_i - m_{\bar{E}_i}\right)^2\right\} d\bar{e}_i} \ , \tag{4.49}$$

where $\sigma_{\bar{E}_i}$ and $m_{\bar{E}_i}$ are the standard deviations and mean values of $\bar{E}_i$. In the same way, we suppose that $\bar{G}_1, \bar{G}_2, \ldots, \bar{G}_5$ and $C_1, C_2, \ldots, C_5$ are independent positive-valued random variables whose prior probability density functions are defined by

$$p_{\bar{G}_i}(\bar{g}_i) = \frac{\mathbb{1}_{\mathbb{R}^+}(\bar{g}_i)\, \frac{1}{\sqrt{2\pi}\sigma_{\bar{G}_i}} \exp\left\{-\frac{1}{2\sigma^2_{\bar{G}_i}}\left(\bar{g}_i - m_{\bar{G}_i}\right)^2\right\}}{\int_0^{+\infty} \frac{1}{\sqrt{2\pi}\sigma_{\bar{G}_i}} \exp\left\{-\frac{1}{2\sigma^2_{\bar{G}_i}}\left(\bar{g}_i - m_{\bar{G}_i}\right)^2\right\} d\bar{g}_i}\,, \tag{4.50}$$

$$p_{C_i}(c_i) = \frac{\mathbb{1}_{\mathbb{R}^+}(c_i)\, \frac{1}{\sqrt{2\pi}\sigma_{C_i}} \exp\left\{-\frac{1}{2\sigma^2_{C_i}}\left(c_i - m_{C_i}\right)^2\right\}}{\int_0^{+\infty} \frac{1}{\sqrt{2\pi}\sigma_{C_i}} \exp\left\{-\frac{1}{2\sigma^2_{C_i}}\left(c_i - m_{C_i}\right)^2\right\} dc_i}\,, \tag{4.51}$$

where $\sigma_{\bar{G}_i}$ and $m_{\bar{G}_i}$ are the standard deviations and mean values of $\bar{G}_i$, and σ_{C_i} and m_{C_i} are the standard deviations and mean values of C_i. Assuming that the random variables $\bar{E}_i$, $\bar{G}_i$, and C_i are independent, the prior model of the joint probability density function of $\bar{E}_i$, $\bar{G}_i$, and C_i is written as

$$p_{\bar{E}_i\bar{G}_iC_i}(\bar{e}_i, \bar{g}_i, c_i) = p_{\bar{E}_i}(\bar{e}_i)\, p_{\bar{G}_i}(\bar{g}_i)\, p_{C_i}(c_i)\ . \tag{4.52}$$

Geometry, load, deterministic and random mechanical properties

Simply supported and clamped macro and microbeams are studied in the following. The values of the geometry parameters are $d_1^{\text{macro}} = 3\times10^{-1}\,\text{m}$, $d_2^{\text{macro}} = 6\times10^{-1}\,\text{m}$, and $\ell^{\text{macro}} = 5\,d_2^{\text{macro}}$ and $d_1^{\text{micro}} = 3\times10^{-6}\,\text{m}$, $d_2^{\text{micro}} = 6\times10^{-6}\,\text{m}$, and $\ell^{\text{micro}} = 5\,d_2^{\text{micro}}$, where d_1^{macro} and d_1^{micro} denote the thickness of cross-sections, d_2^{macro} and d_2^{micro} denote the bases of cross-sections, and ℓ^{macro} and ℓ^{micro} the length of the beams. Concerning the means values and standard deviations of $\bar{E}_i$, $\bar{G}_i$, and C_i, we refer to Tables 1 and 2, where the following reference values are chosen

$$\mu_{\bar{E}_r} = 1.76\times10^{11}\,\text{Pa} \quad , \quad \mu_{\bar{G}_r} = 6.7692\times10^{10}\,\text{Pa} \quad , \quad \mu_{C_r} = 8.6\times10^{10}\,\text{N}\,. \tag{4.53}$$

The applied external load is $q(z) = 1\times10^{6}\,\text{N/m}$ for microbeams and $q(z) = 1\times10^{3}\,\text{N/m}$ for microbeams. The shear correction factor χ is chosen equal to 1 for simplicity.

Stochastic solver

The stochastic solver used is based on the Monte Carlo numerical simulation method. The steps of this stochastic are defined below.

Table 4.1 Dimensionless mean values of the random variables $\bar{E}_i$, $\bar{G}_i$, $\bar{C}_i$ with $i = 1, 2, \ldots, 5$.

$\mu_{\bar{E}_1}/\mu_{\bar{E}_r}$	$\mu_{\bar{E}_2}/\mu_{\bar{E}_r}$	$\mu_{\bar{E}_3}/\mu_{\bar{E}_r}$	$\mu_{\bar{E}_4}/\mu_{\bar{E}_r}$	$\mu_{\bar{E}_5}/\mu_{\bar{E}_r}$
2.5 %	1 %	2 %	1.5 %	2.5 %
$\mu_{\bar{G}_1}/\mu_{\bar{G}_r}$	$\mu_{\bar{G}_2}/\mu_{\bar{G}_r}$	$\mu_{\bar{G}_3}/\mu_{\bar{G}_r}$	$\mu_{\bar{G}_4}/\mu_{\bar{G}_r}$	$\mu_{\bar{G}_5}/\mu_{\bar{G}_r}$
2.5 %	1 %	2 %	1.5 %	2.5 %
μ_{C_1}/μ_{C_r}	μ_{C_2}/μ_{C_r}	μ_{C_3}/μ_{C_r}	μ_{C_4}/μ_{C_r}	μ_{C_5}/μ_{C_r}
2.5 %	1 %	2 %	1.5 %	2.5 %

Table 4.2 Coefficients of variation $\mathrm{Cv}_{\bar{E}_i}$, $\mathrm{Cv}_{\bar{G}_i}$, and Cv_{C_i} of the random variables $\bar{E}_i$, $\bar{G}_i$, and C_i with i=1,2 , ... , 5.

$\mathrm{Cv}_{\bar{E}_1}$	$\mathrm{Cv}_{\bar{E}_2}$	$\mathrm{Cv}_{\bar{E}_3}$	$\mathrm{Cv}_{\bar{E}_4}$	$\mathrm{Cv}_{\bar{E}_5}$
0.9	0.8	0.85	0.9	0.95
$\mathrm{Cv}_{\bar{G}_1}$	$\mathrm{Cv}_{\bar{G}_2}$	$\mathrm{Cv}_{\bar{G}_3}$	$\mathrm{Cv}_{\bar{G}_4}$	$\mathrm{Cv}_{\bar{G}_5}$
0.9	0.8	0.85	0.9	0.95
Cv_{C_1}	Cv_{C_2}	Cv_{C_3}	Cv_{C_4}	Cv_{C_5}
0.9	0.8	0.85	0.9	0.95

1. Generation of m independent realizations $X_i(\theta_1)$, $X_i(\theta_2), \ldots,$ $X_i(\theta_m)$ of the random variables X_i using the probability distributions defined in Eq. (4.52) in which $X_i = (\bar{E}_i, \bar{G}_i, \bar{C}_i)$.

2. Computation of m independent realizations $U(\theta_1), U(\theta_2), \ldots, U(\theta_m)$ using Eqs. (4.34) and (4.42) for both micro and macrobeams.

3. Estimation of the pdfs of the quantities of interest that are limited to the displacements at points $\widetilde{z}_i$, with $i = 1, 2, \ldots, 10$, such that $0 < \widetilde{z}_1 < \widetilde{z}_6 < \widehat{z}_1$, $\widehat{z}_1 < \widetilde{z}_2 < \widetilde{z}_7 < \widehat{z}_2$, $z_2 < \widetilde{z}_3 < \widetilde{z}_8 < \widehat{z}_4$, $z_4 < \widetilde{z}_4 < \widetilde{z}_9 < \widehat{z}_5$, and $\widehat{z}_5 < \widetilde{z}_5 < \widetilde{z}_{10} < \ell$. Using the realizations computed in step 2, the probability density functions of the displacements $U_i = u(X_1, X_2, \ldots, X_5, \widetilde{z}_i)$ with $i = 1, 2, \ldots, 10$ have been estimated with the Kernel Density Estimation (KDE) method from nonparametric statistics.

The same steps are adapted for the solution of the inverse problem, which consists in giving the pdfs of the displacements in several points of the beam axis and in estimating the pdfs of the material parameters in the same points.

Uncertainty propagation

For the simply supported micropolar macrobeams, simply supported micropolar microbeams, cantilever micropolar macrobeams, and cantilever micropolar microbeams, we show in

Fig. 4.1 the probability density functions (pdfs) of the vertical displacements obtained in the 4-th interval of the beams denoted by U_4. The pdfs are estimated by using the realizations computed with the Monte Carlo (MC) simulation method and the kernel density estimation (KDE) method. Once the direct problem is solved, starting from the pdfs of the displacements,

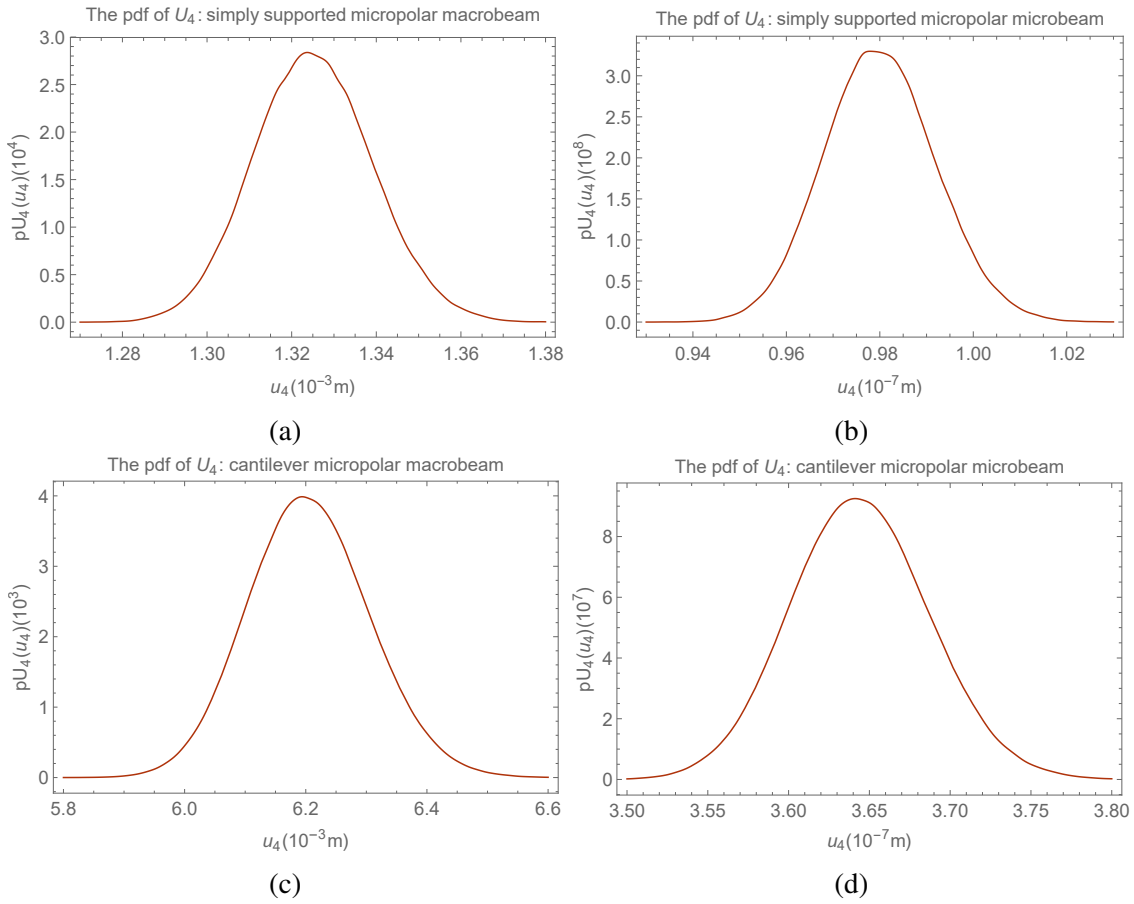

Fig. 4.1 Graph $u_4 \mapsto p_{U_4}(u_4)$ of the pdf of U_4 obtained for (a) simply supported macrobeam (b) simply supported microbeam (c) cantilever macrobeam (d) cantilever microbeam. The pdfs have been built by means of MC numerical simulations and the KDE method. The random variable U_4 model the displacement at $\widetilde{z}_4 = 3\ell/5 + 1/9\ell/5$ of the 4-th interval of the beams.

the pdfs of B_i and T_i are derived. As shown in Fig. 4.2, by recalling that $B_i = \bar{E}_i \iota + C_i \sigma$ and $T_i = \bar{G}_i \sigma/\chi$, we can conclude that

- if a macrobeam is analyzed, the pdf of B_i/ι approximates the pdf of $\bar{E}_i$;
- if a microbeam is analyzed, the pdf of B_i/σ approximates the pdf of C_i;
- in both cases, the pdf of $\bar{T}_i\chi/\sigma$ approximates the pdf of $\bar{G}_i$;

- if M_{Γ_i} is the random variable associated with μ_{Γ_i} (see Eq. (4.1)), the pdf of M_{Γ_i} can be obtained using the relationship,

$$p_{M_{\Gamma i}}\left(\mu_{\Gamma i}\right) = \frac{1}{2} p_{C_i}\left(\frac{\mu_{\Gamma i}}{2}\right) . \tag{4.54}$$

We want to underline that M_{Γ_i} is a material parameter related to the 3D mechanical behavior of the micropolar continuum.

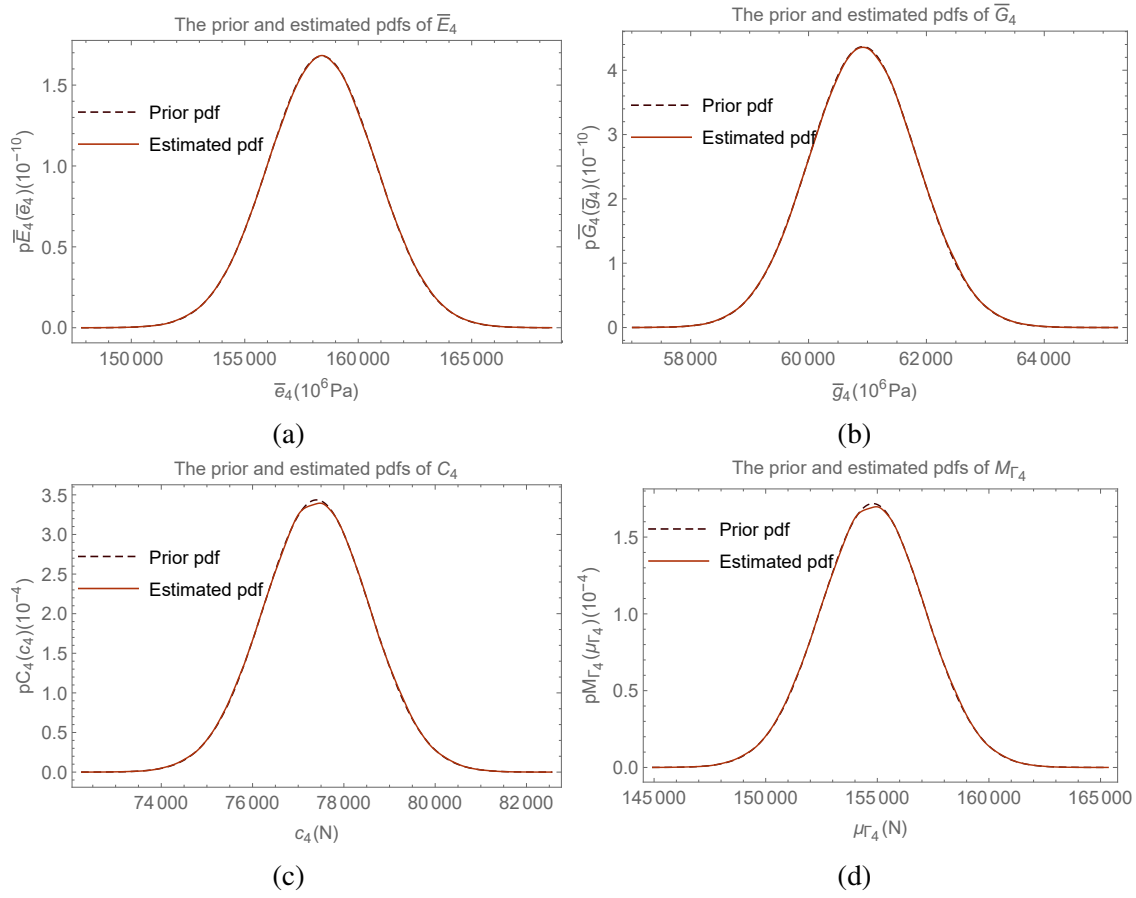

Fig. 4.2 (a) Comparison between the graph $\bar{e}_4 \mapsto p_{\bar{E}_4}(\bar{e}_4)$ of the prior pdf of $\bar{E}_4$ (dashed line) and the graph $\bar{b}_4/\iota \mapsto p_{B_4/\iota}(b_4/\iota) \approx p_{\bar{E}_4}(\bar{e}_4)$ obtained by analyzing the macrobeam (solid line). (b) Comparison between the graph $\bar{g}_4 \mapsto p_{\bar{G}_4}(\bar{g}_4)$ of the prior pdf of $\bar{G}_4$ (dashed line) and the graph $\bar{t}_4\chi/\sigma \mapsto p_{T_4\chi/\sigma}(t_4\chi/\sigma) \approx p_{\bar{G}_4}(\bar{g}_4)$ obtained by analyzing the macro or microbeam (solid line). (c) Comparison between the graph $c_4 \mapsto p_{C_4}(c_4)$ of the prior pdf of C_4 (dashed line) and the graph $\bar{b}_4/\sigma \mapsto p_{B_4/\sigma}(c_4/\sigma) \approx p_{C_4}(c_4)$ obtained by analyzing the microbeam (solid line). (d) Graph $\mu_{\Gamma_4} \mapsto p_{M_{\Gamma_4}}(\mu_{\Gamma_4})$ of the pdf of M_{Γ_4} obtained by means of Eq. (4.54) and the prior (dashed line) and identified (solid line) pdfs of C_4. The pdfs have been estimated using MC numerical simulations and the KDE method.

4.2 Sensitivity of a particle-based homogeneous and isotropic second-gradient continuum model with respect to uncertain parameters

This section concerns the probabilistic analysis of particle-based materials. More precisely, this section is devoted to the stochastic modeling of the particle-based geometric and material microscale parameters associated with particle-pair interactions of an existing particle-based second gradient model. Such an issue is addressed with a probabilistic methodology that relies on the maximum entropy (MaxEnt) principle from information theory. After defining and improving the chosen particle-based second gradient continuum model, it is shown that for micro-homogeneous and micro-isotropic materials, the involved microscale parameters turn out to be statistically independent. More precisely, the particle-pair distance between two consecutive particles is a uniformly distributed random variable and the specific microscale stiffness parameters are Gamma-distributed random variables. For illustration purposes, a micro-homogeneous, micro-isotropic, macro-homogeneous, and macro-isotropic 2D concrete plate subjected to an axial load is considered. A stochastic solver based on Monte Carlo numerical simulations is chosen whose convergence is studied. Finally, uncertainties propagation is discussed, and statistical fluctuations in the macro mechanical response are found to be significant.

Notation

Below A, B, C, D, E, F, and i are integers belonging to $\{1,2,3\}$.

A lowercase letter such as x, η, u is a real deterministic variable except when used as an integer index as i, j, etc. Greek letters α, β, η and τ are neither deterministic variables or integers as subscripts.

A boldface lower case letter such as $\boldsymbol{x}$, $\boldsymbol{\eta}$, $\boldsymbol{u}$ is a real deterministic vector.

An upper case letter such as X, H, U is a real random variable except when used as an integer index as A, B, etc.

A boldface upper case letter such as $\boldsymbol{X}$, $\boldsymbol{H}$, $\boldsymbol{U}$ is a vector random variable.

A lower case letter between brackets such as $[x]$, $[\eta]$, $[u]$ is a real deterministic second-order tensor.

A boldface upper case letter between brackets such as $[\boldsymbol{X}]$, $[\boldsymbol{H}]$, $[\boldsymbol{U}]$ is a real random second-order tensor.

A lower case Gothic letter between brackets such as $[\mathfrak{x}]$, $[\mathfrak{h}]$, $[\mathfrak{u}]$ is a real deterministic third-order tensor.

A boldface upper case Gothic letter between brackets such as $[\boldsymbol{\mathfrak{X}}]$, $[\boldsymbol{\mathfrak{H}}]$, $[\boldsymbol{\mathfrak{U}}]$ is a real random third-order tensor.

A lower case letter between two brackets such as $[[x]]$, $[[z]]$, $[[u]]$ is a real deterministic fourth-order tensor.

A lower case Gothic letter between two brackets such as $[[\mathfrak{x}]]$, $[[\mathfrak{h}]]$, $[[\mathfrak{u}]]$ is a real deterministic fifth-order tensor.

A lower case letter between three brackets such as $[[[x]]]$, $[[[h]]]$, $[[[u]]]$ is a real deterministic sixth-order tensor.

$\mathbb{E}$: Mathematical expectation.

The Levi-Civita tensor calculus is used. Indices denoted by upper case letters are chosen to indicate components in the initial (or Lagrangian) configuration and lowercase letters to indicate components in the Eulerian (or current) one. Summation over the repeated Latin indices is used. There is no summation over repeated Greek indices. Superscripts denote the contravariant components, and subscripts denote the covariant ones.

$\|\boldsymbol{x}\|$: Euclidean norm of $\boldsymbol{x} \in \mathbb{R}^n$

$\|A\|$: $\mathrm{Sup}_{\|\boldsymbol{x}\|\leq 1} \|A\boldsymbol{x}\|$ operator norm of linear operator A.

$[g]_{DC}$: component (D, C) of the metric tensor $[g]$.

$[\delta]^A_B$: component (A, B) of the second-order identity tensor $[I]$.

$[x]^T$: transpose of the second-order tensor $[x]$, and $\left[x^T\right]$ is the second-order tensor of the transposition.

$\mathbb{1}_B$: indicator function of a set B.

r^i: component i of the deterministic configuration field $\boldsymbol{r}$.

v^i: component i of the deterministic displacement field $\boldsymbol{v}$.

$[f]^i_A$: deterministic gradient of the configuration field $[f]$.

$\widehat{n}^A$: component A of the unit vector $\widehat{\boldsymbol{n}}$ defining the orientaton of one pair (α,β).

u^C: component C deterministic objective deformation vector $\boldsymbol{u}$.

ϕ: deterministic specific deformation energy

w: deterministic deformation energy

$[e]^C_B$: component (C,B) of the deterministic Cauchy-Green tensor $[e]$.

$[\mathfrak{h}]^D_{EF}$: component (D,E,F) of the deterministic second-gradient deformation tensor $[\mathfrak{h}]$.

4.2.1 Defining a deterministic particle-based continuum

Discrete model

We summarize the model proposed in [13, 136, 104]. Let β be a rigid particle and let us build a discrete set of n rigid particles at distance ℓ from β (same arguments can be generalized for ℓ variable along the spatial directions). Let us consider the discrete system of rigid particles obtained by assembling s of these sets. It is a discrete grid of rigid particles within a bounded domain $\mathcal{B}$ of $\mathbb{R}^3$ such that the distance between two consecutive particles in the grid is ℓ. Although any particle shape is acceptable, particle sizes must be sufficiently small to justify the passage from the discrete to the equivalent continuum model in Subsection 4.2.1. Let α and β be two consecutive particles in the grid, whose coordinate vectors are $\boldsymbol{q}_\alpha = (q^1_\alpha, q^2_\alpha, q^3_\alpha)$ and $\boldsymbol{q}_\beta = (q^1_\beta, q^2_\beta, q^3_\beta)$ in a given fixed coordinate system defined by a generic basis of $\mathbb{R}^3$. In this section, stochastic considerations are introduced, wherein the symbol $\boldsymbol{q}$ is preferred for denoting the Lagrangian coordinates, as the symbol X is reserved for the random quantities. We define $\boldsymbol{r} = (r^1, r^2, r^3) : \boldsymbol{q} \mapsto \boldsymbol{r}(\boldsymbol{q})$ as the configuration field and we introduce the second-order tensor valued-function $[f]$ such as

$$[f] : \boldsymbol{q} \mapsto [f(\boldsymbol{q})] = \{[f(\boldsymbol{q})]^i_A = \frac{\partial r^i(\boldsymbol{q})}{\partial q^A}, i = 1,2,3; A = 1,2,3\} \tag{4.55}$$

and we define $[f_\beta] = [f(\boldsymbol{q}_\beta)]$. Let $\boldsymbol{u}_{\alpha\beta}$ be the objective deformation vector such that [1]

$$\boldsymbol{u}_{\alpha\beta} = \left[f^T_\beta\right]\left(\boldsymbol{r}\left(\boldsymbol{q}_\alpha\right) - \boldsymbol{r}\left(\boldsymbol{q}_\beta\right)\right) - \left(\boldsymbol{q}_\alpha - \boldsymbol{q}_\beta\right) . \tag{4.56}$$

[1] In components: $u^C_{\alpha\beta} = \left[f^T_\beta\right]^C_i \left(r^i\left(\boldsymbol{q}_\alpha\right) - r^i\left(\boldsymbol{q}_\beta\right)\right) - \left(q^C_\alpha - q^C_\beta\right)$

Truncated at the second-order, the Taylor expansion of $\boldsymbol{r}$ in the neighborhood of $\boldsymbol{q}_\beta$ yields

$$r^i\left(\boldsymbol{q}_\alpha\right) \approx r^i\left(\boldsymbol{q}_\beta\right) + \left.\frac{\partial r^i(\boldsymbol{q})}{\partial q^A}\right|_{\boldsymbol{q}=\boldsymbol{q}_\beta}\left(q_\alpha^A - q_\beta^A\right) + \frac{1}{2}\left.\frac{\partial^2 r^i(\boldsymbol{q})}{\partial q^A \partial q^B}\right|_{\boldsymbol{q}=\boldsymbol{q}_\beta}\left(q_\alpha^A - q_\beta^A\right)\left(q_\alpha^B - q_\beta^B\right) . \quad (4.57)$$

Let $\widehat{\boldsymbol{n}}_{\alpha\beta}$ be the unit vector defining the orientation of one pair (α,β) of two consecutive particles such as

$$\boldsymbol{q}_\alpha - \boldsymbol{q}_\beta = \widehat{\boldsymbol{n}}_{\alpha\beta}\,\ell \, . \quad (4.58)$$

Substituting Eqs. (4.57) and (4.58) in Eq. (4.56) yields

$$\begin{aligned} u_{\alpha\beta}^C &= \left[f_\beta^T\right]_i^C \left(\left[f_\beta\right]_B^i \widehat{n}_{\alpha\beta}^B \ell + \frac{1}{2}\left.\frac{\partial^2 r^i(\boldsymbol{q})}{\partial q^A \partial q^B}\right|_{\boldsymbol{q}=\boldsymbol{q}_\beta} \widehat{n}_{\alpha\beta}^B \ell\, \widehat{n}_{\alpha\beta}^A \ell \right) - \left[\delta\right]_B^C \widehat{n}_{\alpha\beta}^B \ell \\ &= \left(\left[f_\beta^T\right]_i^C \left[f_\beta\right]_B^i - \left[\delta\right]_B^C \right)\left(\widehat{n}_{\alpha\beta}^B \ell\right) + \frac{1}{2}\left[f_\beta^T\right]_i^C \left.\frac{\partial^2 r^i(\boldsymbol{q})}{\partial q^A \partial q^B}\right|_{\boldsymbol{q}=\boldsymbol{q}_\beta} \widehat{n}_{\alpha\beta}^B \widehat{n}_{\alpha\beta}^A \ell^2 \, . \end{aligned} \quad (4.59)$$

Let us define the two deformation tensors $[e] : \boldsymbol{q} \mapsto [e]\,(\boldsymbol{q})$ and $[\mathfrak{h}] : \boldsymbol{q} \mapsto [\mathfrak{h}]\,(\boldsymbol{q})$ such that

$$[e]_B^C = \frac{1}{2}\left(\left[f^T\right]_i^C \left[f\right]_B^i - \left[\delta\right]_B^C \right) , \quad (4.60)$$

$$[\mathfrak{h}]_{AB}^C = \left[f^T\right]_i^C \frac{\partial^2 r^i}{\partial q^A \partial q^B} \, . \quad (4.61)$$

We introduce the notation $\left[e_\beta\right] = [e]\left(\boldsymbol{q}_\beta\right)$ and $\left[\mathfrak{h}_\beta\right] = [\mathfrak{h}]\left(\boldsymbol{q}_\beta\right)$. The tensor $[e]$ is the Cauchy–Green tensor. Substituting Eqs. (4.60) and (4.61) into Eq. (4.59) yields

$$\begin{aligned} u_{\alpha\beta}^C &= 2\left[e_\beta\right]_B^C \widehat{n}_{\alpha\beta}^B \ell + \frac{1}{2}\left[f_\beta^T\right]_i^C \left.\frac{\partial^2 r^i(\boldsymbol{q})}{\partial q^A \partial q^B}\right|_{\boldsymbol{q}=\boldsymbol{q}_\beta} \widehat{n}_{\alpha\beta}^B \widehat{n}_{\alpha\beta}^A \ell^2 \\ &= 2\left[e_\beta\right]_B^C \widehat{n}_{\alpha\beta}^B \ell + \frac{1}{2}\left[\mathfrak{h}_\beta\right]_{AB}^C \widehat{n}_{\alpha\beta}^B \widehat{n}_{\alpha\beta}^A \ell^2 \, . \end{aligned} \quad (4.62)$$

Eq. (4.61) can be written (see [37]) as

$$\left[\mathfrak{h}_\beta\right]_{AB}^C = \frac{1}{2}\left[g\right]^{DC}\left(\left.\frac{\partial\left[e\right]_{AD}(\boldsymbol{q})}{\partial q^B}\right|_{\boldsymbol{q}=\boldsymbol{q}_\beta} + \left.\frac{\partial\left[e\right]_{BD}(\boldsymbol{q})}{\partial q^A}\right|_{\boldsymbol{q}=\boldsymbol{q}_\beta} - \left.\frac{\partial\left[e\right]_{BA}(\boldsymbol{q})}{\partial q^D}\right|_{\boldsymbol{q}=\boldsymbol{q}_\beta} \right) . \quad (4.63)$$

Let us define the elastic energy function $\Delta w_{\alpha\beta} : \boldsymbol{u}_{\alpha\beta} \mapsto \Delta w_{\alpha\beta}\left(\boldsymbol{u}_{\alpha\beta}\right)$ related to the interaction of the pair (α,β) of consecutive particles. Since $\boldsymbol{u}_{\alpha\beta}$ is an objective function, it is considered as a measure of deformation (see Eq. (4.56)). Among all possible choices for the function

$\Delta w_{\alpha\beta}$, it is chosen such that

$$\Delta w_{\alpha\beta}\left(\boldsymbol{u}_{\alpha\beta}\right) = \Delta w_{\alpha\beta\eta}\left(\boldsymbol{u}_{\alpha\beta}\right) + \Delta w_{\alpha\beta\tau}\left(\boldsymbol{u}_{\alpha\beta}\right) \ , \tag{4.64}$$

in which

$$\Delta w_{\alpha\beta\eta}\left(\boldsymbol{u}_{\alpha\beta}\right) = \frac{1}{2}\, k_{\alpha\beta\eta} \left\|\boldsymbol{u}_{\alpha\beta\eta}\right\|^2 \quad , \quad \Delta w_{\alpha\beta\tau}\left(\boldsymbol{u}_{\alpha\beta}\right) = \frac{1}{2}\, k_{\alpha\beta\tau} \left\|\boldsymbol{u}_{\alpha\beta\tau}\right\|^2 \ , \tag{4.65}$$

and where

$$\boldsymbol{u}_{\alpha\beta\eta} = \frac{1}{2}\left(\boldsymbol{u}_{\alpha\beta}\cdot\widehat{\boldsymbol{n}}_{\alpha\beta}\right)\widehat{\boldsymbol{n}}_{\alpha\beta} \quad , \quad \boldsymbol{u}_{\alpha\beta\tau} = \boldsymbol{u}_{\alpha\beta} - \left(\boldsymbol{u}_{\alpha\beta}\cdot\widehat{\boldsymbol{n}}_{\alpha\beta}\right)\widehat{\boldsymbol{n}}_{\alpha\beta} \ , \tag{4.66}$$

in which $k_{\alpha\beta\eta}$ and $k_{\alpha\beta\tau}$ are two given positive local microscale material parameters, and in which $\boldsymbol{u}_{\alpha\beta\eta}$ and $\boldsymbol{u}_{\alpha\beta\tau}$ are the vector decomposition of the deformation vector $\boldsymbol{u}_{\alpha\beta}$ parallel and orthogonal to $\widehat{\boldsymbol{n}}_{\alpha\beta}$, respectively. The vector decomposition of $\boldsymbol{u}_{\alpha\beta}$ in $2\boldsymbol{u}_{\alpha\beta\eta}$ and $\boldsymbol{u}_{\alpha\beta\tau}$ with respect to the local coordinates system $\left(q^{1(\mathrm{lc})}, q^{2(\mathrm{lc})}, q^{3(\mathrm{lc})}\right)$ is shown in Fig. 4.3. For technical

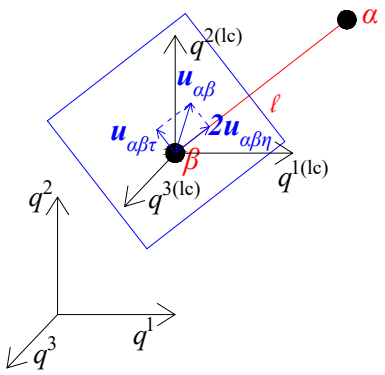

Fig. 4.3 Vector decomposition of $\boldsymbol{u}_{\alpha\beta}$ in the local coordinates system described by $\boldsymbol{q}^{(\mathrm{lc})}=(q^{1(\mathrm{lc})}, q^{2(\mathrm{lc})}, q^{3(\mathrm{lc})})$, in which $2\boldsymbol{u}_{\alpha\beta\eta}$ is the projection of $\boldsymbol{u}_{\alpha\beta}$ with respect to $\widehat{\boldsymbol{n}}_{\alpha\beta}$ and $\boldsymbol{u}_{\alpha\beta\tau}$ is the projection on the plane defined by $\boldsymbol{u}_{\alpha\beta}$ and $\boldsymbol{u}_{\alpha\tau}$. Particles can have different sizes and different shapes. Any particle shape is admissible. Particle sizes need to be small enough to pass from the discrete to the equivalent continuum model. The quantities $\boldsymbol{u}_{\alpha\beta}$, $\boldsymbol{u}_{\alpha\beta\eta}$, and $\boldsymbol{u}_{\alpha\beta\tau}$ have been defined in Eqs. (4.61) and (4.66). They represent deformation measures of the particle-pair (α,β).

needs, no coupling energetic term, such as $\left\|\boldsymbol{u}_{\alpha\beta\eta}\right\| \left\|\boldsymbol{u}_{\alpha\beta\tau}\right\|$, is considered between $\boldsymbol{u}_{\alpha\beta\eta}$ and $\boldsymbol{u}_{\alpha\beta\tau}$. It allows us to state a relationship between the microscale material parameters, $k_{\alpha\beta\eta}$ and $k_{\alpha\beta\tau}$, and the macroscale material parameters, and to obtain an equivalent second-gradient continuum model for particle-based based materials that generalizes the classical (or Cauchy) continuum model. Due to the interactions between all the n consecutive particles of β, the

total energy Δw_β is written as

$$\Delta w_\beta = \sum_{\alpha=1_\beta}^{n_\beta} \Delta w_{\alpha\beta}\left(\boldsymbol{u}_{\alpha\beta}\right) = \sum_{\alpha=1_\beta}^{n_\beta} \left(\frac{1}{2} k_{\alpha\beta\eta} \left\| \boldsymbol{u}_{\alpha\beta\eta} \right\|^2 + \frac{1}{2} k_{\alpha\beta\tau} \left\| \boldsymbol{u}_{\alpha\beta\tau} \right\|^2 \right) , \tag{4.67}$$

Finally, the total energy related to the considered system of particles is equal to

$$w = \sum_{\beta=1}^{s} \sum_{\alpha=1_\beta}^{n_\beta} \Delta w_{\alpha\beta} = \sum_{\beta=1}^{s} \sum_{\alpha=1_\beta}^{n_\beta} \left(\frac{1}{2} k_{\alpha\beta\eta} \left\| \boldsymbol{u}_{\alpha\beta\eta} \right\|^2 + \frac{1}{2} k_{\alpha\beta\tau} \left\| \boldsymbol{u}_{\alpha\beta\tau} \right\|^2 \right) . \tag{4.68}$$

Equivalent continuum model

If the distance ℓ between two consecutive particles is small enough with respect to the smaller characteristic dimension of domain $\mathcal{B}$, we can replace the discrete model by an equivalent continuum model. Let $\widehat{\boldsymbol{n}} : \boldsymbol{\omega} \mapsto \widehat{\boldsymbol{n}}\left(\boldsymbol{\omega}\right)$ be the orientation field in which $\boldsymbol{\omega} \in \Omega = [0, \pi] \times [0, 2\pi]$ and let $\boldsymbol{u} : \boldsymbol{q} \mapsto \boldsymbol{u}\left(\boldsymbol{q}\right)$ such that

$$\begin{aligned} u^C(\boldsymbol{q}, \boldsymbol{\omega}) &= 2\, [e]_B^C(\boldsymbol{q})\, \widehat{n}^B(\boldsymbol{\omega})\, \ell + \frac{1}{2} \left[f^T(\boldsymbol{q}) \right]_i^C \frac{\partial^2 r^i(\boldsymbol{q})}{\partial q^A \partial q^B} \widehat{n}^B(\boldsymbol{\omega})\, \widehat{n}^A(\boldsymbol{\omega})\, \ell^2 \\ &= 2\, [e]_B^C(\boldsymbol{q})\, \widehat{n}^B(\boldsymbol{\omega})\, \ell + \frac{1}{2}\, [\mathfrak{h}]_{AB}^C(\boldsymbol{q})\, \widehat{n}^B(\boldsymbol{\omega})\, \widehat{n}^A(\boldsymbol{\omega})\, \ell^2 . \end{aligned} \tag{4.69}$$

For the continuum model, the deformation energy w is written as

$$\begin{aligned} w &= \int_{\mathcal{B}} \phi\left(\boldsymbol{q}\right) d\boldsymbol{q} = \int_{\mathcal{B}} \int_{\Omega} \psi\left(\boldsymbol{\omega}, \boldsymbol{q}\right) d\boldsymbol{\omega}\, d\boldsymbol{q} \\ &= \int_{\mathcal{B}} \int_{\Omega} \left(\frac{1}{2} \widetilde{k}_\eta\left(\boldsymbol{\omega}, \boldsymbol{q}\right) \left\| \boldsymbol{u}_\eta\left(\boldsymbol{\omega}, \boldsymbol{q}\right) \right\|^2 + \frac{1}{2} \widetilde{k}_\tau\left(\boldsymbol{\omega}, \boldsymbol{q}\right) \left\| \boldsymbol{u}_\tau\left(\boldsymbol{\omega}, \boldsymbol{q}\right) \right\|^2 \right) d\boldsymbol{\omega}\, d\boldsymbol{q} , \end{aligned} \tag{4.70}$$

where $\phi : \boldsymbol{q} \mapsto \phi\left(\boldsymbol{q}\right)$ is the specific deformation energy and $\psi : (\boldsymbol{\omega}, \boldsymbol{q}) \mapsto \psi(\boldsymbol{\omega}, \boldsymbol{q})$ is the specific deformation energy per unit direction, such that

$$\phi\left(\boldsymbol{q}\right) = \int_{\Omega} \psi\left(\boldsymbol{\omega}, \boldsymbol{q}\right) d\boldsymbol{\omega} , \quad \psi\left(\boldsymbol{\omega}, \boldsymbol{q}\right) = \frac{1}{2} \widetilde{k}_\eta\left(\boldsymbol{\omega}, \boldsymbol{q}\right) \left\| \boldsymbol{u}_\eta\left(\boldsymbol{\omega}, \boldsymbol{q}\right) \right\|^2 + \frac{1}{2} \widetilde{k}_\tau\left(\boldsymbol{\omega}, \boldsymbol{q}\right) \left\| \boldsymbol{u}_\tau\left(\boldsymbol{\omega}, \boldsymbol{q}\right) \right\|^2 , \tag{4.71}$$

in which $\boldsymbol{u}_\eta : (\boldsymbol{\omega}, \boldsymbol{q}) \mapsto \boldsymbol{u}_\eta(\boldsymbol{\omega}, \boldsymbol{q})$ and $\boldsymbol{u}_\tau : \boldsymbol{q} \mapsto \boldsymbol{u}_\tau(\boldsymbol{\omega}, \boldsymbol{q})$ are such that

$$\boldsymbol{u}_\eta\left(\boldsymbol{\omega}, \boldsymbol{q}\right) = \frac{1}{2} \left(\boldsymbol{u}\left(\boldsymbol{q}\right) \cdot \widehat{\boldsymbol{n}}\left(\boldsymbol{\omega}\right) \right) \widehat{\boldsymbol{n}}\left(\boldsymbol{\omega}\right) \quad , \quad \boldsymbol{u}_\tau\left(\boldsymbol{\omega}, \boldsymbol{q}\right) = \boldsymbol{u}\left(\boldsymbol{q}\right) - \boldsymbol{u}_\eta\left(\boldsymbol{\omega}, \boldsymbol{q}\right) . \tag{4.72}$$

The mappings $\widetilde{k}_\eta : (\boldsymbol{\omega}, \boldsymbol{q}) \mapsto \widetilde{k}_\eta(\boldsymbol{\omega}, \boldsymbol{q})$ and $\widetilde{k}_\tau : (\boldsymbol{\omega}, \boldsymbol{q}) \mapsto \widetilde{k}_\tau(\boldsymbol{\omega}, \boldsymbol{q})$ are the specific stiffness fields per unit direction. The specific deformation energy $\phi(\boldsymbol{q})$ is written as

$$\begin{aligned}\phi(\boldsymbol{q}) = \frac{1}{2}\,[[c]]^{BL}_{CM}(\boldsymbol{q})\,[e]^{C}_{B}(\boldsymbol{q})\,[e]^{M}_{L}(\boldsymbol{q}) + \frac{1}{2}\,[[\mathfrak{c}]]^{BEF}_{CD}(\boldsymbol{q})\,[e]^{C}_{B}(\boldsymbol{q})\,[\mathfrak{h}]^{D}_{EF}(\boldsymbol{q}) \\ + \frac{1}{2}\,[[[a]]]^{ABFL}_{CM}(\boldsymbol{q})\,[\mathfrak{h}]^{C}_{AB}(\boldsymbol{q})\,[\mathfrak{h}]^{M}_{FL}(\boldsymbol{q})\ ,\end{aligned} \tag{4.73}$$

in which $[[c]]$, $[[[a]]]$ and $[[\mathfrak{c}]]$ are the tensors of the material parameters that are detailed in [13] and where $[[c]]$ is the classical fourth-order tensor of material parameters.

Case of a homogeneous and isotropic equivalent continuum model

Let us call "micro-homogeneous" a continuum characterized by constant specific microscale stiffness fields along spatial direction $\boldsymbol{q}$, *i.e.*, $\widetilde{k}_\eta(\boldsymbol{\omega}, \boldsymbol{q}) = \widetilde{k}^{(hom)}_\eta(\boldsymbol{\omega})$ and $\widetilde{k}_\tau(\boldsymbol{\omega}, \boldsymbol{q}) = \widetilde{k}^{(hom)}_\tau(\boldsymbol{\omega})$. Let us call "micro-isotropic" a continuum in which the specific microscale stiffness fields are constant along the direction of interaction $\boldsymbol{\omega}$, *i.e*, $\widetilde{k}_\eta(\boldsymbol{\omega}, \boldsymbol{q}) = k^{(iso)}_\eta(\boldsymbol{q})$ and $\widetilde{k}_\tau(\boldsymbol{\omega}, \boldsymbol{q}) = k^{(iso)}_\tau(\boldsymbol{q})$. If the continuum is micro-homogeneous and micro-isotropic, we have $\widetilde{k}_\eta(\boldsymbol{\omega}, \boldsymbol{q}) = k_\eta$ and $\widetilde{k}_\tau(\boldsymbol{\omega}, \boldsymbol{q}) = k_\tau$, where k_η and k_τ belongs to $\mathbb{R}^+$. At the macroscale, choosing the coordinate system defined by the canonical (or standard) basis of $\mathbb{R}^3$, it is proven in [13, 136, 104] that the homogeneous and isotropic continuum is characterized by the specific deformation energy $\phi(\boldsymbol{q})$ defined by

$$\begin{aligned}\phi(\boldsymbol{q}) = \xi_2\,[e]^{A}_{B}(\boldsymbol{q})\,[e]^{B}_{A}(\boldsymbol{q}) + \frac{1}{2}\xi_1\,[e]^{A}_{A}(\boldsymbol{q})\,[e]^{B}_{B}(\boldsymbol{q}) \\ + 2\xi_3\,[\mathfrak{h}]^{A}_{AB}(\boldsymbol{q})\,[\mathfrak{h}]^{B}_{CC}(\boldsymbol{q}) + \frac{1}{2}\xi_4\,[\mathfrak{h}]^{A}_{AB}(\boldsymbol{q})\,[\mathfrak{h}]^{C}_{CB}(\boldsymbol{q}) \\ + 2\xi_5\,[\mathfrak{h}]^{A}_{BA}(\boldsymbol{q})\,[\mathfrak{h}]^{B}_{CC}(\boldsymbol{q}) + \xi_6\,[\mathfrak{h}]^{A}_{BC}(\boldsymbol{q})\,[\mathfrak{h}]^{A}_{BC}(\boldsymbol{q}) + 2\xi_7\,[\mathfrak{h}]^{A}_{BC}(\boldsymbol{q})\,[\mathfrak{h}]^{C}_{AB}(\boldsymbol{q})\ .\end{aligned} \tag{4.74}$$

The symbols ξ_1 and ξ_2 are the Lamé coefficients in classical elasticity. The term homogeneous is used here to underline that $\xi_1, \xi_2, \ldots,$ and ξ_7 are constant. The term isotropic is used here to underline that the specific deformation energy is invariant under coordinates rotation (see [2] for more details). By adding the hypotheses of micro-isotropic and micro-homogeneous continua, the functions $\widehat{\xi}_1$ and $\widehat{\xi}_2$ are defined by

$$\xi_1 = \widehat{\xi}_1(\ell, k_\eta, k_\tau) = \frac{4\pi\ell^2}{15}(k_\eta - 4k_\tau) \quad , \quad \xi_2 = \widehat{\xi}_2(\ell, k_\eta, k_\tau) = \frac{4\pi\ell^2}{15}(k_\eta + 6k_\tau)\ . \tag{4.75}$$

The remaining parameters ξ_3, ξ_4, ξ_5, ξ_6 and ξ_7 depend on ξ_1 and ξ_2, which, in turn depend on ℓ, k_η and k_τ,

$$\xi_3 = \widehat{\xi}_3\left(\ell, k_\eta, k_\tau\right) = \frac{\ell^2}{112}\,\widehat{\xi}_1\left(\ell, k_\eta, k_\tau\right) = \xi_4\,, \tag{4.76}$$

$$\xi_5 = \widehat{\xi}_5\left(\ell, k_\eta, k_\tau\right) = \frac{\ell^2}{1120}\left(7\widehat{\xi}_2\left(\ell, k_\eta, k_\tau\right) + 3\widehat{\xi}_1\left(\ell, k_\eta, k_\tau\right)\right) = \xi_7\,, \tag{4.77}$$

$$\xi_6 = \widehat{\xi}_6\left(\ell, k_\eta, k_\tau\right) = \frac{\ell^2}{1120}\left(7\widehat{\xi}_2\left(\ell, k_\eta, k_\tau\right) - 4\widehat{\xi}_1\left(\ell, k_\eta, k_\tau\right)\right)\,. \tag{4.78}$$

In the following, a probabilistic model is proposed for ℓ, k_η and k_τ under the hypotheses of micro-homogeneity and micro-isotropy. Then, the random mechanical response of continua described by Eqs. (4.74), (4.76), (4.77), and (4.78) is studied.

4.2.2 Defining the random particle-based continuum

Let $\boldsymbol{X} : \theta \mapsto \boldsymbol{X}(\theta) = \left(L(\theta), K_\eta(\theta), K_\tau(\theta)\right)$ be the random variable with values in $\mathbb{R}^3$, defined on the probability space $(\Theta, \mathcal{T}, \mathcal{P})$, whose probability distribution is $P_{\boldsymbol{X}}$ on $\mathbb{R}^3$. The random variable L describes the random particle-pair distance between two consecutive particles, K_η and K_τ are the random microscale stiffness fields modeling interactions between two consecutive particles. Under the hypotheses of micro-homogeneity and micro-isotropy, L, K_η, and K_τ are assumed to be independent of the spatial and interaction directions. Eq. (4.75) allows us to define the random variables $\Xi_1 : \theta \mapsto \Xi_1(\theta) = \widehat{\xi}_1\left(L(\theta), K_\eta(\theta), K_\tau(\theta)\right)$ and $\Xi_2 : \theta \mapsto \Xi_2(\theta) = \widehat{\xi}_2\left(L(\theta), K_\eta(\theta), K_\tau(\theta)\right)$ such that

$$\Xi_1 = \frac{4\pi L^2}{15}\left(K_\eta - 4K_\tau\right) \quad , \quad \Xi_2 = \frac{4\pi L^2}{15}\left(K_\eta + 6K_\tau\right)\,. \tag{4.79}$$

The symbols Ξ_1 and Ξ_2 correspond to the random Lamé coefficients in classical elasticity. Eqs. (4.76) and (4.77) lead us to define the random variables $\Xi_3 = \Xi_4 : \theta \mapsto \Xi_3(\theta) = \Xi_4(\theta) = \widehat{\xi}_3\left(L(\theta), K_\eta(\theta), K_\tau(\theta)\right)$, $\Xi_5 : \theta \mapsto \Xi_5(\theta) = \Xi_7(\theta) = \widehat{\xi}_5\left(L(\theta), K_\eta(\theta), K_\tau(\theta)\right)$ and $\Xi_6 : \theta \mapsto \Xi_6(\theta) = \widehat{\xi}_6\left(L(\theta), K_\eta(\theta), K_\tau(\theta)\right)$.

At $\boldsymbol{q}$, the random specific deformation energy $\Phi(\boldsymbol{q}) : \theta \mapsto \Phi(\boldsymbol{q}, \theta)$ is obtained by substituting the deterministic quantities $(\xi_1, \xi_2, [\boldsymbol{e}](\boldsymbol{q}), [\mathfrak{h}](\boldsymbol{q}))$ in Eq. (4.74) by the random ones $(\Xi_1(\theta), \Xi_2(\theta), [\boldsymbol{E}](\boldsymbol{q}, \theta), [\mathfrak{H}](\boldsymbol{q}, \theta))$, and is given by

$$\begin{aligned}
\Phi(\boldsymbol{q}) = {} & \Xi_2\,[E]^A_B(\boldsymbol{q})\,[E]^B_A(\boldsymbol{q}) + \frac{1}{2}\,\Xi_1\,[E]^A_A(\boldsymbol{q})\,[E]^B_B(\boldsymbol{q}) \\
& + 2\Xi_3\,[\mathfrak{H}]^A_{AB}(\boldsymbol{q})\,[\mathfrak{H}]^B_{CC}(\boldsymbol{q}) + \frac{1}{2}\,\Xi_4\,[\mathfrak{H}]^A_{AB}(\boldsymbol{q})\,[\mathfrak{H}]^C_{CB}(\boldsymbol{q}) \\
& + 2\Xi_5\,[\mathfrak{H}]^A_{BA}(\boldsymbol{q})\,[\mathfrak{H}]^B_{CC}(\boldsymbol{q}) + \Xi_6\,[\mathfrak{H}]^A_{BC}(\boldsymbol{q})\,[\mathfrak{H}]^A_{BC}(\boldsymbol{q}) + 2\Xi_7\,[\mathfrak{H}]^A_{BC}(\boldsymbol{q})\,[\mathfrak{H}]^C_{AB}(\boldsymbol{q})\,,
\end{aligned} \tag{4.80}$$

where $[\boldsymbol{E}](\boldsymbol{q}) : \theta \mapsto [\boldsymbol{E}](\boldsymbol{q},\theta)$ is the random Cauchy–Green deformation tensor and $[\mathfrak{H}](\boldsymbol{q}) : \theta \mapsto [\mathfrak{H}](\boldsymbol{q},\theta)$ is the random second-gradient deformation tensor, which depend on the random configuration field $\boldsymbol{R} : \theta \mapsto \{\boldsymbol{q} \mapsto \boldsymbol{R}(\boldsymbol{q},\theta)\}$. The random deformation energy per unit direction, $\Psi(\boldsymbol{\omega},\boldsymbol{q}) : \theta \mapsto \Psi(\boldsymbol{\omega},\boldsymbol{q},\theta)$, is given by

$$\Psi(\boldsymbol{\omega},\boldsymbol{q}) = \frac{1}{2}K_\eta \left\|\boldsymbol{U}_\eta(\boldsymbol{\omega},\boldsymbol{q})\right\|^2 + \frac{1}{2}K_\tau \left\|\boldsymbol{U}_\tau(\boldsymbol{\omega},\boldsymbol{q})\right\|^2, \tag{4.81}$$

in which

$$\boldsymbol{U}_\eta(\boldsymbol{\omega},\boldsymbol{q}) = \frac{1}{2}\left(\boldsymbol{U}(\boldsymbol{q})\cdot\widehat{\boldsymbol{n}}(\boldsymbol{\omega})\right)\widehat{\boldsymbol{n}}(\boldsymbol{\omega}) \quad , \quad \boldsymbol{U}_\tau(\boldsymbol{\omega},\boldsymbol{q}) = \boldsymbol{U}(\boldsymbol{q}) - \boldsymbol{U}_\eta(\boldsymbol{\omega},\boldsymbol{q}) \ , \tag{4.82}$$

and where $\boldsymbol{U} : \theta \mapsto \{\boldsymbol{q} \mapsto \boldsymbol{U}(\boldsymbol{q},\theta)\}$ is the random field defined by

$$\begin{aligned} U^C(\boldsymbol{q}) &= 2\,[E]^C_B(\boldsymbol{q})\,\widehat{n}^B(\boldsymbol{\omega})\,\ell + \frac{1}{2}\left[F^T(\boldsymbol{q})\right]^C_i \frac{\partial^2 R^i(\boldsymbol{q})}{\partial q^A \partial q^B}\,\widehat{n}^B(\boldsymbol{\omega})\,\widehat{n}^A(\boldsymbol{\omega})\,\ell^2 \\ &= 2\,[E]^C_B(\boldsymbol{q})\,\widehat{n}^B(\boldsymbol{\omega})\,\ell + \frac{1}{2}\,[\mathfrak{H}]^C_{AB}(\boldsymbol{q})\,\widehat{n}^B(\boldsymbol{\omega})\,\widehat{n}^A(\boldsymbol{\omega})\,\ell^2 \ , \end{aligned} \tag{4.83}$$

where $[\boldsymbol{F}(\boldsymbol{q})] : \theta \mapsto [\boldsymbol{F}(\boldsymbol{q})](\theta) = \{[F(\boldsymbol{q})]^i_A(\theta) = \frac{\partial R^i(\boldsymbol{q},\theta)}{\partial q^A}, i = 1,2,3\,; A = 1,2,3\}$. The approach proposed in [65] for classical linear elasticity is used in Subsection 4.2.2. In Subsection 4.2.2, the maximum entropy (MaxEnt) principle is used to define a prior probability model for $\boldsymbol{X} = \left(L, K_\eta, K_\tau\right)$, which are the only source of uncertainty of the analyzed continuum model. In the spirit of the previous deterministic model, since we analyze the equivalent continuum model, the geometry of the single rigid particles, which are modeled as material points, are not considered here. The connectivity of the particles is modeled by means of the microscale stiffness parameters K_η and K_τ. The random variables L, K_η, and K_τ are assumed to be independent of the spatial and orientation directions. If we wish to apply the exposed second-gradient continuum model for particle-based materials to granular materials, remarks should be added concerning the geometry and shapes of the grains, granulometry involved, geometry disorder, and structure of the granular medium. The application is immediate for composite materials.

Maximum entropy principle for constructing the prior probability distribution of uncertain parameters

The Shannon entropy $\mathcal{E}(p_{\boldsymbol{X}})$ of a probability density function (pdf) $p_{\boldsymbol{X}}$ on $\mathbb{R}^n$ is defined by $\mathcal{E}(p_{\boldsymbol{X}}) = -\int_{\mathbb{R}^n} p_{\boldsymbol{X}}(\boldsymbol{x}) \log\left(p_{\boldsymbol{X}}(\boldsymbol{x})\right) d\boldsymbol{x}$, which measures the level of uncertainties. Higher uncertainty results in a larger Shannon entropy.

In accordance with the MaxEnt principle, the pdf of the $\mathbb{R}^3$-valued random variable $\boldsymbol{X} = \left(L, K_\eta, K_\tau\right)$ maximizes the Shannon entropy under the constraints defined by the available information (see for instance [129]) that are given as follows:

(Q1) The support of $p_{\boldsymbol{X}}$ is

$$\mathrm{Supp}\, p_{\boldsymbol{X}} = \mathcal{S}_{\boldsymbol{X}} \quad , \quad \mathcal{S}_{\boldsymbol{X}} \subseteq [\zeta_1, \zeta_2] \times \mathbb{R}^+ \times \mathbb{R}^+ \subset \mathbb{R}^3 \, , \tag{4.84}$$

where $0 < \zeta_1 < \zeta_2 < +\infty$.

(Q2) The mean value of K_η and K_τ are given and finite,

$$\mathbb{E}\left\{K_\eta\right\} = \gamma_\eta < +\infty \quad , \quad \gamma_\eta \in \mathbb{R}^+ \, , \tag{4.85}$$

$$\mathbb{E}\left\{K_\tau\right\} = \gamma_\tau < +\infty \quad , \quad \gamma_\tau \in \mathbb{R}^+ \, . \tag{4.86}$$

(Q3) The inverse of the random matrix $[\boldsymbol{K}]$ such that

$$[\boldsymbol{K}] = \begin{bmatrix} K_\eta & 0 \\ 0 & K_\tau \end{bmatrix} , \tag{4.87}$$

has a finite second-order moment (for physical consistencies),

$$\mathbb{E}\left\{\left\|\boldsymbol{K}^{-1}\right\|^2\right\} < +\infty \, . \tag{4.88}$$

This property can be stated as suggested in [125, 126] and can be replaced by the following one: the random variable $\log\left(\det\left([\boldsymbol{K}]\right)\right)$ has a given mean value whose absolute value is finite,

$$\mathbb{E}\left\{\log\left(\det\left([\boldsymbol{K}]\right)\right)\right\} = \gamma_{\det} \quad , \quad |\gamma_{\det}| < +\infty \, . \tag{4.89}$$

Since the random variable $\det\left([\boldsymbol{K}]\right) = K_\eta K_\tau$, Eq. (4.89) can be rewritten as

$$\mathbb{E}\left\{\mu\left(K_\eta, K_\tau\right)\right\} = \gamma_{\det} \quad , \quad \mu\left(K_\eta, K_\tau\right) = \log\left(K_\eta K_\tau\right) \, . \tag{4.90}$$

We now consider the $\mathbb{R}^2$-valued random variable $\left(K_\eta, K_\tau\right)$ defined on $(\Theta, \mathcal{T}, \mathcal{P})$. The constraints stated by propositions (Q2) and (Q3) read

$$\mathbb{E}\left\{\boldsymbol{h}\left(K_\eta, K_\tau\right)\right\} = \boldsymbol{\gamma} \, , \tag{4.91}$$

where $\boldsymbol{\gamma} = \left(\gamma_\eta, \gamma_\tau, \gamma_{\text{det}}\right)$ and $\boldsymbol{h} : \mathbb{R}^2 \mapsto \mathbb{R}^3$ such that

$$\boldsymbol{h}(k_\eta, k_\tau) = (k_\eta, k_\tau, \log(k_\eta\, k_\tau)) \ . \tag{4.92}$$

Let C_{free} (see [129]) be the set of functions on $\mathbb{R}^3$, defined by

$$C_{\text{free}} = \left\{ p \in L^1\left(\mathbb{R}^3, \mathbb{R}^+\right), \text{Supp}\ p = \mathcal{S}_{\boldsymbol{X}} \right\} \ . \tag{4.93}$$

The set C_{ad} of the admissible probability density functions $p : (\ell, k_\eta, k_\tau) \mapsto p(\ell, k_\eta, k_\tau)$ of $\boldsymbol{X} = (L, K_\eta, K_\tau)$ is defined by

$$\begin{aligned} C_{\text{ad}} = \Bigg\{ & p \in C_{\text{free}} \ , \int_{\mathbb{R}^3} p\left(\ell, k_\eta, k_\tau\right) d\ell\, dk_\eta\, dk_\tau = 1 \ , \\ & \int_{\mathbb{R}^3} \boldsymbol{h}\left(k_\eta, k_\tau\right) p\left(\ell, k_\eta, k_\tau\right) d\ell\, dk_\eta\, dk_\tau = \boldsymbol{\gamma} \Bigg\} \ . \end{aligned} \tag{4.94}$$

Under the constraints defined by (Q1), (Q2), and (Q3), and using the MaxEnt principle, it is possible to prove that pdf $p_{\boldsymbol{X}}$ of $\boldsymbol{X}$ is the unique solution of the following optimization problem,

$$p_{\boldsymbol{X}} = \arg\max_{p \in C_{\text{ad}}} \mathcal{E}\left(p\right) \ , \tag{4.95}$$

where $p \mapsto \mathcal{E}(p)$ is the Shannon entropy defined by

$$\mathcal{E}(p) = -\int_{\mathbb{R}^3} p\left(\ell, k_\eta, k_\tau\right) \log\left(p\left(\ell, k_\eta, k_\tau\right)\right) d\ell\, dk_\eta\, dk_\tau \ . \tag{4.96}$$

Effective construction of the prior probability distribution of uncertain parameters

Proposition 1 *For the micro-homogeneous and micro-isotropic continuum in the field of the particle-based theory presented in Section 3.1.1, the expression of the joint probability density function of the random variables L, K_η, and K_τ, constructed using the MaxEnt principle under the constraints defined by (Q1), (Q3), and (Q3), shows that random variables L, K_η and K_τ are statistically independent. It also shows that the random variable L is uniformly distributed in $[\zeta_1, \zeta_2]$, and that K_η and K_τ are Gamma distributed in $\mathbb{R}^+$, whose parameters are*

$$\left(\alpha_\eta, \beta_\eta\right) = \left(1 - \lambda_c, \frac{m_{K_\eta}}{1 - \lambda_c}\right) \quad \text{and} \quad \left(\alpha_\tau, \beta_\tau\right) = \left(1 - \lambda_c, \frac{m_{K_\tau}}{1 - \lambda_c}\right) \ . \tag{4.97}$$

In Eq. (4.97), $m_{K_\eta} = \mathbb{E}\left\{K_\eta\right\}$ *and* $m_{K_\tau} = \mathbb{E}\left\{K_\tau\right\}$ *are the given mean values of* K_η *and* K_τ, *and* $\lambda_c \in \left]-\infty, 1\right[$ *controls the statistical fluctuations. The parameters* $\left(\alpha_\eta, \beta_\eta\right)$ *and* $\left(\alpha_\tau, \beta_\tau\right)$ *can be expressed as a function of the mean values* m_{K_η} *and* m_{K_τ} *and of the coefficients of*

variation $\mathrm{cv}_{K_\eta} = \sigma_{K_\eta}/m_{K_\eta}$ *and* $\mathrm{cv}_{K_\tau} = \sigma_{K_\tau}/m_{K_\tau}$ *of* K_η *and of* K_τ,

$$m_{K_\eta} = \alpha_\eta \beta_\eta \quad , \quad m_{K_\tau} = \alpha_\tau \beta_\tau \quad , \quad \mathrm{cv}_{K_\eta} = \mathrm{cv}_{K_\tau} = \frac{1}{\sqrt{1-\lambda_c}} \, . \tag{4.98}$$

Note that the statistical fluctuations of K_η *and* K_τ*, which are driven by their coefficients of variation, depend only on the same single parameter* λ_c.

Proof The following proof is inspired from [65]. The solution of the optimization problem defined by Eq. (4.95) is written as

$$p_{L K_\eta K_\tau}\left(\ell, k_\eta, k_\tau\right) = \mathbb{1}_{\mathcal{S}_X}(\ell, k_\eta, k_\tau)\, c_0^{\mathrm{sol}} \exp(-\langle \boldsymbol{\lambda}^{\mathrm{sol}}, \boldsymbol{h}\left(k_\eta, k_\tau\right)\rangle) \quad , \quad \forall \left(\ell, k_\eta, k_\tau\right) \in \mathbb{R}^3 \, , \tag{4.99}$$

where $\boldsymbol{h} : \mathbb{R}^2 \mapsto \mathbb{R}^3$ is such that $\boldsymbol{h}(k_\eta, k_\tau) = (k_\eta, k_\tau, \log(k_\eta\, k_\tau))$ (see Eq. (4.92)), the positive normalization constant c_0^{sol} and the Lagrange multiplier $\boldsymbol{\lambda}^{\mathrm{sol}} = \left(\lambda_\eta, \lambda_\tau, \lambda_c\right)$ must be such that $p_{L,K_\eta,K\tau}$ belongs to the admissible set $\mathcal{C}_{\mathrm{ad}}$ defined by Eq. (4.94). An algebraic calculation shows that the support $\mathcal{S}_{\boldsymbol{X}}$ introduced in Eq. (4.84) can be written as $\mathcal{S}_{\boldsymbol{X}} = [\zeta_1, \zeta_2] \times \mathbb{R}^+ \times \mathbb{R}^+$ and that, substuiting Eq. (4.92) into (4.99), $p_{L K_\eta K_\tau}$ can be written as

$$p_{L K_\eta K_\tau}\left(\ell, k_\eta, k_\tau\right) = p_L(\ell)\; p_{K_\eta}\left(k_\eta\right)\; p_{K_\tau}(k_\tau) \, . \tag{4.100}$$

in which

$$p_L(\ell) = \mathbb{1}_{[\zeta_1,\zeta_2]}(\ell)\; c_1 \, , \tag{4.101}$$

$$p_{K_\eta}\left(k_\eta\right) = \mathbb{1}_{\mathbb{R}^+}\left(k_\eta\right)\; c_2\, k_\eta^{-\lambda_c} \exp\left\{-\lambda_\eta\, k_\eta\right\} \, , \tag{4.102}$$

and

$$p_{K_\tau}(k_\tau) = \mathbb{1}_{\mathbb{R}^+}(k_\tau)\; c_3\, k_\tau^{-\lambda_c} \exp\left\{-\lambda_\tau\, k_\tau\right\} \, , \tag{4.103}$$

where c_1, c_2, and c_3 are positive normalization constants such that $c^{\mathrm{sol}} = c_1\, c_2\, c_3$. Hence, L is uniformly distributed, K_η and K_τ are Gamma distributed with parameters $\left(\alpha_\eta, \beta_\eta\right) = \left(1-\lambda_c, 1/\lambda_\eta\right)$ and $(\alpha_\tau, \beta_\tau) = (1-\lambda_c, 1/\lambda_\tau)$. Since

$$1 = \int_{[\zeta_1,\zeta_2]} \mathbb{1}_{[\zeta_1,\zeta_2]}(\ell)\; c_1\, d\ell = c_1\,(\zeta_2 - \zeta_1) \, , \tag{4.104}$$

$$1 = c_2 \int_{\mathbb{R}^+} k_\eta^{-\lambda_c} \exp\left\{-\lambda_\eta k_\eta\right\}\, dk_\eta = c_2 \frac{\Gamma\left(1-\lambda_c\right)}{\lambda_\eta^{1-\lambda_c}} \, , \tag{4.105}$$

$$1 = c_2 \int_{\mathbb{R}^+} k_\tau^{-\lambda_c} \exp\left\{-\lambda_\tau k_\tau\right\}\, dk_\tau = c_2 \frac{\Gamma\left(1-\lambda_c\right)}{\lambda_\tau^{1-\lambda_c}} \, , \tag{4.106}$$

where $\Gamma : z \mapsto \Gamma(z) = \int_0^{+\infty} s^{z-1}\exp(-s)\,ds$ is the Gamma function. The normalization constants are found to be

$$c_1 = \frac{1}{\zeta_2 - \zeta_1} \quad , \quad c_2 = \frac{\lambda_\eta^{1-\lambda_c}}{\Gamma(1-\lambda_c)} \quad , \quad c_3 = \frac{\lambda_\tau^{1-\lambda_c}}{\Gamma(1-\lambda_c)}\,, \tag{4.107}$$

while it can be deduced that $1/\lambda_\eta = m_{K_\eta}/(1-\lambda_c)$ and $1/\lambda_\tau = m_{K_\tau}/(1-\lambda_c)$. To guarantee the finite value of the integrals in Eqs. (4.105) and (4.106), we must have $1-\lambda_c > 0$, $\lambda_\eta > 0$ and $\lambda_\tau > 0$. Using the argument presented in Appendix B of [65], it can be seen that this algebraic solution is the unique solution of the optimization problem defined by Eq. (4.94).

Let us emphasize that the outcomes presented in this section are the result of applying the MaxEnt principle with the available information (Q1), (Q2), and (Q3).

4.2.3 Stochastic boundary value problem and its random solution defined in the application framework

In order to simplify the presentation, for constructing and analyzing the boundary value problem (BVP) for the random particle-based continuum model exposed in Section 4.2.2, the methodology is directly applied to a particular particle-based sample and not presented in a general case. We consider a plate with a hole located in the middle whose mechanical properties are those of concrete and that is subjected to a numerical axial traction test. The domain of this plate is denoted by $\mathcal{B}$ and its boundary is $\partial\mathcal{B} = \partial\mathcal{B}_0 \cup \partial\mathcal{B}_t \cup \partial\mathcal{B}_1$. Zero Dirichlet conditions are applied on $\partial\mathcal{B}_0$ and $\partial\mathcal{B}_t$ (left end and right end), where the body is clamped. A Neumann boundary condition is applied on $\partial\mathcal{B}_t$ (right end), where the uniaxial traction is applied. The displacement field is free on $\partial\mathcal{B}_1$ (see Fig. 4.11).

Geometry, load, deterministic and random mechanical properties

The values of the geometry parameters defined in Fig. (4.11) are $b_1 = 3\times10^{-1}\,m$, $b_2 = 5\times10^{-2}\,\mathrm{m}$, and $b_3 = 1\times10^{-2}\,\mathrm{m}$. The amplitude of the uniaxial traction load is $t = 1.5\times10^{9}\,\mathrm{N/m^2}$. The mean values $m_{\Xi_1} = \mathbb{E}\{\Xi_1\}$ and $m_{\Xi_2} = \mathbb{E}\{\Xi_2\}$ of the random Lamé coefficients Ξ_1 and Ξ_2 are such that $m_{\Xi_1} = 3.529\times10^{9}\,\mathrm{N/m^2}$ and $m_{\Xi_2} = 10^{10}\,\mathrm{N/m^2}$. Using Eq. (4.79) and because L is independent on K_η and K_τ, then, solving the linear equations for the mean values of K_η and K_τ yields

$$m_{K_\eta} = \mathbb{E}\{K_\eta\} = 8.613\times10^{15}\,\mathrm{N/m^4} \quad , \quad m_{K_\tau} = \mathbb{E}\{K_\tau\} = 1.029\times10^{15}\,\mathrm{N/m^4}\,. \tag{4.108}$$

Let σ_{K_η} and σ_{K_τ} be the standard deviations of the random variables K_η and K_τ. Following Proposition 1 we have now to choose the value of $\mathrm{cv}_K := \mathrm{cv}_{K_\eta} = \mathrm{cv}_{K_\tau}$, and of ζ_1 and ζ_2. Since L is uniformly distributed in $[\zeta_1, \zeta_2]$, we have $m_L = (\zeta_1 + \zeta_2)/2$ and $\sigma_L = (\zeta_2 - \zeta_1)/(2\sqrt{3})$. Thus, one has $\zeta_1 = m_L - \mathrm{cv}_L m_L \sqrt{3}$ and $\zeta_2 = m_L + \mathrm{cv}_L m_L \sqrt{3}$. In this application, $m_L = 1 \times 10^{-4}$ m. The sensitivity in the mechanical response of the analyzed continuum sample with respect to cv_L and cv_K is investigated.

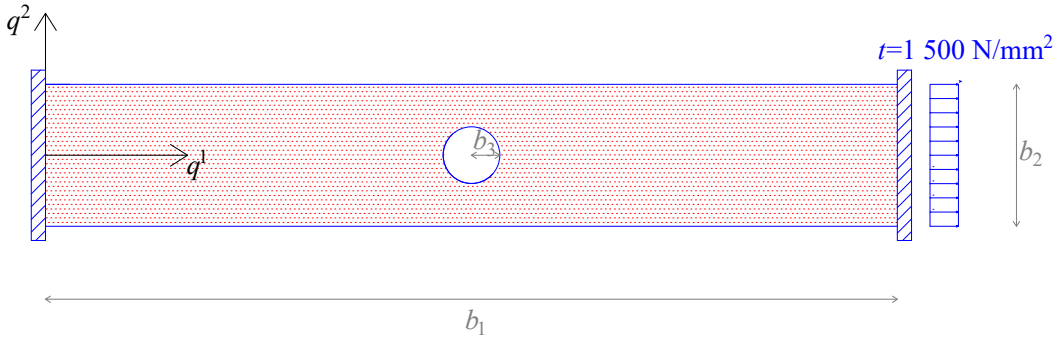

Fig. 4.4 Numerical axial traction test on a plate made of particle-based materials with uncertainties. In the application, the material parameters are the ones of concrete. In the present figure, the red points are used to underline that we are dealing with a particle-based material and, more specifically, with a composite material whose particles (or inclusions) have a random distance that is independent of the spatial and orientation directions. These assumptions on the distance between particles may be relaxed to describe more complex microstructures in which the particle-pair distance, and consequently ℓ, would depend on the spatial directions.

Strong stochastic solution of the weak formulation of the boundary value problem

In this section, first we summarize the weak formulation of the deterministic BVP, which will be used for constructing the computational model based on the mixed Finite Element (FE) method. Then, we introduce stochasticity in this weak formulation yielding the random weak formulation. The strong stochastic solution of this random weak formulation will be searched. Note that such a formulation is adapted to a stochastic solver based on Monte Carlo (MC) numerical simulation that will be introduced in Section 4.2.3.

Derivation of the weak formulation of the deterministic boundary value problem

Let C_V be the admissible space of sufficiently differentiable functions $\boldsymbol{v} : \boldsymbol{q} \mapsto \boldsymbol{v}(\boldsymbol{q})$ defined on $\mathcal{B}$ with values in $\mathbb{R}^2$ satisfying the zero Dirichlet conditions on $\partial\mathcal{B}_0$ and $\partial\mathcal{B}_t$. Since the right-hand side of Eq. (4.74) exhibits the deformation tensors that are a function of $\boldsymbol{v}$ and

since coefficients ξ_1 to ξ_7 depend on $\boldsymbol{x} = (\ell, k_\eta, k_\tau)$, we rewrite function $\phi(\boldsymbol{q})$ as $\widetilde{\phi}(\boldsymbol{v},\boldsymbol{x})(\boldsymbol{q})$ in order to explicit the dependencies in $\boldsymbol{v}$ and $\boldsymbol{x}$, where $\widetilde{\phi} : (\boldsymbol{v},\boldsymbol{x}) \mapsto \widetilde{\phi}(\boldsymbol{v},\boldsymbol{x})$ is such that $\widetilde{\phi}(\boldsymbol{v},\boldsymbol{x})(\boldsymbol{q}) = \phi(\boldsymbol{q})$. The weak formulation of the deterministic BVP is: find $\boldsymbol{v}$ in $C_{\boldsymbol{V}}$ such that

$$(\delta\pi)(\boldsymbol{v},\delta\boldsymbol{v};\boldsymbol{x}) = 0 \quad , \quad \forall \delta\boldsymbol{v} = \left\{\delta v^1, \delta v^2, \delta v^3\right\} \in C_{\boldsymbol{V}} , \tag{4.109}$$

where $\delta\pi$ is the first variation of the energy functional π defined by

$$\pi(\boldsymbol{v};\boldsymbol{x}) = \int_{\mathcal{B}} \widetilde{\phi}(\boldsymbol{v},\boldsymbol{x})(\boldsymbol{q})\, d\boldsymbol{q} \; - \int_{\partial\mathcal{B}_t} t\, v^1(\boldsymbol{q})\, ds(\boldsymbol{q}) , \tag{4.110}$$

in which $ds(\boldsymbol{q})$ is the surface element.

Random weak formulation and its strong stochastic solution

The random weak formulation is derived from Eqs. (4.109) and (4.110) in substituting $\boldsymbol{x}$ by the random vector $\boldsymbol{X}$ whose probability model is defined in Proposition 1. Consequently, displacement field $\boldsymbol{v}$ becomes a random displacement field $\boldsymbol{V} : \theta \mapsto \{\boldsymbol{V}(\theta) : \boldsymbol{q} \mapsto \boldsymbol{V}(\boldsymbol{q},\theta)\}$ such that $\boldsymbol{V}(\theta)$ belongs to $C_{\boldsymbol{V}}$ and configuration $\boldsymbol{r}$ becomes the random configuration field $\boldsymbol{R} : \theta \mapsto \{\boldsymbol{q} \mapsto \boldsymbol{R}(\boldsymbol{q},\theta)\}$ defined in Section 4.2.2. The strong stochastic solution consists in finding $\boldsymbol{V}(\theta)$, for θ in Θ, with values in $C_{\boldsymbol{V}}$ such that

$$(\delta\pi)(\boldsymbol{V}(\theta),\delta\boldsymbol{v};\boldsymbol{X}(\theta)) = 0 \quad , \quad \forall \delta\boldsymbol{v} \in C_{\boldsymbol{V}} \quad , \quad a.s. \tag{4.111}$$

Monte Carlo numerical simulation as stochastic solver

The construction of the strong stochastic solution of the random weak formulation is based on the use of the MC numerical simulation and on Eq. (4.111). Consequently, the steps of the stochastic solver are as follows.

1. Generation of n independent realizations $\boldsymbol{X}(\theta_1), \boldsymbol{X}(\theta_2), \ldots, \boldsymbol{X}(\theta_n)$ of random variable $\boldsymbol{X}$ using the probability distribution $P_X(d\boldsymbol{x}) = p_{\boldsymbol{X}}(\boldsymbol{x})d\boldsymbol{x}$ defined in Proposition 1, in which $\boldsymbol{X} = (L, K_\eta, K_\tau)$.

2. Computation of n independent deterministic solutions $\boldsymbol{V}(\theta_1), \boldsymbol{V}(\theta_2), \ldots, \boldsymbol{V}(\theta_n)$ that satisfy Eq. (4.111). In fact, the mixed FE method is used for each computation, where the displacement field and its gradient are solved both as unknowns under constraints imposed by means of Lagrange multipliers. In the formulation used, the definition of the stress tensors is not required and related issues are avoided. In this regard, one should mention the important issue of symmetry loss of the Cauchy stress tensor

within the framework of second gradient continuum models [14]. For second gradient continuum models, details concerning the application of mixed FE method are presented in [121]. In the present application, the weak formulation of the equivalent continuum model is discretized using finite elements. We are simulating a particle-based material not with a random microstructure, but with random particle-pair distance between consecutive particles and random microscale stiffness parameters. As previously explained, the mesh size does not depend on the random medium properties. Although the equivalent continuum model is derived from the discrete model, this is not a classical homogenization procedure in which the microstructure is a random medium represented by apparent mechanical properties and in which the macrostructure has effective mechanical properties that are deterministic for scale separation. As a consequence, the random fluctuations of the mechanical response do not depend on the mesh size All simulations are performed by a computing node using Intel Xeon E7-4850, in total 64 cores each with a 40 MB cache, equipped with 256 GB memory in total, running Linux Kernel 5 Ubuntu 20.04. The code is written in Python by using multithreading such that thousands of computations are distributed asynchronously to the available resources efficiently. The code in Python is wrapped by the FEniCS software into a C++ code and is solved as a compiled program. Therefore, yet efficient in developing the code in Python, solution is highly optimized by using a massive parallelization under the current implementation. The Python code, generated during the current study, is part of the FEniCS project available at http://www.fenicsproject.org/download, and an example for the computational implementation is available in [1] to be used under the GNU Public license [GNU Public].

3. We consider a finite set of scalar observations expressed in terms of $\boldsymbol{V}$, for instance the energy and some components of the displacement field at a given point $\boldsymbol{q}$. Let Z be the real valued-random variable representing one of the considered observations. For any fixed value n, we estimate the mean value $m_Z^{(n)}$ and the standard deviation $\sigma_Z^{(n)}$.

4. The convergence of the stochastic solver with respect to n is performed for each random variable Z by estimating the quantity $\varepsilon_Z^{(n)} = \eta\,\sigma_Z/\sqrt{n}$ following the procedure in ([129] pp. 35) based on the central limit theorem. For that, we will plot the dimensionless quantity $\widetilde{\varepsilon}_Z^{(n)}/m_Z^{(n)}$ where $\widetilde{\varepsilon}_Z^{(n)} = \eta\,\sigma_Z^{(n)}/\sqrt{n}$.

Convergence analysis and quantification of uncertainty propagation

Let us define two points $\boldsymbol{q}_1 = (b_1/2, b_3/2, 0)$ and $\boldsymbol{q}_2 = (b_1, 0, 0)$. As a function of the number n of realization, we compute the mean value m_{Φ_1} and the standard deviation σ_{Φ_1} of the

specific deformation energy in $\boldsymbol{q}_1$, where $\Phi_1 = \Phi(\boldsymbol{q}_1)$. We also evaluate the mean values $m_{V_1^1}$ and $m_{V_2^1}$ and the standard deviations $\sigma_{V_1^1}$ and $\sigma_{V_2^1}$ of the horizontal displacements at $\boldsymbol{q}_1$ and $\boldsymbol{q}_2$, where $V_1^1 = V^1(\boldsymbol{q}_1)$ and $V_2^1 = V^1(\boldsymbol{q}_2)$. Finally, we compute the mean value $m_{V_1^2}$ and the standard deviation $\sigma_{V_1^2}$ of the transversal displacement in $\boldsymbol{q}_1$, where $V_1^2 = V^2(\boldsymbol{q}_1)$. Fig. 4.5 displays the dimensionless quantities defined by

$$\begin{aligned} \frac{\widetilde{\varepsilon}_{\Phi_1}^{(n)}(\eta)}{m_{\Phi_1}^{(n)}} &= \frac{\eta\,\sigma_{\Phi_1}^{(n)}}{\sqrt{n}\,m_{\Phi_1}^{(n)}} \quad , \quad \frac{\widetilde{\varepsilon}_{V_1^1}^{(n)}(\eta)}{m_{V_1^1}^{(n)}} = \frac{\eta\,\sigma_{V_1^1}^{(n)}}{\sqrt{n}\,m_{V_1^1}^{(n)}} \, , \\ \frac{\widetilde{\varepsilon}_{V_2^1}^{(n)}(\eta)}{m_{V_2^1}^{(n)}} &= \frac{\eta\,\sigma_{V_2^1}^{(n)}}{\sqrt{n}\,m_{V_2^1}^{(n)}} \quad , \quad \frac{\widetilde{\varepsilon}_{V_1^2}^{(n)}(\eta)}{m_{V_1^2}^{(n)}} = \frac{\eta\,\sigma_{V_1^2}^{(n)}}{\sqrt{n}\,m_{V_1^2}^{(n)}} \, . \end{aligned} \tag{4.112}$$

as a function of the number of realizations n. The value of η has been chosen equal to $\mathcal{G}^{-1}(0.95)$, $\eta = \mathcal{G}^{-1}(0.95) = 1.64$, where $\mathcal{G}$ is the standard normal cumulative distribution function. The probability of committing at most an error of 0.49 % with respect to the derived mean values was estimated to be 0.95 by considering $n = 10\,000$. The choice to analyze the mechanical response at points $\boldsymbol{q}_1$ and $\boldsymbol{q}_2$ is due to two reasons: an energy concentration occurs at $\boldsymbol{q}_1$ and the maximum displacement occurs at $\boldsymbol{q}_2$. The coefficients of variation cv_{Φ_1}, $\mathrm{cv}_{V_1^1}$, $\mathrm{cv}_{V_2^1}$, and $\mathrm{cv}_{V_1^2}$ obtained for different values of cv_L and cv_K are shown in Fig. 4.6. Moreover, the mean values $m_{\Delta_{\Phi_1}}$, $m_{\Delta_{V_1^1}}$, $m_{\Delta_{V_2^1}}$, $m_{\Delta_{V_1^2}}$ and the root mean square values $\mathrm{rms}_{\Delta_{\Phi_1}}$, $\mathrm{rms}_{\Delta_{V_1^1}}$, $\mathrm{rms}_{\Delta_{V_2^1}}$, $\mathrm{rms}_{\Delta_{V_1^2}}$ of the dimensionless random variables

$$\Delta_{\Phi_1} = \frac{\Phi_1 - \underline{\Phi_1}}{\underline{\Phi_1}} \quad , \quad \Delta_{V_1^1} = \frac{V_1^1 - \underline{V_1^1}}{\underline{V_1^1}} \quad , \quad \Delta_{V_2^1} = \frac{V_2^1 - \underline{V_2^1}}{\underline{V_2^1}} \quad , \quad \Delta_{V_1^2} = \frac{V_1^2 - \underline{V_1^2}}{\underline{V_1^2}} \tag{4.113}$$

obtained for different values of cv_L and cv_K are shown in Figs. 4.7 and 4.8, where $\underline{\Phi_1}$, $\underline{V_1^1}$, $\underline{V_2^1}$, and $\underline{V_1^2}$ are the specific deformation energy at $\boldsymbol{q}_1$, the horizontal displacements at $\boldsymbol{q}_1$ and $\boldsymbol{q}_2$, the vertical displacement at $\boldsymbol{q}_1$ corresponding to the nominal values of L, K_η and K_τ. For different values of cv_L and cv_K, Fig. 4.9 shows the graph of the dimensionless quantities defined by

$$\begin{aligned} \mathrm{rcv}_{\Phi_1} &= \frac{\left|\mathrm{cv}_{\Phi_1} - \mathrm{rms}_{\Delta_{\Phi_1}}\right|}{\mathrm{cv}_{\Phi_1}} \quad , \quad \mathrm{rcv}_{V_1^1} = \frac{\left|\mathrm{cv}_{V_1^1} - \mathrm{rms}_{V_1^1}\right|}{\mathrm{cv}_{V_1^1}} \, , \\ \mathrm{rcv}_{V_2^1} &= \frac{\left|\mathrm{cv}_{V_2^1} - \mathrm{rms}_{V_2^1}\right|}{\mathrm{cv}_{V_2^1}} \quad , \quad \mathrm{rcv}_{V_1^2} = \frac{\left|\mathrm{cv}_{V_1^2} - \mathrm{rms}_{V_1^2}\right|}{\mathrm{cv}_{V_1^2}} \, . \end{aligned} \tag{4.114}$$

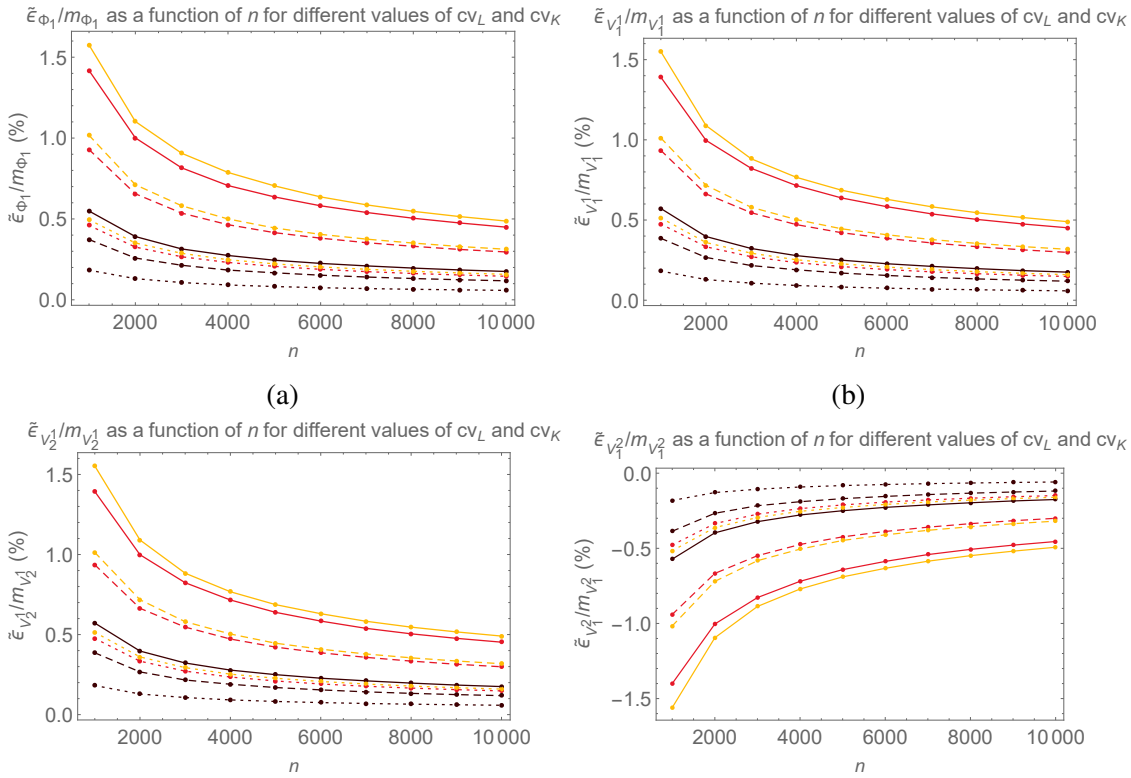

Fig. 4.5 Graphs (a) $n \mapsto \widetilde{\varepsilon}_{\Phi_1}/m_{\Phi_1}$, (b) $n \mapsto \widetilde{\varepsilon}_{V_1^1}/m_{V_1^1}$, (c) $n \mapsto \widetilde{\varepsilon}_{V_2^1}/m_{U_2^1}$, (d) $n \mapsto \widetilde{\varepsilon}_{V_1^2}/m_{V_1^2}$ for different values of cv_L and cv_K to study the convergence with respect to n. Solid line: results for $\mathrm{cv}_L = 15\,\%$ and $\mathrm{cv}_K = 15\,\%$ (yellow), $\mathrm{cv}_L = 15\,\%$ and $\mathrm{cv}_K = 0$ (red), $\mathrm{cv}_L = 0$ and $\mathrm{cv}_K = 15\,\%$ (black). Dashed line: results for $\mathrm{cv}_L = 10\,\%$ and $\mathrm{cv}_K = 10\,\%$ (yellow), $\mathrm{cv}_L = 10\,\%$ and $\mathrm{cv}_K = 0$ (red), $\mathrm{cv}_L = 0$ and $\mathrm{cv}_K = 10\,\%$ (black). Dotted line: results for $\mathrm{cv}_L = 5\,\%$ and $\mathrm{cv}_K = 5\,\%$ (yellow), $\mathrm{cv}_L = 5\,\%$ and $\mathrm{cv}_K = 0$ (red), $\mathrm{cv}_L = 0$ and $\mathrm{cv}_K = 5\,\%$ (black).

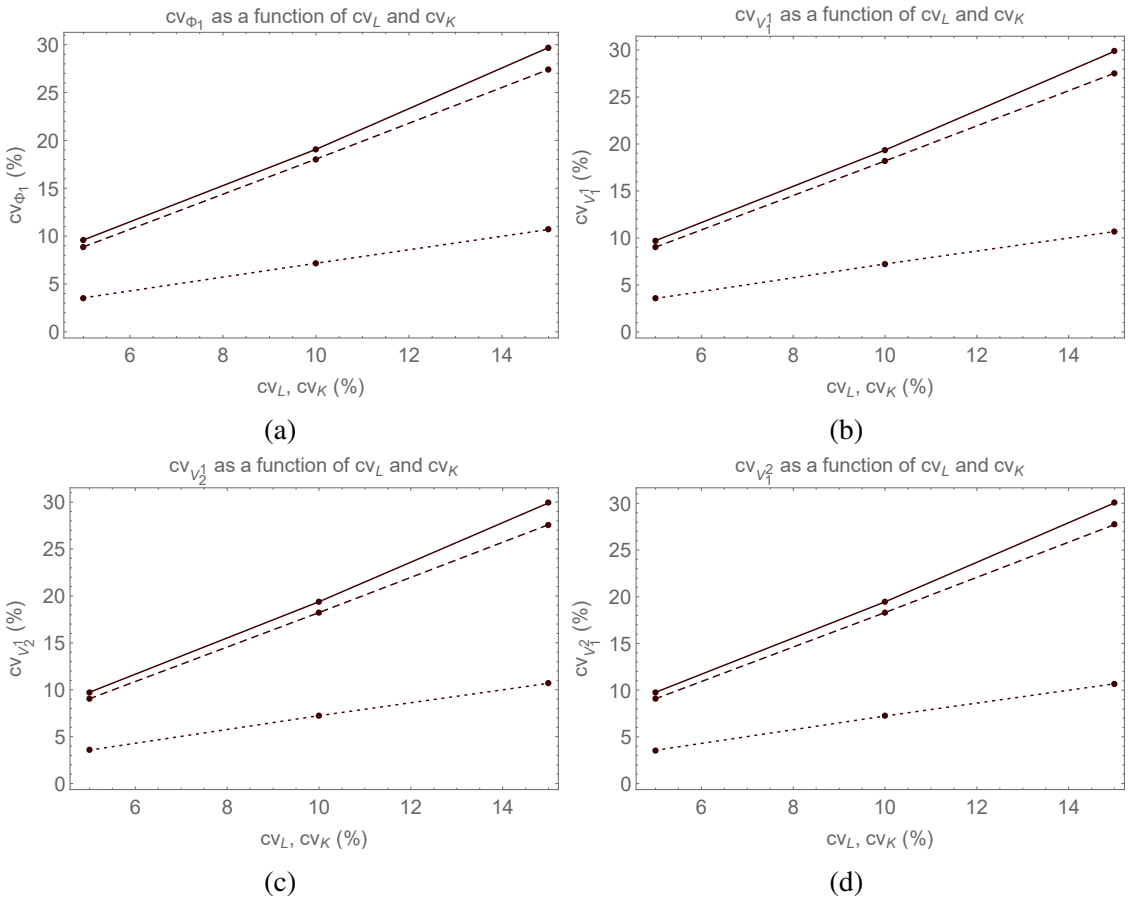

Fig. 4.6 Graphs of (a) cv_{Φ_1}, (b) $\mathrm{cv}_{V_1^1}$, (c) $\mathrm{cv}_{V_2^1}$, (d) $\mathrm{cv}_{V_1^2}$ for different values of cv_L and cv_K. Solid line: results for cv_L equal to cv_K both different from zero. Dashed line: results for cv_L different from zero and cv_K equal to zero. Dotted line: results for cv_L equal to zero and cv_K different form zero.

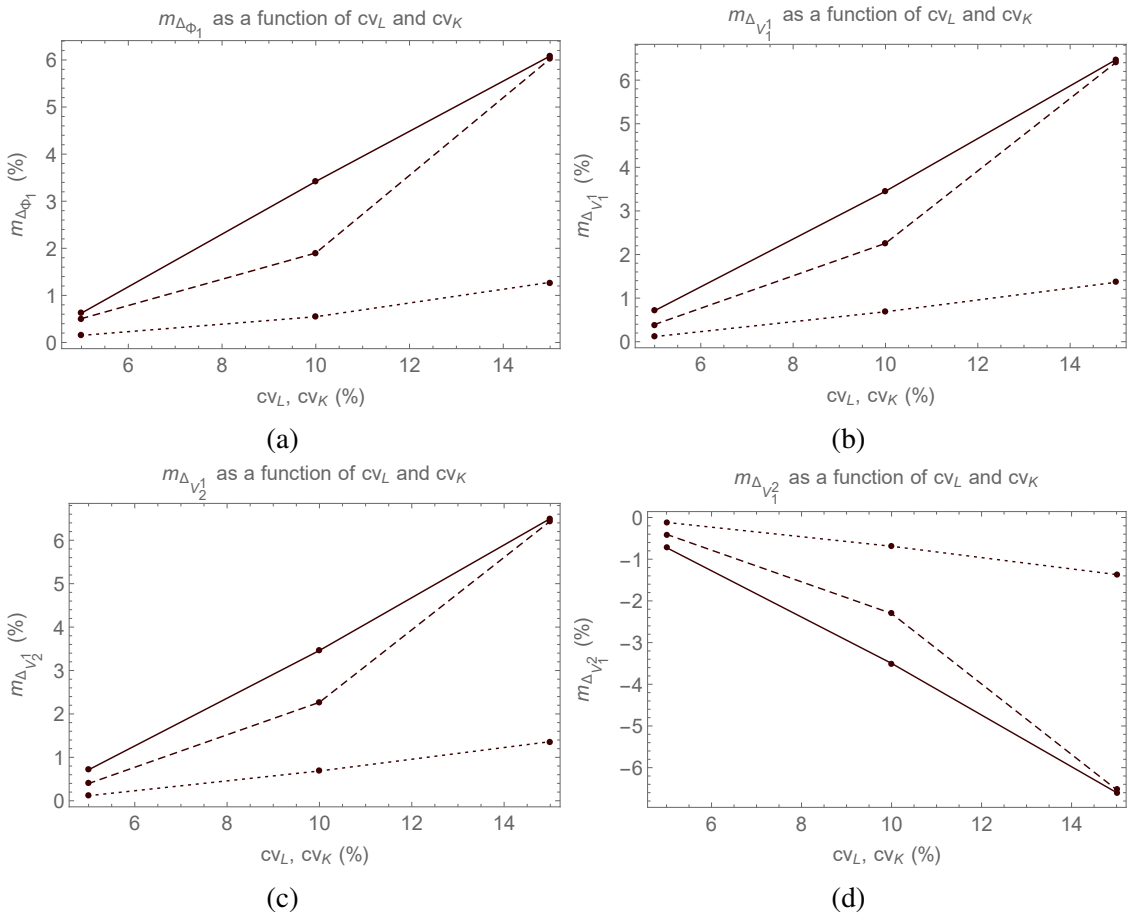

Fig. 4.7 Graphs of (a) $m_{\Delta_{\Phi_1}}$, (b) $m_{\Delta_{V_1^1}}$, (c) $m_{\Delta_{V_2^1}}$, (d) $m_{\Delta_{V_1^2}}$ for different values of cv_L and cv_K. Solid line: results for cv_L equal to cv_K both different from zero. Dashed line: results for cv_L different from zero and cv_K equal to zero. Dotted line: results for cv_L equal to zero and cv_K different from zero.

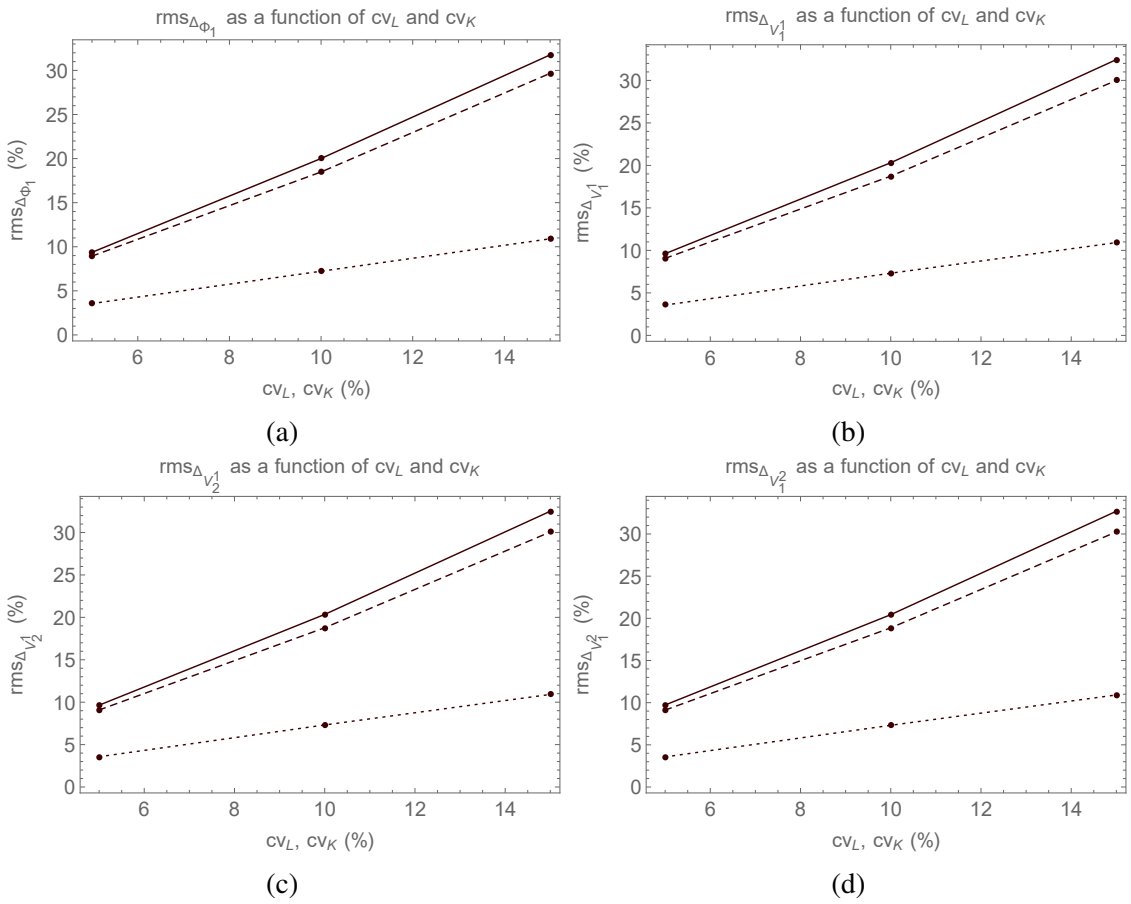

Fig. 4.8 Graphs of (a) $\text{rms}_{\Delta_{\Phi_1}}$, (b) $\text{rms}_{\Delta_{V_1^1}}$, (c) $\text{rms}_{\Delta_{V_2^1}}$, (d) $\text{rms}_{\Delta_{V_1^2}}$ for different values of cv_L and cv_K. Solid line: results for cv_L equal to cv_K both different from zero. Dashed line: results for cv_L different from zero and cv_K equal to zero. Dotted line: results for cv_L equal to zero and cv_K different form zero.

Equation (4.114) defines the relative differences between the coefficients of variation of Φ_1, V_1^1, V_2^1, V_1^2 and the coefficients of variation of the same variables that would result from replacing their means values with the nominal ones.

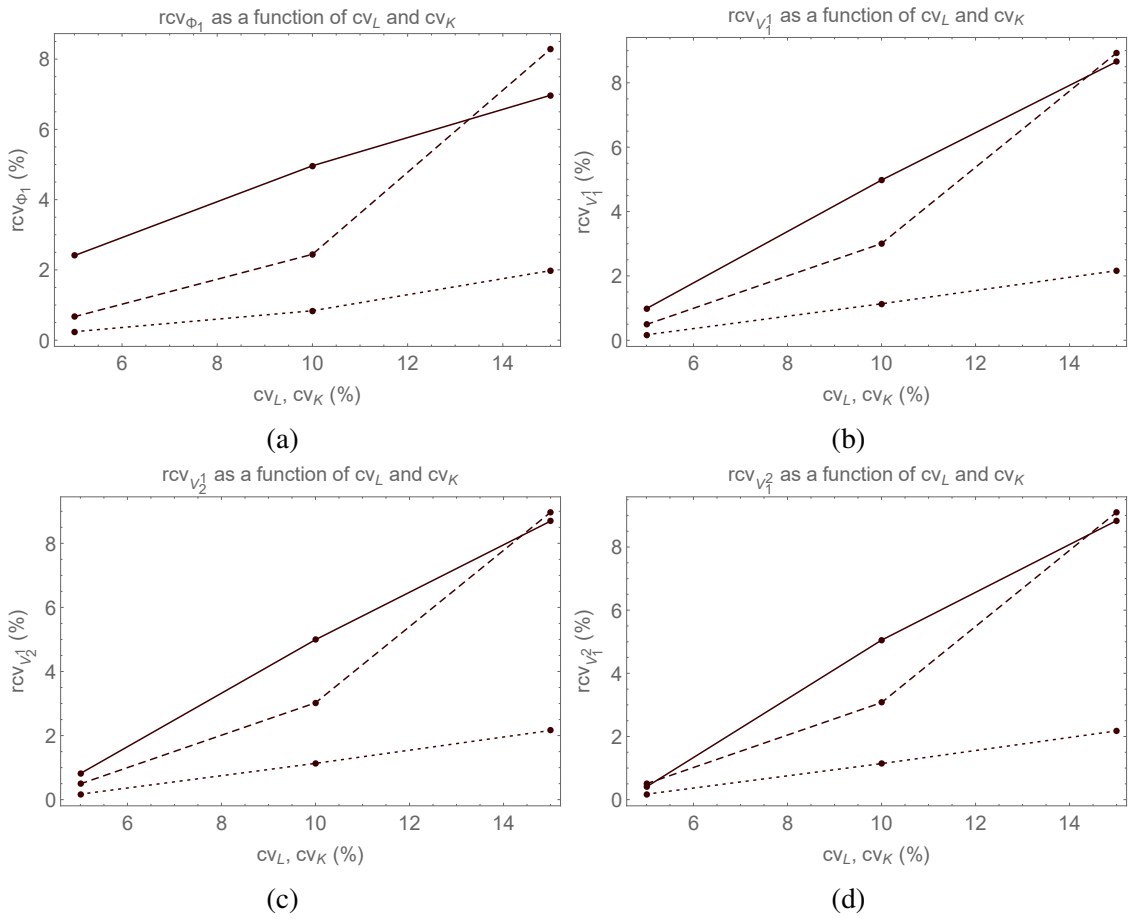

Fig. 4.9 Graphs of (a) rcv$_{\Phi_1}$, (b) rcv$_{V_1^1}$, (c) rcv$_{V_2^1}$, (d) rcv$_{V_1^2}$ for different values of cv$_L$ and cv$_K$. Solid line: results for cv$_L$ equal to cv$_K$ both different from zero. Dashed line: results for cv$_L$ different from zero and cv$_K$ equal to zero. Dotted line: results for cv$_L$ equal to zero and cv$_K$ different from zero.

4.3 Sensitivity of a particle-based homogeneous and isotropic second-gradient continuum model with respect to uncertain constitutive fields

This section is the outcome of collaboration with Professor Christian Soize and continues in line with Section 4.2. It presents a comprehensive study on the development and

application of a stochastic second-gradient continuum model for particle-based materials, with an application focused on disorder colloidal crystals. Colloidal crystals represent an important class of particle-based materials. They find applications in material sciences and Biomedical engineering [26], as optical materials [144], and have the potential to improve 3D printing technologies due to their tunable electrical, optical, mechanical, and rheological properties [150]. Currently, significant scientific efforts are underway to realize complex colloidal crystals and novel colloidal crystal microsensing systems [143, 85]. In a perfectly ordered colloidal crystal, particles are arranged in a regular, periodic lattice structure. However, deviations from this ideal structure, such as sphere vacancies, line dislocations, and random position errors, can degrade the optical properties, leading to disorder colloidal crystals [101, 113]. Since we are dealing with particle-based materials and not granular materials, factors such as the topology of contacts, granulometry, grain sizes, shapes, and geometric structure are not considered. The model incorporates random fields to capture the spatial variability and heterogeneity present in the geometric and material properties of these materials. The computational framework is based on the mixed Finite Element (FE) method applied to the equivalent second-gradient continuum. The Monte Carlo (MC) numerical simulation method is used as a stochastic solver of the random formulation of the Boundary Value Problem (BVP). The paper begins with an overview of an existing second-gradient continuum model for particle-based materials. Then, it incorporates random fields into this model to provide a more realistic representation of the geometric and material properties. Finally, the resulting stochastic second-gradient model is applied to analyze disorder colloidal crystals, which have wide-ranging applications.

4.3.1 Defining the stochastic particle-based second-gradient equivalent continuum

We hereby introduce the key aspects of the stochastic particle-based second-gradient equivalent continuum. Further details can be found in [94, 13, 136, 104].

Let us consider a particle 3D-lattice structure contained within an open bounded domain $\mathcal{B} \subset \mathbb{R}^3$ with a sufficiently smooth boundary $\partial\mathcal{B}$. The 3D-lattice structure is assumed to be composed of n_{pts} at constant spacing $\underline{\ell}$. Two particles at distance $\underline{\ell}$ are here named consecutive particles (see Fig. 4.10). Let $\underline{\boldsymbol{q}}_i$ and $\underline{\boldsymbol{q}}_j$ be two consecutive particles in the nominal configuration. Let $\underline{\widehat{\boldsymbol{n}}}(\underline{\boldsymbol{q}}_i, \underline{\boldsymbol{q}}_j)$ be the unit vector that describes the direction of the particle-pair consisting of the one at $\underline{\boldsymbol{q}}_i$ and the other one at $\underline{\boldsymbol{q}}_j$. In this section, stochastic considerations are introduced, wherein the symbol $\boldsymbol{q}$ is preferred for denoting the Lagrangian coordinates, as the symbol X is reserved for the random quantities. For the stochastic

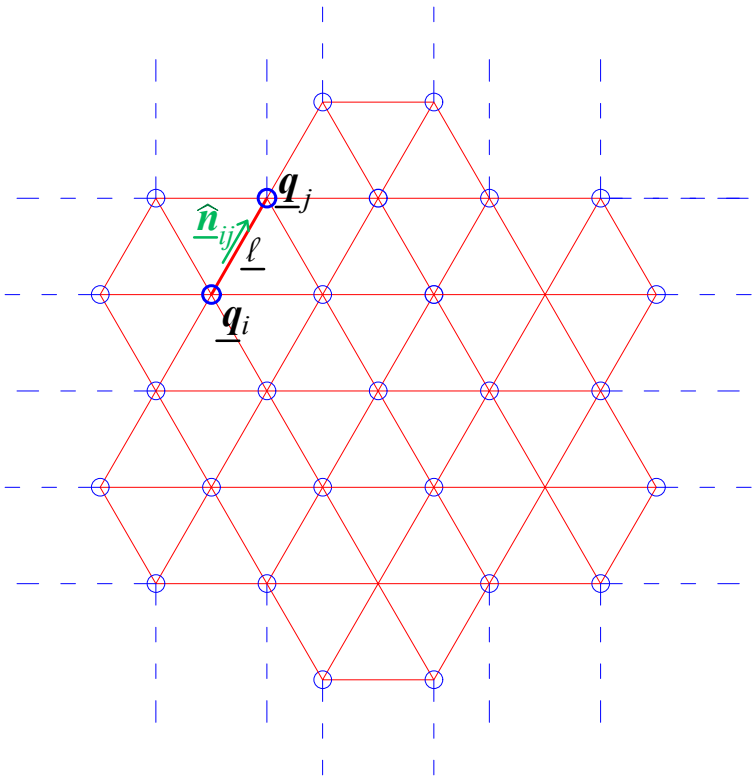

Fig. 4.10 Illustration of a 2D material made up of particles placed at constant spacing. We depict the geometrical significance of $\underline{\ell}$ and $\underline{\hat{n}}_{ij}$. The model takes into account both the interactions in the direction described by $\underline{\hat{n}}_{ij}$ and in the direction orthogonal to $\underline{\hat{n}}_{ij}$. In particular, stiffness is assumed constant in the plane orthogonal to $\underline{\hat{n}}_{ij}$.

description, $\underline{\boldsymbol{q}}_i$ and $\underline{\boldsymbol{q}}_j$ are modeled by the random variables $\boldsymbol{Q}_i$ and $\boldsymbol{Q}_j$. Let $L_{ij}(\boldsymbol{Q}_i, \boldsymbol{Q}_j)$ be the distance between $\boldsymbol{Q}_i$ and $\boldsymbol{Q}_j$, and let $\widehat{\boldsymbol{N}}_{ij}(\boldsymbol{Q}_i, \boldsymbol{Q}_j)$ describing the direction connecting $\boldsymbol{Q}_i$ and $\boldsymbol{Q}_j$, which can also be described by means of the random Euler angles $\boldsymbol{\Omega}_{ij}(\boldsymbol{Q}_i, \boldsymbol{Q}_j)$. Let $K_{\eta ij}(\boldsymbol{Q}_i, \boldsymbol{Q}_j)$ and $K_{\tau ij}(\boldsymbol{Q}_i, \boldsymbol{Q}_j)$ be the random stiffnesses associated with the deformation in the direction defined by $\widehat{\boldsymbol{N}}_{ij}(\boldsymbol{Q}_i, \boldsymbol{Q}_j)$ and any direction orthogonal to it, respectively. We assume that the level of particle disordering is small enough to approximate the initial domain transformed by the disordering as the initial domain itself. Let $\{\{L(\boldsymbol{q};\theta), \theta \in \Theta\}, \boldsymbol{q} \in \mathcal{B}\}$ be the random field defined such that, at $\boldsymbol{q} = \boldsymbol{Q}_i(\theta)$,

$$L\left(\boldsymbol{Q}_i(\theta);\theta\right) = \frac{1}{n_i} \sum_j L_{ij}(\boldsymbol{Q}_i(\theta), \boldsymbol{Q}_j(\theta)), \tag{4.115}$$

with j such that $\underline{\boldsymbol{q}}_j$ is consecutive to $\underline{\boldsymbol{q}}_i$, n_i being the number of particles consecutive to $\underline{\boldsymbol{q}}_i$. Let $\{\{K_\eta(\boldsymbol{q};\theta), \theta \in \Theta\}, \boldsymbol{q} \in \mathcal{B}\}$ and $\{\{K_\tau(\boldsymbol{q};\theta), \theta \in \Theta\}, \boldsymbol{q} \in \mathcal{B}\}$ be the random fields associated with the stiffnesses such that, at $\boldsymbol{q} = \boldsymbol{Q}_i(\theta)$,

$$K_\eta\left(\boldsymbol{Q}_i(\theta);\theta\right) = \frac{1}{n_i} \sum_j K_{\eta ij}(\boldsymbol{Q}_i(\theta), \boldsymbol{Q}_j(\theta)). \tag{4.116}$$

$$K_\tau\left(\boldsymbol{Q}_i(\theta),\theta\right) = \frac{1}{n_i} \sum_j K_{\eta ij}(\boldsymbol{Q}_i(\theta), \boldsymbol{Q}_j(\theta)). \tag{4.117}$$

Using the same approach, which some authors refer to as the Piola Ansatz [36], we introduce the deterministic field $\widehat{\boldsymbol{n}}(\boldsymbol{\omega})$, where $\boldsymbol{\omega}$ belongs to $\mathcal{S} = [0,\pi] \times [0,2\pi]$. At $\boldsymbol{\omega}(\theta) = \Omega_{ij}(\boldsymbol{Q}_i(\theta), \boldsymbol{Q}_j(\theta))$, this field satisfies $\widehat{\boldsymbol{n}}(\boldsymbol{\omega}(\theta)) = \widehat{\boldsymbol{N}}_{ij}(\boldsymbol{Q}_i(\theta), \boldsymbol{Q}_j(\theta))$. We also introduce the random objective deformation field $\boldsymbol{U}(\boldsymbol{q}, \overline{\boldsymbol{q}}; \boldsymbol{\omega})$ that is defined by

$$U^C(\boldsymbol{q}, \overline{\boldsymbol{q}}; \boldsymbol{\omega}) = 2\,[E]_B^C(\boldsymbol{q})\,\widehat{n}^B(\boldsymbol{\omega})\,L(\boldsymbol{q}, \overline{\boldsymbol{q}}) + \frac{1}{2}\,[\mathfrak{H}]_{AB}^C(\boldsymbol{q})\,\widehat{n}^B(\boldsymbol{\omega})\,\widehat{n}^A(\boldsymbol{\omega})\,L^2(\boldsymbol{q}, \overline{\boldsymbol{q}}), \tag{4.118}$$

where $[\boldsymbol{E}](\boldsymbol{q})$ is the random Cauchy–Green deformation tensor defined by

$$[E]_B^C(\boldsymbol{q}) = \frac{1}{2} g^{MC} \left(\frac{\partial R^i(\boldsymbol{q})}{\partial q^B} \frac{\partial R^j(\boldsymbol{q})}{\partial q^M} g_{ij} - \delta_{BM} \right), \tag{4.119}$$

in which $\{\{\boldsymbol{R}(\boldsymbol{q};\theta), \theta \in \Theta\}, \boldsymbol{q} \in \mathcal{B}\}$ is the random configuration field defined by

$$\boldsymbol{R}\left(\widetilde{\boldsymbol{Q}}_i(\theta);\theta\right) = \boldsymbol{R}_i(\boldsymbol{Q}_i(\theta)), \tag{4.120}$$

where $\boldsymbol{R}_i(\boldsymbol{Q}_i(\theta))$ defines the position of $\boldsymbol{Q}_i(\theta)$, and $[\mathfrak{H}](\boldsymbol{q})$ is the random second-gradient

deformation tensor defined by

$$\left[\mathfrak{H}_\beta\right]^C_{AB}(\boldsymbol{q}) = \frac{1}{2}\left[g\right]^{DC}\left(\left.\frac{\partial\left[E\right]^A_D(\boldsymbol{q})}{\partial q^B}\right|_{\boldsymbol{q}=\boldsymbol{q}_\beta} + \left.\frac{\partial\left[E\right]_{BD}(\boldsymbol{q})}{\partial q^A}\right|_{\boldsymbol{q}=\boldsymbol{q}_\beta} - \left.\frac{\partial\left[E\right]_{BA}(\boldsymbol{q})}{\partial q^D}\right|_{\boldsymbol{q}=\boldsymbol{q}_\beta}\right). \tag{4.121}$$

For $\boldsymbol{\omega}$ in $\mathcal{S}$, let us introduce the random deformation energy per unit direction, $\{\Psi(\boldsymbol{q},\overline{\boldsymbol{q}};\boldsymbol{\omega}),\boldsymbol{q}\in\mathcal{B}\}$, such that

$$\Psi(\boldsymbol{q},\overline{\boldsymbol{q}};\omega)) = \frac{1}{2}K_\eta(\boldsymbol{q},\overline{\boldsymbol{q}})\left\|\boldsymbol{U}_\eta(\boldsymbol{q},\overline{\boldsymbol{q}};\omega))\right\|^2 + \frac{1}{2}K_\tau(\boldsymbol{q},\overline{\boldsymbol{q}})\left\|\boldsymbol{U}_\tau(\boldsymbol{q},\overline{\boldsymbol{q}};\omega)\right\|^2, \tag{4.122}$$

in which

$$\boldsymbol{U}_\eta(\boldsymbol{q},\overline{\boldsymbol{q}};\omega)) = \frac{1}{2}\left(\boldsymbol{U}(\boldsymbol{q},\overline{\boldsymbol{q}};\omega)\cdot\widehat{\boldsymbol{n}}(\omega)\right)\widehat{\boldsymbol{n}}(\omega) \quad , \quad \boldsymbol{U}_\tau(\boldsymbol{q},\overline{\boldsymbol{q}};\omega)) = \boldsymbol{U}(\boldsymbol{q};\overline{\boldsymbol{q}};\omega) - \boldsymbol{U}_\eta(\boldsymbol{q},\overline{\boldsymbol{q}};\omega)\,. \tag{4.123}$$

Hence, let us define the random fields $\{\Xi_1(\boldsymbol{q}),\ \boldsymbol{q}\in\mathcal{B}\}$ and $\{\Xi_2(\boldsymbol{q}),\ \boldsymbol{q}\in\mathcal{B}\}$ such that

$$\Xi_1(\boldsymbol{q}) = \frac{4\pi L^2(\boldsymbol{q})}{15}\left(K_\eta(\boldsymbol{q}) - 4K_\tau(\boldsymbol{q})\right) \quad , \quad \Xi_2(\boldsymbol{q}) = \frac{4\pi L^2(\boldsymbol{q})}{15}\left(K_\eta(\boldsymbol{q}) + 6K_\tau(\boldsymbol{q})\right), \tag{4.124}$$

which are the random Lamé coefficients. Let us define the random fields $\{\Xi_3(\boldsymbol{q}),\ \boldsymbol{q}\in\mathcal{B}\}$ to $\{\Xi_7(\boldsymbol{q}),\ \boldsymbol{q}\in\mathcal{B}\}$ such that

$$\Xi_3(\boldsymbol{q}) = \frac{L^2(\boldsymbol{q})}{112}\Xi_1(\boldsymbol{q}), \tag{4.125}$$

$$\Xi_4(\boldsymbol{q}) = \Xi_3(\boldsymbol{q})\,, \tag{4.126}$$

$$\Xi_5(\boldsymbol{q}) = \frac{L^2(\boldsymbol{q})}{1120}\left(7\Xi_2(\boldsymbol{q}) + 3\Xi_1(\boldsymbol{q})\right), \tag{4.127}$$

$$\Xi_6(\boldsymbol{q}) = \frac{L^2(\boldsymbol{q})}{1120}\left(7\Xi_2(\boldsymbol{q}) - 4\Xi_1(\boldsymbol{q})\right), \tag{4.128}$$

and

$$\Xi_7(\boldsymbol{q}) = \Xi_5(\boldsymbol{q})\,. \tag{4.129}$$

Let us define the random displacement field $\{\boldsymbol{V}(\boldsymbol{q}),\ \boldsymbol{q}\in\mathcal{B}\}$ such that $\boldsymbol{R}(\boldsymbol{q}) = \boldsymbol{q} + \boldsymbol{V}(\boldsymbol{q})$. Let $\{\Phi(\boldsymbol{q}),\ \boldsymbol{q}\in\mathcal{B}\}$ be the random field associated with the specific deformation energy defined by

$$\Phi(\boldsymbol{q}) = \int_{\mathcal{S}}\Psi(\boldsymbol{q};\omega)\,d\boldsymbol{\omega}. \tag{4.130}$$

Considering that deformation tensors $[\boldsymbol{E}]$ and $[\mathfrak{H}]$ depend on $\boldsymbol{V}$, to explicitly represent the dependencies of $\Phi(\boldsymbol{q})$ on $\boldsymbol{V}$, L, K_η, and K_τ, we introduce the functional ϕ such that

$\Phi(\boldsymbol{q}) = \phi\left(\boldsymbol{V}; L, K_\eta, K_\tau\right)(\boldsymbol{q})$. Searching for an equivalent continuum in the isotropic symmetry class, Eq. (4.130) yields the following expression

$$\begin{aligned}\Phi(\boldsymbol{q}) = \Xi_2(\boldsymbol{q})\ [E]^A_B(\boldsymbol{q})\ [E]^B_A(\boldsymbol{q}) + \frac{1}{2}\Xi_1(\boldsymbol{q})\ [E]^A_A(\boldsymbol{q})\ [E]^B_B(\boldsymbol{q})\\ +2\Xi_3(\boldsymbol{q})\ [\mathfrak{H}]^A_{AB}(\boldsymbol{q})\ [\mathfrak{H}]^B_{CC}(\boldsymbol{q}) + \frac{1}{2}\Xi_4(\boldsymbol{q})\ [\mathfrak{H}]^A_{AB}(\boldsymbol{q})\ [\mathfrak{H}]^C_{CB}(\boldsymbol{q})\\ +2\Xi_5(\boldsymbol{q})\ [\mathfrak{H}]^A_{BA}(\boldsymbol{q})\ [\mathfrak{H}]^B_{CC}(\boldsymbol{q}) + \Xi_6(\boldsymbol{q})\ [\mathfrak{H}]^A_{BC}(\boldsymbol{q})\ [\mathfrak{H}]^A_{BC}(\boldsymbol{q}) + 2\Xi_7(\boldsymbol{q})\ [\mathfrak{H}]^A_{BC}(\boldsymbol{q})\ [\mathfrak{H}]^C_{AB}(\boldsymbol{q}).\end{aligned} \tag{4.131}$$

The total deformation energy functional w is obtained by integrating the specific deformation energy as follows,

$$w\left(\boldsymbol{V}; L, K_\eta, K_\tau\right) = \int_{\mathcal{B}} \phi\left(\boldsymbol{V}; L, K_\eta, K_\tau\right)(\boldsymbol{q})\, d\boldsymbol{q}. \tag{4.132}$$

In the same way as before, w is written to explicitly show its dependencies on $\boldsymbol{V}$, L, K_η, and K_τ. It is crucial to emphasize that the introduced continuum model is not obtained by means of a homogenization procedure. It serves as an equivalent continuum model at the same scale.

4.3.2 Constructing the prior probability model of the involved random fields

Construction of the random field $\{L(\boldsymbol{q}), \boldsymbol{q} \in \mathcal{B}\}$

The objective is to define a prior probability model for the random field $\{L(\boldsymbol{q}), \boldsymbol{q} \in \mathcal{B}\}$. Let $\boldsymbol{Q}_i$ denote the random variable describing the position of the i-th particle in the given 3D-lattice structure. Random variable $\boldsymbol{Q}_i$ is uniformly distributed within a sphere of diameter $\rho_{\max} = \underline{\ell}/2 - d_{\max}/2$, centered at $\underline{\boldsymbol{q}}_i$ (where $\underline{\boldsymbol{q}}_i = (\underline{q}_i^1, \underline{q}_i^2, \underline{q}_i^3)$ is the nominal position of the i-th particle), and $\rho_{\max} > 0$. Here, $\underline{\ell}$ denotes the nominal particle spacing, which is assumed to be constant along the space, and $d_{\max}$ represents the maximum diameter of the particles. The assumptions on $\rho_{\max}$ ensure that there is nneither overlap nor contact among the particles. Let us introduce the random fields $\{A(\boldsymbol{q}), \boldsymbol{q} \in \mathcal{B}\}$, $\{\mathfrak{F}_1(\boldsymbol{q}), \boldsymbol{q} \in \mathcal{B}\}$, and $\{\mathfrak{F}_2(\boldsymbol{q}), \boldsymbol{q} \in \mathcal{B}\}$, related to spherical coordinates (one radius and two angles), which are assumed to be independent. Each one of these three random fields is assumed to be an uncountable collection of independent random variables having the same probability distribution. For all $\boldsymbol{q}$ in $\mathcal{B}$, the real-valued random variable $A(\boldsymbol{q})$ is uniformly distributed in $[0, \rho_{\max}]$, the real-valued random variable $\mathfrak{F}_1(\boldsymbol{q})$ is uniformly distributed in $[0, 2\pi]$, and the real-valued random variable $\mathfrak{F}_2(\boldsymbol{q})$ is uniformly distributed in $[0, \pi]$. The random position,

$\boldsymbol{Q}_i = \left(Q_i^1, Q_i^2, Q_i^3\right)$, of the i-th particle, is defined by

$$Q_i^1 = \underline{q}_i^1 + A(\underline{\boldsymbol{q}}_i)\cos(\mathfrak{F}_1(\underline{\boldsymbol{q}}_i))\sin(\mathfrak{F}_2(\underline{\boldsymbol{q}}_i))\,, \tag{4.133}$$

$$Q_i^2 = \underline{q}_i^2 + A(\underline{\boldsymbol{q}}_i)\sin(\mathfrak{F}_1(\underline{\boldsymbol{q}}_i))\sin(\mathfrak{F}_2(\underline{\boldsymbol{q}}_i))\,, \tag{4.134}$$

and

$$Q_i^3 = \underline{q}_i^3 + A(\underline{\boldsymbol{q}}_i)\cos(\mathfrak{F}_2(\underline{\boldsymbol{q}}_i))\,. \tag{4.135}$$

For each realization $\theta \in \Theta$, the trajectories $\boldsymbol{q} \mapsto L(\boldsymbol{q}, \theta)$ of random field $\{L(\boldsymbol{q}), \boldsymbol{q} \in \mathcal{B}\}$ are constructed by means of Eq. (4.115).

Construction of random field $\{[\boldsymbol{K}(\boldsymbol{q})], \boldsymbol{q} \in \mathcal{B}\}$ and its generator of realizations at sampling points

In accordance with the MaxEnt principle from information theory, our goal is to develop a prior probability model for the random fields $\{K_\eta(\boldsymbol{q}), \boldsymbol{q} \in \mathcal{B}\}$, and $\{K_\tau(\boldsymbol{q}), \boldsymbol{q} \in \mathcal{B}\}$. To achieve this, we construct the prior probability model for the matrix-valued random field $\{[\boldsymbol{K}(\boldsymbol{q})], \boldsymbol{q} \in \mathcal{B}\}$ such that

$$[\boldsymbol{K}(\boldsymbol{q})] = \begin{bmatrix} K_\eta(\boldsymbol{q}) & 0 \\ 0 & K_\tau(\boldsymbol{q}) \end{bmatrix}, \tag{4.136}$$

while taking into account the available information outlined below. Matrix-valued random field $\{[\boldsymbol{K}(\boldsymbol{q})], \boldsymbol{q} \in \mathcal{B}\}$ is a restriction to $\mathcal{B}$ of the homogeneous and second-order random field $\{[\boldsymbol{K}(\boldsymbol{q})], \boldsymbol{q} \in \mathbb{R}^3\}$ indexed by $\mathbb{R}^3$. It must take values in the ensemble $\mathbb{M}^+_{2\,\mathrm{diag}}$ of diagonal positive-definite random matrices. The mean function of $\{[\boldsymbol{K}(\boldsymbol{q})], \boldsymbol{q} \in \mathbb{R}^3\}$, which is independent of $\boldsymbol{q}$, is a constant matrix given in $\mathbb{M}^+_{\mathrm{diag}}$,

$$\mathbb{E}\{[\boldsymbol{K}(\boldsymbol{q})]\} = [\underline{\boldsymbol{k}}] \quad , \quad \left[\underline{\boldsymbol{k}}\right] = \begin{bmatrix} \underline{k}_\eta & 0 \\ 0 & \underline{k}_\tau \end{bmatrix} \in \mathbb{M}^+_{\mathrm{diag}}\,. \tag{4.137}$$

The second-order moment of $[\boldsymbol{K}(\boldsymbol{q})]^{-1}$ must be finite for physical consistency. Note that, random matrix $[\boldsymbol{K}(\boldsymbol{q})]$ is almost-surely invertible, which does not imply neither the existence of a second-order moment of its inverse nor the existence of a deterministic lower bound. Following the formulation proposed in [129], a deterministic lower bound is introduced, which assures the existence of the second-order moment of the inverse. Consequently, the

algebraic representation of $[\boldsymbol{K}(\boldsymbol{q})]$ is defined as

$$[\boldsymbol{K}(\boldsymbol{q})] = \frac{1}{1+\varepsilon}\left(\varepsilon\,[\underline{\boldsymbol{k}}] + \left[\underline{\boldsymbol{k}}\right]^{1/2}[\boldsymbol{G}(\boldsymbol{q})]\left[\underline{\boldsymbol{k}}\right]^{1/2}\right). \tag{4.138}$$

In Eq. (4.138), ε is an arbitrarily sufficiently small positive number, $\left[\underline{\boldsymbol{k}}\right]^{1/2}$ is the square root of $\left[\underline{\boldsymbol{k}}\right]$, and $\{[\boldsymbol{G}(\boldsymbol{q})], \boldsymbol{q} \in \mathbb{R}^3\}$ is a homogeneous, second-order, non-Gaussian $\mathbb{M}^+_{\text{diag}}$-valued random field, which must satisfies

$$\mathbb{E}\{[\boldsymbol{G}(\boldsymbol{q})]\} = [I_2] \;,\; \mathbb{E}\{\log(\det[\boldsymbol{G}(\boldsymbol{q})])\} = \nu,\; |\nu| < +\infty \;,\; \forall \boldsymbol{q} \in \mathbb{R}^3, \tag{4.139}$$

as proposed in [127] and where ν is independent of $\boldsymbol{q}$. Matrix-valued random field $\{[\boldsymbol{G}(\boldsymbol{q})], \boldsymbol{q} \in \mathbb{R}^3\}$ is constructed using the MaxEnt principle under constraints defined by Eq. (4.139) following the methodology and developments proposed in [127, 66, 129], which are summarized in the following.

Construction of random germ $\{Z(\boldsymbol{q}), \boldsymbol{q} \in \mathbb{R}^3\}$ of random field $\{[\boldsymbol{G}(\boldsymbol{q})], \boldsymbol{q} \in \mathbb{R}^3\}$ and its generator at sampling points

The random germ $\{Z(\boldsymbol{q}), \boldsymbol{q} \in \mathbb{R}^3\}$ is a Gaussian, second-order, centered, homogeneous random field for which the autocorrelation function is expressed as

$$R_Z(\boldsymbol{\eta}) = \prod_{j=1}^{3} \varrho_j(\eta_j) \quad , \quad \forall \boldsymbol{\eta} = (\eta_1, \eta_2, \eta_3) \in \mathbb{R}^3, \tag{4.140}$$

where, for all $j = 1, 2, 3$,

$$\varrho_j(0) = 1 \quad , \quad \varrho_j(\eta_j) = \frac{4\lambda_j^2}{\pi^2\eta_j^2}\sin^2\left(\frac{\pi\eta_j}{2\lambda_j}\right) \quad \text{for} \quad \eta_j \neq 0. \tag{4.141}$$

The symbols λ_1, λ_2, λ_3 denote positive real numbers that represent the spatial correlation lengths of random germ $\{Z(\boldsymbol{q}), \boldsymbol{q} \in \mathbb{R}^3\}$. Since the objective is to simulate $\{Z(\boldsymbol{q}), \boldsymbol{q} \in \mathbb{R}^3\}$ at given points $\boldsymbol{q}_1, \ldots, \boldsymbol{q}_m$ of $\mathcal{B} \subset \mathbb{R}^3$, we define the random vector $\boldsymbol{Z} = \left(Z(\boldsymbol{q}_1), \ldots, Z(\boldsymbol{q}_m)\right)$ that belongs to $\mathbb{R}^m$. Different procedures exist in the literature. As explained in [127], we can use neither the method proposed in [122–124] adapted for large values of m or a method adapted for small values of m, which involves the Cholesky factorization of the covariance matrix of $\boldsymbol{Z}$ [127]. Below, we summarize the procedure adapted for small values of m that will be used in Section 4.2.3, devoted to the numerical application. Since random vector $\boldsymbol{Z}$ is

centered, the covariance matrix $[C_{\boldsymbol{Z}}] \in \mathbb{M}_m^+$ of Z is given by the formula

$$[C_{\boldsymbol{Z}}]_{ij} = R_Z\left(\boldsymbol{q}_i - \boldsymbol{q}_j\right). \tag{4.142}$$

Then, the Cholesky factorization $[C_{\boldsymbol{Z}}] = [L_{\boldsymbol{Z}}]^T [L_{\boldsymbol{Z}}]$ can be performed. We can express the random vector $\boldsymbol{Z}$ as the linear transformation

$$\boldsymbol{Z} = [L_{\boldsymbol{Z}}]^T \widetilde{\boldsymbol{Z}}, \tag{4.143}$$

in which $\widetilde{\boldsymbol{Z}} = (\widetilde{Z}_1, \ldots, \widetilde{Z}_m)$ is a $\mathbb{R}^m$-random variable whose components $\widetilde{Z}_1, \ldots, \widetilde{Z}_m$ are m independent normalized Gaussian random variables, i.e., $\mathbb{E}\{\widetilde{Z}_j\} = 0$ and $\mathbb{E}\{(\widetilde{Z}_j)^2\} = 1$ for $j = 1, \ldots, m$. To finish the construction of the family of random matrices $\{[\boldsymbol{G}(\boldsymbol{q}_i)], i = 1, \ldots, m\}$ as a function of the family of random matrices $\{\boldsymbol{Z}(\boldsymbol{q}_i), i = 1, \ldots, m\}$, it is necessary to introduce a family of functions $\{y \mapsto h(\alpha, y)\}_{\alpha>0}$ defined in Section 4.3.2.

Definition of the family of functions $\{y \mapsto h(\alpha, y)\}_{\alpha>0}$

Let us consider a positive real number α. Let $y \mapsto h(\alpha, y)$ be a function from $\mathbb{R}$ into $]0, +\infty[$ such that $\Gamma_\alpha = h(\alpha, Y)$ is a Gamma random variable with parameter α and Y is a normalized Gaussian random variable, i.e., $\mathbb{E}\{Y\} = 0$ and $\mathbb{E}\{Y^2\} = 1$. For all $y \in \mathbb{R}$, mapping $h(\alpha, \cdot)$ is written as

$$h(\alpha, y) = F_{\Gamma_\alpha}^{-1}(F_Y(y)), \tag{4.144}$$

in which $\gamma \mapsto F_{\Gamma_\alpha}(\gamma)$ is the cumulative distribution of random variable Γ_α, $y \mapsto F_Y(y)$ is the cumulative distribution of random variable Y,

$$F_{\Gamma_\alpha}(\gamma) = \int_0^\gamma \frac{1}{\Gamma(\alpha)} t^{\alpha-1} e^{-t}\, dt \quad , \quad F_Y(y) = \int_0^y \frac{1}{\sqrt{2\pi}} e^{-t^2/2}\, dt, \tag{4.145}$$

$\alpha \mapsto \Gamma(\alpha)$ is the Gamma function defined by

$$\Gamma(\alpha) = \int_0^{+\infty} t^{\alpha-1} e^{-t}\, dt, \tag{4.146}$$

in which $F_{\Gamma_\alpha}^{-1}$ is the inverse function of F_{Γ_α}.

Construction of the family of matrices $\{[\boldsymbol{G}(\boldsymbol{q}_i)], i=1,\ldots,m\}$ **and** $\{[\boldsymbol{K}(\boldsymbol{q}_i)], i=1,\ldots,m\}$

Let $Z_{11}(\boldsymbol{q}_i)$ and $Z_{22}(\boldsymbol{q}_i)$ be two independent copies of the random variable $Z(\boldsymbol{q}_i)$, with $i=1,\ldots,m$, built as in Section 4.3.2. Eq. (4.143) implies $\mathbb{E}\{Z_{jj}(\boldsymbol{q}_i)\}=0$ and $\mathbb{E}\{Z_{jj}^2(\boldsymbol{q}_i)\}=1$. Let $\delta_{[\boldsymbol{G}]}$ be a real number independent of $\boldsymbol{q}_i$ such that $0<\delta_{[\boldsymbol{G}]}<\sqrt{3/7}$, which enables to control the statistical fluctuation of the random field $\{[\boldsymbol{G}(\boldsymbol{q})], \boldsymbol{q}\in\mathbb{R}^3\}$. Let us define the random matrix $[\boldsymbol{L}_2(\boldsymbol{q}_i)]$ such that

$$[\boldsymbol{L}_2(\boldsymbol{q}_i)] = \begin{bmatrix} \sigma_2\sqrt{2\,h(\alpha_1, Z_{11}(\boldsymbol{q}_i))} & 0 \\ 0 & \sigma_2\sqrt{2\,h(\alpha_2, Z_{22}(\boldsymbol{q}_i))} \end{bmatrix}, \tag{4.147}$$

in which $\sigma_2=\delta_{[\boldsymbol{G}]}/\sqrt{3}$, $\alpha_1=3/(2\delta_{[\boldsymbol{G}]}^2)$, $\alpha_2=3/(2\delta_{[\boldsymbol{G}]}^2)-1/2$, and $h(\alpha,y)$ is defined by Eq. (4.144). Finally, the random matrix $[\boldsymbol{G}(\boldsymbol{q}_i)]$ is given by

$$[\boldsymbol{G}(\boldsymbol{q}_i)] = [\boldsymbol{L}_2(\boldsymbol{q}_i)]^T [\boldsymbol{L}_2(\boldsymbol{q}_i)]\,. \tag{4.148}$$

The objective is to simulate the family of random matrices $\{[\boldsymbol{K}(\boldsymbol{q}_i)], i=1,\ldots,m\}$. Taking into account Eq. (4.138), the random matrix $[\boldsymbol{K}(\boldsymbol{q}_i)]$ is written as,

$$[\boldsymbol{K}(\boldsymbol{q}_i)] = \frac{1}{1+\varepsilon}\left(\varepsilon\,[\underline{\boldsymbol{k}}] + [\underline{\boldsymbol{k}}]^{1/2}[\boldsymbol{L}_2(\boldsymbol{q}_i)]^T[\boldsymbol{L}_2(\boldsymbol{q}_i)][\underline{\boldsymbol{k}}]^{1/2}\right), \tag{4.149}$$

which depends on three correlation lengths $\lambda_1,\lambda_2,\lambda_3$ and dispersion parameter $\delta_{[\boldsymbol{G}]}$.

Weak formulation of the stochastic boundary value problem and its strong stochastic solution

Let $C_{\boldsymbol{v}}$ representing the set of admissible displacements $\boldsymbol{v}:\boldsymbol{q}\mapsto\boldsymbol{v}(\boldsymbol{q})$ defined on $\mathcal{B}$ with values in $\mathbb{R}^3$ satisfying the zero Dirichlet conditions on $\partial\mathcal{B}_0$ and $\partial\mathcal{B}_t$ in $\partial\mathcal{B}$. Let $\mathbb{H}=\mathbb{L}^2(\Theta, C_{\boldsymbol{v}})$ be the set of the random fields $\boldsymbol{V}=\{\boldsymbol{V}(\boldsymbol{q}), \boldsymbol{q}\in\mathcal{B}\}$ defined on probability space $(\Theta,\mathcal{T},\mathcal{P})$ with values in $C_{\boldsymbol{v}}$, which are of second-order: for all $\boldsymbol{q}$ in $\mathcal{B}$, $\mathbb{E}\{\|\boldsymbol{V}(\boldsymbol{q})\|^2\}<+\infty$. The strong stochastic solution of the weak formulation of the stochastic BVP is: find $\boldsymbol{V}$ in $\mathbb{H}$, such that

$$\delta\pi(\boldsymbol{V},\delta\boldsymbol{v};L,K_\eta,K_\tau)=0 \quad , \quad \forall\,\delta\boldsymbol{v}\in C_{\boldsymbol{v}} \quad , \quad a.s., \tag{4.150}$$

where $\delta\pi$ is the first variation of the energy functional π defined on $C_{\boldsymbol{v}}$ by

$$\pi(\boldsymbol{v};L,K_\eta,K_\tau) = w(\boldsymbol{v};L,K_\eta,K_\tau) - s(\boldsymbol{v}) \quad , \quad \boldsymbol{v}\in C_{\boldsymbol{v}}\,, \tag{4.151}$$

in which the functional w is defined in Eq. (4.132), and where the functional s is defined by

$$s(\boldsymbol{v}) = -\int_{\partial\mathcal{B}} \langle \widetilde{\boldsymbol{t}}^{\text{ext}}(\boldsymbol{q}), \boldsymbol{v}(\boldsymbol{q}) \rangle \, d\sigma(\boldsymbol{q}) \,, \tag{4.152}$$

where $\widetilde{\boldsymbol{t}}^{\text{ext}}(\boldsymbol{q})$ denotes the vector of the external actions at $\boldsymbol{q}$, and $d\sigma(\boldsymbol{q})$ is the surface element. It is assumed that there is a unique strong solution $\boldsymbol{V}$ in $\mathbb{H}$. In Section 4.2.3, this strong stochastic solution is constructed using a stochastic solver based on Monte Carlo (MC) numerical simulation [118, 115].

4.3.3 Application to 2D disorder colloidal crystals

Colloidal crystals consist of particles arranged in ordered arrays. However, imperfections can occur, causing perturbations in the ordered structure. When perturbations occur, we refer to the resulting structure as disordered colloidal crystals. Hereafter, we study a rectangular 2D disorder colloidal crystal using the random particle-based equivalent continuum model presented in Section 4.3.1, where random fields are built as described in Section 4.2.2. The rectangular domain is denoted by $\mathcal{B} \subset \mathbb{R}^2$ and its boundary is represented by $\partial\mathcal{B} = \partial\mathcal{B}_0 \cup \partial\mathcal{B}_t \cup \partial\mathcal{B}_1$. Zero Dirichlet conditions are applied on the left-end boundary denoted as $\partial\mathcal{B}_0$ and on the right-end boundary denoted as $\partial\mathcal{B}_t$. A uniaxial traction force is applied on $\partial\mathcal{B}_t$. The displacement field is free on the boundaries $\partial\mathcal{B}_1$ as shown in Fig. 4.11.

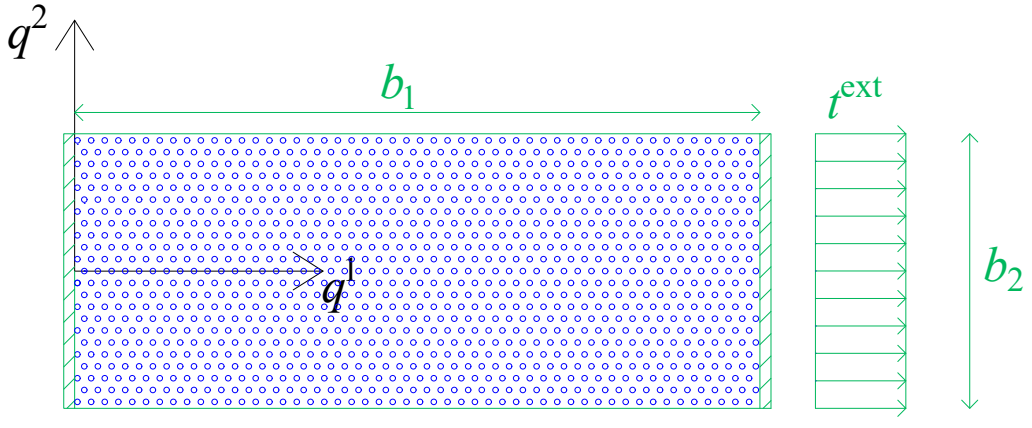

Fig. 4.11 Scheme of the considered colloidal crystal and of the simulated axial traction test.

Geometry characteristics, load magnitude, and random fields parameters

The 2D domain $\mathcal{B}$ occupied by the colloidal crystal is defined as a rectangle (see Fig. 4.11) whose dimensions are $b_1 = 1.38 \times 10^{-5}\,\mathrm{m}$ and $b_2 = 5.52 \times 10^{-6}\,\mathrm{m}$. Regarding the diameters of the colloidal particles, the particle spacing, and the mechanical properties, we refer to [84]. 2D samples are considered, consisting of particles with a diameter of $1.09 \times 10^{-7}\,\mathrm{m}$ ($0.109\,\mu\mathrm{m}$) forming a 2D triangular lattice structure. We examine the impact of three different values of nominal particle spacing $\underline{\ell} = \mathbb{E}\{L(\boldsymbol{q})\}$, which is assumed to remain constant throughout the space. The investigated values are $2.76 \times 10^{-7}\,\mathrm{m}$ ($0.276\,\mu\mathrm{m}$), $2.3 \times 10^{-7}\,\mathrm{m}$ ($0.23\,\mu\mathrm{m}$), and $2.1 \times 10^{-7}\,\mathrm{m}$ ($0.21\,\mu\mathrm{m}$). When considering $\underline{\ell} = 2.76 \times 10^{-7}\,\mathrm{m}$, these samples correspond to an area fraction of 0.12 and a particle concentration of $1.2 \times 10^{14}\,\mathrm{particles/cm^3}$ (for density calculation, we consider a thickness equal to the particle diameter). The mean shear modulus of the equivalent continuum is $\underline{\Xi}_1 = 20\,\mathrm{Pa}$ ($200\,\mathrm{dyn/cm^2}$). Moreover, we choose $\underline{\Xi}_2 = 8\,\mathrm{Pa}$ ($80\,\mathrm{dyn/cm^2}$), resulting in a ratio between the bulk modulus and shear modulus of 1.06. This choice corresponds to a physical state that is far from the melting point of the phase transition [149]. It is important to note that there exists a wide range of studies investigating the mechanical properties of colloidal crystals. These properties can vary due to factors such as particle size and shape, interparticle interactions, packing, ordering, temperature, surface effects, external environment, and more. One of the advantages of the equivalent second-gradient continuum model summarized in Section 4.3.1, together with the probability model introduced in Section 4.2.2, is its applicability to any colloidal crystal. The effect of line forces t^{ext} of different amplitudes ranging from zero to $2.5 \times 10^{-6}\,\mathrm{N/m}$ is investigated. Using Eq. (4.79), choosing $\underline{\ell} = 2.76 \times 10^{-7}\,\mathrm{m}$, considering that $L(\boldsymbol{q})$ is statistically independent on $K_\eta(\boldsymbol{q})$ and $K_\tau(\boldsymbol{q})$, and solving the linear equations for the mean values $\underline{k}_\eta = \mathbb{E}\left\{K_\eta(\boldsymbol{q})\right\}$ and $\underline{k}_\tau = \mathbb{E}\{K_\tau(\boldsymbol{q})\}$ yield

$$\underline{k}_\eta = 1.47 \times 10^{-13}\,\mathrm{N/m^4} \quad , \quad \underline{k}_\tau = 1.57 \times 10^{-14}\,\mathrm{N/m^4}\,, \tag{4.153}$$

which are used in all the computations. We consider two different scenarios: one with random stiffnesses and deterministic particle spacing (i.e., without disordering), and another with random stiffnesses and random particle spacing (i.e., with disordering). Random stiffnesses are controlled by the dispersion parameter $\delta_{[\boldsymbol{G}]}$ and the two correlation lengths λ_1 and λ_2 in the two directions defined by the global Cartesian coordinate system. We assume that the two correlation lengths are equal and we introduce the correlation length λ defined by $\lambda := \lambda_1 = \lambda_2$. A parametric study is conducted for three different values of $\delta_{[\boldsymbol{G}]}$, $0.1, 0.2, 0.3$ ($10\,\%, 20\,\%, 30\,\%$), and three different values of λ, $10^{-3}\,\underline{\ell}$, $\underline{\ell}$, and $2\,\underline{\ell}$. The sensitivity of

the mechanical response of the disordered colloidal crystal is investigated with respect to variations in $\delta_{[\boldsymbol{G}]}$ and λ.

Computational model and Monte Carlo numerical simulation

As explained in Section 4.3.2, the strong stochastic solution is obtained via a stochastic solver based on Monte Carlo (MC) numerical simulation. The domain $\mathcal{B}$ is divided into m subdomains, and their centroids are denoted as $\boldsymbol{q}_1, \ldots, \boldsymbol{q}_m$. After selecting the parameters $\delta_{[\boldsymbol{G}]}$ and λ for the random fields $\{K_\eta(\boldsymbol{q}), \boldsymbol{q} \in \mathcal{B}\}$ and $\{K_\tau(\boldsymbol{q}), \boldsymbol{q} \in \mathcal{B}\}$, we generate n independent realizations of them at $\boldsymbol{q}_1, \ldots, \boldsymbol{q}_m$. Similarly, if the particle spacing is assumed to be random, then we compute n realizations of the random field $\{L(\boldsymbol{q}), \boldsymbol{q} \in \mathcal{B}\}$. Conversely, if the particle spacing is assumed to be deterministic, then we replace random field L with its nominal value $\underline{\ell}$. For each realization θ, the trajectories of random fields K_η, K_τ, and L are constructed as piecewise constant functions. For the i-th subdomain, we assume that the values are constant and equal to $L(\boldsymbol{q}_i)(\theta)$, $K_\eta(\boldsymbol{q}_i)(\theta)$, and $K_\tau(\boldsymbol{q}_i)(\theta)$. Using the mixed FE method with a 2D triangular mesh, we compute n independent realizations of the strong solution of the BVP. The convergence of the obtained results is monitored by selecting three different values for the characteristic mesh length h^{mesh}: 2.76×10^{-7} m, 2.3×10^{-7} m, and 2.1×10^{-7} m. These values correspond to 2 408, 3 248, and 4 108 mesh elements, as well as 24 646, 33 134, and 41 822 degrees of freedom. The displacement field $\boldsymbol{V}$ and its gradient $\nabla_{\boldsymbol{q}} \boldsymbol{V}$ are treated as unknowns, subject to constraints imposed via Lagrange multipliers. The Python code used in this study is based on the FEniCS project, accessible at http://www.fenicsproject.org/download. To perform massive parallelization, the MPI library is used. An example of the computational implementation is provided in [1] and is available for use under the GNU Public License [GNU Public]. We use SNES (Scalable Nonlinear Equations Solvers) as a nonlinear solver for the computations.

The sensitivity of the mechanical response with respect to uncertainties is analyzed by examining a finite set of scalar observations that are expressed in terms of $\boldsymbol{V}$. These observations include certain components of the displacement field at a specific point $\boldsymbol{q}$. Let X be the real valued-random variable that represents one of these observations. Let $\mathbb{E}^{(n)}\{X\}$ and $\delta_X^{(n)}$ be the estimation of the mean value $\mathbb{E}\{X\}$ and coefficient of variation δ_X performed with n realizations. For each random variable X, the convergence of the stochastic solver with respect to n is monitored by the quantity $\varepsilon_X^{(n)} / \mathbb{E}^{(n)}\{X\}$ that can be expressed as $= \eta \, \delta_X^{(n)} / \sqrt{n}$ with $\eta = \mathcal{G}^{-1}(0.95)$, in which $\mathcal{G}$ is the standard normal cumulative distribution function (see ([129] pp. 35)). The probability density function of X is estimated using the Gaussian Kernel Density Estimation (KDE) method with $n = 10\,000$ realizations. Moreover, we analyze the graph $x_{(p)} \mapsto t^{\text{ext}} = \widehat{t}_1^{\text{ext}}(x_{(p)})$, where $x_{(p)}$ is the p-th percentile of X and t^{ext} defines the axial

external load, to determine whether the crystal exhibits hardening or softening mechanical behavior. Confidence intervals are constructed for these graphs. Finally, we introduce the random variable $\mathcal{K}^{\text{eff}}$ defined as the ratio between the effective axial stiffness $\mathrm{K}^{\text{eff}} = t^{\text{ext}}/V_2^1$, where V_2^1 is the horizontal displacement at the middle point of the right-end boundary $\partial\mathcal{B}_t$, and its mean value $\mathbb{E}\{\mathrm{K}^{\text{eff}}\}$,

$$\mathcal{K}^{\text{eff}} = \frac{\mathrm{K}^{\text{eff}}}{\mathbb{E}\{\mathrm{K}^{\text{eff}}\}} \quad , \quad \mathrm{K}^{\text{eff}} = \frac{t^{\text{ext}}}{V_2^1} \quad , \quad \mathbb{E}\{\mathrm{K}^{\text{eff}}\} = \frac{t^{\text{ext}}}{\mathbb{E}\{V_2^1\}}. \tag{4.154}$$

Random variable $\mathcal{K}^{\text{eff}}$ provides insight into the fluctuations of effective global axial stiffness relative to the mean value. To estimate the pdf $\mathrm{k} \mapsto p_{\mathcal{K}^{\text{eff}}}(\mathrm{k})$ of $\mathcal{K}^{\text{eff}}$, we use the Gaussian KDE method. Additionally, we integrate the obtained pdf of $\mathcal{K}^{\text{eff}}$ to estimate the cumulative distribution function (cdf) $\mathrm{k} \mapsto \mathcal{F}_{\mathcal{K}^{\text{eff}}}(\mathrm{k})$. Following the approach in [128], we define the function $\beta \mapsto \mathbb{P}(\beta)$ such that

$$\mathbb{P}(\beta) = \mathcal{P}(1-\beta < \mathcal{K}^{\text{eff}} \leq 1+\beta) = \mathcal{F}_{\mathcal{K}^{\text{eff}}}(1+\beta) - \mathcal{F}_{\mathcal{K}^{\text{eff}}}(1-\beta)\,. \tag{4.155}$$

The value $\mathbb{P}(\beta)$ represents the probability that $\mathcal{K}^{\text{eff}}$ lies within the interval $]1-\beta, 1+\beta]$. Probability $\mathbb{P}(\beta)$ allows for quantifying the level of the statistical fluctuations of K^{eff} with respect to its mean value.

Analyzing convergences and quantifying uncertainty propagation

Let $\boldsymbol{q}_1 = (b_1/2, b_2/2)$ represent a point inside domain $\mathcal{B} \in \mathbb{R}^2$ and $\boldsymbol{q}_2 = (b_1, 0)$ represent a point on the boundary $\partial\mathcal{B}$. Let $V_1^2 = V^2(\boldsymbol{q}_1)$ and $V_2^1 = V^1(\boldsymbol{q}_2)$ denote the horizontal and transversal displacements at $\boldsymbol{q}_1$ and $\boldsymbol{q}_2$, respectively.

Convergence of stochastic solver

We check the convergence of the results as a function of the number n of realizations increases by evaluating the quantities $\widetilde{\varepsilon}_{|V_1^2|}/\mathbb{E}^{(n)}\{|V_1^2|\}$ and $\widetilde{\varepsilon}_{V_2^1}/\mathbb{E}^{(n)}\{V_2^1\}$ defined as

$$\frac{\widetilde{\varepsilon}^{(n)}_{|V_1^2|}(\eta)}{\mathbb{E}^{(n)}\{|V_1^2|\}} = \frac{\eta\,\delta^{(n)}_{|V_1^2|}}{\sqrt{n}} \quad , \quad \frac{\widetilde{\varepsilon}^{(n)}_{V_2^1}(\eta)}{\mathbb{E}^{(n)}\{V_2^1\}} = \frac{\eta\,\delta^{(n)}_{V_2^1}}{\sqrt{n}}\,. \tag{4.156}$$

Fig. 4.5 shows that there is the 95% probability of having an error of at most 0.51% in the mean values of V_1^2, and an error of at most 0.03% in the mean values of V_2^1 when considering the number of realizations $n = 10000$. Hence, good convergence is obtained.

The results are provided for axial external load $t^{\text{ext}} = 1 \times 10^{-8}\,\text{N/m}$, nominal particle spacing $\underline{\ell} = 2.76 \times 10^{-7}\,\text{m}\,(0.276\,\mu\text{m})$, mesh size $h^{\text{mesh}} = \underline{\ell}$, correlation length $\lambda = 10^{-3}\,\underline{\ell}$ and $\delta_{[\boldsymbol{G}]}$ less than or equal to 30 %.

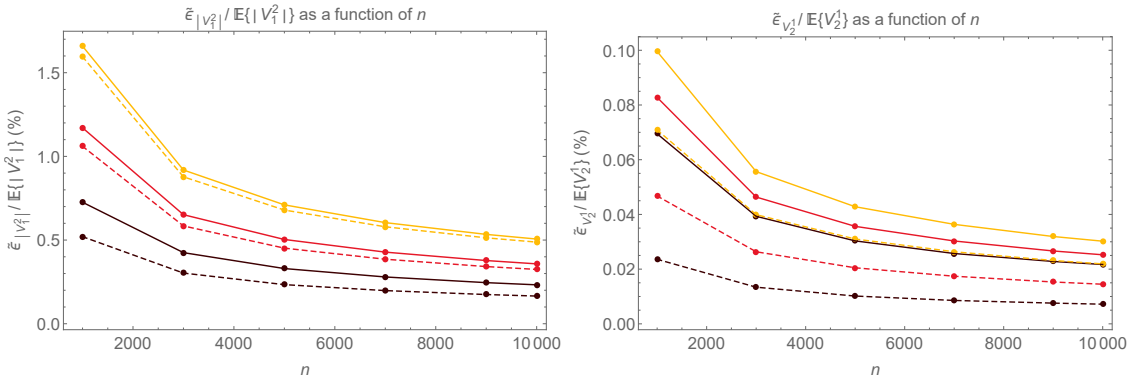

(a) (b)

Fig. 4.12 Convergence analysis of the stochastic solver. Graphs (a) $n \mapsto \widetilde{\varepsilon}_{|V_1^2|}/\mathbb{E}\{|V_1^2|\}$, (b) $n \mapsto \widetilde{\varepsilon}_{V_2^1}/\mathbb{E}\{V_2^1\}$, obtained for $t^{\text{ext}} = 1 \times 10^{-8}\,\text{N/m}$, nominal particle spacing $\underline{\ell} = 2.76 \times 10^{-7}\,\text{m}$, mesh size $h^{\text{mesh}} = \underline{\ell}$, correlation length $\lambda = 10^{-3}\,\underline{\ell}$, and $\delta_{[\boldsymbol{G}]} = 30\,\%$ (yellow), $\delta_{[\boldsymbol{G}]} = 20\,\%$ (red), $\delta_{[\boldsymbol{G}]} = 10\,\%$ (black), for both without disordering (dashed line) and with disordering (solid line).

Probability density functions and coefficients of variation of V_2^1 and $|V_1^2|$ for fixed correlation length λ

We build the pdfs $v_2^1 \mapsto p_{V_2^1}(v_2^1)$ and $v_1^2 \mapsto p_{|V_1^2|}(v_1^2)$ using the Gaussian KDE method based on a number of realizations $n = 10\,000$. We assume axial external load $t^{\text{ext}} = 1 \times 10^{-8}\,\text{N/m}$, nominal particle spacing $\underline{\ell} = 2.76 \times 10^{-7}\,\text{m}\,(0.276\,\mu\text{m})$, mesh size $h^{\text{mesh}} = \underline{\ell}$, correlation length $\lambda = 10^{-3}\,\underline{\ell}$, and $\delta_{[\boldsymbol{G}]}$ less than or equal to 0.3. Concerning component V_2^1, in Fig. 4.13, it can be observed, that the mean value and the standard deviation are increasing with the values of $\delta_{[\boldsymbol{G}]}$, but the mean value is smaller for disordering while the standard deviation is greater. Concerning component V_1^2, in Fig. 4.14, it can be observed that, for both disordering and without disordering, the mean value is approximately constant as a function of $\delta_{[\boldsymbol{G}]}$, while the standard deviation is increasing with $\delta_{[\boldsymbol{G}]}$. These remarks are further supported by Fig. 4.15 displaying the coefficients of variation $\delta_{V_2^1}$ and $\delta_{|V_1^2|}$ of V_2^1 and V_1^2, respectively. In this figure, it can be seen that, for the longitudinal component of the displacement, the dispersion is larger with disordering than without disordering. It is approximately the same for the transversal component of the displacement. In addition, we observe that $\delta_{|V_1^2|}$ is much larger than $\delta_{V_2^1}$. This result can be attributed to the comparable standard deviations $\sigma_{|V_1^2|}$

of $|V_1^2|$ and $\sigma_{V_2^1}$ of V_2^1, as shown in Fig. 4.16, despite the much smaller mean value of $|V_1^2|$ compared to the mean value of V_2^1. Continuing our analysis with Fig. 4.16, we notice that $\sigma_{V_2^1}$ is slightly larger than $\sigma_{|V_1^2|}$ since the horizontal particle spacing, $\underline{\ell}$, is slightly larger than the vertical particle spacing, $\ell\sqrt{3}/3$ (see red dotted line). In particular, without disordering, the ratio $\sigma_{V_2^1}/\sigma_{|V_1^2|}$ remains approximately constant as well as the coefficient of variation $\delta_{[\boldsymbol{G}]}$ increases since the system characteristics (particle spacing and correlation length of stiffness random fields) remain unchanged. With disordering, the ratio $\sigma_{V_2^1}/\sigma_{|V_1^2|}$ increases compared to the case without disordering. The lower horizontal particle spacing compared to the vertical one contributes to the increase in the ratio. As the randomness associated with the stiffness parameters, controlled by $\delta_{[\boldsymbol{G}]}$, becomes dominant, the ratio decreases towards a constant value.

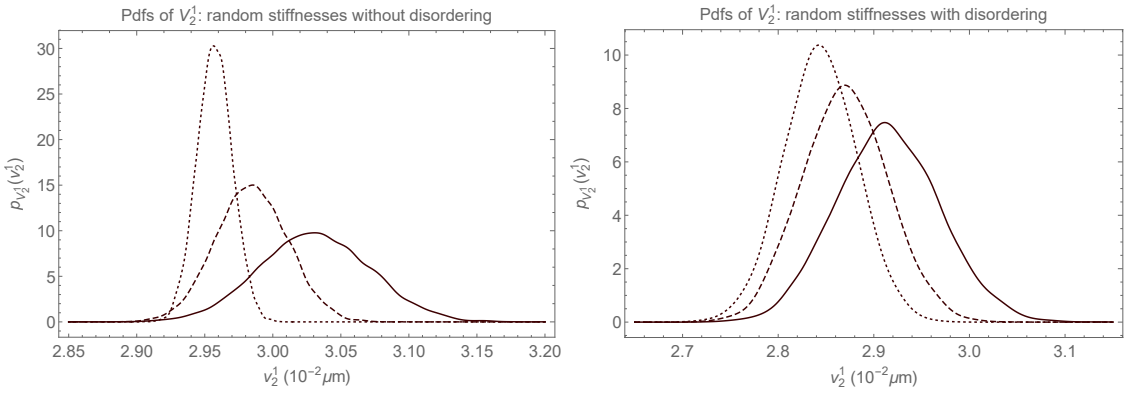

(a) (b)

Fig. 4.13 Graphs of $v_2^1 \mapsto p_{V_2^1}(v_2^1)$: (a) without disordering and (b) with disordering. External load $t^{\text{ext}} = 1\times10^{-8}\,\text{N/m}$, nominal particle spacing $\underline{\ell} = 2.76\times10^{-7}\,\text{m}$, mesh size $h^{\text{mesh}} = \underline{\ell}$, correlation length $\lambda = 10^{-3}\,\underline{\ell}$, $\delta_{[\boldsymbol{G}]} = 10\,\%$ (dotted line), $\delta_{[\boldsymbol{G}]} = 20\,\%$ (dashed line), and $\delta_{[\boldsymbol{G}]} = 30\,\%$ (solid line).

Accuracy of the computational model with respect to mesh size h^{mesh}

The accuracy of the computational model with respect to the mesh size is analyzed by considering h^{mesh} equal to $\underline{\ell}$, $0.83\underline{\ell}$, and $0.76\underline{\ell}$, where $\underline{\ell}$ is the nominal particle spacing chosen as $2.76\times10^{-7}\,\text{m}\,(0.276\,\mu\text{m})$. Fig. 4.17 shows the sensitivity to the mesh size h^{mesh} of the coefficients of variation $\delta_{|V_1^2|}$ and $\delta_{V_2^1}$. The results are obtained for number of realizations $n = 10\,000$, $t^{\text{ext}} = 1\times10^{-8}\,\text{N/m}$, correlation length $\lambda = 10^{-3}\,\underline{\ell}$, with disordering, and $\delta_{[\boldsymbol{G}]} = 0.3$. Choosing $h^{\text{mesh}} = \underline{\ell}$, it can be concluded that the results are sufficiently accurate.

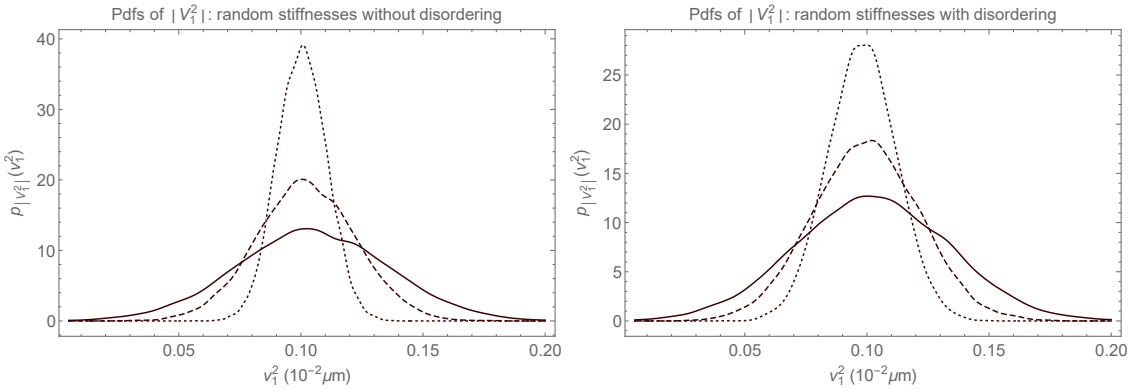

(a) (b)

Fig. 4.14 (a) Graphs of $v_1^2 \mapsto p_{|V_1^2|}(v_1^2)$: (a) without disordering (b) with disordering that are obtained for $t^{\text{ext}} = 1 \times 10^{-8}\,\text{N/m}$, nominal particle spacing $\underline{\ell} = 2.76 \times 10^{-7}\,\text{m}$, mesh size $h^{\text{mesh}} = \underline{\ell}$, correlation length $\lambda = 10^{-3}\,\underline{\ell}$, for $\delta_{[\boldsymbol{G}]} = 10\,\%$ (dotted line), $\delta_{[\boldsymbol{G}]} = 20\,\%$ (dashed line), and $\delta_{[\boldsymbol{G}]} = 30\,\%$ (solid line).

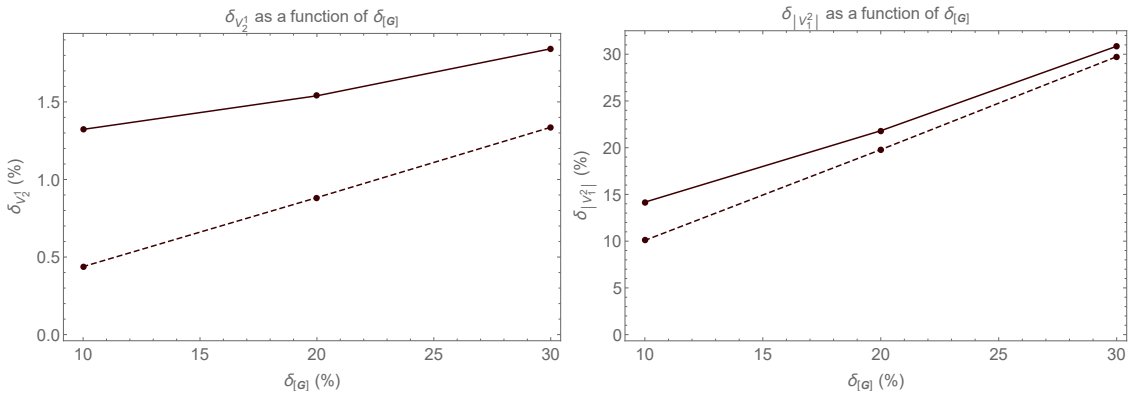

(a) (b)

Fig. 4.15 Graphs of (a) $\delta_{|V_1^2|}$ and (b) $\delta_{V_2^1}$ as a function of $\delta_{[\boldsymbol{G}]}$ obtained for $t^{\text{ext}} = 1 \times 10^{-8}\,\text{N/m}$, nominal particle spacing $\underline{\ell} = 2.76 \times 10^{-7}\,\text{m}$, mesh size $h^{\text{mesh}} = \underline{\ell}$, correlation length $\lambda = 10^{-3}\,\underline{\ell}$, with disordering (solid line), without disordering (dashed line).

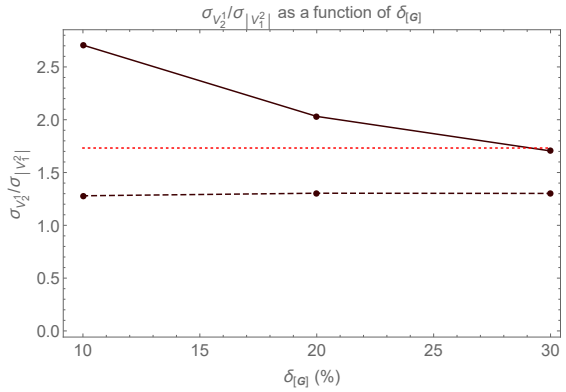

Fig. 4.16 Graphs of $\sigma_{|V_1^2|}/\sigma_{V_2^1}$ as a function of $\delta_{[\boldsymbol{G}]}$ obtained for $t^{\text{ext}} = 1\times10^{-8}\,\text{N/m}$, nominal particle spacing $\underline{\ell} = 2.76\times10^{-7}\,\text{m}$, mesh size $h^{\text{mesh}} = \underline{\ell}$, correlation length $\lambda = 10^{-3}\,\underline{\ell}$, with disordering (black solid line), without disordering (black dashed line). The red dotted line represents the ratio between the horizontal and vertical particle spacing.

Accuracy of the computational model with respect to mesh size h^{mesh}

The accuracy of the computational model with respect to the mesh size is analyzed by considering h^{mesh} equal to $\underline{\ell}$, $0.83\underline{\ell}$, and $0.76\underline{\ell}$, where $\underline{\ell}$ is the nominal particle spacing chosen as $2.76\times10^{-7}\,\text{m}\,(0.276\,\mu\text{m})$. Fig. 4.17 shows the sensitivity to the mesh size h^{mesh} of the coefficients of variation $\delta_{|V_1^2|}$ and $\delta_{V_2^1}$. The results are obtained for number of realizations $n = 10000$, $t^{\text{ext}} = 1\times10^{-8}\,\text{N/m}$, correlation length $\lambda = 10^{-3}\,\underline{\ell}$, with disordering, and $\delta_{[\boldsymbol{G}]} = 0.3$. Choosing $h^{\text{mesh}} = \underline{\ell}$, it can be concluded that the results are sufficiently accurate.

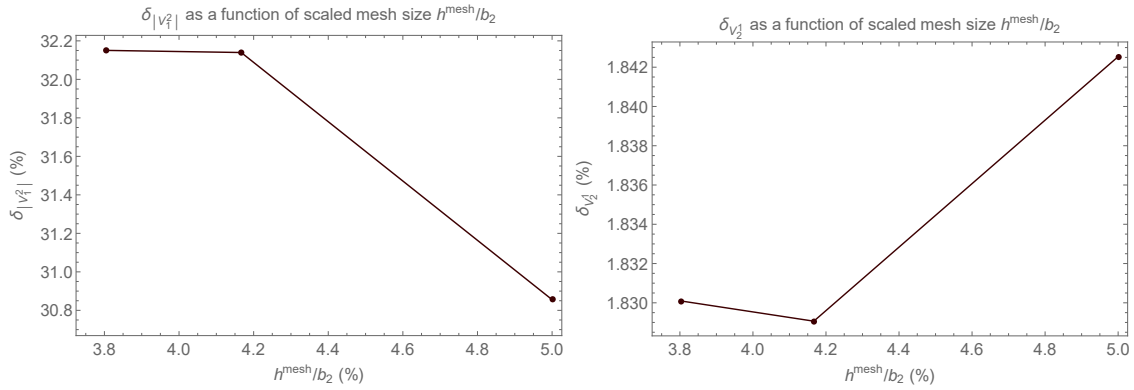

(a) (b)

Fig. 4.17 Graphs of (a) $\delta_{|V_1^2|}$ and (b) $\delta_{V_2^1}$ for different values of h^{mesh} obtained for $t^{\text{ext}} = 1\times10^{-8}\,\text{N/m}$, nominal particle spacing $\underline{\ell} = 2.76\times10^{-7}\,\text{m}$, with disordering, correlation length $\lambda = 10^{-3}\,\underline{\ell}$, and $\delta_{[\boldsymbol{G}]} = 30\,\%$. The symbol $b_2 = 20\underline{\ell}$ denotes the vertical side of the rectangular crystal.

Effects of the correlation length λ on the axial displacements V_2^1

Let us consider $t^{\text{ext}} = 1 \times 10^{-8}\,\text{N/m}$, nominal particle spacing $\underline{\ell} = 2.76 \times 10^{-7}\,\text{m}\,(0.276\,\mu\text{m})$, mesh size $h^{\text{mesh}} = \underline{\ell}$, and $\delta_{[\boldsymbol{G}]} = 30\%$, with disordering, and number of realizations $n = 10\,000$. Fig. 4.18 shows how the probability density function $v_2^1 \mapsto p_{V_2^1}(v_2^1)$ of V_2^1 changes as the correlation length λ changes. These functions are built using the Gaussian KDE method. The differences are negligible when $\lambda = 10^{-3}\underline{\ell}$ and $\lambda = \underline{\ell}$. They become significant when $\lambda = 2\underline{\ell}$. The results are consistent with the used continuum model. For $\lambda = 10^{-3}\underline{\ell}$ and $\lambda = \underline{\ell}$, consecutive particles are uncorrelated. For $\lambda = 2\underline{\ell}$, correlation occurs contributing to an increase in the randomness of the system. This analysis is improved by quantifying the deviation of the effective stiffness from its mean value in terms of probability. To this aim, in Fig. 4.18, we show the function $\beta \mapsto \mathbb{P}(\beta)$ defined in Eq. 4.155 obtained under the same conditions as before regarding geometry, applied load, $\delta_{[\boldsymbol{G}]}$, mesh size, and the number of realizations. The value $\mathbb{P}(\beta)$ gives the probability that $1-\beta < \mathcal{K}^{\text{eff}} < 1+\beta$, where $\mathcal{K}^{\text{eff}} = \text{K}^{\text{eff}}/\mathbb{E}\{\text{K}^{\text{eff}}\}$ and K^{eff} is the global axial stiffness of the analyzed crystal as defined in Eq. 4.154.

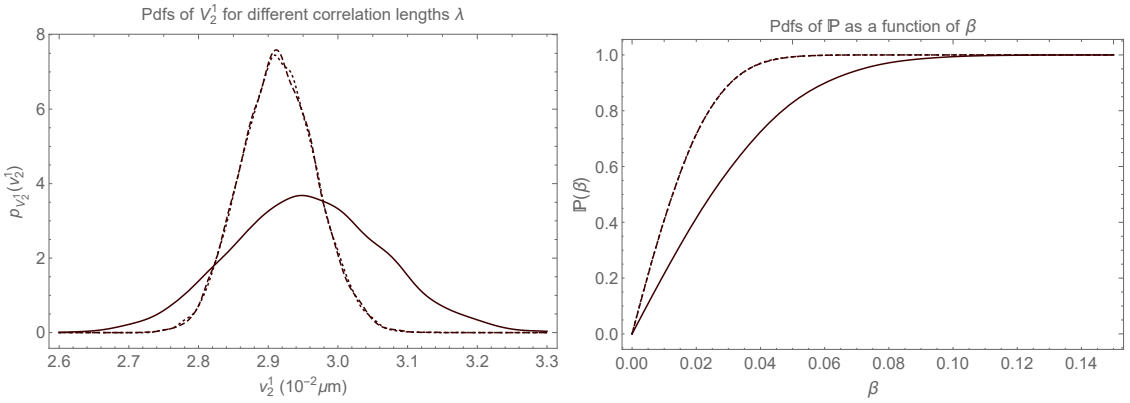

(a) (b)

Fig. 4.18 Graph of (a) $v_2^1 \mapsto p_{V_2^1}(v_2^1)$ and (b) $\beta \mapsto \mathbb{P}(\beta)$ for $t^{\text{ext}} = 1 \times 10^{-8}\,\text{N/m}$, nominal particle spacing $\underline{\ell} = 2.76 \times 10^{-7}\,\text{m}$, mesh size $h^{\text{mesh}} = \underline{\ell}$, $\delta_{[\boldsymbol{G}]} = 30\%$, with disordering, number of realizations $n = 10\,000$, and for $\lambda = 10^{-3}\underline{\ell}$ (solid line), $\lambda = \underline{\ell}$ (dashed line), and $\lambda = 2\underline{\ell}$ (dotted line).

Effects of the number of particles on the coefficients of variation of V_2^1 and $\left|V_1^2\right|$

Let us consider $t^{\text{ext}} = 1 \times 10^{-8}\,\text{N/m}$, $\delta_{[\boldsymbol{G}]} = 30\%$, with disordering, number of realizations $n = 10\,000$, $\underline{k}_\eta$ and $\underline{k}_\tau$ as given in Eq. 4.153. In this case, we consider three different values of the nominal distance $\underline{\ell}$ between consecutive particles in order to progressively increase the

number of particles, considering the same domain $\mathcal{B}$. The mesh size h^{mesh} is chosen equal to $\underline{\ell}$. In Fig. 4.19, we show that the coefficients of variation of V_2^1 and $\left|V_1^2\right|$ decrease as the nominal distance $\underline{\ell}$ between particles decreases. As expected, the randomness of the system decreases as the number of particles increases.

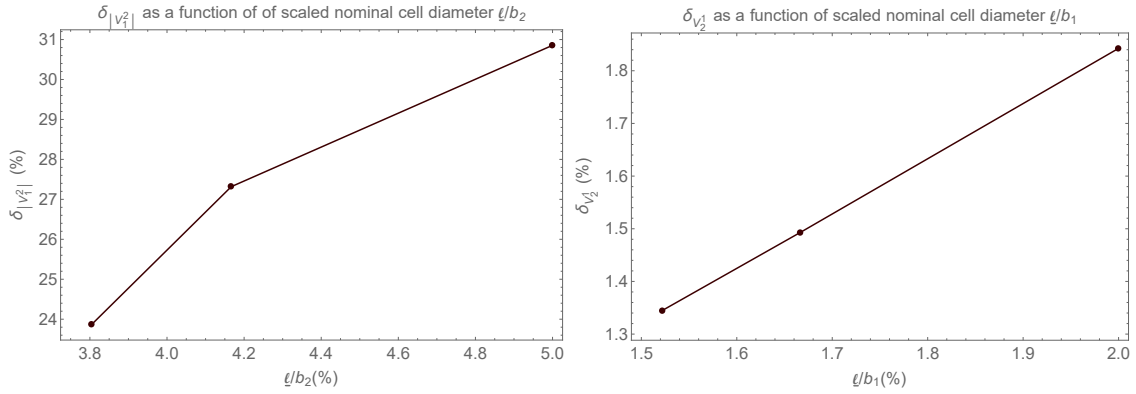

(a) (b)

Fig. 4.19 Graphs of (a) $\delta_{|V_1^2|}$ and (b) $\delta_{V_2^1}$ for different values of nominal distance $\underline{\ell}$ between consecutive particles. The results are obtained for $t^{\text{ext}} = 1 \times 10^{-8}\,\text{N/m}$, mesh size $h^{\text{mesh}} = \underline{\ell}$, correlation length $\lambda = 10^{-3}\underline{\ell}$, with disordering, and $\delta_{[\boldsymbol{G}]} = 30\,\%$. The symbol $b_2 = 20\underline{\ell}$ denotes the short side of the rectangular crystal, $b_1 = 50\underline{\ell}$ the vertical side.

Graphs of the force-displacement relationships and their confidence regions

Fig. 4.20 displays the confidence regions with the probability level 95 % of the force-displacement relationships

$$v_{2(p)}^1/b_1 \mapsto t^{\text{ext}}(v_{2(p)}^1/b_1)/\bar{t}^{\text{ext}}, \tag{4.157}$$

and

$$|v_{1(p)}^2|/b_1 \mapsto t^{\text{ext}}(|v_{1(p)}^2|/b_1)/\bar{t}^{\text{ext}} \tag{4.158}$$

where $\bar{t}^{\text{ext}} = 1 \times 10^{-8}\,\text{N/m}$, $v_{1(p)}^2$ and $v_{2(p)}^1$ are the p-th percentile of V_1^2 and V_2^1. The results are obtained for nominal particle spacing $\underline{\ell} = 2.76 \times 10^{-7}\,\text{m}\,(0.276\,\mu\text{m})$, mesh size $h^{\text{mesh}} = \underline{\ell}$, correlation length $\lambda = 10^{-3}\,\underline{\ell}$, $n = 10000$ realizations, $\delta_{[\boldsymbol{G}]} = 30\,\%$, and with disordering. The confidence region for the relationship related to displacement in the axial direction V_2^1 is smaller due to the smaller coefficient of variation $\delta_{V_2^1}$ compared to $\delta_{|V_1^2|}$. The relationship related to V_2^1 exhibits a hardening behavior, where the strength increases with displacement. This behavior is attributed to the presence of nonlocal grid effects considered in a second-gradient model, which are plausible in small specimens like those analyzed in this application.

In the literature, we have not found results regarding force-displacement curves of colloidal crystals. However, it is plausible to expect a hardening behavior, as evidence of hardening has been observed in colloidal gels with increasing shear deformation [29] and in colloidal crystals with increasing temperature [9].

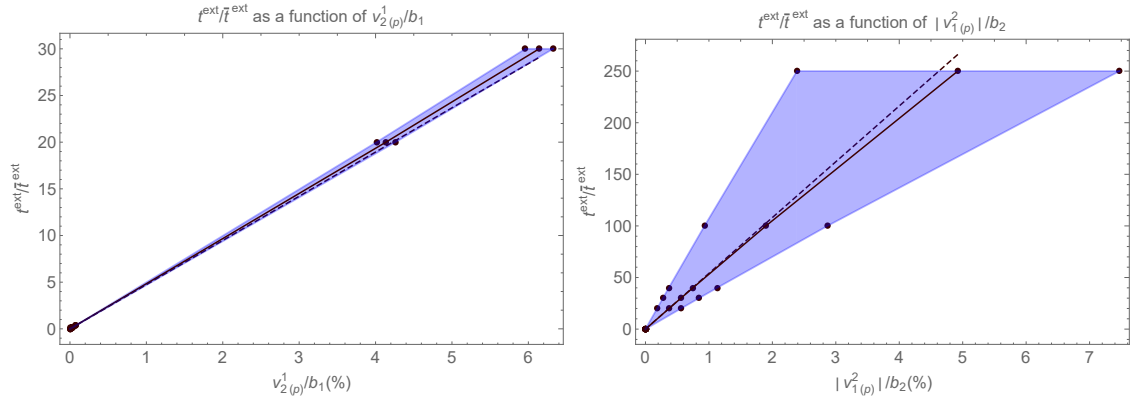

(a) (b)

Fig. 4.20 Confidence regions with the probability level 95 % (a) for the graphs $v^1_{2(p)}/b_1 \mapsto t^{ext}(v^1_{2(p)}/b_1)/\bar{t}^{ext}$ truncated at $t^{ext}(v^1_{2(p)}/b_1)/\bar{t}^{ext} = 30$ and (b) for the graph $|v^2_{1(p)}|/b_1 \mapsto t^{ext}(|v^2_{1(p)}|/b_1)/\bar{t}^{ext}$ truncated at $t^{ext}(|v^2_{1(p)}|/b_1)/\bar{t}^{ext} = 250$, where $\bar{t}^{ext} = 1\times10^{-8}\,\mathrm{N/m}$, and $v^1_{2(p)}$ correspond to the p-th percentile of V^1_2, $|v^2_{1(p)}|$ correspond to the p-th percentile of $|V^2_1|$. The results are obtained considering nominal particle spacing $\underline{\ell} = 2.76\times10^{-7}\,\mathrm{m}$, mesh size $h^{\mathrm{mesh}} = \underline{\ell}$, correlation length $\lambda = 10^{-3}\,\underline{\ell}$, $n = 10\,000$ realizations, and $\delta_{[\boldsymbol{G}]} = 30\,\%$. The solid line represents the statistical mean value. The dashed line represents the linearized statistical mean value.

4.4 Summarizing the main results

- In Section 4.1.1 the equilibrium equations of the axially functionally graded micropolar Timoshenko-Ehrenfest beams have been derived. The presented simplified model can predict scale effects. Novel solutions have been presented for simply supported and cantilever beams (see Eqs.(4.34) and (4.42)).

- In Section 4.1.2 the random response and identification of the micropolar Timoshenko-Ehrenfest beams have been analyzed via a prior noninformative probabilistic model. It has been proven that the study of an isotropic microbeam allows us to derive the stochastic information of a nonclassical material parameter of the 3D micropolar model.

- Section 4.2 has been devoted to the construction of a probabilistic model for the geometric and material microscale parameters of the particle-based second-gradient model. In Section 4.2.1, the literature-proposed relationship between the Cauchy deformation tensor and the second-gradient deformation tensor has been improved (see Eq. (4.63)).

- In Section 4.2.2, for the micro-homogeneous and micro-isotropic continuum model developed for particle-based materials, the statistical dependence between the particle-pair distance between two consecutive particles and the microscale-specific stiffness parameters has been investigated.

- A probabilistic model for these uncertain parameters has been developed using the maximum entropy principle. Using the available information, it has been shown that the three considered uncertain parameters are statistically independent. The particle-pair distance between two consecutive particles is uniformly distributed, and the microscale-specific stiffness parameters are Gamma-distributed (see Eq. (4.97)).

- For the application under consideration, it has been proven that the random mechanical response, such as the specific deformation energy and displacements at certain points, exhibits significant statistical fluctuation with respect to the level of uncertainties. Observations indicate that the particle-pair distance between two consecutive particles of a particle-based material has a greater effect on the statistical fluctuations of random mechanical responses.

- Section 4.3 has been devoted to developing random field models for disorder particle-based materials, which have been described using an equivalent second-gradient continuum model at the same scale. The construction of these random field models has been based on the Maximum Entropy principle (see Section 4.3.1). Numerical simulations have been conducted on disordered colloidal crystals.

- In Section 4.3.2, a simulated axial test shows that the mean value of axial displacements and their fluctuations increase as the fluctuations of mesoscale stiffness parameters and positions increase. The mean value of transversal displacements remains relatively constant, while its fluctuations increase with fluctuations in mesoscale stiffness parameters and positions. The coefficients of variation for displacements decrease as the number of particles increases, indicating higher homogenization levels. Fluctuations in effective macroscale axial stiffness increase as the correlation lengths of mesoscale stiffness fields increase.

- The techniques employed in Sections 4.2 and 4.3 can also be used to construct a stochastic model for the second-gradient continuum recently introduced by [106].

Chapter 5

Conclusion and perspectives

5.1 General conclusion

This dissertation is devoted to the mechanics of generalized continua. The foundations of the micropolar continuum, the micromorphic continuum, the second-gradient continuum, and the second-gradient-micropolar continuum have been presented in detail. A comprehensive discussion of stress and strain measures and the derivation of the Euler-Lagrange equations are included. The treatment is organized to emphasize the connection between the various analyzed continuum models. Euler-Lagrange equations have been derived using the least action principle (or the principle of virtual work) and the Levi-Civita tensor calculus. Throughout the text, it is emphasized that least action principle entails the type of admissible external loads for the various continuum models and the type of static actions exchanged by the continuum subdomains.

Generalized continua are widely used in the analysis of architectured metamaterials. Since pantographic structures represent a paradigmatic case, pantographic sheets (2D) and pantographic blocks (3D) have been investigated. First, we have proposed and experimentally validated a novel torsional energy for modeling the torsional behavior of pivots of polyamide and metallic pantographic sheets. Although the proposed energy has been developed within the framework of discrete mechanics (Hencky-Type discrete models), it is still applicable within the framework of second-gradient continua. Then, a novel second-gradient continuum model for modeling pantographic blocks has been proposed. Digital volume correlation techniques have been applied to experimentally validate the theoretical model. The proposed continuum model is capable to reproduce the nonclassical mechanical behavior of pantographic blocks that exhibit synclastic deformation rather than anticlastic deformation under a 3-point flexural test. Finally, the effect of material-related local defects in the mechanical response of pantographic sheets has been analyzed in which the mechanical properties have been

considered uncertain. A prior noninformative probabilistic model has been constructed and a stochastic solver has been developed. Due to redundant connections inside pantographic sheets, it has been demonstrated that pivots-related local defects have minimal influence on the random horizontal displacements of pantographic sheets.

Generalized continua are also suitable for the analysis of particle-based materials. Micropolar beams and particle-based second-gradient continuum models have been investigated to encourage engineering applications. First, equilibrium equations for micropolar Timoshenko-Ehrenfest beams have been derived under the assumption of continuously varying material parameters along the axis. Novel approximated closed-form solutions have been derived. The derived solutions have been used to perform the response and identification of beams characterized by material-related uncertainties that have been modeled by means of prior noninformative probabilistic models. On the one hand, it has been shown that the statistical inverse analysis of macrobeams permits the identification of the probability density functions of the Young modulus at various points along the beam axis. On the other hand, the statistical inverse analysis of microbeams enables us to identify the probability density functions at various points along the beam axis of one 3D micropolar parameter responsible for scale effects. Second, the sensitivity of a previously published particle-based second-gradient continuum model with respect to material-related uncertainties has been performed. The deterministic model is theoretically refined by improving the relationship between the first- and second-gradient deformation measures. The sensitivity analysis has been approached using the maximum entropy principle from information theory. First, it is assumed that particle-pair distance and microscale stiffness parameters are independent of spatial and orientation directions. Using the available information, it has been demonstrated that the particle-pair distance between two consecutive particles and the microscale stiffness parameters are, respectively, uniformly and Gamma-distributed. For the considered application, it has been proven that the random mechanical response is subjected to significant fluctuations due to uncertainties. In addition, it is shown that the particle-pair distance has a greater effect on the statistical fluctuations of mechanical response. Second, particle-pair distance and microscale stiffness parameters are modeled as random fields. In contrast to the previous scenario, the performed numerical application shows that fluctuations in microscale stiffness have a more substantial impact on the statistical fluctuations in mechanical response.

5.2 Future perspectives

Throughout this thesis, the focus has been on gradient-type nonlocal theories rather than integral nonlocal theories [70]. Integral nonlocal theories are suitable for continua where

interaction forces rapidly diminish with distance, following the attenuating neighborhood hypothesis [45]. Furthermore, assuming a smooth neighborhood, these integral theories lead to gradient-type nonlocal theories [92]. Eringen nonlocal elasticity stands as one of the prominent integral nonlocal theories, extensively used for analyzing nanomaterials and microstructured materials [44, 15, 107, 7]. This dissertation chooses to not deal with integral nonlocal elasticity acknowledging that the topic deserves additional exploration.

Recently, in collaboration with Professor Christian Soize, we have introduced a model for particle-based materials capable of encompassing Piola peridynamics and Eringen nonlocal elasticity [77]. Furthermore, we have adapted this novel model into a stochastic formulation [78] based on the Maximum Entropy principle, following a similar procedure as in Section 4.3. Papers [77] and [78] are currently under revision. Moreover, our ongoing work addresses dynamic aspects and identification issues.

Additionally, it is necessary to spend some more words on the modeling of pivots in pantographic structures. As previously highlighted, we distinguish three analysis scales: a macroscopic scale viewing the pantographic structure as a continuous medium, a mesoscopic scale where the pantographic structure is modeled as a set of extensional and rotational springs, and finally, a microscopic scale wherein the pantographic structure is represented as a collection of beams and pivots. In Section 3.1, it has been proposed a novel model for describing pivots at the mesoscale. However, together with Professor Boris Desmorat, we are concurrently working on a novel mesoscale model corresponding to a microscale plastic model within the framework of generalized standard materials featuring von Mises yield surface and isotropic hardening. The following research directions can be also identified.

- Investigating the ability of the proposed generalized continua with uncertainties to characterize the mechanical behavior of biological tissues.
- Designing novel architectured metamaterials with nonclassical mechanical behaviors using the proposed generalized continua.
- Performing design optimization under uncertainties of architectured metamaterials requiring the use of probabilistic machine learning tools.

In future works, the author of this dissertation will further investigate the role of probabilistic machine learning tools [130] in the theory of generalized continua.

References

[1] Abali, B. E. (2020). Supply code for computations.

[2] Abali, B. E., Müller, W. H., and Eremeyev, V. A. (2015). Strain gradient elasticity with geometric nonlinearities and its computational evaluation. *Mechanics of Advanced Materials and Modern Processes*, 1(1):1–11.

[3] Alibert, J.-J., Seppecher, P., and dell'Isola, F. (2003). Truss modular beams with deformation energy depending on higher displacement gradients. *Mathematics and Mechanics of Solids*, 8(1):51–73.

[4] Altenbach, J., Altenbach, L. H., and Eremeyev, V. A. (2010). On generalized cosserat-type theories of plates and shells: a short review and bibliography. *Archive of Applied Mechanics*, 80(1):73–92.

[5] Altenbach, L. H. and Eremeyev, V. A. (2013). *Generalized Continua from the Theory to Engineering Applications.* Springer, Vienna.

[6] Andreaus, U., Spagnuolo, M., Lekszycki, T., and Eugster, S. R. (2018). A Ritz approach for the static analysis of planar pantographic structures modeled with nonlinear Euler–Bernoulli beams. *Continuum Mechanics and Thermodynamics*, 30(5):1103–1123.

[7] Arash, B. and Wang, Q. (2014). *A Review on the Application of Nonlocal Elastic Models in Modeling of Carbon Nanotubes and Graphenes*, pages 57–82. Springer International Publishing, Cham.

[8] Auger, P., Lavigne, T., Smaniotto, B., Spagnuolo, M., dell'Isola, F., and Hild, F. (2021). Poynting Effects in Pantographic Metamaterial Captured via Multiscale DVC. *Journal of Strain Analysis for Engineering Design*.

[9] Babacic, V., Varghese, J., Coy, E., Kang, E., Pochylski, M., Gapinski, J., Fytas, G., and Graczykowski, B. (2020). Mechanical reinforcement of polymer colloidal crystals by supercritical fluids. *Journal of Colloid and Interface Science*, 579:786–793.

[10] Barchiesi, E., dell'Isola, F., and Hild, F. (2021a). On the validation of homogenized modeling for bi-pantographic metamaterials via digital image correlation. *International Journal of Solids and Structures*, 208–209:49–62.

[11] Barchiesi, E., dell'Isola, F., Laudato, M., Placidi, L., and Seppecher, P. (2018). A 1D continuum model for beams with pantographic microstructure: Asymptotic micro-macro identification and numerical results. In *dell'Isola, F., Eremeyev, V. A., Porubov, A. (Eds.) Advances in Mechanics of Microstructured Media and Structures*. Springer, Cham.

[12] Barchiesi, E., Eugster, S. R., dell'Isola, F., and Hild, F. (2020). Large in-plane elastic deformations of bi-pantographic fabrics: asymptotic homogenization and experimental validation. *Mathematics and Mechanics of Solids*, 25(3):739–767.

[13] Barchiesi, E., Misra, A., Placidi, L., and Turco, E. (2021b). Granular micromechanics-based identification of isotropic strain gradient parameters for elastic geometrically nonlinear deformations. *Zeitschrift für angewandte Mathematik und Mechanik*, 101(11):e202100059–1–21.

[14] Bardet, J. and Vardoulakis, I. (2001). The asymmetry of stress in granular media. *International Journal of Solids and Structures*, 38(2):353–367.

[15] Bažant, Z. P. (1994). Nonlocal damage theory based on micromechanics of crack interactions. *Journal of Engineering Mechanics*, 120(3):1–25.

[16] Berkache, K., Deogekar, S., Goda, I., Picu, R. C., and Ganghoffer, J. F. (2017). Construction of second gradient continuum models for random fibrous networks and analysis of size effects. *Composite Structures*, 181:347–357.

[17] Boutin, C., dell'Isola, F., Giorgio, I., and Placidi, L. (2017). Linear pantographic sheets: asymptotic micro-macro models identification. *Mathematics and Mechanics of Complex Systems*, 5(2):127–162.

[18] Buffière, J., Maire, E., Adrien, J., Masse, J., and Boller, E. (2010). In Situ Experiments with X ray Tomography: an Attractive Tool for Experimental Mechanics. *Experimental Mechanics*, 50(3):289–305.

[19] Cauchy, A.-L. (1827). *Exercices de mathématiques. Année 2*. De Bure fréres, Paris.

[20] Ciallella, A., Giorgio, I., Eugster, S. R., Rizzi, N. L., and dell'Isola, F. (2022a). Generalized beam model for the analysis of wave propagation with a symmetric pattern of deformation in planar pantographic sheets. *Wave Motion*, 113:102986.

[21] Ciallella, A., La Valle, G., Vintache, A., Smaniotto, B., and Hild, F. (2023). Deformation mode in 3-point flexure on pantographic block. *International Journal of Solids and Structures*, 265-266:112129.

[22] Ciallella, A., Pasquali, D., D'Annibale, F., and Giorgio, I. (2022b). Shear rupture mechanism and dissipation phenomena in bias-extension test of pantographic sheets: Numerical modeling and experiments. *Mathematics and Mechanics of Solids*, 27(10):2170–2188.

[23] Ciallella, A., Pasquali, D., Gołaszewski, M., D'Annibale, F., and Giorgio, I. (2021). A rate-independent internal friction to describe the hysteretic behavior of pantographic structures under cyclic loads. *Mechanics Research Communications*, 116:103761–1–5.

[24] Ciallella, A. and Steigmann, D. J. (2023). Unusual deformation patterns in a second-gradient cylindrical lattice shell: Numerical experiments. *Mathematics and Mechanics of Solids*, 28(1):141–153.

[25] Ciarlet, P. G. (1988). *Mathematical Elasticity, Volume I: Three-Dimensional Elasticity*. North-Holland, Amsterdam.

[26] Cong, H., Yu, B., Tang, J., Li, Z., and Liu, X. (2013). Current status and future developments in preparation and application of colloidal crystals. *Chemical Society Reviews*, 42:7774–7800.

[27] Cosserat, E. and Cosserat, F. (1909). *Théorie des corps déformables*. A. Hermann et Fils, Paris.

[28] De Angelo, M., Placidi, L., Nejadsadeghi, N., and Misra, A. (2022). Non-standard timoshenko beam model for chiral metamaterial: Identification of stiffness parameters. *Mechanics Research Communications*, 103:103462.

[29] de Oliveira Reis, G., Gibaud, T., Saint-Michel, B., Manneville, S., Leocmach, M., Vaysse, L., Bonfils, F., Sanchez, C., and Menut, P. (2019). Irreversible hardening of a colloidal gel under shear: The smart response of natural rubber latex gels. *Journal of Colloid and Interface Science*, 539:287–296.

[30] dell'Isola, F., Andreaus, U., Cazzani, A., Esposito, R., Luca Placidi, U. P., Maier, G., and Seppecher, P. (2019a). *The complete works of Gabrio Piola: Volume II*. Springer.

[31] dell'Isola, F., Andreaus, U., and Placidi, L. (2015a). At the origins and in the vanguard of peridynamics, non-local and highergradient continuum mechanics: An underestimated and still topical contribution of Gabrio Piola. *Mathematics and Mechanics of Solids*, 20(8):887–928.

[32] dell'Isola, F., Corte, A. D., and Giorgio, I. (2015b). Higher-gradient continua: The legacy of Piola, Mindlin, Sedov and Toupin and some future research perspectives. *Mathematics and Mechanics of Solids*, 22(4):852–872.

[33] dell'Isola, F., Giorgio, I., Pawlikowski, M., and Rizzi, N. (2016a). Large deformations of planar extensible beams and pantographic lattices: heuristic homogenization, experimental and numerical examples of equilibrium. *Proceedings of the Royal Society A: Mathematical, Physical and Engineering Sciences*, 472(2185):20150790–1–23.

[34] dell'Isola, F., Maier, G., Perego, U., Andreaus, U., Esposito, R., and Forest, S. (2016b). *The complete works of Gabrio Piola: Volume I*. Springer.

[35] dell'Isola, F., Seppecher, P., Spagnuolo, M., Barchiesi, E., Hild, F., Lekszycki, T., Giorgio, I., Placidi, L., Andreaus, U., Cuomo, M., Eugster, S., Pfaff, A., Hoschke, K., Langkemper, R., Turco, E., Sarikaya, R., Misra, A., De Angelo, M., D'Annibale, F., Bouterf, A., Pinelli, X., Misra, A., Desmorat, B., Pawlikowski, M., Dupuy, C., Scerrato, D., Peyre, P., Laudato, M., Manzari, L., Göransson, P., Hesch, C., Hesch, S., Franciosi, P., Dirrenberger, J., Maurin, F., Vangelatos, Z., Grigoropoulos, C., Melissinaki, V., Farsari, M., Muller, W., Abali, E., Liebold, C., Ganzosch, G., Harrison, P., Drobnicki, R., Igumnov, L., Alzahrani, F., and Hayat, T. (2019b). Advances in Pantographic Structures: Design, Manufacturing, Models, Experiments and Image Analyses. *Continuum Mechanics and Thermodynamics*, 31(4):1231–1282.

[36] dell'Isola, F. and Stilz, M. (2023). The «materialization» of forces: Why confounding mathematical concept and physical entity makes the design of metamaterials arduous. *Zeitschrift für Angewandte Mathematik und Mechanik*, 103(2):e202200433.

[37] dell'Isola, F., Andreaus, U., and Placidi, L. (2015). At the origins and in the vanguard of peridynamics, non-local and higher-gradient continuum mechanics: an underestimated and still topical contribution of gabrio piola. *Mathematics and Mechanics of Solids*, 20(8):887–928.

[38] Desmorat, B., Spagnuolo, M., and Turco, E. (2020). Stiffness optimization in nonlinear pantographic structures. *Mathematics and Mechanics of Solids*, 25(12):2252–2262.

[39] Dong, X.-J., Meng, G., Li, H.-G., and Ye, L. (2005). Vibration analysis of a stepped laminated composite timoshenko beam. *Mechanics Research Communications*, 32(5):572–581.

[40] Eremeyev, V. A., Alzahrani, F. S., Cazzani, A., Hayat, T., Turco, E., and Konopińska-Zmysłowska, V. (2019). On existence and uniqueness of weak solutions for linear pantographic beam lattices models. *Continuum Mechanics Thermodynamics*, 31:1843–1861.

[41] Eremeyev, V. A., Leonid, P., and Altenbach, L. H. (2013). *Foundations of Micropolar Mechanics*. Springer-Verlag, Berlin, Heidelberg.

[42] Eremeyev, V. A. and Pietraszkiewicz, W. (2016). Material symmetry group and constitutive equations of micropolar anisotropic elastic solids. *Mathematics and Mechanics of Solids*, 21(2):210–221.

[43] Eringen, A. (1968). *Mechanics of Micromorphic Continua*. Springer Berlin Heidelberg, Berlin, Heidelberg.

[44] Eringen, A. C. (1992). Vistas of nonlocal continuum physics. *International Journal of Engineering Science*, 30(10):1551–1565.

[45] Eringen, A. C. (2002). *Nonlocal Continuum Field Theories*. Springer, New York.

[46] Eugster, S., dell'Isola, F., and Steigmann, D. (2019). Continuum theory for mechanical metamaterials with a cubic lattice substructure. *Mathematics and Mechanics of Complex Systems*, 7(1):75–98.

[47] Eugster, S. R. (2022). Numerical analysis of nonlinear wave propagation in a pantographic sheet. *Mathematics and Mechanics of Complex Systems*, 9(3):293–310.

[48] Falsone, G. and Impollonia, N. (2002). A new approach for the stochastic analysis of finite element modelled structures with uncertain parameters. *Computer Methods in Applied Mechanics and Engineering*, 191(44):5067–5085.

[49] Fedele, R. (2015). Simultaneous assessment of mechanical properties and boundary conditions based on Digital Image Correlation. *Experimental Mechanics*, 55:139–153.

[50] Fedele, R., Ciani, A., Galantucci, L., , Bettuzzi, M., and Andena, L. (2013). A regularized, pyramidal multi-grid approach to global 3d-volume digital image correlation based on x-ray micro-tomography. *Fundamenta Informaticae*, 125(3-4):361–376.

[51] Finzi, B. and Pastori, M. (1949). *Calcolo tensoriale e applicazioni*. Zanichelli, Bologna.

[52] Frenzel, T., Köpfler, J., Jung, E., Kadic, M., and Wegener, M. (2019). Ultrasound experiments on acoustical activity in chiral mechanical metamaterials. *Nature Communications*, 10:3384.

[53] Germain, P. (1973). The method of virtual power in continuum mechanics. Part 2: Microstructure. *SIAM Journal on Applied Mathematics*, 25(3):556–575.

[54] Geuzaine, C. and Remacle, J.-F. (2009). Gmsh: A 3-D finite element mesh generator with built-in pre- and post-processing facilities. *International Journal for Numerical Methods in Engineering*, 79(11):1309–1331.

[55] Giorgio, I. (2016). Numerical identification procedure between a micro-Cauchy model and a macro-second gradient model for planar pantographic structures. *Zeitschrift für angewandte Mathematik und Physik*, 67(4):1–17.

[56] Giorgio, I. (2020). A discrete formulation of Kirchhoff rods in large-motion dynamics. *Mathematics and Mechanics of Solids*, 25(5):1081–1100.

[57] Giorgio, I. (2021). Lattice shells composed of two families of curved Kirchhoff rods: an archetypal example, topology optimization of a cycloidal metamaterial. *Continuum Mechanics and Thermodynamics*, 33(4):1063–1082.

[58] Giorgio, I., dell'Isola, F., and Misra, A. (2020). Chirality in 2D Cosserat media related to stretch-micro-rotation coupling with links to granular micromechanics. *International Journal of Solids and Structures*, 202:28–38.

[59] Giorgio, I., Harrison, P., Dell'Isola, F., Alsayednoor, J., and Turco, E. (2018). Wrinkling in engineering fabrics: a comparison between two different comprehensive modelling approaches. *Proceedings of the Royal Society A: Mathematical, Physical and Engineering Sciences*, 474(2216):20180063.

[60] Giorgio, I., Rizzi, N. L., and Turco, E. (2017). Continuum modelling of pantographic sheets for out-of-plane bifurcation and vibrational analysis. *Proceedings of the Royal Society A: Mathematical, Physical and Engineering Sciences*, 473(2207):20170636.

[GNU Public] GNU Public. Gnu general public license.

[62] Grammenoudis, P. and Tsakmakis, C. (2009). Micromorphic continuum. Part I: Strain and stress tensors and their associated rates. *International Journal of Non Linear Mechanics*, 44(9):943–956.

[63] Greco, L. (2020). An iso-parametric G^1-conforming finite element for the nonlinear analysis of Kirchhoff rod. Part I: the 2D case. *Continuum Mechanics and Thermodynamics*, 32(5):1473–1496.

[64] Greco, L., Giorgio, I., and Battista, A. (2017). In plane shear and bending for first gradient inextensible pantographic sheets: numerical study of deformed shapes and global constraint reactions. *Mathematics and Mechanics of Solids*, 22(10):1950–1975.

[65] Guilleminot, J. and Soize, C. (2013a). On the statistical dependence for the components of random elasticity tensors exhibiting material symmetry properties. *Journal of Elasticity*, 111(2):109–130.

[66] Guilleminot, J. and Soize, C. (2013b). Stochastic model and generator for random fields with symmetry properties: application to the mesoscopic modeling of elastic random media. *Multiscale Modeling & Simulation (A SIAM Interdisciplinary Journal)*, 11(3):840–870.

[67] Hansen, P. (2000). The L-Curve and its Use in the Numerical Treatment of Inverse Problems. In *in Computational Inverse Problems in Electrocardiology, ed. P. Johnston, Advances in Computational Bioengineering*, pages 119–142. WIT Press.

[68] Hild, F., Bouterf, A., Chamoin, L., Mathieu, F., Neggers, J., Pled, F., Tomičević, Z., and Roux, S. (2016). Toward 4D Mechanical Correlation. *Advanced Modeling and Simulation in Engineering Sciences*, 3(1):1–26.

[69] Koizumi, M. (1997). Fgm activities in japan. *Composites Part B: Engineering*, 28(1):1–4.

[70] Kröner, E. (1967). Elasticity theory of materials with long range cohesive forces. *International Journal of Solids and Structures*, 3(5):731–742.

[71] La Valle, G. (2022). A new deformation measure for the nonlinear micropolar continuum. *Zeitschrift für angewandte Mathematik und Physik*, 73(2):78–1–26.

[72] La Valle, G., Abali, B. E., Falsone, G., and Soize, C. (2023). Sensitivity of a homogeneous and isotropic second-gradient continuum model for particle-based materials with respect to uncertainties. *Zeitschrift für Angewandte Mathematik und Mechanik*, n/a(n/a):e202300068.

[73] La Valle, G., Ciallella, A., and Falsone, G. (2022). The effect of local random defects on the response of pantographic sheets. *Mathematics and Mechanics of Solids*, 27(10):2147–2169.

[74] La Valle, G. and Falsone, G. (2023). On the random axially functionally graded micropolar timoshenko-ehrenfest beams. In dell'Isola, F., Barchiesi, E., and León Trujillo, F. J., editors, *Advances in Mechanics of Materials for Environmental and Civil Engineering*, pages 65–90. Springer International Publishing, Cham.

[75] La Valle, G. and Falsone, G. (2023). Random micropolar beams: response and identification. *International Journal of Non-Linear Mechanics*, 150:104367.

[76] La Valle, G. and Massoumi, S. (2022). A new deformation measure for micropolar plates subjected to in-plane loads. *Continuum Mechanics Thermodynamics*, 34:243–257.

[77] La Valle, G. and Soize, C. (2023a). A higher-order nonlocal elasticity continuum model for deterministic and stochastic particle-based materials. *Zeitschrift für angewandte Mathematik und Mechanik*, Under revision.

[78] La Valle, G. and Soize, C. (2023b). Stochastic second-gradient continuum theory for particle-based materials. Part II. *Zeitschrift für angewandte Mathematik und Mechanik*, Under revision.

[79] La Valle, G., Spagnuolo, M., Turco, E., and Desmorat, B. (2023). A new torsional energy for pantographic sheets. *Zeitschrift für angewandte Mathematik und Mechanik*, 74(2):67–1–14.

[80] Lamb, H. (1891). Xxiii. On the flexure of a flat elastic spring. *The London, Edinburgh, and Dublin Philosophical Magazine and Journal of Science*, 31(190):182–188.

[81] Landau, L. D. and Lifshitz, E. M. (1970). *Theory of Elasticity*. Pergamon Press, Bristol.

[82] Lebedev, L. P., Cloud, M. J., and Eremeyev, V. A. (2010). *Tensor Analysis With Applications In Mechanics*. Wspc.

[83] Leclerc, H., Neggers, J., Mathieu, F., Hild, F., and Roux, S. (2015). *Correli 3.0*. IDDN.FR.001.520008.000.S.P.2015.000.31500, Agence pour la Protection des Programmes, Paris (France).

[84] Lindsay, H. M. and Chaikin, P. M. (1982). Elastic properties of colloidal crystals and glasses. *The Journal of Chemical Physics*, 76(7):3774–3781.

[85] Liu, K., Ding, H., Li, S., Niu, Y., Zeng, Y., Zhang, J., Du, X., and Gu, Z. (2022). 3D printing colloidal crystal microstructures via sacrificial-scaffold-mediated two-photon lithography. *Nature Communications*, 13:4563.

[86] Love, A. (1892). *A treatise on the mathematical theory of elasticity*, volume 1. University Press, Cambridge.

[87] Ma, H., Gao, X.-L., and Reddy, J. (2008). A microstructure-dependent timoshenko beam model based on a modified couple stress theory. *Journal of the Mechanics and Physics of Solids*, 56(12):3379–3391.

[88] Maghsoodi, A., Ghadami, A., and Mirdamadi, H. R. (2013). Multiple-crack damage detection in multi-step beams by a novel local flexibility-based damage index. *Journal of Sound and Vibration*, 332(2):294–305.

[89] Maire, E. and Withers, P. J. (2014). Quantitative X-ray tomography. *International Materials Reviews*, 59(1):1–43.

[90] Manzari, M. T. (2004). Application of micropolar plasticity to post failure analysis in geomechanics. *International Journal for Numerical and Analytical Methods in Geomechanics*, 28(10):1011–1032.

[91] Massoumi, S. and La Valle, G. (2022). Static analysis of 2d micropolar model for describing granular media by considering relative rotations. *Mechanics Research Communications*, 119:103812.

[92] Maugin, G. A. (1979). Nonlocal theories or gradient-type theories: a matter of convenience? *Archives of Mechanics*, 3(1):15–26.

[93] Misra, A., Nejadsadeghi, N., De Angelo, M., and Placidi, L. (2020). Chiral metamaterial predicted by granular micromechanics: verified with 1D example synthesized using additive manufacturing. *Continuum Mechanics and Thermodynamics*, 32(5):1497–1513.

[94] Misra, A., Placidi, L., dell'Isola, F., and Barchiesi, E. (2021a). Identification of a geometrically nonlinear micromorphic continuum via granular micromechanics. *Zeitschrift für angewandte Mathematik und Physik*, 72(157):1–21.

[95] Misra, A., Placidi, L., dell'Isola, F., et al. (2021b). Identification of a geometrically nonlinear micromorphic continuum via granular micromechanics. *Zeitschrift für angewandte Mathematik und Physik*, 72:157.

[96] Mohan, L. S., Nott, P. R., and Rao, K. K. (2002). A frictional Cosserat model for the slow shearing of granular materials. *Journal of Fluid Mechanics*, 457:377–409.

[97] Nastasi, P. and Tazzioli, R. (2005). Toward a scientific and personal biography of Tullio Levi-Civita (1873–1941). *Historia Mathematica*, 32(2):203–236.

[98] Navier, M. and de Saint-Venant, A. J. C. B. (1864). *Résumé des leçons données à École des ponts et chaussées sur l'application de la mécanique à l'établissement des constructions et des machines*, volume 1. Dunod.

[99] Ostoja-Starzewski, M. (2002). Lattice models in micromechanics. *Applied Mechanics Reviews*, 55:35–60.

[100] Ostoja-Starzewsky, M. (1993). Random fields and processes in mechanics of granular materials. *Mechanics of Materials*, 16(1):55–64.

[101] Pertsinidis, A. and Ling, X. S. (2001). Diffusion of point defects in two-dimensional colloidal crystals. *Nature*, 413(6852):147–150.

[102] Pietraszkiewicz, W. and Eremeyev, V. A. (2009). On natural strain measures of the non-linear micropolar continuum. *International Journal of Solids and Structures*, 46(3-4):774–787.

[103] Placidi, L., Andreaus, U., and Giorgio, I. (2017). Identification of two-dimensional pantographic structure via a linear d4 orthotropic second gradient elastic model. *Journal of Engineering Mathematics*, 103(1):1–21.

[104] Placidi, L., Barchiesi, E., Misra, A., and Timofeev, D. (2021). Micromechanics-based elasto-plastic–damage energy formulation for strain gradient solids with granular microstructure. *Continuum Mechanics and Thermodynamics*, 33(5):2213–2241.

[105] Placidi, L., Timofeev, D., Maksimov, V., Barchiesi, E., Ciallella, A., Misra, A., and Dell'isola, F. (2022a). Micro-mechano-morphology-informed continuum damage modeling with intrinsic 2nd gradient (pantographic) grain–grain interactions. *International Journal of Solids and Structures*, 254–255.

[106] Placidi, L., Timofeev, D., Maksimov, V., Barchiesi, E., Ciallella, A., Misra, A., and dell'Isola, F. (2022b). Micro-mechano-morphology-informed continuum damage modeling with intrinsic 2nd gradient (pantographic) grain–grain interactions. *International Journal of Solids and Structures*, 254-255:111880.

[107] Povstenko, Y. Z. (1999). The nonlocal theory of elasticity and its applications to the description of defects in solid bodies. *Journal of Mathematical Sciences*, 97:3840–3845.

[108] Pressley, A. N. (2010). *Elementary differential geometry*. Springer Science & Business Media.

[109] Rahali, Y., Giorgio, I., Ganghoffer, J.-F., and dell'Isola, F. (2015). Homogenization à la Piola produces second gradient continuum models for linear pantographic lattices. *International Journal of Engineering Science*, 97:148–172.

[110] Reda, H., Berkache, K., Ganghoffer, J. F., and Lakiss, H. (2020). Dynamical properties of random fibrous networks based on generalized continuum mechanics. *Waves in random and complex media*, 30(1):27–53.

[111] Reddy, J. (2011). Microstructure-dependent couple stress theories of functionally graded beams. *Journal of the Mechanics and Physics of Solids*, 59(11):2382–2399.

[112] Reddy, J. and Kim, J. (2012). A nonlinear modified couple stress-based third-order theory of functionally graded plates. *Composite Structures*, 94(3):1128–1143.

[113] Rengarajan, R., Mittleman, D., Rich, C., and Colvin, V. (2005). Effect of disorder on the optical properties of colloidal crystals. *Phys. Rev. E*, 71:016615.

[114] Rivlin, R. S. and Rideal, E. K. (1948). Large elastic deformations of isotropic materials iv. further developments of the general theory. *Philosophical Transactions of the Royal Society of London. Series A, Mathematical and Physical Sciences*, 241(835):379–397.

[115] Rosenblatt, M. (2012). *Stationary Sequences and Random Fields*. Springer Science & Business Media.

[116] Roux, S., Hild, F., Viot, P., and Bernard, D. (2008). Three dimensional image correlation from X-Ray computed tomography of solid foam. *Composites Part A: Applied Science and Manufacturing*, 39(8):1253–1265.

[117] Roy Chowdhury, S. and Reddy, J. (2019). Geometrically exact micropolar timoshenko beam and its application in modelling sandwich beams made of architected lattice core. *Composite Structures*, 226:111228.

[118] Rubinstein, R. Y. and Kroese, D. P. (2008). *Simulation and the Monte Carlo Method*. Second Edition, John Wiley & Sons, New York.

[119] Sankar, B. (2001). An elasticity solution for functionally graded beams. *Composites Science and Technology*, 61(5):689–696.

[120] Searle, G. F. C. (1908). *Experimental Elasticity: A Manual for the Laboratory*. University Press.

[121] Shekarchizadeh, N., Abali, B. E., and Bersani, A. M. (2022). A benchmark strain gradient elasticity solution in two-dimensions for verifying computational approaches by means of the finite element method. *Mathematics and Mechanics of Solids*, 27(10):2218–2238.

[122] Shinozuka, M. (2005). Simulation of Multivariate and Multidimensional Random Processes. *The Journal of the Acoustical Society of America*, 49(1B):357–368.

[123] Shinozuka, M. and Jan, C.-M. (1972). Digital simulation of random processes and its applications. *Journal of Sound and Vibration*, 25(1):111–128.

[124] Shinozuka, M. and Wen, Y.-K. (1972). Monte Carlo solution of nonlinear vibrations. *AIAA Journal*, 10(1):37–40.

[125] Soize, C. (2000). A nonparametric model of random uncertainties for reduced matrix models in structural dynamics. *Probabilistic Engineering Mechanics*, 15(3):277–294.

[126] Soize, C. (2001). Maximum entropy approach for modeling random uncertainties in transient elastodynamics. *The Journal of the Acoustical Society of America*, 109(1979):1979–1996.

[127] Soize, C. (2006). Non-gaussian positive-definite matrix-valued random fields for elliptic stochastic partial differential operators. *Computer Methods in Applied Mechanics and Engineering*, 195(1):26–64.

[128] Soize, C. (2008). Tensor-valued random fields for meso-scale stochastic model of anisotropic elastic microstructure and probabilistic analysis of representative volume element size. *Probabilistic Engineering Mechanics*, 23(2):307–323. 5th International Conference on Computational Stochastic Mechanics.

[129] Soize, C. (2017). *Uncertainty Quantification*. Springer, New York.

[130] Soize, C. and Ghanem, R. (2016). Data-driven probability concentration and sampling on manifold. *Journal of Computational Physics*, 321:242–258.

[131] Spagnuolo, M. (2020). Circuit analogies in the search for new metamaterials: Phenomenology of a mechanical diode. In *Altenbach H., Eremeyev V., Pavlov I., Porubov A. (eds) Nonlinear Wave Dynamics of Materials and Structures. Advanced Structured Materials, vol 122*, pages 411–422. Springer, Cham, Swizerland.

[132] Spagnuolo, M., Barcz, K., Pfaff, A., Franciosi, P., and dell'Isola, F. (2017). Qualitative pivot damage analysis in aluminum printed pantographic sheets: Numerics and experiments. *Mechanics Research Communications*, 83:47–52.

[133] Spagnuolo, M., Ciallella, A., and Scerrato, D. (2022a). The loss and recovery of the works by Piola and the Italian tradition of mechanics. In *dell'Isola, F., Eugster, S.R., Spagnuolo, M., Barchiesi, E. (eds) Evaluation of Scientific Sources in Mechanics. Advanced Structured Materials*, pages 315–340. Springer, Cham.

[134] Spagnuolo, M., Yildizdag, M. E., Pinelli, X., Cazzani, A., and Hild, F. (2022b). Out-of-plane deformation reduction via inelastic hinges in fibrous metamaterials and simplified damage approach. *Mathematics and Mechanics of Solids*, 27(6):1011–1031.

[135] Taillandier-Thomas, T., Roux, S., Morgeneyer, T., and Hild, F. (2014). Localized strain field measurement on laminography data with mechanical regularization. *Nuclear Instruments and Methods in Physics Research Section B*, 324:70–79.

[136] Timofeev, D., Barchiesi, E., Misra, A., and Placidi, L. (2021). Hemivariational continuum approach for granular solids with damage-induced anisotropy evolution. *Mathematics and Mechanics of Solids*, 26(5):738–770.

[137] Turco, E., Barcz, K., Pawlikowski, M., and Rizzi, N. L. (2016a). Non-standard coupled extensional and bending bias tests for planar pantographic lattices. Part I: numerical simulations. *Zeitschrift für angewandte Mathematik und Physik*, 67(5):122–1–16.

[138] Turco, E., dell'Isola, F., Cazzani, A., and Rizzi, N. L. (2016b). Hencky-type discrete model for pantographic structures: numerical comparison with second gradient continuum models. *Zeitschrift für angewandte Mathematik und Physik*, 67(4):85–1–28.

[139] Turco, E., Gołaszewski, M., Cazzani, A., and Rizzi, N. L. (2016c). Large deformations induced in planar pantographic sheets by loads applied on fibers: Experimental validation of a discrete Lagrangian model. *Mechanics Research Communications*, 76:51–56.

[140] Turco, E., Gołaszewski, M., Giorgio, I., and D'Annibale, F. (2017). Pantographic lattices with non-orthogonal fibres: experiments and their numerical simulations. *Composites Part B: Engineering*, 118:1–14.

[141] Turco, E., Misra, A., Pawlikowski, M., dell'Isola, F., and Hild, F. (2018). Enhanced Piola-Hencky discrete models for pantographic sheets with pivots without deformation energy: Numerics and experiments. *International Journal of Solids and Structures*, 147:94–109.

[142] Valmalle, M., Vintache, A., Smaniotto, B., Gutmann, F., Spagnuolo, M., Ciallella, A., and Hild, F. (2022). Local-global DVC analyses confirm theoretical predictions for deformation and damage onset in torsion of pantographic metamaterial. *Mechanics of Materials*, 172:104379.

[143] Wang, S., Lee, S., Du, J. S., Partridge, B. E., Cheng, H. F., Zhou, W., Dravid, V. P., Lee, B., Glotzer, S. C., and Mirkin, C. A. (2022). The emergence of valency in colloidal crystals through electron equivalents. *Nature Materials*, 21:580–587.

[144] Wang, Y., Jenkins, I. C., McGinley, J. T., Sinno, T., and Crocker, J. C. (2017). Colloidal crystals with diamond symmetry at optical lengthscales. *Nature Communications*, 8(1):14173.

[145] Yang, F., Chong, A., Lam, D., and Tong, P. (2002). Couple stress based strain gradient theory for elasticity. *International Journal of Solids and Structures*, 39(10):2731–2743.

[146] Yang, Y. and Misra, A. (2012). Micromechanics based second gradient continuum theory for shear band modeling in cohesive granular materials following damage elasticity. *International Journal of Solids and Structures*, 49(18):2500–2514.

[147] Yildizdag, M. E., Barchiesi, E., and dell'Isola, F. (2020). Three-point bending test of pantographic blocks: numerical and experimental investigation. *Mathematics and Mechanics of Solids*, 25(10):1965–1978.

[148] Yildizdag, M. E., Placidi, L., and Turco, E. (2022). Modeling and numerical investigation of damage behavior in pantographic layers using a hemivariational formulation adapted for a Hencky-type discrete model. *Continuum Mechanics and Thermodynamics*, pages 1–14.

[149] Zhang, K.-Q. and Liu, X. Y. (2009). Determination of elastic constants of two-dimensional close-packed colloidal crystals. *Langmuir*, 25(10):5432–5436.

[150] Zhu, C., Pascall, A. J., Dudukovic, N., Worsley, M. A., Kuntz, J. D., Duoss, E. B., and Spadaccini, C. M. (2019). Colloidal materials for 3D printing. *Annual Review of Chemical and Biomolecular Engineering*, 10(1):17–42.

Appendix A

A few mathematical tools

A.1 Tensor algebra

This section is derived from the course given by *Francesco dell'Isola* at the University of L'Aquila. The presented tools have been used to derive the Euler-Lagrange equations for second-gradient continuum models.

A.1.1 Levi-Civita tensor algebra

Let us analyze how the components of a vector V belonging to the subspace $\mathcal{V}$ of $\mathbb{R}^N$ change when the basis $E = \{E_i\}_{i=1,..,N}$ of $\mathcal{V}$ changes. The following rules underlie the Levi-Civita tensor algebra:

1. for any given equality, the number of free (*i.e.*, uninvolved in a summation) subscripts or superscripts on the right must be equal to the number of free subscripts or superscripts on the left;

2. for any given equality, it is possible to change the symbol of the indices involved in a summation without consequences. It is always better to change the symbol if it is possible.

Using the convention of summation on repeated indices, the summation is implied over a term in which an index variable appears twice as subscript and superscript and is not otherwise defined. It holds

$$V = \sum_{i=1}^{N} V^i E_i = V^i E_i = V^j E_j = \dots \tag{A.1}$$

Let us introduce a change of basis from $\{E_i\}_{i=1,\dots,N}$ to $\left\{E'_i\right\}_{i=1,\dots,N}$ using the transformation matrix T defined by

$$E'_{j'} = T^i_{j'} E_i \quad , \quad E_i = \left(T^{-1}\right)^{j'}_i E'_{j'} \, . \tag{A.2}$$

Since $\{E_i\}_{i=1,\dots,N}$ and $\left\{E'_i\right\}_{i=1,\dots,N}$ are both bases of $\mathcal{V}$, the vector V is a linear combination of $\{E_i\}_{i=1,\dots,N}$ and $\left\{E'_{i'}\right\}_{i'=1,\dots,N}$. It is

$$V = V^{j'} E'_{j'} = V^j E_j \, . \tag{A.3}$$

Eq. (A.2) implies

$$V = V^{j'} E'_{j'} = V^j \left(T^{-1}\right)^{j'}_j E'_{j'} \tag{A.4}$$

and

$$\left(V^{j'} - V^j \left(T^{-1}\right)^{j'}_j\right) E'_{j'} = 0 \, . \tag{A.5}$$

Thanks to the linear independence of $\left\{E'_{i'}\right\}_{i'=1,\dots,N}$, we arrive to

$$V^{j'} = \left(T^{-1}\right)^{j'}_j V^j \, . \tag{A.6}$$

Since when the basis changes, the components of V change in accordance with the matrix T^{-1}, we say that the components of V vary in a *contravariant* way, or that they are *contravariant components* of the vector V.

A.1.2 Covariant components of a covector

Let us consider the algebraic dual space $\mathcal{V}^*$ of subspace $\mathcal{V}$ of $\mathbb{R}^N$. The elements of $\mathcal{V}$ are named *covectors* or *linear forms*. For any covector ℓ in $\mathcal{V}^*$, we have

$$\ell(V) = \ell\left(V^i E_i\right) = V^i \ell(E_i) \, . \tag{A.7}$$

Let ℓ_E be the standard representation of the covector ℓ with respect to the basis E defined by

$$\ell^j_E : V \mapsto \ell^j_E(V) = V^j \tag{A.8}$$

such that $V = V^j E_j$. It yields

$$\ell(V) = \ell\left(V^i E_i\right) = \ell^i_E(V) \, \ell(E_i) \, . \tag{A.9}$$

Eq. (A.9) implies that ℓ is a linear combination of $\left\{\ell_E^i\right\}_{i=1,\dots,N}$. In addition, since it is

$$\alpha_i \ell_E^i(V) = \alpha_i V^i = 0 \quad \Leftrightarrow \quad \alpha_i = 0\,, \tag{A.10}$$

thanks to the arbitrariness of V, the elements $\left\{\ell_E^i\right\}_{i=1,\dots,N}$ are linearly independent and define a basis of $\mathcal{V}^*$. Now, our main purpose is to study how the components $\ell(E_i)$ change if the basis changes from $\{E_i\}_{i=1,\dots,N}$ to $\left\{E_i'\right\}_{i=1,\dots,N}$ following transformation (A.2). It is

$$\ell(V) = V^i \ell(E_i) \quad , \quad \ell(V) = V^i \left(T^{-1}\right)_i^{j'} \ell\left(E_{j'}'\right)\,, \tag{A.11}$$

and, thanks to the arbitrariness of V, we get

$$\ell\left(E_{j'}'\right) = T_{j'}^i \ell(E_i)\ . \tag{A.12}$$

Since the components of covector ℓ with respect to the basis $\left\{\ell_E^i\right\}_{i=1,\dots,N}$ vary in accordance with the matrix T, we say that they change in a *covariant* way.

A.1.3 Definition of tensor

Two distinct but equivalent definitions are provided below.

Definition 1. *A tensor is a linear function* $\mathfrak{L}$ *that arranges* $k-$copies *of* $\mathcal{V}$ *and* $h-$copies *of* $\mathcal{V}^*$ *to a scalar quantity* $\alpha \in \mathbb{R}$*,*

$$\mathfrak{L} : \left(\underbrace{\mathcal{V}\times\dots\times\mathcal{V}}_{k-copies} \times \underbrace{\mathcal{V}^*\times\dots\mathcal{V}^*}_{h-copies}\right) \to \mathbb{R}\,. \tag{A.13}$$

The linear function $\mathfrak{L}$ acts on the elements of $\mathcal{V}$ and $\mathcal{V}^*$, therefore, the image of $\mathfrak{L}$ is independent of the bases considered in $\mathcal{V}$ and $\mathcal{V}^*$. A multi-index function L can be associated to $\mathfrak{L}$ defined by

$$L : (i_1,\dots,i_k;j_1,\dots,j_h) \mapsto L_{i_1,\dots,i_k}^{j_1,\dots,j_h} \tag{A.14}$$

such that

$$L_{i_1,\dots,i_k}^{j_1,\dots,j_h} V^{i_1}\dots V^{i_k}\ell_{j_1}\dots\ell_{j_h} = \mathfrak{L}\left(V^{i_1}E_{i_1},\dots,V^{i_k}E_{i_k},\ell_{j_1}\ell_E^{j_1},\dots,\ell_{j_h}\ell_E^{j_h}\right)\,. \tag{A.15}$$

We are naturally led to the second definition of a tensor as a multi-index function.

Definition 2. *A tensor is a multi-index function L defined by*

$$L : (i_1, ..., i_k; j_1, ..., j_h) \mapsto L_{i_1 ... i_k}^{j_1 ... j_h} , \tag{A.16}$$

where $L_{i_1 ... i_k}^{j_1 ... j_h}$ *arranges k-contravariant components of a vector V of* $\mathcal{V}$ *and h-covariant components of a covector* ℓ *of* $\mathcal{V}^*$ *to the element of* $\mathbb{R}$ *given by*

$$L_{i_1 ... i_k}^{j_1 ... j_h} V^{i_1} ... V^{i_k} \ell_{j_1} ... \ell_{j_h} \tag{A.17}$$

that is basis independent.

A.1.4 Scalar product and covariant components of a vector

Scalar product

Let $\mathcal{V}$ be a real vector space of dimension N equipped with the scalar product $\langle \cdot, \cdot \rangle_{\mathcal{V}} : \mathcal{V} \times \mathcal{V} \to \mathbb{R}$. Let $\{E_i\}_{1,...,N}$ be a basis of $\mathcal{V}$. Given two vectors V and W of $\mathcal{V}$, we have

$$\langle V, W \rangle_{\mathcal{V}} = \left\langle V^i E_i, W^j E_j \right\rangle_{\mathcal{V}} = \left\langle E_i, E_j \right\rangle_{\mathcal{V}} V^i W^j . \tag{A.18}$$

Let g be the metric tensor defined by

$$g_{ij} = \left\langle E_i, E_j \right\rangle_{\mathcal{V}} , \tag{A.19}$$

we get

$$\langle V, W \rangle_{\mathcal{V}} = g_{ij} V^i W^j . \tag{A.20}$$

If basis $\{E_i\}_{i=1,...,N}$ is orthonormal in $\mathcal{V}$, then g_{ij} is equal to the Kronecker delta δ_{ij}. With an abuse of notation, it is usually written $(g^{-1})^{ij} = g^{ij}$.

Covariant components of a vector

Let $\mathcal{V}$ a subspace of $\mathbb{R}^N$ and $\mathcal{V}^*$ its dual. Let us consider the function φ defined by

$$\varphi : \mathcal{V} \to \mathcal{V}^* \quad , \quad \varphi(V) : W \mapsto \langle V, W \rangle_{\mathcal{V}} , \tag{A.21}$$

with V and W in $\mathbb{R}^N$. The function φ is bijective and we have $\langle V, W \rangle_{\mathcal{V}} = g_{ij} V^i W^j$, where V^i and W^j are the components of V and W with respect to a basis of $\mathcal{V}$. Consequently, given a vector V in $\mathbb{R}^N$, there exists a one-to-one relationship between V and the covector defined by $g_{ij} V^i$. with an abuse of nomenclature, the quantities $V_j = g_{ij} V^i$ are usually named *covariant*

components of vector V. In our notation, superscripts denote the contravariant components of a vector, and subscripts denote the covariant ones.

A.2 Gauss divergence theorem for bounded surfaces

Theorem 1. *Let us consider a basis $\{e_i\}_{i=1,2,3}$ of $\mathbb{R}^3$. All tensor fields in $\mathbb{R}^3$ will be represented by their components with respect to this basis. Let $\mathcal{M}$ be a compact subset of $\mathbb{R}^3$ with a smooth boundary $\partial\mathcal{M}$. Let N be the outward-pointing unit normal of $\partial\mathcal{M}$. For any differentiable vector field W, it yields*

$$\int_{\mathcal{M}} \frac{\partial W^a}{\partial x^a}\, dV = \int_{\partial\mathcal{M}} W^a\, N_a\, ds\,. \tag{A.22}$$

Hereafter, the generalization of the divergence theorem for bounded surfaces is given. This result is fundamental for deriving boundary conditions in second-gradient continuum models.

Theorem 2. *Let us consider a basis $\{e_i\}_{i=1,2,3}$ of $\mathbb{R}^3$. All tensor fields in $\mathbb{R}^3$ will be represented by their components with respect to this basis. Let $\partial\mathcal{M}$ be a smooth bounded surface of $\mathbb{R}^2$ and let $\partial\partial\mathcal{M}$ its smooth boundary. Let P be the field of projection operator on tangent space and let ν be the outward-pointing unit normal of $\partial\partial\mathcal{M}$. For any vector field W, it yields*

$$\int_{\partial\mathcal{M}} \frac{\partial W^a_{\parallel}}{\partial x^c}\, P^c_a\, ds = \int_{\partial\partial\mathcal{M}} W^a_{\parallel}\, \nu_a\, d\ell\,, \tag{A.23}$$

where $W^a_{\parallel} = P^a_b W^b$.

Appendix B

DVC additional details

B.1 DVC hardware and DVC parameters

Table B.1 reports the hardware parameters of the experiment, and Table B.2 the DVC parameters.

Table B.1 DVC hardware parameters

Tomograph	North Star Imaging X50+
X-ray source	XRayWorX XWT-240-CT
Target / Anode	W (reflection mode)
Filter	none
Voltage	120 kV
Current	180 µA
Tube to detector	500 mm
Tube to object	272.685 mm
Detector	Dexela 2923
Definition	1536×1944 pixels (2×2 binning)
Number of projections	1200
Angular amplitude	360°
Frame average	5 per projection
Frame rate	10 fps
Acquisition duration	25 min 58 s
Reconstruction algorithm	filtered back-projection
Gray Levels amplitude	8 bits
Volume size	$1723 \times 491 \times 813$ voxels (after crop)
Field of view	$143 \times 40.75 \times 67.48$ mm^3 (after crop)
Image scale	83 µm/voxel

Table B.2 DVC analysis parameters.

DIC software	Correli 3.0 [83]
Image filtering	none
Element length (mean)	6 vx
Shape functions	linear (T4 elements [68])
Mesh	see Figure 3.16
Matching criterion	penalized sum of squared differences
Regularization length	$\ell_m = 25$ vx
Interpolant	cubic

B.2 Gray level residuals

The gray level residual fields are reported in Figure B.1 for each loading step. The residual field was fairly homogeneous, except in the immediate vicinity of the supports (particularly at the top and bottom right), where high local flexure of the beam ends was not fully captured, partly because of the presence of cardboard. Higher RMS residuals found for the fourth scan were due to a residual field that had larger values on average throughout the sample. In that case, the larger deflection and especially more significant flexure of the beams produced a larger residual over the whole specimen.

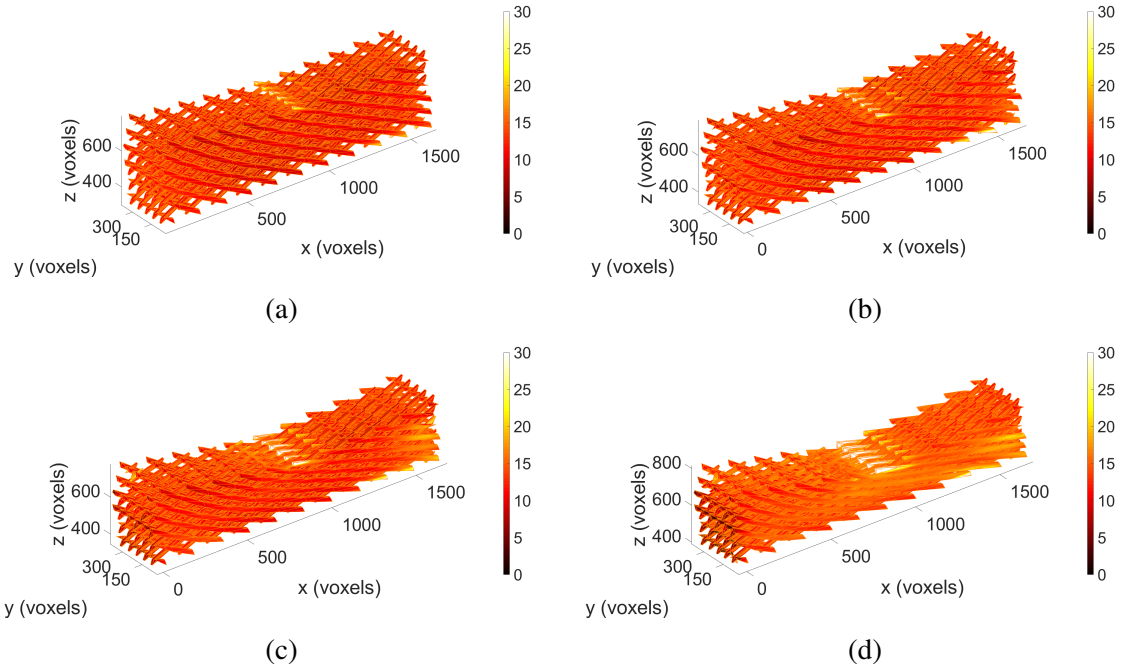

Fig. B.1 Gray level residual fields for the different considered loading steps: (a) 24 mm, (b) 29 mm, (c) 34 mm and (d) 39 mm deflections. Axis labels are expressed in voxels, the dynamic range for registered volumes was 255 (8 bits). The residuals are shown on the meshes in their deformed configuration.